Signal Processing for Next Generation Coriolis Flow Metering



Ming Li

Pembroke College

University of Oxford

A thesis submitted for the degree of

Doctor of Philosophy

November 2018

Signal Processing for Next Generation Coriolis Flow Metering

Ming Li

Pembroke College, Oxford

Submitted in partial fulfilment of the requirements of the Degree of Doctor of Philosophy at the University of Oxford.

Trinity 2018

ABSTRACT

This thesis aims to develop new signal processing techniques for Coriolis flowmeters. Two/multi-phase flow metering is a long established problem in many applications (e.g. the oil & gas, chemical, biotech, pharmaceutical industries) and no perfect solution is available.

In the light of this challenge, recent developments in the Coriolis flowmeters are explored and issues for applying Coriolis flowmeter in two-phase flow conditions are identified. Benchmarks for both empty-to-full batch and continuous two-phase flow reflecting real-world applications are developed for evaluating signal processing techniques. Then current Coriolis flowmeter signal processing techniques are reviewed and tested using the benchmark examples.

A new family of signal processing techniques based on complex signal processing are developed: these include Complex Bandpass Filter (CBF), Complex Notch Filter (CNF) and a combination of CBF with CNF (CBF-CNF). The new techniques are compared with the current methods via the benchmarks and exhibit good performance.

CBF and CBF-CNF are implemented in a prototype transmitter to test alongside with an ‘Oxbox’ transmitter which is a laboratory version of the Foxboro CFT-50/1 (a commercial transmitter developed by the Oxford research group). Signal generator tests are carried out first in order to validate the proper operation of each new technique. Next, single-phase flow tests are carried out to demonstrate that the new algorithms running on the prototype transmitter measure accurately and, joined to a flow tube, can perform as a basic Coriolis flowmeter. Finally, two-phase (water/air) flow tests are carried out with the new algorithms. The performance is compared with that of the Oxbox. From the results, the new CBF and CBF-CNF algorithms perform comparably with the Oxbox at low Gas Void Fraction (GVF), while at high GVF they reduce frequency and phase difference standard deviation by as much as 10 times.

Finally, a new non-linear state space model with Extended Kalman Filter (EKF) is developed as a further promising signal processing technique for Coriolis flowmeter. The new model shows good performance compared with both existing and complex signal processing based techniques but some challenges need to be solved before EKF can be implemented in a prototype transmitter.

ACKNOWLEDGEMENT

I would thank my supervisors Prof. Manus Henry and Prof. Stephen Duncan for their help and support during my whole DPhil research life. Their guidance and assistance has always helped direct me to the right path and to provoke innovative ideas which have led to the completion of this thesis. Prof. Manus Henry brings me to the Coriolis flowmeter world and opens a new research door for me. I deeply enjoy the theory combined with experiment research style and am excited when good results come out. He gives me tremendous advices not only in research area but also personal lives with great kindness and patience. We also enjoy our conference and experimental test travelling in Taiwan, Florence (last minute flight cancellation), Coventry and Glasgow. Prof. Stephen Duncan helps me to improve my theoretical analysis area where I have been particularly weak in the past. He gives me lots of innovative ideas and pathways to carry them out which helps me learn a lot in the statistical and system identification area. Also I interrupt him a lot with many questions and he is always giving me very useful feedback.

I also give many thanks to the senior research members at The Advanced Instrumentation Research Group – Dr. Michael Tombs, Dr. Feibiao Zhou, Prof. David Clarke, Mr. Jez Bowles and Dr. Salah Karout for their constant support. Dr. Michael Tombs has helped me to solve endless coding and hardware platform problems with great patience. We have also frequently discussed useful ideas and experiment results. Dr. Feibiao Zhou has guided me to carry out experimental work in the Oxford lab smoothly. He is always ready to help me when I meet tricky challenges during experiments. All of them are very keen to share ideas and discuss with me to inspire new ideas and convey correct experiment trials.

I would also like to thank all the friends I met in Oxford and other places during my DPhil research. We have relaxed together and enjoyed life during my long research journey. Finally I would like to thank all the members of my family including my parents and my younger brother for their tolerance and support over this DPhil research. Without their help, support and encouragement, I would have achieved very little in my life.

CONTENTS

1. INTRODUCTION 1

1.1 THE CORIOLIS MASS FLOW METER 1

1.2 HISTORICAL DEVELOPMENT 5

1.3 SINGLE-PHASE FLOW TUBE MODELLING 9

1.3.1 The Coriolis Force 9

1.3.2 Forces Acting on the Flow Tube 10

1.3.3 Translational Motion 12

1.3.4 Rotational Motion 13

1.3.5 Calculation of the Mass-Flow Rate 15

1.3.6 Calculation of Fluid Density 17

1.4 THE CHALLENGE OF BATCHING FROM EMPTY 18

1.5 TWO/THREE-PHASE FLOW CHALLENGE 20

1.5.1 Fluid Measurement Error Sources 27

1.5.2 Signal Tracking Error Sources 34

1.5.3 Three-phase/Multi-phase Measurement Outlook 36

1.5.4 Existing Solutions 41

1.6 CORIOLIS FLOW METER SIGNAL PROCESSING 43

2. BENCHMARK TESTS 48

2.1 BATCHING FROM EMPTY-TO-FULL SIMULATION BENCHMARK 49

2.2 TWO-PHASE FLOW EXPERIMENTAL AND SIMULATION BENCHMARKS 57

3. CURRENT CORIOLIS FLOW METER SIGNAL PROCESSING METHODS 67

3.1 CURRENT METHODS 68

3.1.1 Adaptive Notch Filters for Frequency Tracking *68*

3.1.2 Discrete Fourier Transform for Amplitude and Phase Difference Tracking *70*

3.1.3 Zero-crossing Method *72*

3.1.4 Digital Phase Locked Loop for Frequency Tracking *74*

3.1.5 Quadrature Demodulation for Amplitude and Phase Difference Tracking *75*

3.1.6 Digital Correlation *77*

3.1.7 Hilbert Transform *78*

3.2 SIMULATION RESULTS 79

3.2.1 Batching from Empty-to-full Benchmark Simulation *80*

3.2.2 Batching from Empty-to-full Experimental Data *84*

3.2.3 Two-phase Benchmark Simulation *87*

3.2.4 Two-phase Flow Experimental data with Varying GVF *93*

3.3 SUMMARY 94

4. COMPLEX SIGNAL PROCESSING 96

4.1 COMPLEX BANDPASS FILTER 97

4.2 COMPLEX NOTCH FILTER 101

4.3 COMPLEX BANDPASS FILTER WITH COMPLEX NOTCH FILTER 104

4.4 SIMULATION RESULTS 105

4.4.1 Batching from Empty-to-full Benchmark Simulation *105*

4.4.2 Batching from Empty-to-full Sensor Data Test *109*

4.4.3 Two-phase Benchmark Simulation *110*

4.4.4 Two-phase Flow Experimental Data Test *116*

4.4.5 Algorithm Complexity *118*

4.5 SUMMARY 119

5. EXPERIMENTS 120

5.1 HARDWARE PLATFORM 121

5.2 SIGNAL GENERATOR TEST 122

5.3 SINGLE-PHASE EXPERIMENTS 128

5.4 BATCHING FROM EMPTY-TO-FULL EXPERIMENTS 132

5.5 TWO-PHASE EXPERIMENTS 142

5.6 SUMMARY 156

6. NON-LINEAR STATE SPACE MODEL 158

6.1 EXISTING STATE SPACE MODELS 159

6.1.1 Modified Cartesian Model 159

6.1.2 Nearly Constant Frequency Model 160

6.2 NEW CONTINUOUS TIME MODEL 161

6.3 CONTINUOUS-DISCRETE EXTENDED KALMAN FILTER 163

6.4 DISCRETE TIME MODEL 165

6.5 EXTENDED KALMAN FILTER 167

6.6 SIMULATION 168

6.6.1 Batching from Empty-to-full Benchmark Simulation 168

6.6.2 Batching from Empty-to-full Experimental Sensor Data Test 172

6.6.3 Two-phase Flow Benchmark 174

6.6.4 Two-phase Flow Varying GVF Sensor Data Test 179

6.7 SUMMARY 181

7. CONCLUSION 182

7.1 FURTHER IMPROVEMENTS 186

7.1.1 Experimental Facility 186

7.1.2 Faster Batching Applications *187*

7.1.3 Fluid Measurement Error Correction *187*

7.1.4 Two/Multi-mode Vibration *188*

7.1.5 Better Control Algorithm Design *190*

7.1.6 Kalman Filter Improvement *190*

8. REFERENCES **192**

9. APPENDICES **209**

LIST OF TABLES

TABLE 1.1: COMPARING CORIOLIS FLOWMETERS' TWO/THREE-PHASE MEASUREMENT ABILITY 42

TABLE 4.1: COMPLEXITY OF EACH ALGORITHM 118

TABLE 5.1: TOTALIZED MASS MEASUREMENT RESULT OF CBF BASED TRANSMITTER 140

TABLE 5.2: TOTALIZED MASS MEASUREMENT RESULT OF CBF-CNF BASED TRANSMITTER 140

TABLE 5.3: TOTALIZED MASS MEASUREMENT RESULT OF OXBOX TRANSMITTER 140

TABLE 9.1: SIGNAL GENERATOR TEST MEAN RESULT OF NEW METHODS 210

TABLE 9.2: SIGNAL GENERATOR TEST STANDARD DEVIATION RESULT OF NEW TRANSMITTERS 211

LIST OF FIGURES

FIGURE 1.1: DIFFERENT CORIOLIS FLOWMETER FLOW TUBE DESIGNS [2] 2

FIGURE 1.2: FOXBORO CORIOLIS MASS FLOW METER 4

FIGURE 1.3: THE CORIOLIS EFFECT ON A ROTATING FLOW TUBE 9

FIGURE 1.4: CORIOLIS FLOWMETER FLOW TUBE MODEL [28] 11

FIGURE 1.5: TIME DIFFERENCE OF INPUT SENSOR SIGNALS 16

FIGURE 1.6: TWO-PHASE VERTICAL FLOW PATTERN [41] 21

FIGURE 1.7: TWO-PHASE HORIZONTAL FLOW PATTERN [41] 21

FIGURE 1.8: ERRORS OF TWO-PHASE MASS FLOW RATE MEASUREMENT USING OXBOX 24

FIGURE 1.9: TWO-PHASE DENSITY MEASUREMENT ERROR USING OXBOX 25

FIGURE 1.10: MAXIMUM AND MINIMUM MASS FLOW RATE RESULTS USING OXBOX 26

FIGURE 1.11: MAXIMUM AND MINIMUM DENSITY RESULTS USING OXBOX 26

FIGURE 1.12: DECOUPLING EFFECT OF TWO-PHASE FLOW IN CORIOLIS FLOWMETERS 29

FIGURE 1.13: ASYMMETRIC BUBBLE DISTRIBUTION AT LOW FLOW RATE [44] 30

FIGURE 1.14: SPEED OF SOUND FOR AIR-WATER TWO-PHASE FLOW [45] 32

FIGURE 1.15: CONVENTIONAL WELL-TESTING LAYOUT [41] 38

FIGURE 1.16: IMPROVED WELL-TESTING LAYOUT INTEGRATING MFPMS [41] 38

FIGURE 1.17: THREE-PHASE FLOW MEASUREMENT NET OIL SKID [53] 39

FIGURE 1.18: SENSOR SIGNALS DURING STEADY SINGLE-PHASE FLOW (2 KG/S WATER) 44

FIGURE 1.19: SENSOR SIGNALS DURING TWO-PHASE FLOW (2 KG/S, 15% GVF) 45

FIGURE 1.20: TIMING DIAGRAM FOR CORIOLIS FLOWMETER TRANSMITTER (FROM [38]) 46

FIGURE 2.1: EXPERIMENTAL SENSOR DATA FROM EMPTY-FULL TRANSITION 50

FIGURE 2.2: MEASURED SENSOR PARAMETERS FROM EMPTY-FULL TRANSITION 50

FIGURE 2.3: SENSOR PARAMETERS DURING TRANSITION PERIOD FOR BATCHING FROM EMPTY-TO-FULL 52

FIGURE 2.4: SENSOR DATA DURING TRANSITION PERIOD FOR BATCHING FROM EMPTY-TO-FULL 52

FIGURE 2.5: OXBOX SENSOR SIGNAL DURING BATCHING FROM EMPTY-TO-FULL 53

FIGURE 2.6: OXBOX SENSOR SIGNAL PARAMETERS DURING BATCHING FROM EMPTY-TO-FULL 54

FIGURE 2.7: SENSOR SIGNALS FOR EMPTY-TO-FULL BATCH PROCESS DURING TRANSITION PERIOD 56

FIGURE 2.8: SENSOR SIGNAL INPUT PARAMETERS FOR EMPTY-TO-FULL BATCH PROCESS 56

FIGURE 2.9: SENSOR SIGNALS DURING TWO-PHASE FLOW (3 KG/S, 5% GVF) 58

FIGURE 2.10: SENSOR PARAMETERS DURING TWO-PHASE FLOW (3 KG/S, 5% GVF) 59

FIGURE 2.11: SENSOR SIGNALS DURING FAST VARYING GVF TWO-PHASE FLOW 60

FIGURE 2.12: SENSOR PARAMETERS DURING FAST VARYING GVF TWO-PHASE FLOW (MEASURED BY NEW RESEARCH TRANSMITTER) 60

FIGURE 2.13: SENSOR SIGNALS DURING SLOWLY VARYING GVF TWO-PHASE FLOW 61

FIGURE 2.14: CALCULATED SENSOR PARAMETERS DURING SLOWLY VARYING GVF TWO-PHASE FLOW 61

FIGURE 2.15: COMPARISON BETWEEN RWM AND MRWM 65

FIGURE 2.16: SENSOR SIGNALS GENERATED BY MRWM 66

FIGURE 3.1: A TYPICAL STRUCTURE OF SMM-ANF REPRODUCED FROM[79] (THIS STRUCTURE DOES NOT REFLECT EQUATION (3.1)) 68

FIGURE 3.2: ZERO-CROSSING METHOD DIAGRAM 73

FIGURE 3.3: DIGITAL PHASE LOCKED LOOP DIAGRAM [89] 75

FIGURE 3.4 : EMPTY-TO-FULL BATCHING SIMULATION: AMPLITUDE TRACKING PERFORMANCE 80

FIGURE 3.5: EMPTY-TO-FULL BATCHING SIMULATION: FREQUENCY TRACKING PERFORMANCE 81

FIGURE 3.6: EMPTY-TO-FULL BATCHING SIMULATION: PHASE DIFFERENCE TRACKING PERFORMANCE 81

FIGURE 3.7: AMPLITUDE TRACKING RMSES COMPARISON FOR BATCH SIMULATION 82

FIGURE 3.8: FREQUENCY TRACKING RMSES COMPARISON FOR BATCH SIMULATION 83

FIGURE 3.9: PHASE DIFFERENCE TRACKING RMSES COMPARISON FOR BATCH SIMULATION 83

FIGURE 3.10: AMPLITUDE TRACKING DELAY COMPARISON 84

FIGURE 3.11: AMPLITUDE TRACKING PERFORMANCE USING BATCHING SENSOR DATA 85

FIGURE 3.12: FREQUENCY TRACKING PERFORMANCE USING BATCHING SENSOR DATA 85

FIGURE 3.13: PHASE DIFFERENCE TRACKING PERFORMANCE USING BATCHING SENSOR DATA 86

FIGURE 3.14: AMPLITUDE TRACKING PERFORMANCE WITH NO ADDED NOISE 87

FIGURE 3.15: FREQUENCY TRACKING PERFORMANCE WITH NO ADDED NOISE 88

FIGURE 3.16: PHASE DIFFERENCE TRACKING PERFORMANCE WITH NO ADDED NOISE 88

FIGURE 3.17: AMPLITUDE TRACKING RMSES COMPARISON FOR TWO-PHASE SIMULATION 89

FIGURE 3.18: FREQUENCY TRACKING RMSES COMPARISON FOR TWO-PHASE SIMULATION 89

FIGURE 3.19: PHASE DIFFERENCE TRACKING RMSES COMPARISON FOR TWO-PHASE SIMULATION 90

FIGURE 3.20: AMPLITUDE TRACKING RMSES AT DIFFERENT LEVEL OF NOISE 91
FIGURE 3.21: FREQUENCY TRACKING RMSES AT DIFFERENT LEVEL OF NOISE 91
FIGURE 3.22: PHASE DIFFERENCE TRACKING RMSES AT DIFFERENT LEVEL OF NOISE 92
FIGURE 3.23: AMPLITUDE TRACKING PERFORMANCE USING TWO-PHASE SENSOR DATA ... 93
FIGURE 3.24: FREQUENCY TRACKING PERFORMANCE USING TWO-PHASE SENSOR DATA .. 93
FIGURE 3.25: PHASE DIFFERENCE TRACKING PERFORMANCE USING TWO-PHASE SENSOR DATA 94
FIGURE 4.1: ZEROS AND POLES ROTATION FOR CBF 98
FIGURE 4.2: ORIGINAL ELLIPTIC FILTER AND SHIFTED CBF MAGNITUDE RESPONSE 98
FIGURE 4.3: FILTERING PROCESS OF CBF 99
FIGURE 4.4: FILTERING PROCESS OF CNF 102
FIGURE 4.5: ZEROS AND POLES ROTATION FOR CNF 103
FIGURE 4.6: GROUP DELAY OF 5TH ORDER CNF 103
FIGURE 4.7: FILTERING PROCESS OF CBF-CNF 104
FIGURE 4.8: AMPLITUDE TRACKING OF CBF DURING EMPTY-TO-FULL BATCH PROCESS 105
FIGURE 4.9: FREQUENCY TRACKING OF CBF DURING EMPTY-TO-FULL BATCH PROCESS 106
FIGURE 4.10: PHASE DIFFERENCE TRACKING OF CBF DURING EMPTY-TO-FULL BATCH PROCESS 106
FIGURE 4.11: AMPLITUDE TRACKING RMSES COMPARISON FOR BATCH SIMULATION ... 107
FIGURE 4.12: FREQUENCY TRACKING RMSES COMPARISON FOR BATCH SIMULATION ... 107
FIGURE 4.13: PHASE DIFFERENCE TRACKING RMSES COMPARISON FOR BATCH SIMULATION 108
FIGURE 4.14: AMPLITUDE TRACKING DELAY COMPARISON 108
FIGURE 4.15: AMPLITUDE TRACKING PERFORMANCE USING BATCHING SENSOR DATA ... 109

FIGURE 4.16: FREQUENCY TRACKING PERFORMANCE USING BATCHING SENSOR DATA ..109

FIGURE 4.17: PHASE DIFFERENCE TRACKING PERFORMANCE USING BATCHING SENSOR DATA ..110

FIGURE 4.18: AMPLITUDE TRACKING PERFORMANCE WITH NO NOISE ..111

FIGURE 4.19: FREQUENCY TRACKING PERFORMANCE WITH NO NOISE..111

FIGURE 4.20: PHASE DIFFERENCE TRACKING PERFORMANCE WITH NO NOISE..112

FIGURE 4.21: AMPLITUDE TRACKING RMSES COMPARISON FOR TWO-PHASE SIMULATION ..112

FIGURE 4.22: FREQUENCY TRACKING RMSES COMPARISON FOR TWO-PHASE SIMULATION ..113

FIGURE 4.23: PHASE DIFFERENCE TRACKING RMSES COMPARISON FOR TWO-PHASE SIMULATION ..113

FIGURE 4.24: AMPLITUDE TRACKING RMSES AT DIFFERENT LEVEL OF NOISE ..114

FIGURE 4.25: FREQUENCY TRACKING RMSES AT DIFFERENT LEVEL OF NOISE ..115

FIGURE 4.26: PHASE DIFFERENCE TRACKING RMSES AT DIFFERENT LEVEL OF NOISE ...115

FIGURE 4.27: AMPLITUDE TRACKING PERFORMANCE USING TWO-PHASE SENSOR DATA.116

FIGURE 4.28: FREQUENCY TRACKING PERFORMANCE USING TWO-PHASE SENSOR DATA 117

FIGURE 4.29: PHASE DIFFERENCE TRACKING PERFORMANCE USING TWO-PHASE SENSOR DATA ..117

FIGURE 5.1: HARDWARE PLATFORM FOR TRANSMITTER..121

FIGURE 5.2: SIGNAL GENERATOR INPUT PARAMETERS AND CBF TRACKED RESULTS (0.1V INPUT MEASUREMENT) ..124

FIGURE 5.3: SIGNAL GENERATOR INPUT PARAMETERS AND CBF-CNF TRACKED RESULTS (0.1V INPUT MEASUREMENT) ..124

FIGURE 5.4: CBF TRANSMITTER STEADY STATE TEST RESULT OF SIGNAL GENERATOR (INPUT AND OUTPUT NORMALIZED TO 1V) 125
FIGURE 5.5: CBF-CNF TRANSMITTER STEADY STATE TEST RESULT OF SIGNAL GENERATOR (INPUT AND OUTPUT NORMALIZED TO 1V) 126
FIGURE 5.6: MRWM SIGNAL PROGRAMMED INTO SIGNAL GENERATOR 127
FIGURE 5.7: CBF TRANSMITTER MRWM TEST RESULT OF SIGNAL GENERATOR 127
FIGURE 5.8: CBF-CNF TRANSMITTER MRWM TEST RESULT OF SIGNAL GENERATOR ... 128
FIGURE 5.9: SINGLE-PHASE EXPERIMENT FACILITY 129
FIGURE 5.10: EXPERIMENT FACILITY 130
FIGURE 5.11: FLUID MEASUREMENT CONTROLLER USER INTERFACE 130
FIGURE 5.12: ZERO-INTERCEPT LINEAR FITTING FOR PHASE DIFFERENCE AND MASS FLOW RATE 131
FIGURE 5.13: BATCHING FROM EMPTY-TO-FULL EXPERIMENT FACILITY DIAGRAM 133
FIGURE 5.14: CBF BASED TRANSMITTER PERFORMANCE OF BATCHING PROCESS 135
FIGURE 5.15: CBF-CNF BASED TRANSMITTER PERFORMANCE OF BATCHING PROCESS .. 136
FIGURE 5.16: OXBOX PERFORMANCE OF BATCHING PROCESS 136
FIGURE 5.17: CBF TRACKED PARAMETERS DURING THE TRANSITION 137
FIGURE 5.18: CBF-CNF TRACKED PARAMETERS DURING THE TRANSITION 138
FIGURE 5.19: OXBOX TRACKED PARAMETERS DURING THE TRANSITION 138
FIGURE 5.20: MEAN AND SPREAD OF SHIFT MASS 141
FIGURE 5.21: SPREAD OF MODIFIED CMF TOTALIZED MASS RESULT COMPARISON 142
FIGURE 5.22: TWO-PHASE FLOW EXPERIMENT DIAGRAM 143
FIGURE 5.23: TWO-PHASE FLOW EXPERIMENT TESTING POINTS 144

FIGURE 5.24: AMPLITUDE STANDARD DEVIATION COMPARISON BETWEEN CBF AND OXBOX 146

FIGURE 5.25: AMPLITUDE STANDARD DEVIATION COMPARISON BETWEEN CBF-CNF AND OXBOX 147

FIGURE 5.26: FREQUENCY STANDARD DEVIATION COMPARISON BETWEEN CBF AND OXBOX 147

FIGURE 5.27: FREQUENCY STANDARD DEVIATION COMPARISON BETWEEN CBF-CNF AND OXBOX 148

FIGURE 5.28: PHASE DIFFERENCE STANDARD DEVIATION COMPARISON BETWEEN CBF AND OXBOX 148

FIGURE 5.29: PHASE DIFFERENCE STANDARD DEVIATION COMPARISON BETWEEN CBF-CNF AND OXBOX 149

FIGURE 5.30: MASS FLOW RATE STANDARD DEVIATION COMPARISON BETWEEN CBF AND OXBOX 149

FIGURE 5.31: MASS FLOW RATE STANDARD DEVIATION COMPARISON BETWEEN CBF-CNF AND OXBOX 150

FIGURE 5.32: DENSITY STANDARD DEVIATION COMPARISON BETWEEN CBF AND OXBOX 150

FIGURE 5.33: DENSITY STANDARD DEVIATION COMPARISON BETWEEN CBF-CNF AND OXBOX 151

FIGURE 5.34: RESULT OF AMPLITUDE STANDARD DEVIATION RATIO 153

FIGURE 5.35: RESULT OF FREQUENCY STANDARD DEVIATION RATIO 153

FIGURE 5.36: RESULT OF PHASE DIFFERENCE STANDARD DEVIATION RATIO 154

FIGURE 5.37: RESULT OF MASS FLOW RATE STANDARD DEVIATION RATIO 154

FIGURE 5.38: RESULT OF DENSITY STANDARD DEVIATION RATIO 155

FIGURE 6.1: AMPLITUDE TRACKING PERFORMANCE FOR EMPTY-TO-FULL BATCH PROCESS 169

FIGURE 6.2: FREQUENCY TRACKING PERFORMANCE FOR EMPTY-TO-FULL BATCH PROCESS 169

FIGURE 6.3: PHASE DIFFERENCE TRACKING PERFORMANCE FOR EMPTY-TO-FULL BATCH PROCESS 170

FIGURE 6.4: AMPLITUDE TRACKING RMSES COMPARISON FOR BATCH SIMULATION 170

FIGURE 6.5: FREQUENCY TRACKING RMSES COMPARISON FOR BATCH SIMULATION 171

FIGURE 6.6: PHASE DIFFERENCE TRACKING RMSES COMPARISON FOR BATCH SIMULATION 171

FIGURE 6.7: AMPLITUDE TRACKING DELAY COMPARISON 172

FIGURE 6.8: AMPLITUDE TRACKING PERFORMANCE USING BATCHING SENSOR DATA 173

FIGURE 6.9: FREQUENCY TRACKING PERFORMANCE USING BATCHING SENSOR DATA 173

FIGURE 6.10: PHASE DIFFERENCE TRACKING PERFORMANCE USING BATCHING SENSOR DATA 173

FIGURE 6.11: AMPLITUDE TRACKING PERFORMANCE WITH NO NOISE 174

FIGURE 6.12: FREQUENCY TRACKING PERFORMANCE WITH NO NOISE 175

FIGURE 6.13: PHASE DIFFERENCE TRACKING PERFORMANCE WITH NO NOISE 175

FIGURE 6.14: AMPLITUDE TRACKING RMSES COMPARISON FOR TWO-PHASE SIMULATION 176

FIGURE 6.15: FREQUENCY TRACKING RMSES COMPARISON FOR TWO-PHASE SIMULATION 176

FIGURE 6.16: PHASE DIFFERENCE TRACKING RMSES COMPARISON FOR TWO-PHASE SIMULATION 177

FIGURE 6.17: AMPLITUDE TRACKING RMSES AT DIFFERENT LEVEL OF NOISE 178

FIGURE 6.18: FREQUENCY TRACKING RMSES AT DIFFERENT LEVEL OF NOISE 178

FIGURE 6.19: PHASE DIFFERENCE TRACKING RMSES AT DIFFERENT LEVEL OF NOISE ... 179

FIGURE 6.20: AMPLITUDE TRACKING PERFORMANCE USING TWO-PHASE SENSOR DATA. 180

FIGURE 6.21: FREQUENCY TRACKING PERFORMANCE USING TWO-PHASE SENSOR DATA 180

FIGURE 6.22: PHASE DIFFERENCE TRACKING PERFORMANCE USING TWO-PHASE SENSOR DATA 180

FIGURE 7.1: COMPARISON OF STANDARD DEVIATIONS FOR OXBOX AND CBF TECHNIQUES FOR MASS FLOW RATE AT 0.5 KG/S 184

FIGURE 7.2: COMPARISON OF STANDARD DEVIATIONS FOR OXBOX AND CBF TECHNIQUES FOR DENSITY AT 0.5 KG/S 185

ACADEMIC OUTPUT

Ming Li, Manus Henry and Stephen Duncan, “A New Method of using Extended Kalman Filtering to Extract Harmonic Signals from Noisy Measurements”, in *2019 American Control Conference (ACC)*, 2019 *(Accepted)*

Ming Li, Manus Henry and Stephen Duncan, “A New Non-linear State Space Model for Tracking Non-stationary Sinusoidal Signal”, *IEEE Transactions on Signal Processing (In writing up process)*

Ming Li, Manus Henry, Michael Tombs and Feibiao Zhou, “Two-phase Flow Experiments with Coriolis Mass Flow Metering using Complex Signal Processing”, *IEEE Transactions on Instrumentation and Measurement (Submitted)*

Ming Li and Manus Henry, “Complex signal processing for Coriolis mass flow metering in two-phase flow,” *Flow Measurement and Instrumentation*, vol. 64, pp. 104–115, Dec. 2018.

Ming Li and Manus Henry, “Complex bandpass filtering for Coriolis mass flow meter signal processing,” in *IECON 2016 - 42nd Annual Conference of the IEEE Industrial Electronics Society*, 2016, pp. 4952–4957.

Ming Li and Manus Petrick Henry, “Signal Processing Methods for Coriolis Mass Flow Metering in Two-Phase Flow Conditions,” in *2016 IEEE International Conference on Industrial Technology (ICIT)*, 2016, pp. 690–695.

NOMENCLATURE

A : Amplitude of sensor signal

A_f : Flow tube cross-sectional area

$\boldsymbol{A_r}$: Centripetal acceleration

$\boldsymbol{A_t}$: Coriolis acceleration

e : Un-correlated white noise processes

E_d : Density error due to speed of sound effect

$E_{\dot{m}}$: Mass flow rate error due to speed of sound effect

f : Frequency of sensor signal

f_s : Sampling rate of sensor signal

H : Filter transfer function

I : Moment of inertia

k : Spring stiffness

$\dot{m}$: Mass flow rate

Δm_l : Unit mass element across the flow tube

$\Delta \boldsymbol{P}$: The Coriolis force

r : Distance between the shaded mass and the centre of rotation of the flow tube

Δt : Time difference between two sensors

v : Gaussian white noise embedded in sensor signal

$\boldsymbol{v}$: Flow velocity

w : Process noise of state space model

x : Sensor signal

α : Gas void fraction

θ_r : Angle between rotated flow tube and horizontal direction

λ : Damping factor

ζ : Damping ratio

ρ_f : Fluid density

σ : Gain factor for the generated random noise

ϕ : Phase difference between two sensors

φ : Phasor of sensor signal

$\boldsymbol{\omega}$: Flow tube rotating angular velocity

LIST OF ABBREVIATIONS AND ACRONYMS

ADC: Analog-to-Digital Converter

ANF: Adaptive Notch Filter

AANF: Amplitude Adaptive Notch Filter

CBF: Complex Bandpass Filter

CNF: Complex Notch Filter

CD-EKF: Continuous-Discrete Extended Kalman Filter

DAC: Digital-to-Analog Converter

DTFT: Discrete Time Fourier Transform

DPLL: Digital Phase Locked Loop

EKF: Extended Kalman Filter

EIT: Electrical Impedance Tomography

FIR: Finite Impulse Response

FFT: Fast Fourier Transform

FCTM: Full Continuous-Time Model

FDTM: Full Discrete-Time Model

GVF: Gas Void Fractions

IIR: Infinite Impulse Response

MCM: Modified Cartesian Model

MLP: Multi-layer Perceptron

MPFMs: Multi-phase Flow Meters

MRWM: Modified Random Walk Model

NCF: Nearly Constant Frequency

ODE: Ordinary Differential Equation

PLL: Phase-Locked Loop

QD: Quadrature Demodulation

RMS: Recursive Mean Square

RMSE: Root Mean Square Error

RSWs: Rectangular Self-Convolution Windows

SEVA: Self-validating Sensor

SMM-ANF: Steiglitz-McBride Adaptive Notch Filter

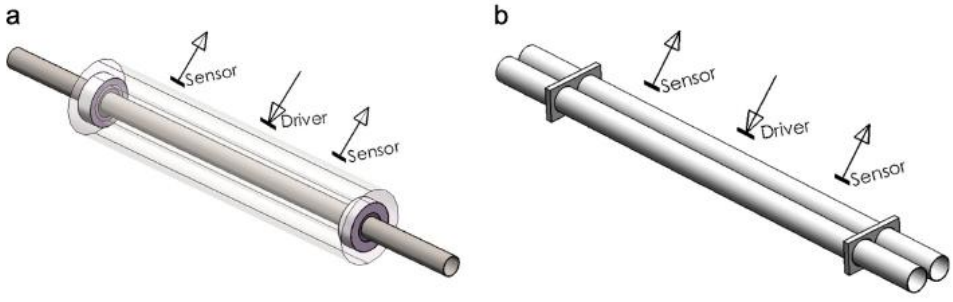
LIST OF APPENDICES

APPENDIX 1 210

1. INTRODUCTION

1.1 The Coriolis Mass Flow Meter

A Coriolis flowmeter consists of two components: a vibrating flow tube in series with the process piping, and an electronic transmitter that maintains flow tube vibration, performs measurement calculations, and transmits measurement data to the user [1]. Examples of different flow tube designs are shown in Figure 1.1, varying from single tube to four tube designs [2]. In each case the locations of two motion sensors and at least one driver are indicated.



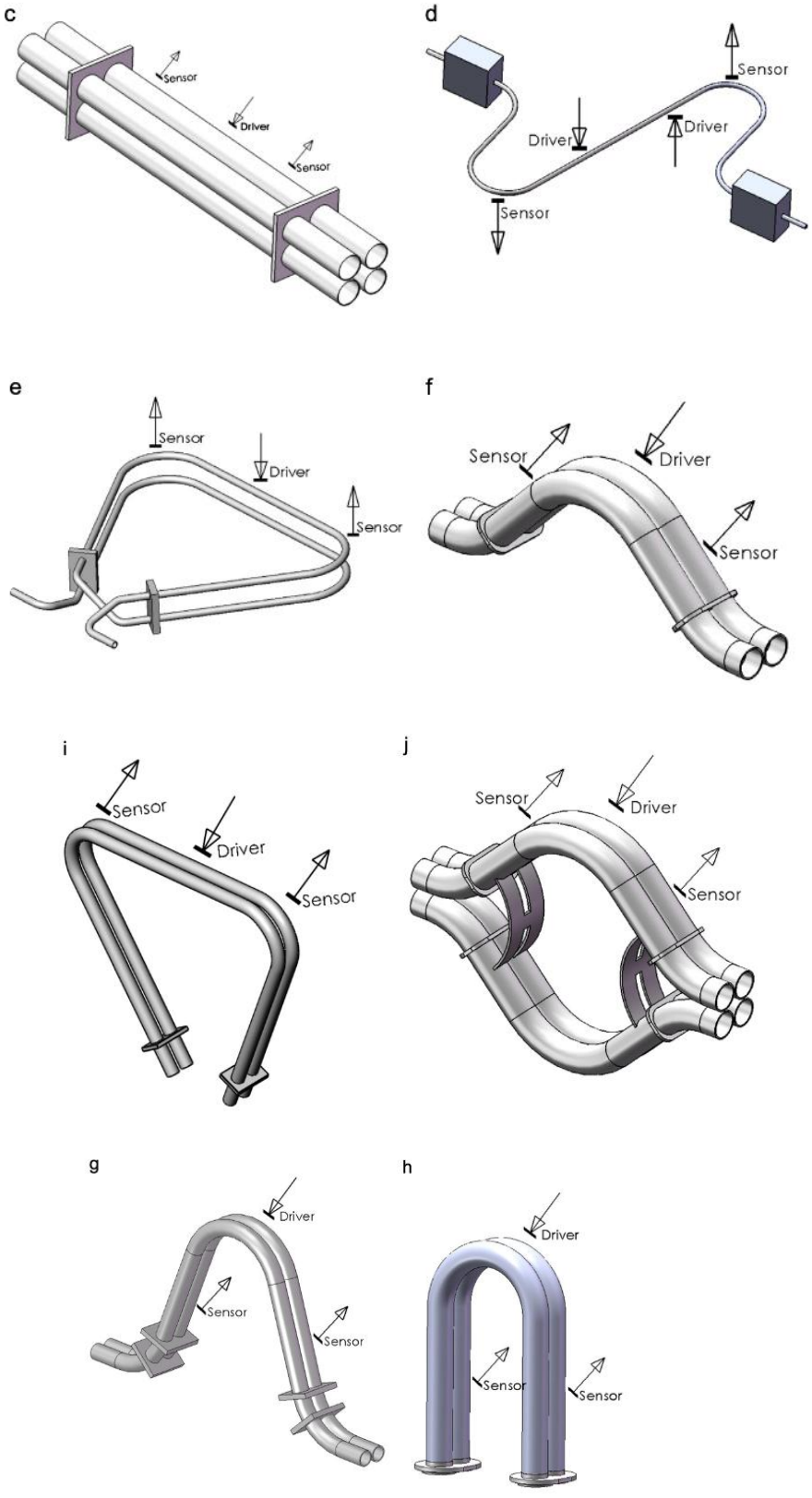


Figure 1.1**:** Different Coriolis Flowmeter Flow Tube Designs [2]

During normal operation, the flow tube vibrates at its natural resonant frequency in a selected mode of vibration (typically the lowest). As the natural resonant frequency varies with the total mass of the flow tube, including the liquid it contains, this frequency is measured and used to calculate the density of the process fluid. In order to vibrate the flow tube and to measure the sensor signal parameters, a transmitter containing electronic processing circuitry is connected to the flow tube: together these form a commercial Coriolis flowmeter. Figure 1.2 shows the Foxboro Coriolis flowmeter combining a CFS-10 flow tube with a CFT-50/51 transmitter, which was co-developed by Oxford University and Invensys and launched as a product in 2002. As described in the next section, this product has been used in two-phase, and more recently three-phase (oil/water/gas) applications, and so may be considered representative of current two-phase capable Coriolis meters. A laboratory version of the CFT50/51 transmitter has been used in the Oxford research group for many years. Known as the 'OxBox', it is able to store high bandwidth data (including raw sensor and drive output data and high speed measurements) unavailable from the commercial version, and permits simple code changes, which may be used to support research work. Performance comparisons will be made between the new algorithms developed in this thesis with those used in the OxBox.

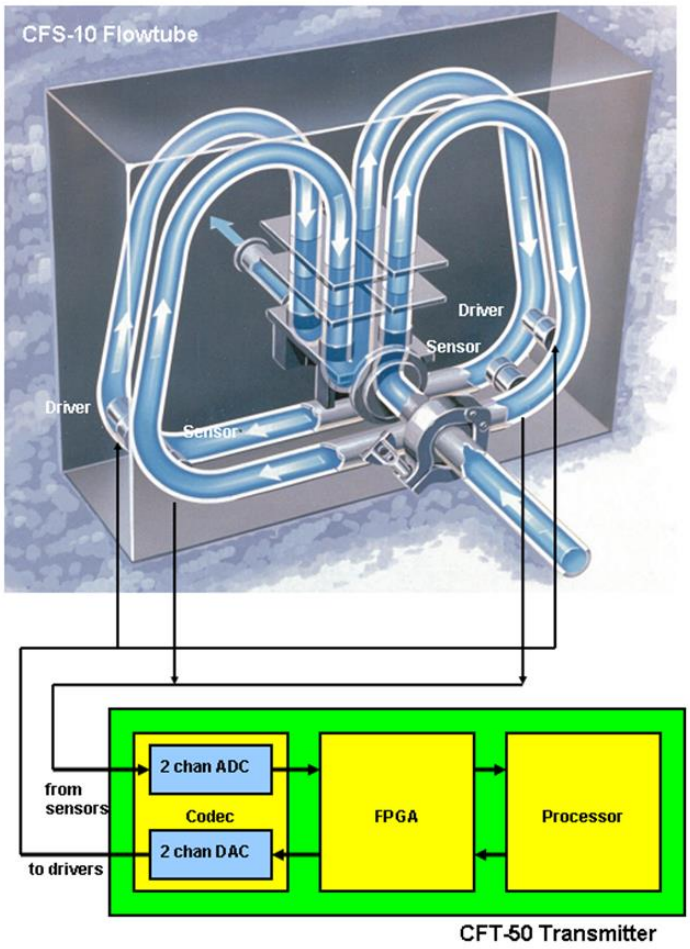


Figure 1.2**:** Foxboro Coriolis Mass Flow Meter

With zero flow under ideal conditions, there is no time delay or phase shift between the two signals generated by the symmetric sensors located on the flow tube. But when liquid or gas flow passes through the flow tube, a time delay or phase shift is generated which is related to the mass flow rate (as discussed in detail in section 1.3).

Accordingly, in a state-of-the-art Coriolis transmitter, the flow tube sensor signals are sampled at high frequency using ADCs, parameter values are extracted (including frequency, phase, amplitude, phase difference, time difference) and then a suitable drive signal is constructed to be sent back via a DAC to maintain flow tube oscillation.

1.2 Historical Development

Baker and Wang describe, in two papers, developments in Coriolis metering up to 1994 [3] and up to 2014 [2]; these periods can conveniently be labelled pre-and post-digital Coriolis development. Possibly the first application of the Coriolis effect for mass flow measurement was proposed by Li and Lee [4]. A T-piece flow tube rotates with the outer casing and is linked to it by a torque tube. As the flow increases, so the T-piece experiences a displacing torque due to the Coriolis acceleration, and this is measured from the displacement of the T-piece relative to the main body [2]. A number of different designs followed, before the proposal of Smith et al. [5] found commercial success in what was to become the first Micro Motion designs (Tulliss and Smith [6]).

Early theoretical developments soon followed the new designs. Durst and Raszillier [7] computed the perturbation of the flow in a rotating pipe and considered the relevance of the resulting flow field and forces to the modelling of Coriolis Meters. Various 3D plots of the flow perturbation were published and the question arose as to whether secondary flows might be a source of asymmetry in the pipe oscillations. Raszillier et al. [8] derived the equation of motion for a straight tube meter while Sultan et al. [9] developed a theory for a U-tube meter.

Based on the founding experiments and theories, the first commercial Coriolis flowmeter was produced by Micro Motion Inc. in 1981 resulting from the patents filed in the 1970s using an analogue transmitter circuit [3]. The initial device consisted of a single U-tube. A twin tube Coriolis flowmeter was introduced in 1983 [10]. The main features of all such meters are: a single inlet splitting into the two tubes; a drive system causing the tubes to vibrate; a pair of sensors to detect the movement of the tubes past

the mid-plane; a strong point around which the tubes vibrate; and an outer cover. Twin tube designs improved the measured sensor signal amplitude while using the same drive energy. This is helpful in improving measurement accuracy and repeatability. Also by adopting two tubes, the deflection is measured from one tube to the other, so that external vibrations are largely eliminated and the measured shift between the tubes has the effect of adding the flows in the two tubes, even if the flow split is not equal. Since its invention, the Coriolis flowmeter market share has increased rapidly in the food, pharmaceutical, chemical, paper, petroleum and petrochemical industries. Liu et al.[11] report that Coriolis flowmeters provide significant capital and operating cost savings compared with more conventional measurement techniques.

As digital techniques have developed, the Coriolis flowmeter has also steadily changed from analogue implementation towards digital implementation. Henry et al. [12] developed Self-validating Sensor (SEVA) technologies, which eventually became the British National Standard (BSI7986:2001 - Specification for data quality metrics for industrial measurement and control systems). By applying the SEVA technique, Henry et al. [13] developed a SEVA digital Coriolis flowmeter. A number of improvements have been achieved over the analogue implementation performance, which can be summarised as:

- High-precision control of flow tube operation, including at very low vibrating amplitudes
- The maintenance of flow tube operation even in highly damped conditions
- High-precision, high-speed measurement

- Compensation for dynamic changes in amplitude
- Compensation for two-phase flow
- Batching to/from empty

Tombs et al. [14] and Henry et al. [15] discussed their all-digital Coriolis flowmeter transmitter, which was able to maintain flow tube operation throughout all conditions of two-phase flow. Key to this technology was the transmitter's ability to respond quickly to flow condition changes and this was also reflected in the flow meter's ability to track changes in flow rates accurately with a fast dynamic response. The results from two- and three-phase flow experiments at Cranfield University based on the transmitter have been presented [16], which suggest how such a meter may be applied as part of a multi-phase metering system.

Morita and Yoshimura [17] also described digital signal processing of the sensor signals and self-calibration. They claimed that the result was "100 times as accurate" as using a conventional discrete Fourier transform in sensor signal measurement. Henry et al. [18] highlighted the differences and advantages of an "all-digital" transmitter design in comparison to existing designs where the signal path had been partly or wholly analogue. One of the most important differences in the all-digital design is the capability of digitally generating a synthesized drive signal in addition to digitally processing the motion signals. Harrold [19] confirmed the improved performance from digital signal processing. Commercial companies such as Micro Motion Inc.[20] and Invensys Inc.[21] have been granted patents for digital signal processing methods for Coriolis flowmeters resulting in improved performance compared to conventional analogue signal processing.

For the digital drive aspect, Clarke [22] discussed a digital implementation of non-linear control of the oscillation amplitude of a Coriolis flow meter using positive feedback of the output velocity to cancel the internal damping, and described a method of determining the gain, and inserting an inverse non-linearity in the loop to create a linear system. After simulations and experiments, the Clarke controller improves the dynamic response of the flow meter. Henry [23] reviewed the improvements due to the digital approach, in particular the possibility of using the flow meter for batching, due to its robustness to conditions when batching to and from empty. Clark et al. [24] described a very fast dynamic response Coriolis flowmeter based on a commercial twin straight-tube meter coupled to a prototype digital transmitter. Their results suggested an order of magnitude, at least, increase in response speed. Kutin et al. [25] implemented a Phase-Locked Loop (PLL) controller using the LabVIEW and the characteristics of such a resonance control system were presented together with some theoretical simulations. Rock et al. [26] presented a control method for a Coriolis transmitter using phasor information of the sensor signals where phase and amplitude control can be done simultaneously by adopting an extended Kalman Filter instead of a conventional low pass filter. Using the Kalman Filter for quadrature demodulation allows much faster estimation of the phasors and reduce the control period by the cycle time by a factor of two compared to Clarke's [22] work. This increases the dynamic response of the meter and can control two modes (Drive Mode and Coriolis Mode) of vibration simultaneously.

1.3 Single-phase Flow Tube Modelling

1.3.1 The Coriolis Force

The relationship between the single-phase liquid mass flow rate and the observed phase difference or time delay is illustrated in Figure 1.3, which shows a rotating straight tube with liquid flow:

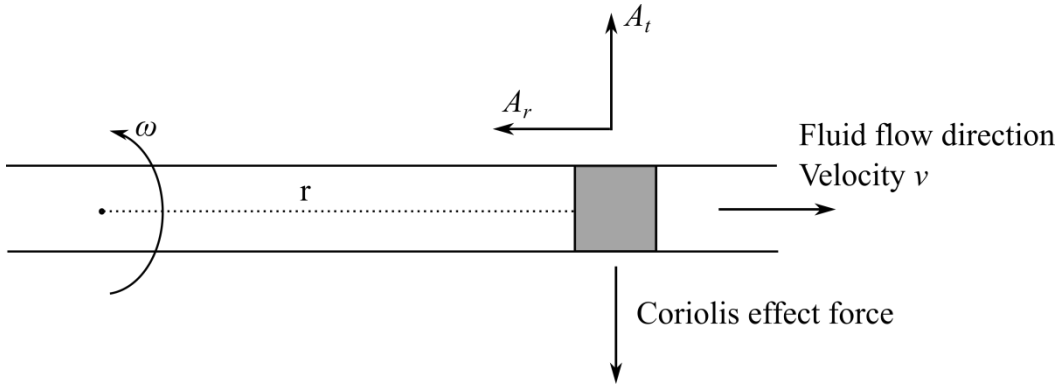


Figure 1.3**:** The Coriolis Effect on a rotating flow tube

Here $\boldsymbol{\omega}$ represents the flow tube rotating angular velocity (rad/s) while $\boldsymbol{A_r}$ represents centripetal acceleration, $\boldsymbol{A_t}$ represents Coriolis acceleration, $\boldsymbol{v}$ represents the flow velocity and r represents the distance between the shaded mass and the centre of rotation of the flow tube. A Coriolis force affects a mass moving inside a rotating system. Considering the shaded mass element, of mass Δm_l , it generates two components of acceleration while rotating as [27]:

$$\begin{aligned} \boldsymbol{A_r} &= \boldsymbol{\omega}^2 r \\ \boldsymbol{A_t} &= 2\boldsymbol{v} \times \boldsymbol{\omega} \end{aligned} \tag{1.1}$$

Here the force to maintain the Coriolis acceleration $\boldsymbol{A_t}$ is provided by the tube rotation, while the shaded mass generates an equal and opposite force on the tube as shown in

Figure 1.3. The Coriolis force $\boldsymbol{\Delta P}$ exerted on the shaded mass unit has a magnitude given by:

$$\boldsymbol{\Delta P} = 2\Delta m_l \boldsymbol{v} \times \boldsymbol{\omega} \tag{1.2}$$

The total Coriolis force P is calculated by integrating ΔP over the length of measurement section which is $2r$ (considering the symmetric part of the other side tube):

$$\boldsymbol{P} = 4\Delta m_l r \boldsymbol{v} \times \boldsymbol{\omega} = 4r\dot{\boldsymbol{m}} \times \boldsymbol{\omega} \tag{1.3}$$

where $\dot{\boldsymbol{m}}$ is the product of Δm_l (mass/length) and $\boldsymbol{v}$ (length/time), and represents the mass flow rate (mass/time) of the fluid enclosed in the vibrating flow tube. The Coriolis force $\boldsymbol{P}$ can be calculated from the time delay between the two sensor signals, while $\boldsymbol{\omega}$ can be calculated from the resonant frequency of the flow tube, and r represents the length of the measurement flow tube. By measuring the above parameters, the mass flow can be directly calculated along with the fluid density.

1.3.2 Forces Acting on the Flow Tube

Taking the vibrating parts from the tube shown in Figure 1.2, we can form a flow tube model with two stiff tubes connected by springs and dampers as shown in Figure 1.4, which is first described in [28].

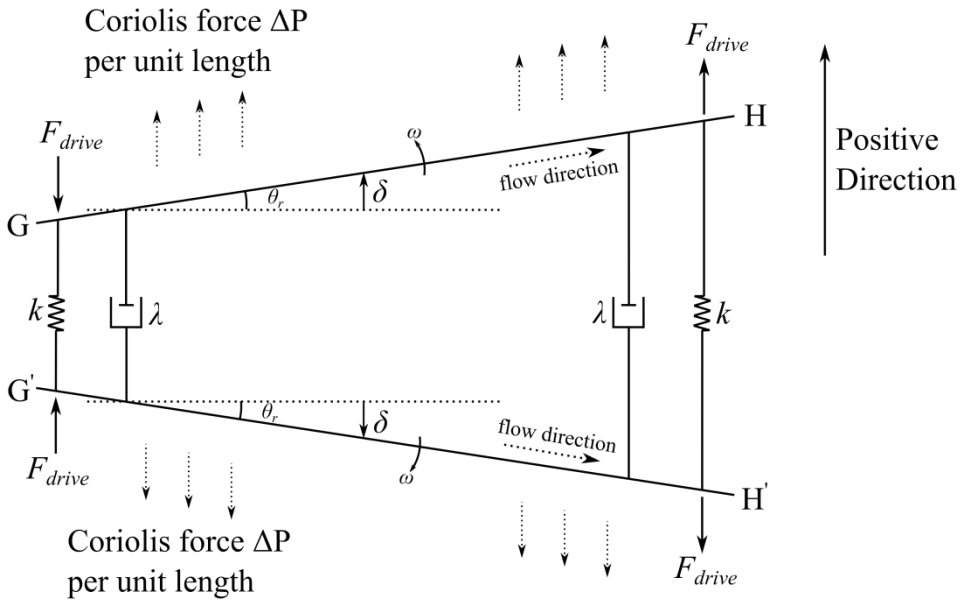


Figure 1.4: Coriolis flowmeter Flow Tube Model [28]

In the model, the driver forces F_{drive} are generated to be in-phase with the sensor signal, with the force directions shown in the figure. The forces cause the two measurement sections GH and G′H′ to rotate in opposite direction with the same magnitude (i.e. using the second mode of vibration of the flow tube). Similar analyses are derived when using other modes of vibration.

Consider the top measurement section GH, for the case when it is in the first half cycle of vibration (rotating anti-clockwise). Let the angle between this tube section and the horizontal be θ_r, given by:

$$\theta_r = A_\theta \sin(\omega t) \tag{1.4}$$

where A_θ is the rotation amplitude. Assume δ is the translational displacement of the section GH, and *2l* is the length of GH. The instantaneous displacement of each of the measurement section ends d_G, $d_{G'}$, d_H and $d_{H'}$ from their position of rest, are

$$\begin{aligned} d_H &= l\theta_r + \delta \\ d_G &= -l\theta_r + \delta \\ d_{H'} &= -l\theta_r - \delta \\ d_{G'} &= l\theta_r - \delta \end{aligned} \tag{1.5}$$

Defining the upwards direction as positive, and recalling equation (1.3), the Coriolis force acting on the measurement section GH are

$$P = -4\dot{\theta}_r \dot{m} l \tag{1.6}$$

From equation (1.5), the force exerted by the spring at point H due to the extension is given by:

$$-k(d_H - d_{H'}) = -2k(l\theta_r + \delta) \tag{1.7}$$

Again the force exerted by the spring at point G due to compression is:

$$-k(d_G - d_{G'}) = 2k(l\theta_r - \delta) \tag{1.8}$$

The force exerted by the damper at point H due to the upward velocity is:

$$-\lambda(\dot{d}_H - \dot{d}_{H'}) = -2\lambda(l\dot{\theta}_r + \dot{\delta}) \tag{1.9}$$

The force exerted by the damper at point G due to the downwards velocity is:

$$-\lambda(\dot{d}_G - \dot{d}_{G'}) = 2\lambda(l\dot{\theta}_r - \dot{\delta}) \tag{1.10}$$

Combining the above equations, we can analyse the motion of the flow tube and form relevant translational and rotational motion equations in the next subsections.

1.3.3 Translational Motion

Assuming *m* is the sum of the mass of the measurement section GH and the enclosed fluid, and taking the upwards direction as positive, we can calculate the translational motion of the GH section by summing the translational motions from equations (1.7) – (1.10):

$$m\ddot{\delta} = -2k(-l\theta_r + \delta) - 2k(l\theta_r + \delta) - 2\lambda(-l\dot{\theta}_r + \dot{\delta}) - 2\lambda(l\dot{\theta}_r + \dot{\delta}) - 4\dot{\theta}_r\dot{m}l \quad (1.11)$$

or:

$$m\ddot{\delta} + 4\lambda\dot{\delta} + 4k\delta = -4\dot{\theta}_r\dot{m}l \quad (1.12)$$

Equation (1.12) is a linear 2nd order differential equation, which can be represented in terms of the Laplace transform by:

$$\Delta(s) = -\frac{-4\dot{m}ls}{ms^2 + 4\lambda s + 4k}\Theta(s) \quad (1.13)$$

Equation (1.13) is a linear 2nd-order non-homogeneous differential equation. By solving equation (1.12), the particular integral for δ is given by [29]:

$$\delta = A_{\delta c}\cos(\omega t) - A_{\delta s}\sin(\omega t) \quad (1.14)$$

where

$$\begin{aligned} A_{\delta c} &= \frac{4\omega A_\theta l\dot{m}(m\omega^2 - 4k)}{(4k - m\omega^2)^2 + 16\lambda^2\omega^2} \\ A_{\delta s} &= \frac{16\omega^2 A_\theta l\dot{m}\lambda}{(4k - m\omega^2)^2 + 16\lambda^2\omega^2} \end{aligned} \quad (1.15)$$

1.3.4 Rotational Motion

Similarly, we can calculate the rotational motion for the measurement section GH. Assuming the rotating moment of inertia is *I* across section GH, we sum the rotational motion from equations (1.7) – (1.10) taking the anti-clockwise direction as positive:

$$I\ddot{\theta}_r = -2k(l\theta_r + \delta)l - 2k(l\theta_r - \delta)l - 2\lambda(l\dot{\theta}_r + \dot{\delta})l - 2\lambda(l\dot{\theta}_r - \dot{\delta})l + 2lF_{drive} \quad (1.16)$$

This can be further simplified as:

$$\ddot{\theta}_r + \frac{4\lambda l^2\dot{\theta}_r}{I} + \frac{4kl^2\theta_r}{I} = \frac{2lF_{drive}}{I} \quad (1.17)$$

which can be matched to a second-order mass spring damper system as:

$$\ddot{x} + 2\zeta\omega_n\dot{x} + \omega_n^2 x = F \quad (1.18)$$

So the natural angular resonant frequency of the flow tube ω_n and damping ratio ζ are:

$$\omega_n = 2l\sqrt{\frac{k}{I}}$$
$$\zeta = \frac{\lambda l}{\sqrt{kI}} \tag{1.19}$$

and

$$F = \frac{2F_{drive}l}{I} \tag{1.20}$$

Replacing I with the moment of inertia of a uniform rod about its end point $\frac{ml^2}{3}$ and taking the Laplace transform of equation (1.17) :

$$\Theta(s) = \frac{6F_{drive}}{mls^2 + 12\lambda ls + 12kl}F(s) \tag{1.21}$$

The driving force is proportional to the sensor voltage which is proportional to the derivative of the rotational component

$$F = K_0\dot{\theta}_r \tag{1.22}$$

where K_0 is a gain value calculated by the controller and is adjusted to place the system poles so that the flow tube oscillation follows a continuously oscillating stable system, and the amplitude of the rotational component θ_r is steady. The controller gain K_0 is calculated in real time by a control algorithm to cancel out the effect of damping, so that $\lambda \approx 0$. Then equation (1.21) becomes:

$$(ms^2 + 12k)\Theta(s) = 0 \tag{1.23}$$

which represents a simple harmonic motion. Thus the frequency ω_{res} of this simple harmonic motion is the same as ω_n and can be described as:

$$\omega_{res} = \omega_n = \sqrt{\frac{12k}{m}} \tag{1.24}$$

1.3.5 Calculation of the Mass-Flow Rate

Assuming the distance between the section GH and G′H′ is D when the flow tube is stationary, then the instantaneous distance between GH and G′H′ when the tube is oscillating is given by:

$$\begin{aligned} D_{HH'} &= D + 2\delta + 2l\theta_r \\ D_{GG'} &= D + 2\delta - 2l\theta_r \end{aligned} \tag{1.25}$$

As mentioned previously, since $\lambda \approx 0$, equation (1.14) becomes

$$\delta = A_{\delta c}\cos(\omega t) \tag{1.26}$$

where

$$A_{\delta c} = \frac{4\omega A_\theta l\dot{m}}{m\omega^2 - 4k} \tag{1.27}$$

Substituting equation (1.4) and (1.26) into (1.25) and differentiating gives the rate of change of the distance between both flow tube ends as:

$$\begin{aligned} \dot{D}_{HH'} &= 2\omega\sqrt{(A_\theta l)^2 + A_{\delta c}^2}\cos(\omega t + \phi/2) \\ \dot{D}_{GG'} &= -2\omega\sqrt{(A_\theta l)^2 + A_{\delta c}^2}\cos(\omega t - \phi/2) \end{aligned} \tag{1.28}$$

Where ϕ is half of the phase difference between two sensor signals and $\tan\phi = 2\frac{A_{\delta c}}{A_\theta l}$.

Here ω represents the flow tube resonant frequency which is the same as ω_{res}.

Since the phase difference is small (typically between $0° \sim 4°$), $\tan\phi \approx \phi$. The measurement algorithm estimates the phase difference ϕ between two sensor signals which is

$$\phi \approx \tan\phi = 2\frac{A_{\delta c}}{A_\theta l} \tag{1.29}$$

Substituting equation (1.27) into (1.29) yields:

$$\phi \approx 2\frac{4\omega A_\theta l\dot{m}}{m\omega^2 - 4k}\frac{1}{A_\theta l} \tag{1.30}$$

Replacing ω with equation (1.24), gives:

$$\phi \approx \frac{\omega\dot{m}}{k} \tag{1.31}$$

Hence the mass flow rate $\dot{m}$ can be represented by:

$$\dot{m} = k\frac{\phi}{\omega} \tag{1.32}$$

where ϕ is the phase difference between two sensors, ω is the resonant frequency and k is the calibration constant which can be deduced from experimental results. This equation can also be represented in terms of the time difference Δt between the two input sensor signals as:

$$\dot{m} = k\Delta t \tag{1.33}$$

The time difference is illustrated by Figure 1.5:

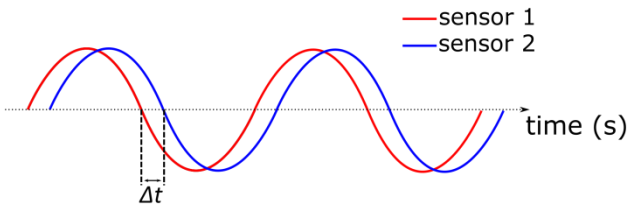


Figure 1.5: Time difference of input sensor signals

From the formula, we observe that there is a linear relationship between the time difference and mass flow rate which is the basic relationship in Coriolis flowmeters [30], [31]. Some Coriolis signal processing techniques (for example the zero crossing method, described later) calculate the time difference directly. However, most of the techniques discussed in this thesis calculate the phases of the sensor signals from which the phase difference is derived. The phase difference, being the ratio of time difference to the resonant period multiplied by 2π, is a useful metric of flow tube sensitivity (for example

when comparing different flow tube designs) and, for any steady resonant frequency, is also proportional to mass flow. Furthermore, the resonant frequency is always calculated directly, and is thus readily available for the calculation of time difference.

However, the assumed linear relationship between time difference and mass flow is no longer valid in the case of two-phase (gas/liquid) flow [32]. Furthermore, the primary focus of this thesis is accurate tracking of the basic parameters of the flow tube sensor signals given their rapid change in two-phase conditions, these parameters being frequency, amplitude and phase, which are required for the generation of a suitable drive output in a digital Coriolis implementation.

Accordingly, throughout this thesis, phase difference will customarily be presented as the final variable for the calculation of mass flow: the further steps of calculating time difference and applying a calibration factor will be assumed as a given for single phase flow.

1.3.6 Calculation of Fluid Density

From equation (1.24), the resonant frequency can be further represented by:

$$\omega = \sqrt{\frac{12k}{m}} = \sqrt{\frac{12k}{m_0 + m_f}} = \sqrt{\frac{12k}{m_0 + 2A_f l \rho_f}} \tag{1.34}$$

where m_0 is the mass of the empty flow tube measurement section GH, m_f is the mass of the enclosed fluid, A_f is the flow tube cross-sectional area and ρ_f is the density of enclosed fluid. Thus the flow density is given by:

$$\rho_f = \frac{1}{2A_f l}\left[\frac{12kl^2}{\omega^2 l^2} - m_0\right] \tag{1.35}$$

This can be further simplified as:

$$\rho_f = a + \frac{b}{\omega^2} \tag{1.36}$$

where *a* and *b* are calibration constants that can be calculated from experimental observations.

In this way, we can calculate the density and the mass flow rate from a Coriolis flowmeter for single phase fluids using the measured frequency and phase difference.

1.4 The Challenge of Batching from Empty

In many industrial applications (e.g. marine fuel bunkering, filling, tanker loading, injecting additives [33]–[35]), a liquid batching from empty process, where the Coriolis flow tube is initially full of air, is considered convenient, while recirculation loops or other arrangements to keep the flowmeter full are seen as expensive and unwieldy. However, accurate measurement is needed to avoid inefficiency or out of specification product. Batching from empty-to-full can be classified as a special case of two-phase flow, since it can be interpreted as the GVF ranging from 100% to 0% in a short period. Some Coriolis flowmeters manufacturers are thus unable to recommend the use of their products in batch applications unless the flow tube can be kept full [15]. The main challenges in batch processes for Coriolis flowmeters is the rapid simultaneous change in frequency, amplitude, phase difference and damping of the flow tube. Hence the Coriolis flowmeter needs to track the varying sensor signal fast enough to generate an in-phase driver signal as well as to update the measurements quickly. The ability to track rapid changes can be described as the dynamic response. A poor dynamic response during batching from empty may result in a flow meter stall, whereby product passes through the meter unmeasured until flow tube oscillation is restored. Clark et al. [24],

[36] have explored the importance of dynamic performance and Henry [23], [34] used the Oxbox to develop improved dynamic performance in batching from empty experiments. Many manufacturers including Krohne, Micro Motion, Endress+Hauser, and Bronkhorst have reported their products' batching from empty ability but do not generally provide information on the dynamic response of their meters [37].

Another industrial application, for example in the food and beverage sector, is to meter fast filling with batches of 0.5 second or less. Accuracy is required despite potential interference from pumps with pulsating flows (e.g. lobe, diaphragm and piston pumps). This problem can be classified as fast batch from full. From a signal processing point of view, this is less challenging because while the phase difference will change rapidly, the amplitude and frequency behaviour is likely to be more stable than for batching from empty.

Overall, Coriolis flowmeters' dynamic performance (which may also be described in terms of their response time) plays a critical role in both batching from empty and fast batching from full applications. However, as stated in [37], for a given flow tube design, the best opportunity to improve the dynamic performance lies in the transmitter. More specifically, most of the delay comes from the signal processing that is used to track the sensor signals' changing characteristics in order to control the flow tube oscillation. For the Oxbox, the total delay is 3 drive signal period cycles [38] between the first datum of a step change being read by the ADC and the corresponding change appearing in the drive output via the DAC. For example, if the flow tube oscillation frequency is 100 Hz, the overall transmitter delay would be 30 ms. Clark et al. [36] state the importance of dynamic performance for Coriolis flowmeters especially for improving batching from

empty measurement accuracy. Improvements that could be introduced into signal processing for Coriolis flowmeters will be discussed later in Section 1.6.

1.5 Two/Three-phase Flow Challenge

With continuing improvements, Coriolis Mass Flow Meter technology has in recent years been touted as the "ideal" flow metering technology except for its 'dirty little secret' which is its two-phase flow performance [39]. Jim Reizner, Technology Leader for Proctor and Gamble (P&G), described Coriolis as the 'meter of choice' for process fluids but that aerated liquids are a big problem for P&G, stating "we have scrapped significant quantities of finished product because of Coriolis flowmeter inaccuracies due to aerated liquids". 'Two-phase' describes a flow of liquid mixed with gas in a closed conduit and is important in an increasing number of applications and industries. Two-phase flow occurs in heat exchangers, steam generators, chemical reactors, oil transportation and many other types of process equipment. The development of accurate instrumentation for on-line monitoring and measurement of solid/liquid concentration and velocity in gas-solid/liquid two-phase flows has proven to be a challenging problem with many scientists and engineers worldwide developing novel techniques for this application [40]. In the oil & gas industry, especially as fields become more economically marginal there is growing demand to meter the individual components of oil, water and gas. Henry et al. [15], [26] reviewed the requirements for a Coriolis flowmeter to obtain mass and density measurements in two-phase flow. Due to the importance and challenges of gas/liquid two-phase flow measurement in the oil and gas industry, this thesis will focus on gas/liquid two-phase flow.

The structure of two-phase flow in a stationary closed conduit has been studied for many years (see for example [38]). Figure 1.6 and Figure 1.7 shows typical two-phase flow patterns observed for liquid superficial velocities against gas superficial velocities.

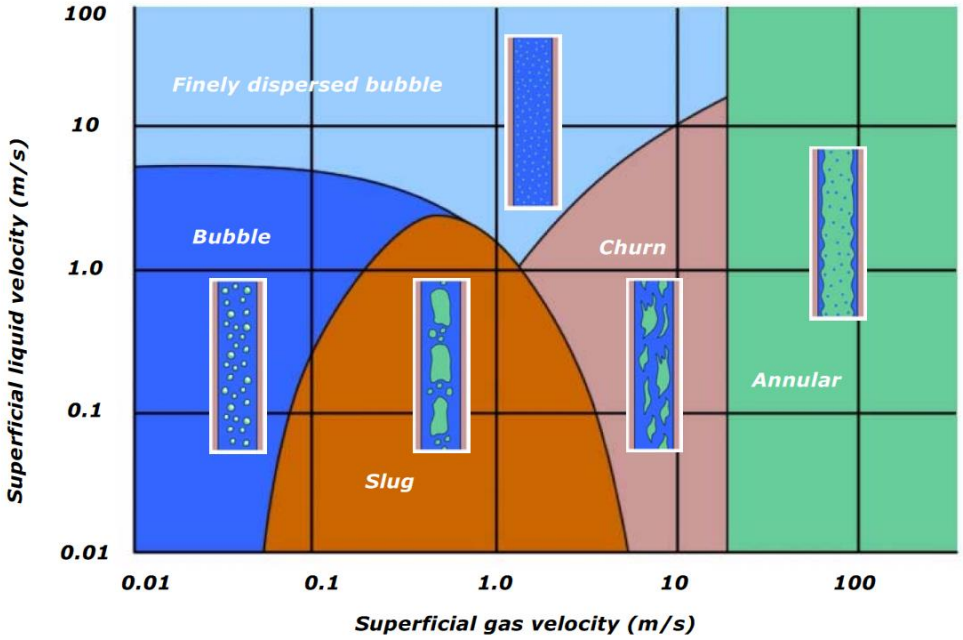


Figure 1.6: Two-phase vertical flow pattern [41]

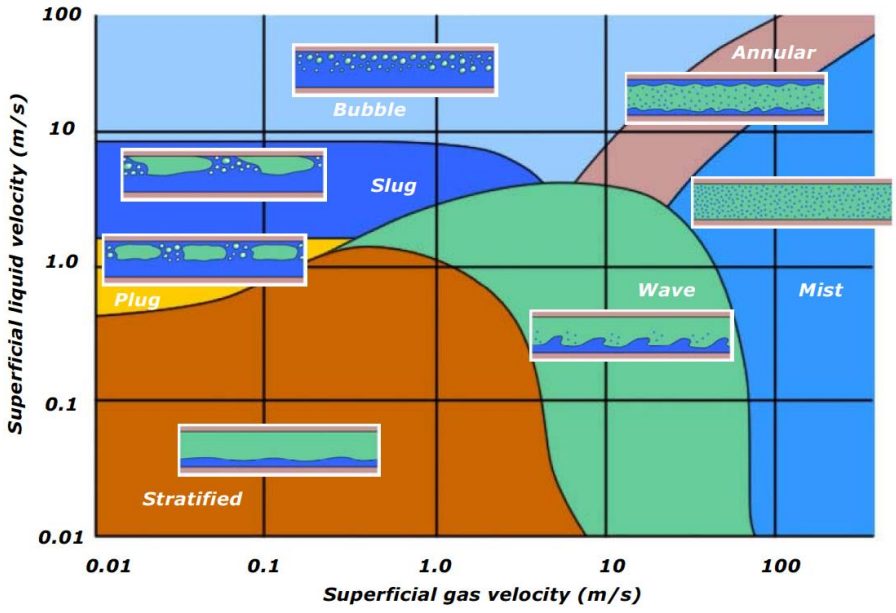


Figure 1.7: Two-phase horizontal flow pattern [41]

However, the flow patterns shown above apply only to a stationary closed conduit with fully developed flow. For Coriolis flowmeters, the flow tube geometry, flow tube orientation, mode of oscillation and other factors also have influence so that the flow patterns may be more complicated.

There are many different error sources in two-phase flow measurement using Coriolis flowmeters. The central motivation of this thesis can be explained by partitioning them into two major error groups: a 'lower level' set of errors associated with the process of tracking frequency, amplitude and phase/phase difference of the Coriolis flow tube sensor signals (from here onwards these will be referred to as the *signal tracking errors*); and a 'higher level' set of errors associated with the process of mapping the measured frequency and phase/time difference to the two-phase bulk mass flow rate and density (referred to as *fluid measurement errors).* Excluding the possibility of flow tube stalling, signal tracking errors are characterised by delay and noise: over any reasonably extended period of time, on average the tracking error for the parameters frequency, amplitude and phase should be zero. Accordingly a "good" tracking algorithm will be characterised by robustness to a wide range of two-phase flow conditions and a low root mean square error. In real experimental conditions, the instantaneous distribution of gas and liquid within the flow tube, the dynamics of the flow tube and the flow tube control response all result in a situation where the true signal parameter values are not known. Here, the best approximation to mean square error is the standard deviation, although this includes the actual variation of the true parameter value as well as the tracking errors. Accordingly, when comparing two algorithms under the same two-phase flow conditions, the better algorithm will have the lower standard deviation, but there may be a limitation on the reduction in standard deviation possible, due to the true variation of

the signal parameter being tracked. While experimental results are the ultimate test of algorithm performance, simulation studies play an important role because here the true parameter values are usually known, so the true tracking errors (via the root mean square error) can be separated from parameter variation.

Fluid measurement errors are typically non-zero on average and repeatable – these may be described as systematic errors. For example, assuming the same relationship between signal parameters and fluid measurements for single-phase measurement (as given in equations (1.33) and (1.36)), then for a given flow tube, liquid, flow rate and GVF, there are likely to be mass flow and density measurement errors: these are likely to be negative (i.e. the meter under-reads), large (with errors exceeding -50% in some conditions), but are often found to be repeatable. Hence compensation techniques can be developed to reduce the fluid measurement errors, as discussed in a later section.

The signal tracking errors feed into the fluid measurement parameter errors, by way of increasing the standard deviation of the mass flow and density measurements. Even in nominally steady two-phase flow, the true instantaneous mass flow and density values will vary, for example during a slugging regime. Another potential error source is variation in the true liquid and gas mass flow rate caused by limitations in the rig control, particularly at higher GVFs. At 0.5 kg/s mass flow rate with 85% GVF, the reference liquid flow rate varies by as much as 15% from its desired value due to high and varying back pressure applied to the water pump by the injected gas and rig control limitations. This type of error is reflected in the measurement standard deviation which cannot be reduced by the signal processing algorithms but can be improved by modifying the two-phase flow experiment rig. However, by temporarily assuming that,

for nominally constant two-phase flow conditions, all measurement variation is attributable to signal tracking errors, the following two graphs illustrate the relationship between the impact of the first (signal tracking) and second (fluid measurement) errors on the observed mass flow and density errors for experimental data collected using the Oxbox and its tracking and measurement algorithms. The GVF reaches as high as 85% where the flow regime is dominated by gas. This is approaching the ‘wet gas’ region (usually defined as GVF > 95%) which is also an important industrial application [42], [43].

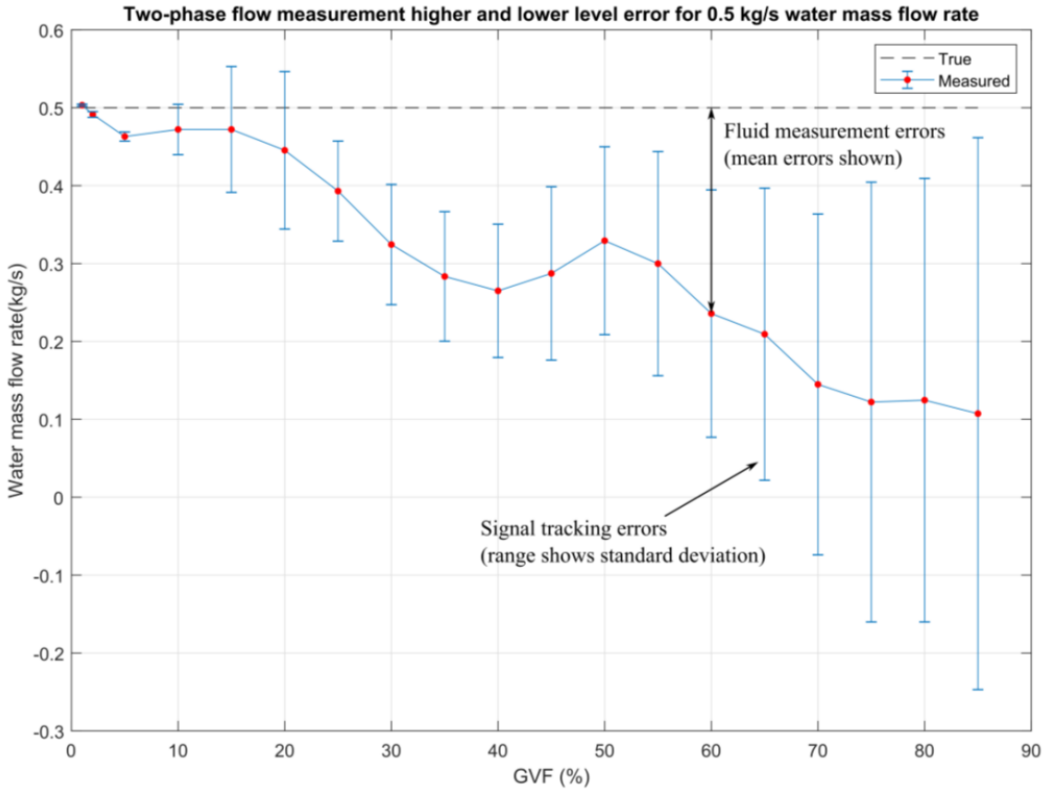


Figure 1.8: Errors of two-phase mass flow rate measurement using Oxbox

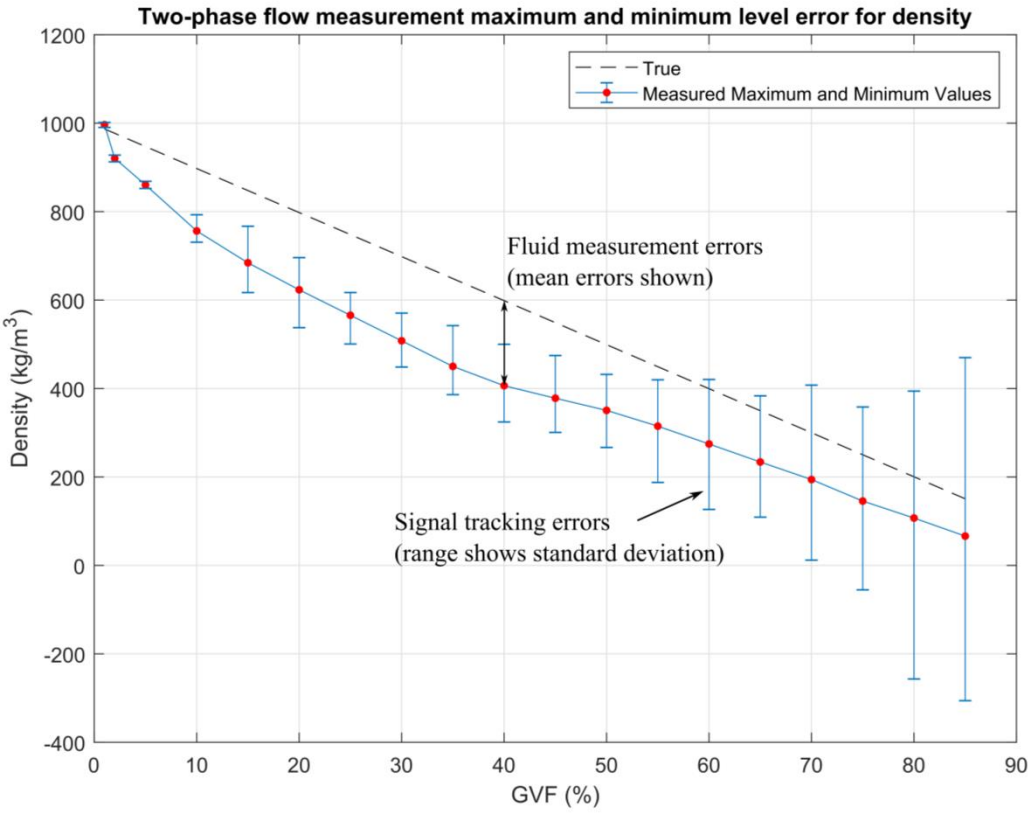


Figure 1.9: Two-phase density measurement error using Oxbox

In the data plotted above, the mean values and standard deviations were calculated using approximately 60 seconds of data under nominally constant experimental conditions. The influence of the signal tracking errors on both the instantaneous process measurements and their averages (which may be used for the development of correction models) are clear. Furthermore, the maximum and minimum measurement values of the instantaneous mass flow rate and density values show far greater variation, making the problem of on-line correction very difficult. The plots below show the range of instantaneous mass flow and density values calculated for the same experiment: it is clear that the signal to noise ratio is poor, especially for high GVFs, making on-line correction difficult.

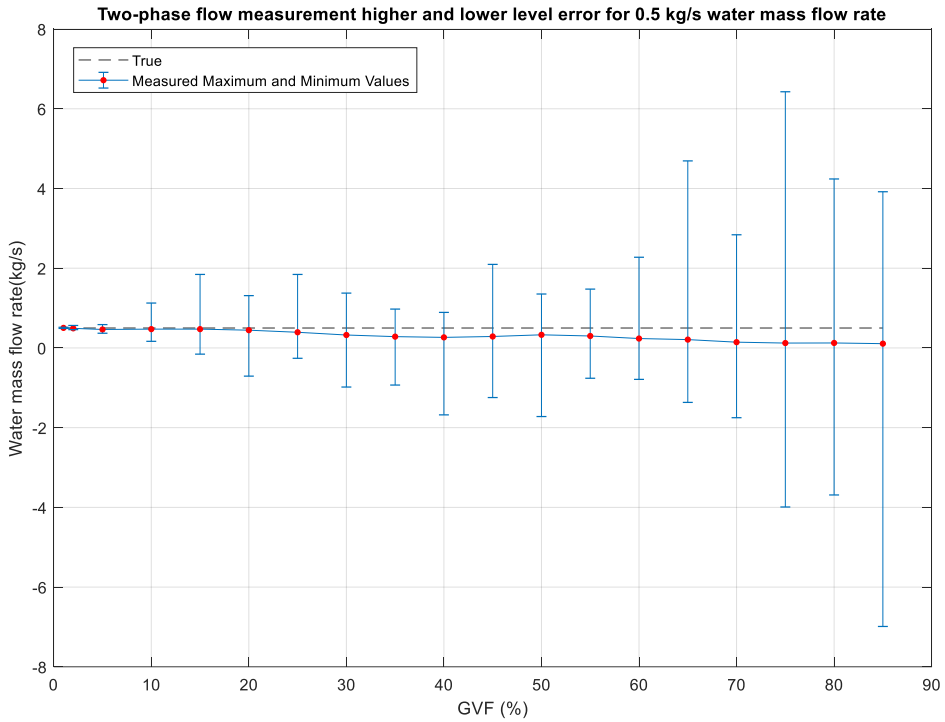


Figure 1.10: Maximum and minimum mass flow rate results using Oxbox

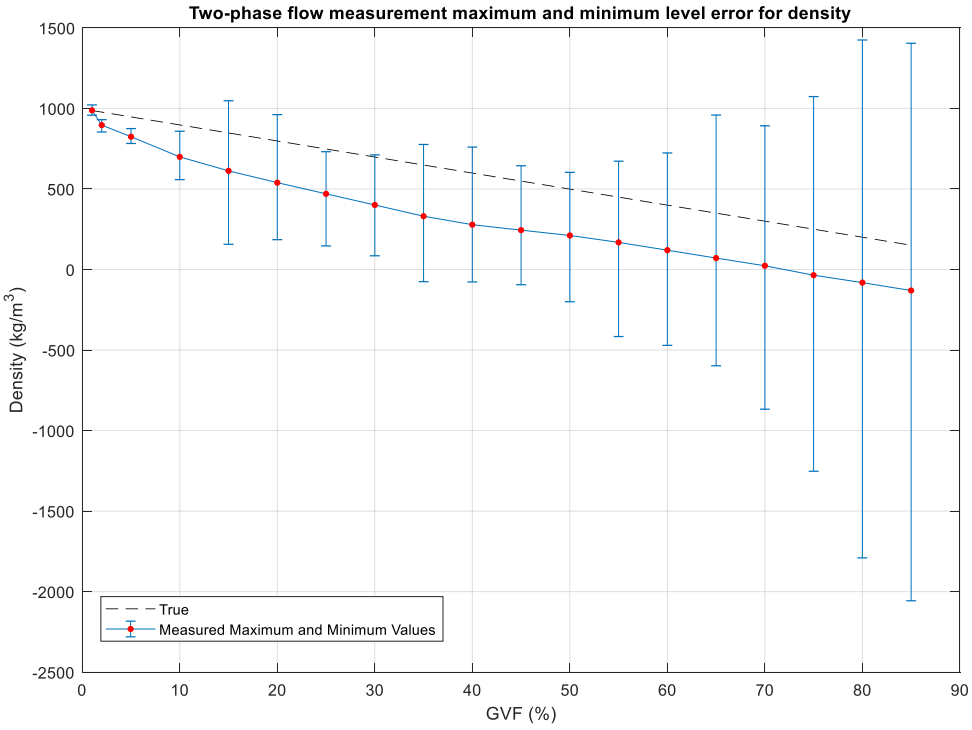


Figure 1.11: Maximum and minimum density results using Oxbox

These plots therefore summarise the primary motivation of this thesis. While much previous work (as discussed below) has been devoted to correcting for the fluid measurement errors, there has been little work on reducing the influence of the signal tracking errors on the resulting two-phase flow measurements, both for model development and for real-time industrial applications, by developing better tracking algorithms in order to reduce the standard deviations of both the signal parameters themselves, and hence of the corresponding mass flow and density measurements. For model development, experimental results with reduced random noise will result in more accurate models, and assist in the analysis of detailed features. For real-time applications, reduced random noise will provide more accurate and responsive tracking of process measurements.

1.5.1 Fluid Measurement Error Sources

To understand the difficulty of measuring two-phase flow with a Coriolis flowmeter, it is important to explore the underlying physical model changes and fluid measurement error sources for two-phase flow inside Coriolis flowmeters compared to single-phase conditions. Fluid measurement error sources have been widely examined in the hope that some of them can be physically modelled and perhaps compensated for since they are generally systematic. Weinstein [44] explored various error sources for two-phase flow measurement using Coriolis flowmeters and carried out a theoretical analysis. Basse [45], [46] also thoroughly reviewed multi-phase flow errors, exploring damping change and its contribution to measurement errors due to the decoupling effect. Liu et al. [47] investigated two-phase error theories due to decoupling and compressibility and carried out experiments for validation. Hemp and Kutin [48], and Gysling and Banach

[49] also explored two-phase flow measurement errors caused by the compressibility of the fluid and the speed of sound in the fluid, using as a first approximation, a small degree of compressibility physical model. Other researchers [50]–[52] have explored different error sources for two-phase flow measurement using Coriolis flowmeters and have developed a range of physical models to understand and to compensate for errors. Currently there is no generally applicable physical mode of two-phase flow behaviour, but techniques have been developed for specific flow tube geometries, applications and fluids [53].

Compared to single-phase flow, the first difference is the “decoupling” effect, which happens due to the presence of entrained gas bubbles inside the liquid. The decoupling error occurs because the accelerations of the liquid phase and gas phase are different [46]. The gas phase experiences a higher acceleration than the liquid phase in the direction of the tube oscillation, which causes mass and density measurement errors. With faster moving gas bubbles, it is possible to imagine the corresponding volume of liquid moving in the opposite direction (i.e. against the motion of the flow tube); this has also been called the “hidden mass” effect. Assuming one volume of gas is moving faster than the surrounding liquid towards the vibrating direction, then it has the effect of masking two volumes of liquid mass. Figure 1.12 shows the decoupling effect of two-phase flow due to the different acceleration of liquid and gas from the transverse view of vibrating tube (GH or G’H’ section in Figure 1.4).

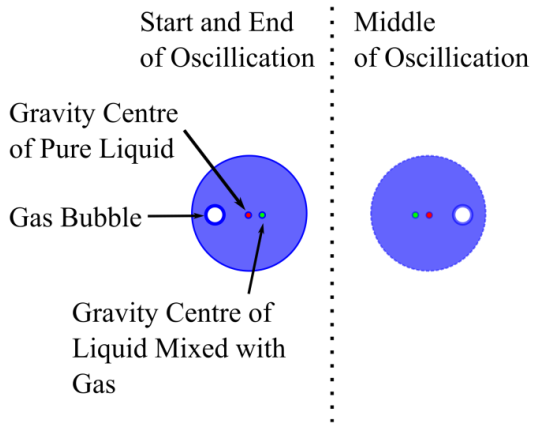


Figure 1.12: Decoupling effect of two-phase flow in Coriolis flowmeters

Additionally, different flow patterns as shown in Figure 1.6 and Figure 1.7 will result in different accelerations of the gas and liquid phases and generate varying decoupling effects, which will cause more complex measurement error behaviour.

In summary, the decoupling effect will cause some of the liquid mass to be "hidden", which leads to under-reading of the mass flow rate and density. To address this under-read, the "bubble theory" [50], [54] was developed to provide a first approximation of the error, enabling a compensation to be applied to the mass flow rate and density measurement. The "bubble theory" considered the inertial losses generated by a single bubble surrounded by much denser fluid, when passing through a vibrating pipe. This model predicts monotonic, negative errors which are a function only of the gas void fraction (GVF), i.e. the proportion of gas by volume in the two-phase mixture. Specifically, the mass flow error takes the form:

$$\frac{\dot{m}_o - \dot{m}_t}{\dot{m}_t} = \frac{-2\alpha}{1-\alpha} \tag{1.37}$$

where $\dot{m}_o$ is observed mass flow rate, $\dot{m}_t$ is true mass flow rate and α is the GVF on the scale 0 to 1. The density error similarly takes the form:

$$\frac{\rho_0 - \rho_t}{\rho_t} = -3\alpha \tag{1.38}$$

where ρ_0 is observed density, and ρ_t is true density. In practice, incorporating "bubble theory" alone does not provide an accurate two-phase flow error model as other error sources also have an influence.

Another error source arises from asymmetric damping caused by an uneven distribution of bubbles inside the flow tube as shown below:

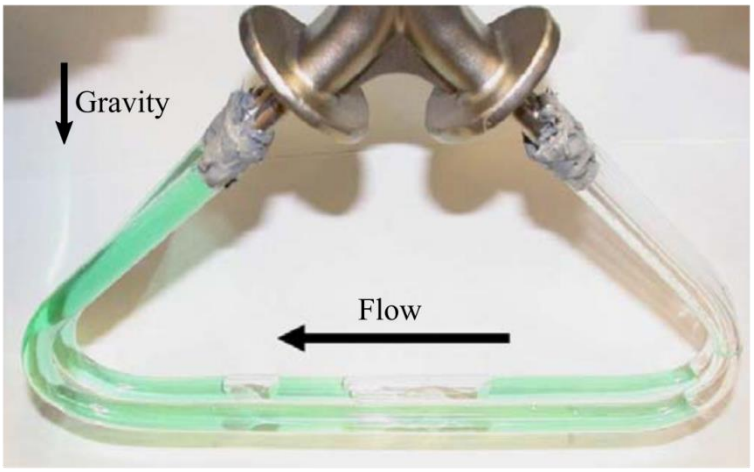


Figure 1.13: Asymmetric bubble distribution at low flow rate [44]

This asymmetric distribution will cause a damping difference at the two ends of the flow tube and will introduce errors into the mass flow rate and density calculations as described in Section 1.3. The asymmetric distribution effect tends to be more significant at lower flow rates and is hard to model since many factors such as flow tube geometry, flow tube orientation, pressure, temperature, viscosity and so on will affect the bubble distribution.

Coriolis flowmeters also suffer from compressibility (also referred to as speed of sound effects) during two-phase flow operation. When the fluid in a Coriolis flowmeter is compressible, the fluid centre of gravity will not move exactly with the flow tube in its

transverse vibrating motion. This will cause the fluid to move in a direction perpendicular to the tube axis, becoming denser in, for example, the upper half of the tube and less dense in the lower half [48]. It can be imagined that some of the liquid is moving faster than the rest in the direction of vibration, which is the opposite effect to the decoupling effect mentioned above. Thus compressibility will cause an over reading of the mass flow rate, while decoupling will cause under reading. The compressibility problem is more serious for gas-liquid two-phase flow since its speed of sound is much smaller than either single-phase gas or liquid as shown in Figure 1.14. Density and mass flow rate measurement errors due to compressibility effects have been derived in [45], [48] as:

$$E_d = \frac{1}{4}\left(\frac{\omega}{c}b\right)^2$$
$$E_{\dot{m}} = \frac{1}{2}\left(\frac{\omega}{c}b\right)^2 \tag{1.39}$$

where c and b are the mixture speed of sound and the tube radius, respectively. ω is the oscillation frequency and E_d and $E_{\dot{m}}$ represent density and mass flow rate error respectively on a 0 to 1 scale. Since the error is related to the mixture speed of sound, it is also referred to as the speed of sound effect error. Even though the assumptions of these theoretical equations are limited, they identify relevant parameters and provide a way to correlate between parameters and error curve changes [47].

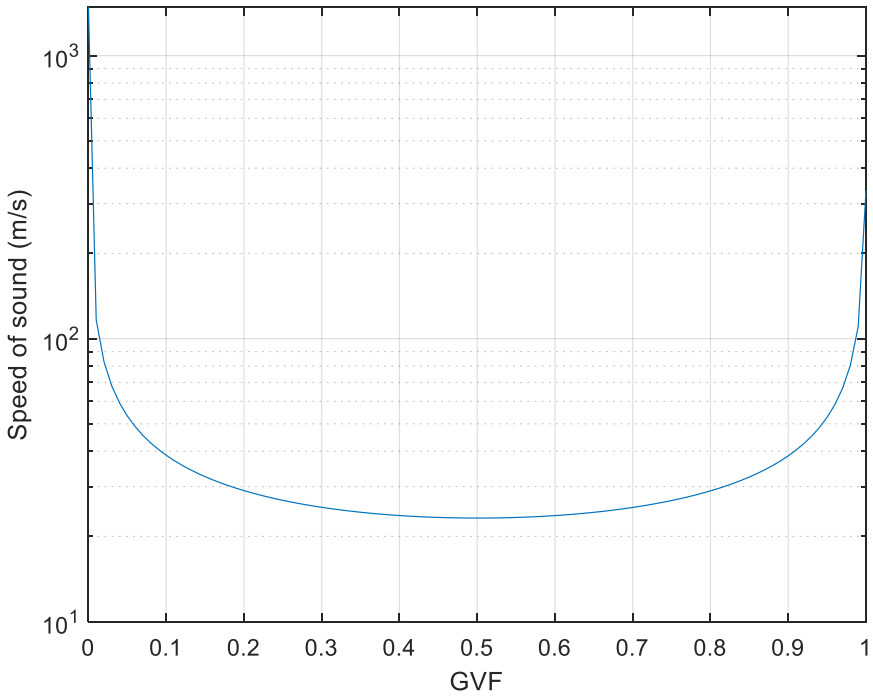


Figure 1.14: Speed of sound for air-water two-phase flow [45]

The speed of sound decreases in two-phase flow [44] as shown above and thus the compressibility error is positive compared with the single-phase flow measurement (here we consider only air-water two-phase flow).

Another relatively unexplored error source for two-phase flow measurement is the compressibility error due to the pressure drop across the flow tube, which is the pressure difference between inlet and outlet of the flow tube (inlet pressure > outlet pressure). The pressure drop depends on the tube design, i.e. mainly upon the length of the tube and its inner diameter [55]; the combination of high flows and high GVFs can lead to a large pressure drop across the flow-tube [56]. Hence gas bubbles will expand towards the outlet of the flow tube and cause different speed of sound effect errors at the two ends, as well as an imbalanced vibration which may have an impact on both the signal tracking and fluid measurement errors.

For twin flow tube designs (e.g. designs *b, f, i, g,* and *h* in Figure 1.1), gas bubbles may not split evenly between the two flow tubes, resulting in an unbalanced vibration. This is an additional error source for the measurements. Wang designed a novel 4 straight tube design to make the flow split more even across each tube [57], [58].

Detailed two-phase physical model exploration for fluid measurement errors analysis is beyond the scope of this thesis, but this overview offers general insight into the fluid measurement errors sources for two-phase flow measurement. In summary, all these error sources make two-phase flow measurement using Coriolis flowmeters challenging and currently there is no simple and efficient physical or compensation model to deal with it. Hence some soft computing and neural network techniques have been adopted to try to compensate for two-phase systematic fluid measurement errors based on the default single-phase mass flow rate and density calculations.

Liu et al. [4] adopt a neural network for on-line compensation of two-phase flow measurement errors based on work at Oxford University. They noted that a Multi-layer Perceptron (MLP) network can give a compact solution suitable for real-time implementation. The trained neural network can take internal sensor parameters (such as observed density, damping, sensor balance, phase sensor signal, apparent flow rate and temperature) and provide corrections. On-line correction in a digital transmitter showed mass flow errors corrected from magnitudes as high as -20% to be within 2% and most are considerably better, while uncorrected experimental errors under high flow rates and low density drops could provide positive errors as high as +1%. Henry et al. [32] explored the two-phase flow metering of heavy oil using Coriolis Mass Flow Metering, arising from the growing industrial need for two-phase flow measurement with high

density and viscosity fluids (most importantly ‘heavy’ oils). Yan et al. [59] provide a recent review of soft computing techniques applied to multi-phase flow metering, including Coriolis meters.

1.5.2 Signal Tracking Error Sources

A less discussed aspect of two-phase flow measurement for Coriolis flowmeters are the signal tracking errors involved in tracking the amplitude, frequency and phase and/or phase difference of the rapidly varying sensor signal. Frequency and phase difference errors propagate into the mass flow and density errors. However, since the instantaneous true values of amplitude, frequency and phase difference are generally unknown in real experimental work, the observed standard deviation can be an alternative means of quantifying the signal tracking errors. The signal tracking errors are directly caused by intrinsic measurement algorithm error, increased noise in the sensor signals and tracking delay which can be considered as the dynamic performance of the tracking algorithm.

Signal tracking algorithms normally have very small intrinsic errors in steady single phase flow conditions. But in two-phase flow, as the amplitude, frequency and phase difference of the sensor signals change rapidly, some algorithms cannot track accurately and will generate intrinsic errors [60] which will contribute to the overall signal tracking error.

When driving Coriolis flowmeters in two-phase flow, the main effect is a dramatic rise and rapid fluctuation in the flow tube damping, since mechanical oscillation energy is lost in the reaction between gas bubbles and the liquid [15]. For any intrinsically safe

flow tube, there is an absolute limit on the current supplied to the drivers. For traditional analogue transmitters, the drive gain (the ratio of the current of the driver to the amplitude of oscillation) may become saturated due to analog amplifier limitations, resulting in a maximum multiplier limit between the sensor amplitude in and the drive signal out. Once this limit is reached or exceeded, the flow tube is liable to stalling i.e. it ceases to vibrate. Should the flow tube damping rise beyond the saturation point, then a further rise in drive current to compensate for the increased damping is not possible, due to drive saturation. As a consequence, the sensor amplitude starts to reduce, but because of drive saturation, this in turn leads to a drop in the drive signal output; the end result is a catastrophic collapse in oscillation amplitude i.e. a flow tube stall. Restarting the flow tube is not possible until damping drops below the saturation limit. The drive gain can have a higher dynamic range using a digital implementation and so it is usually possible to keep the flow tube vibrating, as long as the sensor parameters can be successfully tracked. However, a second limit, shared by both analog and digital designs, is the intrinsic safety limit on the maximum drive current that may be supplied to the flow tubes. With high damping caused by two phase flow, the drive current output may itself become saturated, and if this is insufficient to maintain the desired amplitude of oscillation, then the amplitude will drop, but worse yet, it is liable to vary with the constantly changing damping on the flow tube. One approach to maintaining active control of the drive amplitude is to reduce the amplitude setpoint to a level where the drive current output is no longer saturated, so that compensation can be applied for short-term variations in damping [12]. Background noise levels will also increase due to harmonic noise generated by the excitation of other modes of vibration and white noise generated by the interaction between gas bubbles and liquid. Hence the SNR of the

sensor signal will decrease and makes the measurement result less accurate than that of single phase conditions.

Another error source for the signal tracking level is the amplitude control performance of Coriolis flowmeters. As mentioned previously, the dynamic performance of the measurement process has an impact on generating an appropriate driver signal. Tracking delay causes control dead time which will result in less stable amplitude control. If the drive control update rate is too slow, or there is too much dead-time, the flow tube may stall due to inattention (e.g. resulting from a large phase mismatch between sensor and driver signal) [37]. A second, possibly worse, alternative, is where oscillation is maintained, but inaccurate tracking leads to a phase shift between input and output leading to forced oscillation, and hence wayward frequency of oscillation and poor repeatability. In the high damping conditions of two-phase flow, this may be difficult to detect and correct [15].

In order to decrease the signal tracking error during two-phase flow measurement, an appropriate and fast signal processing technique needs to be developed and it is the focus of this thesis. The improved dynamic performance from the new signal processing technique will benefit the batching from empty-to-full challenge as well.

1.5.3 Three-phase/Multi-phase Measurement Outlook

The logical next step from two-phase flow is three-phase measurement. ‘Three-phase’ or ‘Multi-phase’ is usually used to describe mixtures of oil, water and gas, typically produced in the upstream oil and gas industry [41].

The fluids produced from oil wells are rarely purely liquid or gaseous hydrocarbon mixtures. Most often, the fluid emerges as a multi-phase mixture which is mainly a mixture of oil, water and gas. Traditionally, the flow rates of well fluids have been measured using physical separation of each stream. However, the economics of offshore oil recovery have moved towards subsea completions with multi-phase pipelines over long distances to either the shore or to existing platforms. Hence multi-phase flow measurement technology may be an attractive alternative since it enables measurement of unprocessed well streams very close to the well and the use of Multi-phase Flow Meters (MPFMs) may lead to cost savings in the initial installation [41]. Within the oil and gas industry, it is generally recognised that MPFMs could lead to greater benefits including layout of production facilities, well testing, reservoir management, production allocation, production monitoring, subsea/downhole metering and costs [61].

The use of MPFMs reduces the hardware needed for onshore, offshore topside and offshore subsea applications. Of primary importance is the removal of a dedicated test separator for well-testing applications which brings lots of flexibility for pipeline arrangement, minimises platform space and reduces cost in a big margin. Also by stripping costly well test lines from production facilities, it will benefit unmanned well production, deep water developments and satellite fields. Figures below show conventional well-testing layout and well-testing facilities integrated with MFPMs.

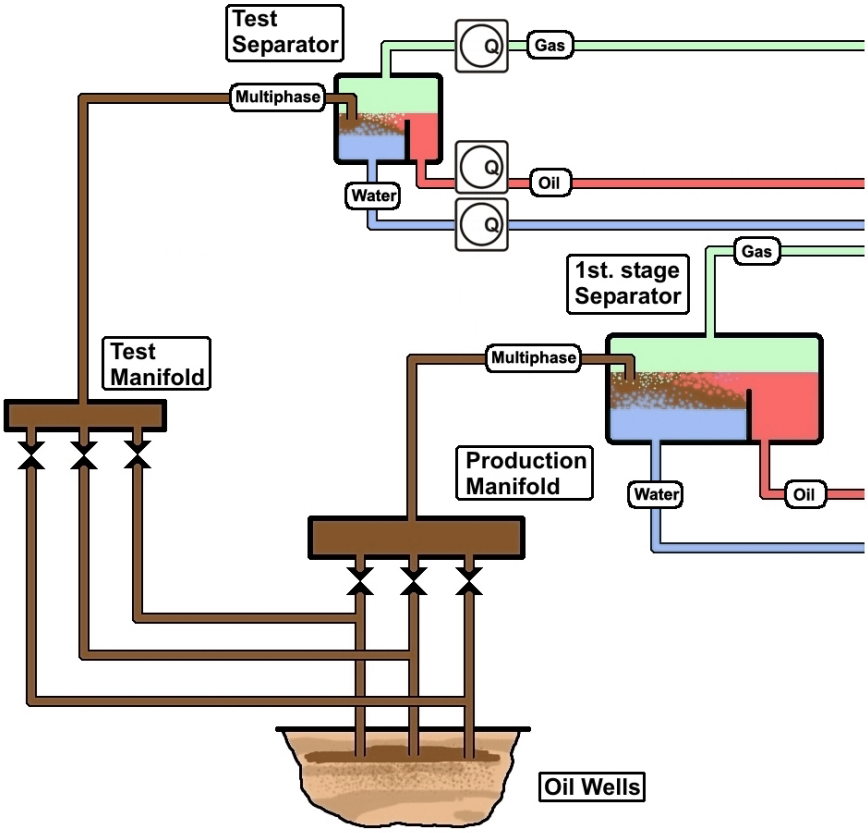


Figure 1.15: Conventional well-testing layout [41]

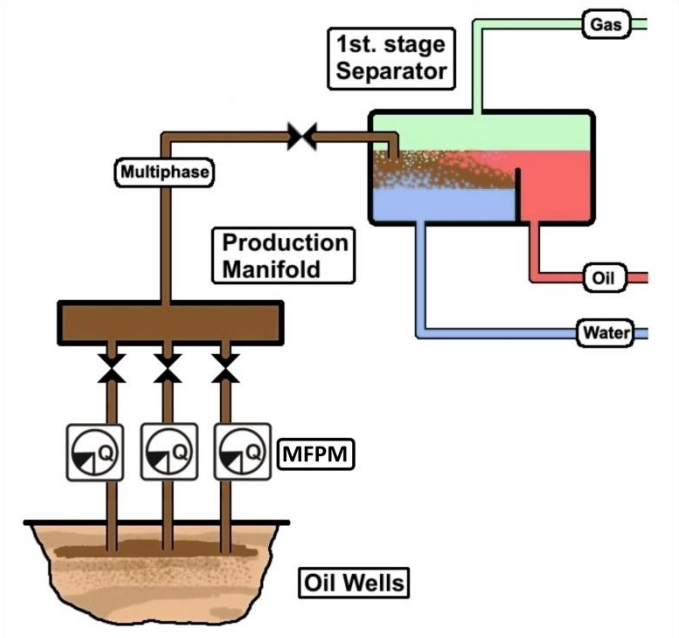


Figure 1.16: Improved well-testing layout integrating MFPMs [41]

In terms of multi-phase flow metering techniques, one of commonly used methods for measuring multi-phase flows is based on γ-ray (nuclear) attenuation, Radio-frequency (RF)/microwave and/or electrical impedance techniques in combination with a differential-pressure device such as a Venturi flowmeter [62], [63]. Phase fraction measurement based on γ-ray attenuation methods is elegant; there are however practical or logistical difficulties to overcome when an intense radiation source is used to achieve the temporal resolution at the expense of increasing safety precautions [64].

Another approach is to use Electrical Impedance Tomography (EIT) to image and measure each phase of a multi-phase flow using the conductivity contrast between oil, water and gas [65]. However, due to the nonlinear nature of the low frequency electric field distribution and the limited number of measurements (a trade-off with high measurement speed), an EIT system presents a low spatial resolution and non-uniform sensitivity distribution over the domain to be imaged [66].

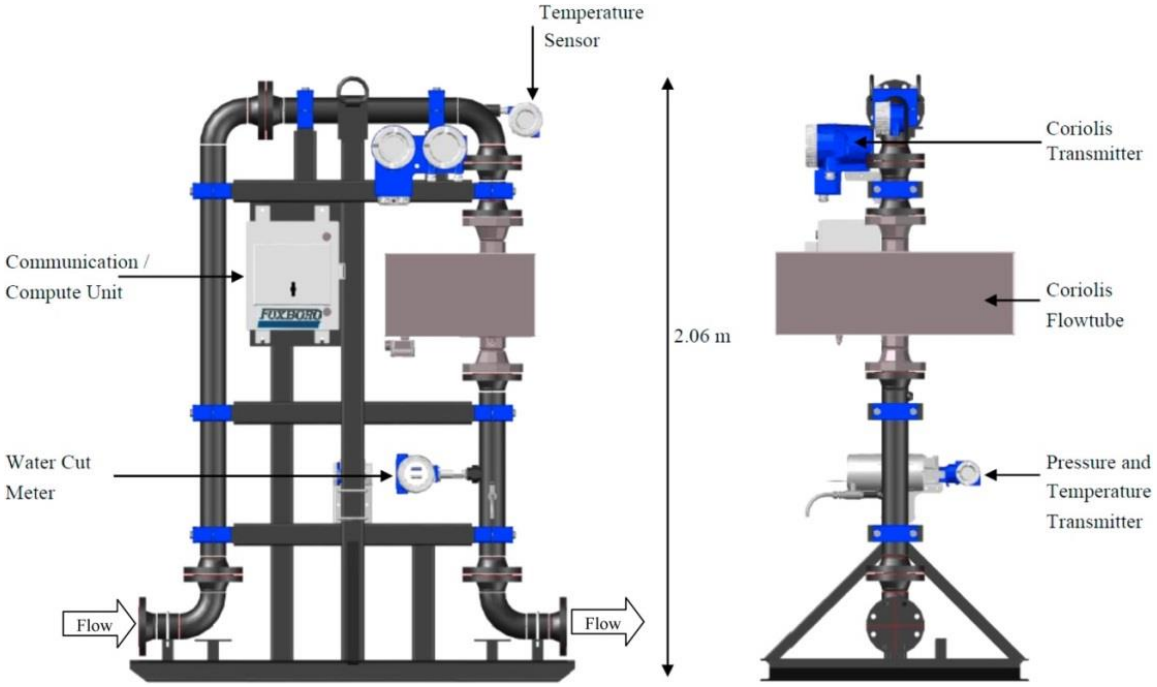


Figure 1.17: Three-phase flow measurement net oil skid [53]

Henry et al. [67] presented a case study on three-phase flow measurement using a net oil skid with Foxboro CFT-51 Coriolis flowmeter which is shown in Figure 1.17 [53].

As the Coriolis meter provides both mass flow and density measurements, it is possible to resolve the mass flows of the gas and liquid in a two-phase mixture if their respective densities are known. To apply Coriolis metering to a three-phase (oil/water/gas) mixture, an additional measurement is required. So they combined a Coriolis Flow Meter with a water cut meter to achieve three-phase measurement. Good measurement performance was demonstrated meeting with Russian Standard GOST 8.165 which has the following key specifications:

- Total liquid flow accuracy requirement $\pm 2.5\%$
- Total gas flow accuracy requirement $\pm 5.0\%$
- Total oil flow accuracy requirement dependent upon water cut:
- For water cuts less than 70%, oil accuracy requirement $\pm 6.0\%$
- For water cuts between 70% and 95%, oil accuracy requirement $\pm 15.0\%$

Field experience of the three-phase flow metering system is described in [53], while extending the system to work with high viscosity fuel is reported in [68].

Even though the first industrial use of two-phase, and even three-phase, Coriolis metering has been reported, there is much scope for improvement especially with regard to fast dynamic response and sensor signal tracking [24]. Specifically, the current basic measurement algorithms, which extract frequency, amplitude and phase from the sensor signals, are essentially designed to track steady sinusoidal signals with only slowly changing properties.

1.5.4 Existing Solutions

In the ISO 10790:2015 Coriolis flowmeters standard, only recommendations for single-phase flow measurement are described. In the NAMUR NE 107 standard, Coriolis flowmeters are not recommended for operation where the GVF is above 5% since the measurement error becomes unreliable.

Due to the high demand and importance of two/three-phase flow measurement, many manufacturers and researchers have explored possible solutions for two-phase flow measurement using Coriolis flowmeters and claim to have some capability for two/three-phase flow measurement. Here we select some commercial products from leading companies which claim to operate and measure during two/three-phase flow (some companies also describe two-phase flow as entrained gas in liquid) in the market. These are Emerson Micro Motion ELITE Peak series, Endress+Hauser PROMASS series, Krohne OPTIMASS series and Schneider FOXBORO series. Also due to the importance of digital signal processing as mentioned before, many manufacturers patented their digital signal processing technologies focusing on batching from empty-to-full and two-phase flow measurement [69]–[72]. Hence we also include digital signal processing algorithms for comparison.

Table 1.1 shows each product's two/three-phase flow measurement abilities according to their datasheet. From the table, all products are able to detect two-phase flow and give warnings since it is considered to be an undesirable condition for many applications. From the measurement accuracy side, due to the lack of a common standard and the relative immaturity of the technology, only Schneider Foxboro Coriolis flowmeters present measurement error performance based on the Russian GOST 8.165

standard. Hence in this thesis, the Schneider Foxboro CFS10 flow tube with CFT51 transmitter is considered a state-of-art product[1] for two/three-phase measurement.

	Micro Motion	**Endress+Hauser**	**Krohne**	**Schneider**
Flow tube (1-inch)	CMFS100M	Promass 84F	OPTIMASS 6000	Foxboro CFS10
Transmitter	Micro Motion MVD 5700	Promass 84	MFC 400	Foxboro CFT51
Batching from empty-to-full	Yes	Yes	Yes	Yes
Two-phase Detection	Yes	Yes	Yes	Yes
Signal Processing Algorithms	Hilbert Transform [72]	Digital Phase-Locked Loop with Quadrature Demodulation [70]	Digital Phase-Locked Loop with Quadrature Demodulation [69]	Zero-crossing [71]
Three-phase Measurement	N/A	N/A	N/A	Yes
Two/Three-Phase Measurement Accuracy	N/A	N/A	N/A	Russian GOST 8.165

Table 1.1: Comparing Coriolis flowmeters' two/three-phase measurement ability

1. This declaration is only representing the author's personal view specifically focusing on two/three-phase measurement area directly observed from each manufacturer's commercial datasheet online. Other Coriolis flowmeter design and performance parameters such as pressure drop, material, zero-stability and so on are not considered here for comparison.

On the other hand, none of the existing products provide perfect solutions for two/three-phase measurement and even the Russian GOST 8.165 still accepts large errors (e.g. ±2.5% for liquid flow and ±5% for gas flow). Hence there are many potential areas which can be explored to improve measurement accuracy including flow tube geometry design, signal processing algorithms, control algorithms, application specification and so on.

1.6 Coriolis Flow Meter Signal Processing

By exploring the fluid measurement and signal tracking error sources for two/three-phase flow measurement using Coriolis flowmeters, the main challenge for compensating fluid measurement errors remains the development of a better understanding and modelling of the complicated physical phenomenon; while for improving signal tracking errors, the challenge remains developing better signal processing algorithms to track fast changing parameters of sensor signal in low SNR due to high and fluctuating damping. As mentioned in the previous section, there has been much effort towards compensating fluid measurement errors but there are fewer explorations towards improving the fundamental signal tracking errors. Hence this thesis focuses on developing new signal processing algorithms to provide rapid and accurate tracking of Coriolis flowmeters' signal characteristics and to allow improved flow tube control and measurement during multi-phase flow, in order to reduce the final process measurement errors.

To illustrate the rapid changes in the sensor signals under two-phase flow, Figure 1.18 shows typical sensor signals observed when the flow tube is filled with a single-phase

fluid, working with a 1-inch Foxboro CFS10 flow tube attached to the ‘Oxbox’ transmitter (laboratory version of the Foxboro CFT51 transmitter). The amplitude and frequency of the sensor signals are steady. By contrast, Figure 1.19 shows typical sensor signals with a mixture of liquid and a moderate level of gas. Changes in the distribution of liquid and gas in the flow tube lead to variable damping and rapid changes in the frequency and amplitude of oscillation. The challenge to the amplitude control system is significant, and a fast dynamic response for the measurement of frequency, phase and amplitude should lead to improved flow tube control, as well as measurement, in the presence of two-phase flow.

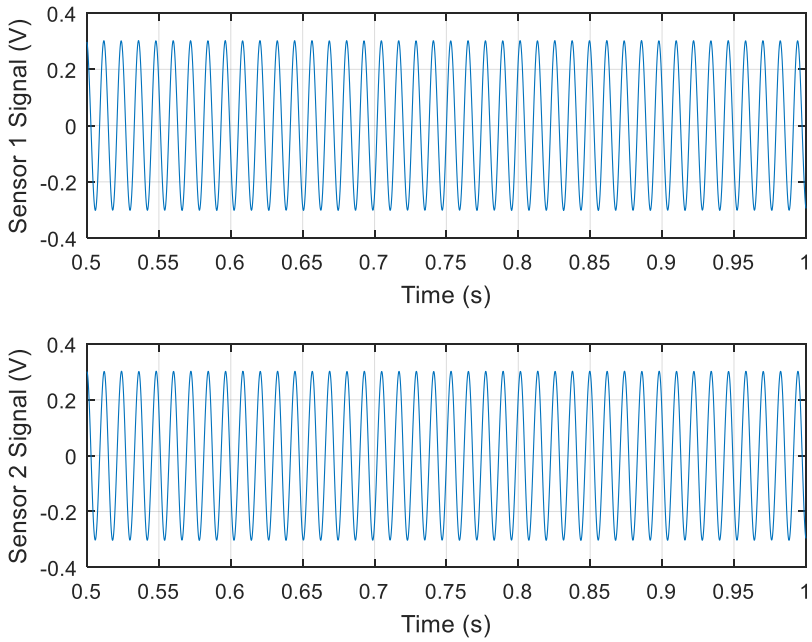


Figure 1.18: Sensor signals during steady single-phase flow (2 kg/s water)

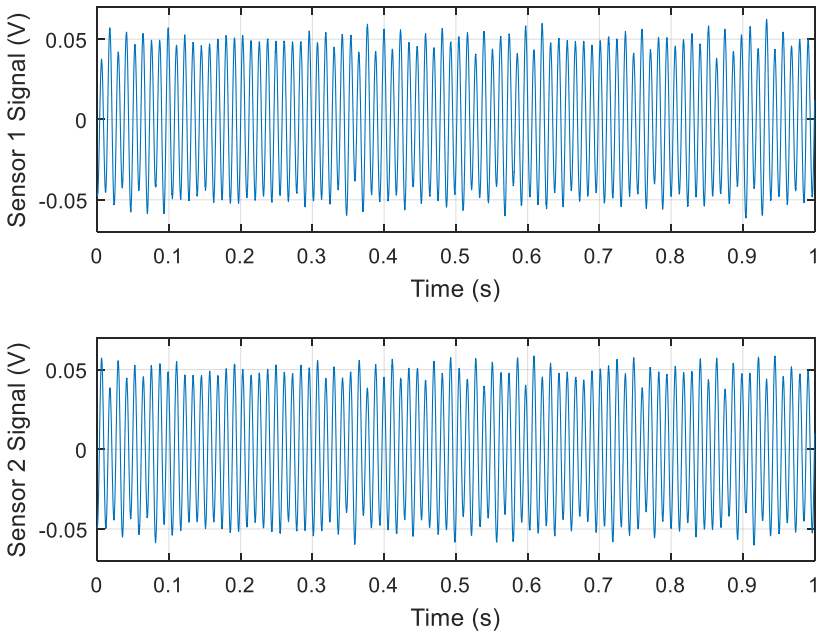


Figure 1.19: Sensor signals during two-phase flow (2 kg/s, 15% GVF)

Coriolis flowmeters need to maintain the flow tube vibration at its natural resonant frequency via the generation of a suitable drive signal, based on the measured sensor signal parameters. Essentially this is achieved by ensuring the drive signal has the same frequency and is in phase with (the sum and hence midpoint of) the sensor signals. Note that this phase arrangement assumes the sensor signals indicate velocity, which is often the case where coils are used as detectors; other sensing technologies may require a nonzero phase offset between drive output and sensor inputs, for example $\pm \pi/2$ radians. In addition, the amplitude of the drive signal is selected to achieve a desired control objective, typically to maintain a steady amplitude of oscillation [22]. With a modern digital drive, time lags occur between the sensor and driver signals due to Analog-to-Digital Converter (ADC) and Digital-to-Analog Converter (DAC) operations, signal processing and phase synchronization. Figure 1.20 (from [38]) shows a typical timing diagram for the drive generation process using the zero-crossing method which in this

case shows a lag of three resonant cycles. Note that a large proportion of this delay is due to the measurement process itself, i.e. the extraction of frequency, phase and

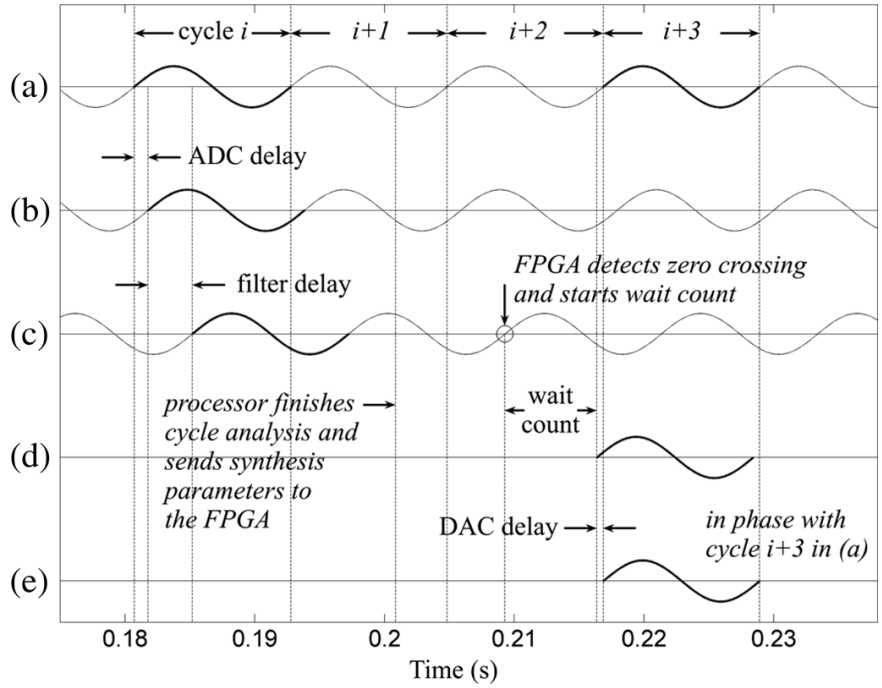


Figure 1.20: Timing diagram for Coriolis flowmeter transmitter (from [38])

amplitude information from the sensor signal. Minimizing this delay improves the dynamic response of the amplitude control, which is becoming more important in a number of applications including two-phase flow [24], [73], [74].

Returning to Figure 1.18, and noting that the signal characteristics observed (e.g. amplitude stability) are a function of both the flow tube itself and the drive control system, conventional digital signal processing and drive control works well for single-phase conditions. However in Figure 1.19, the variations in amplitude and other parameters may be caused in part by measurement error, delay and controller action, as well as by the dynamics of the two-phase fluid interacting with the resonating flow tube. Accordingly, accurate tracking of the sinusoidal signals, when subject to time-varying

amplitude and frequency, while at the same time minimizing the measurement delay, are important technical challenges for the next generation of two-phase flow capable Coriolis flowmeter. The computational complexity is sometimes also considered by manufacturers in terms of designing cost-efficient products and also reducing transmitter size and required input energy which is beneficial in some applications.

In summary, for designing signal processing algorithms of the next generation Coriolis flowmeters, the requirements can be summarized as:

- Continuous tracking of the varying amplitude/frequency/phase of sensor signal.
- Minimum tracking delay.
- Noise suppression.
- Low computational power.

Following these guidelines, this thesis will firstly review existing signal processing methods' performance and then develop and demonstrate the new signal processing methods.

2.BENCHMARK TESTS

In order to develop new techniques, existing techniques need to be described and compared. Thus a good set of benchmarks, representing challenging situations including batching and two-phase flow, are needed to compare each conventional method's performance and then newly developed methods have targets for showing improvement. In this chapter, inspired from real sensor data, we describe two benchmark examples where each benchmark is used to explore rapidly changing conditions as might to be experienced during batching from empty-to-full, and during continuous two-phase flow respectively. The input signal sampling rate is assumed to be consistent with the widely used audio technology i.e. up to around 50 kHz. One means of minimizing delay is to assume the tracking algorithm generates a new measurement result every sample. Accordingly, the computing power of the hardware is assumed to be sufficient to carry out algorithms at a sampling rate as high as 50 kHz, which in practice has been achieved with the techniques developed in this thesis.

In this chapter, two benchmarks are presented – an empty-full batch benchmark for testing the dynamic response of batching from empty-to-full application, and a Modified Random Walk Model (MRWM) for simulating continuous two-phase flow conditions. In addition, experimental sensor data from Coriolis flowmeters from the above two conditions are presented as extra benchmarks while also demonstrating their limitations. In later chapters, these benchmarks are used to test each technique and quantified results are given in order to compare performance.

2.1 Batching from Empty-to-full Simulation Benchmark

One particularly challenging condition for maintaining good measurement tracking and flow tube control occurs during a rapid transition from empty-to-full as mentioned in Section 1.4. This condition typically arises in a batching operation, where the Coriolis meter starts (and perhaps ends) empty, and is required to report the total flow of liquid in the batch [75]–[77]. Such a transition, with the associated changes in mass flow, density and flow tube damping, is likely to result in simultaneous changes in frequency, amplitude and phase difference on the two sensor signals, over a period as short as 0.5 s (or, as will be seen in the experimental data, even shorter).

The figures below show sensor data and parameter tracking results using a newly developed transmitter (introduced later in Chapter 5) with 48 kHz update rate for both sensor signals and their parameters, along with a newly developed tracking algorithm, working with a 1/4 inch Foxboro flow tube over a 9 second batching from empty-to-full process. Note that the 1/4 inch meter was selected due to the practicality of using it for a batching experiment in the Oxford laboratory. One unusual characteristic of this flow

tube is that it has a small difference (only 2 Hz) in the resonant frequency between air and water. For sensor data, the transition and recovery period during the batch is shown for better observation.

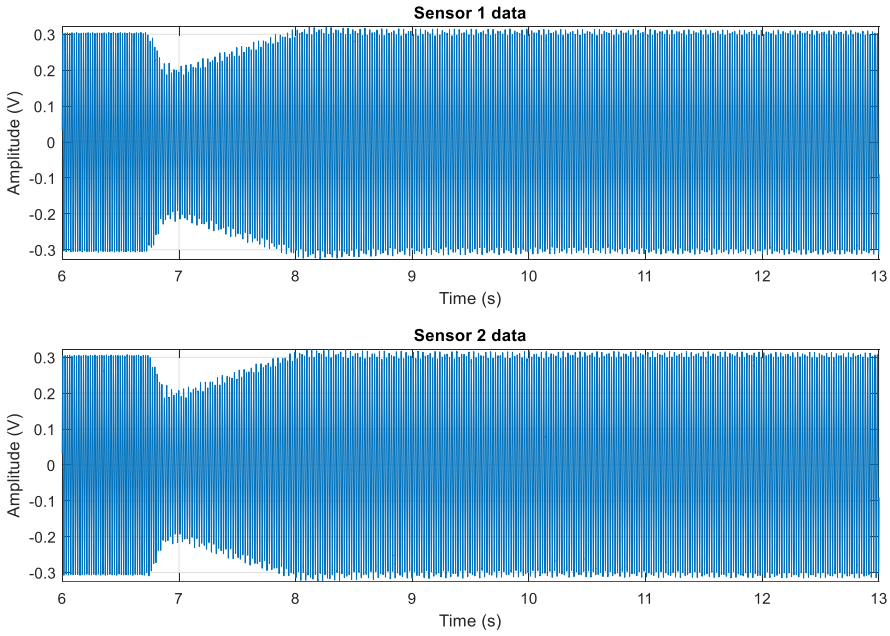


Figure 2.1: Experimental sensor data from empty-full transition

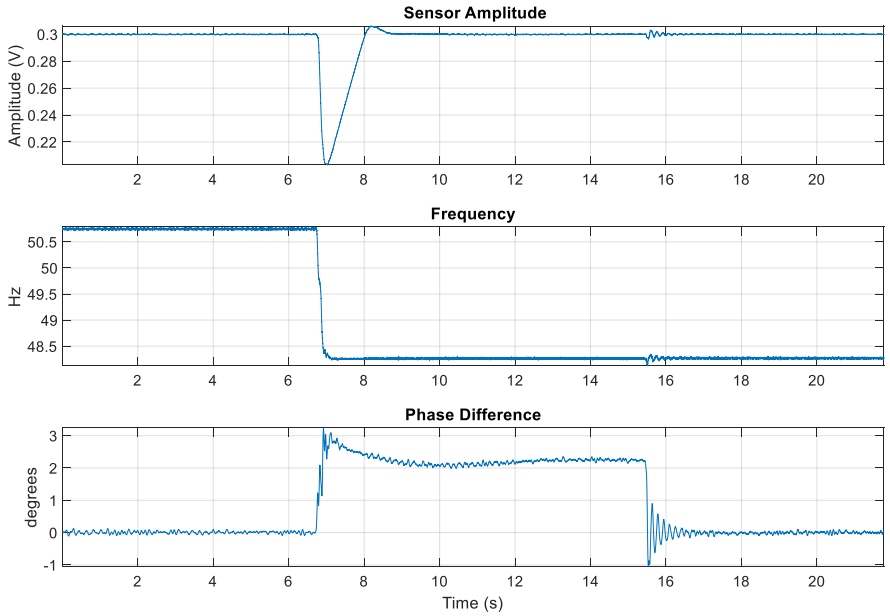


Figure 2.2: Measured sensor parameters from empty-full transition

The flow tube is empty and steady up to around t = 6.7s. There is a short period (approximately 0.3s) of very sudden change as the flow tube fills with water. Throughout this period, the damping on the flow tube dramatically increases and the control amplitude drops due to drive control delay and the drive current limit. Once the flow becomes pure water, the damping returns to normal and the amplitude slowly recovers in response to the amplitude control algorithm keeping the drive current high. The amplitude has fully recovered by around t = 9s. The batch continues until around t = 15.5s after which the flow is shut off (as indicated by the drop in phase difference, settling at zero). In the Oxford laboratory setup, it is not possible to finish the experiment with an empty flow tube. As can be seen, the end of the batch causes far less disturbance to the flow tube and its parameters than its start.

From the figures, it can be seen that the meter does not stall during the batching process and, for the algorithm used, measurement results are generated continuously through the whole process. The primary interest is in the challenging transition period from empty-to-full as the amplitude, frequency and phase difference of the sensor signals are all changing rapidly. The figures below show the transition period in detail.

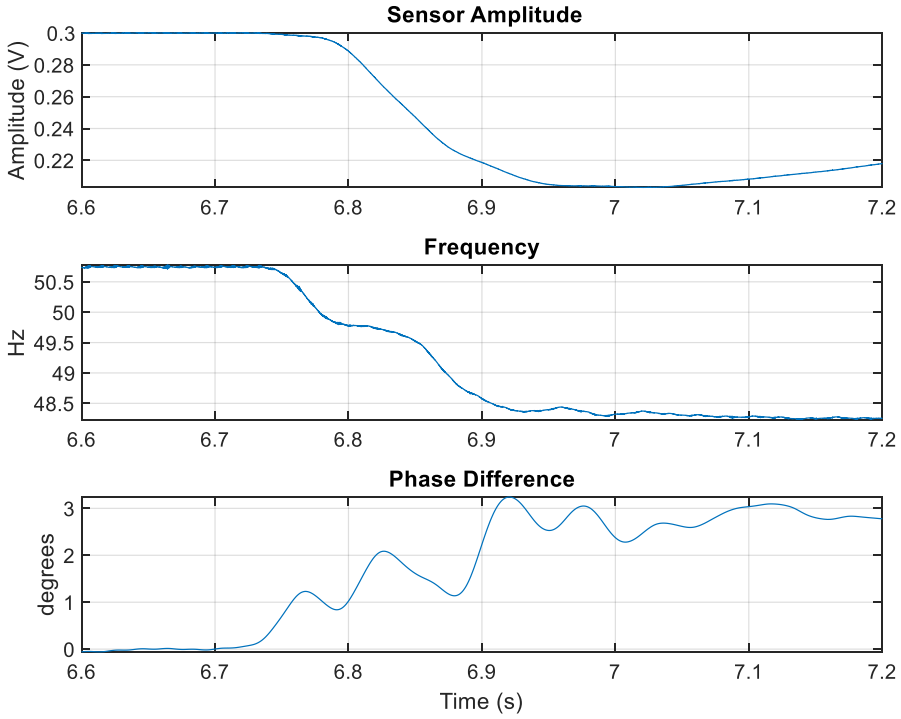


Figure 2.3: Sensor parameters during transition period for batching from empty-to-full

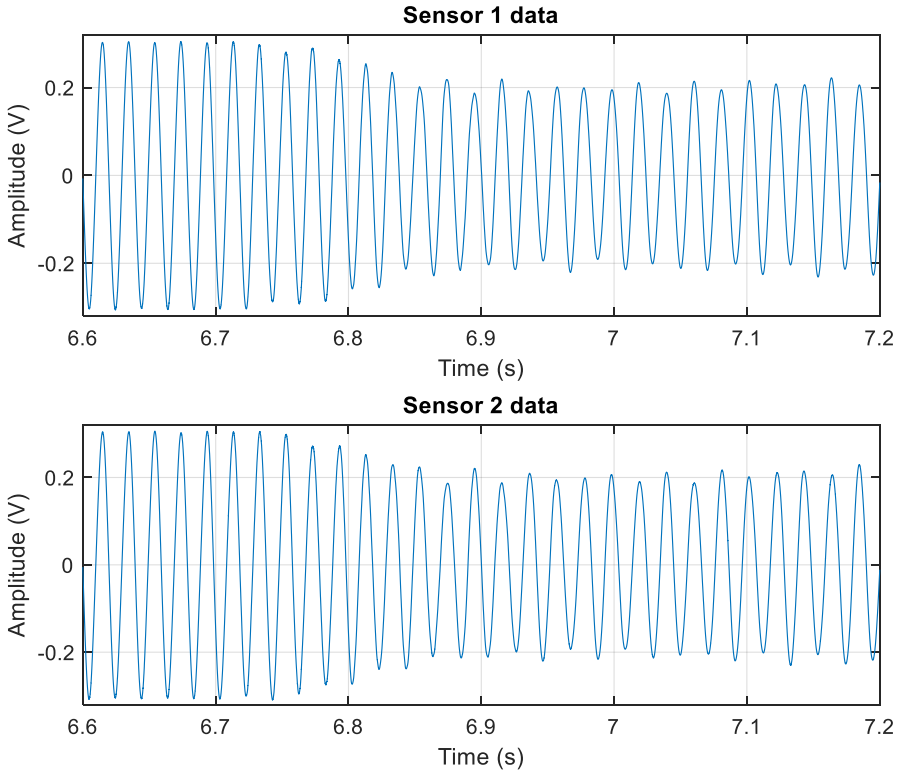


Figure 2.4: Sensor data during transition period for batching from empty-to-full

One problem using the sensor data as a benchmark is that the true values of dynamically changing sensor parameters are unknown. The instantaneous values of each parameter during the batching from empty-to-full are not repeatable and every time they behave slightly differently. Hence the output of any measurement algorithm cannot be compared to 'true' experimental values in order to determine dynamic performance, root mean squared error etc.

Another problem arises from the fact that a complete assessment of any algorithm would need to be closed loop i.e. to take into account the flow tube control performance arising from the measurement performance. A different measurement tracking delay will affect control amplitude performance and in turn, affect measurement results. This is demonstrated in the figures below showing the sensor signal and its calculated parameter values where the same batching process and flow tube is used, but working with the Oxbox. Here the Oxbox tracking algorithms are slower.

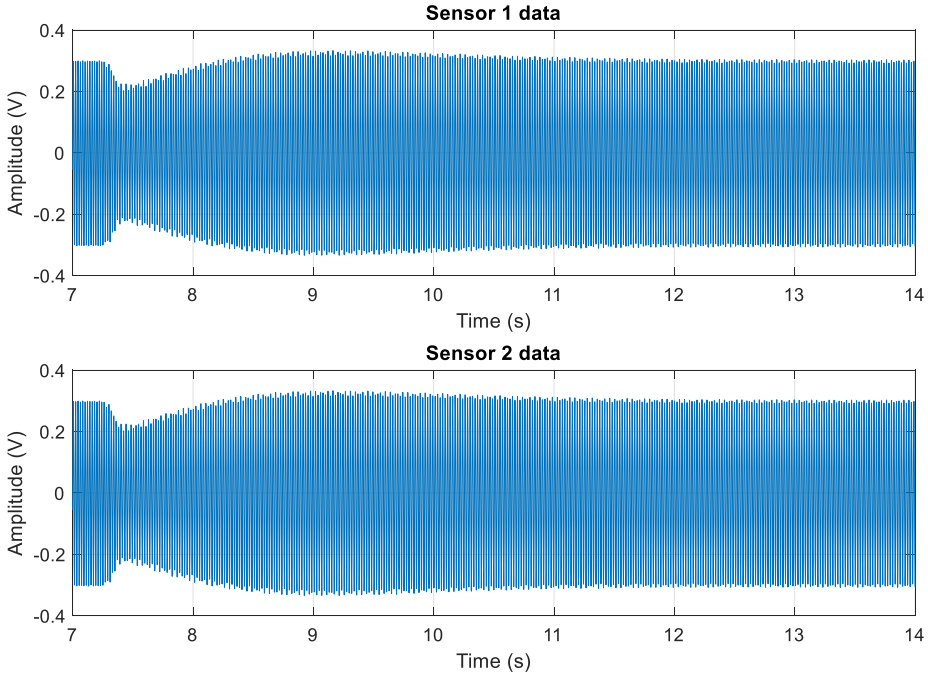


Figure 2.5: Oxbox sensor signal during batching from empty-to-full

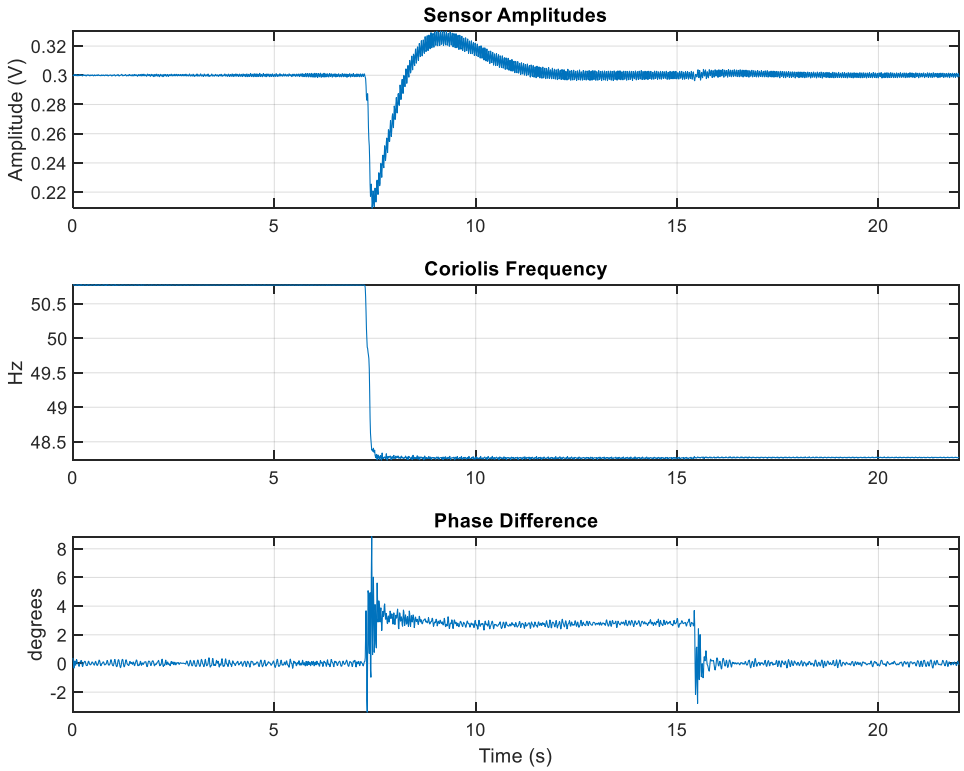


Figure 2.6: Oxbox sensor signal parameters during batching from empty-to-full

The ‘ringing effect’ noise during batching from empty-to-full is caused by flow pulsation itself, not from other modes of vibration inference, and can also be observed at the reference Coriolis flowmeter.

From the figures, we can observe that the recovery period of the Oxbox is longer than for the newly developed transmitter. This is most likely due to a larger amplitude tracking delay since the input of the PI control algorithm is the tracked amplitude.

One useful basis for comparing signal processing algorithms using batching from empty-to-full sensor data, is to do an off-line calculation using identical sensor data sets, so that tracked parameter values from each algorithm can be visualized and compared on a single plot. This approach provides one basis for assessing both the dynamic

response and the noise suppression of a variety of algorithms, using real, as opposed to simulated, sensor data.

Given the limitations of using real sensor data as batching from empty-to-full benchmark, a numerically simulated benchmark has also been developed. Here an empty-to-full flow tube filling process is simulated via otherwise noise-free sensor signals, where the common frequency drops linearly from 100 Hz down to 85 Hz, the amplitude drops linearly from 0.3 V down to 0.05 V and the phase difference increases linearly from $0°$ up to $4°$, all simultaneously over 0.5s. Note that these parameter changes are greater than those available in the experimental data, especially for frequency. In a real Coriolis flowmeter, the rate of change of each parameter is physically limited due to such issues as mechanical inertia and fluid dynamics, so that step changes in sensor parameters or their rates of change are unrealistic - as illustrated by Figure 2.3. Simple ramp-like parameter changes will include discrete steps in the rate of change, which is physically unrealistic. Hence here low-pass filters are adopted to remove step changes. Note that different flow tubes have different vibrating frequencies and ranges and here we pick a reasonable set of values without losing the generality of the benchmark, since the algorithms can be adjusted to adapt to different frequency ranges for different flow tubes.

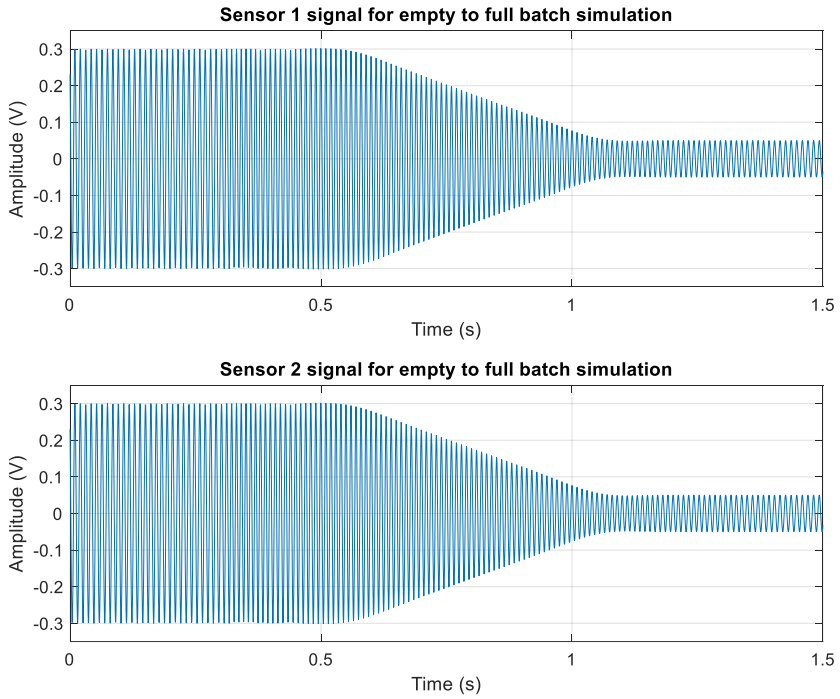


Figure 2.7: Sensor signals for empty-to-full batch process during transition period

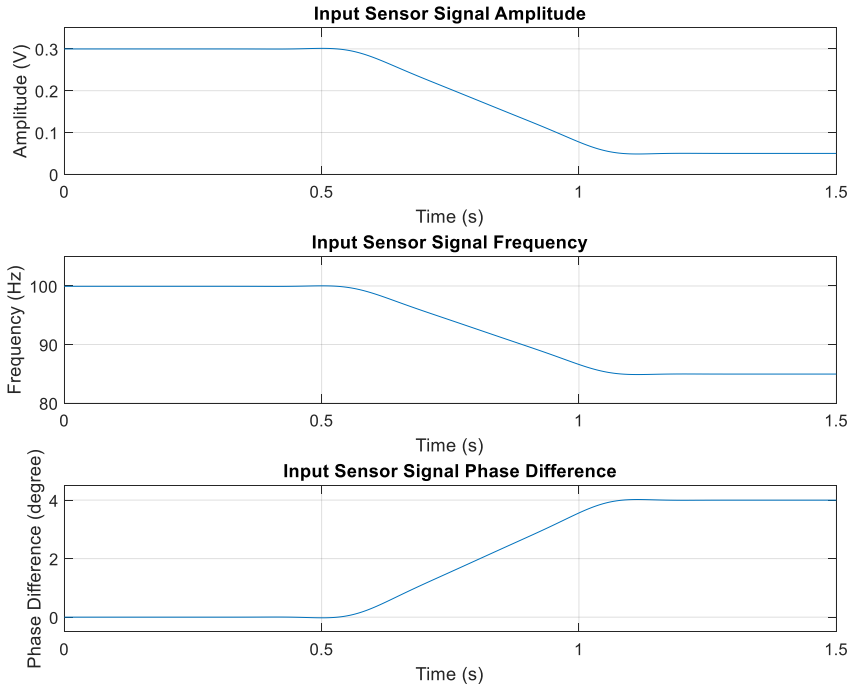


Figure 2.8: Sensor signal input parameters for empty-to-full batch process

Figure 2.7 shows the simulated sensor signals while Figure 2.8 shows the corresponding signal parameter values. The simulated empty-to-full batch process benchmark, as it involves noise free linear parameter change, can also be used to calculate the tracking time delay of each new technique which is a good way to compare dynamic performance. The average tracking time delay Δt for the empty-to-full batch process can be calculated as follows:

$$\Delta t = \frac{T_p}{R_c} E \tag{2.1}$$

where T_p is empty-to-full batch process time which is 0.5 s here, R_c is one of the parameters' changing range (e.g. 0.25 V for amplitude, 15 Hz for frequency or 4 ^{o} for phase difference) and E is the average error during the empty-full transition (i.e. only during the period of linear change from 0.5s – 1s). Since the measurement algorithm's amplitude dynamic response is important for the control of the flow tube, amplitude tracking delay is compared in later chapters.

2.2 Two-phase Flow Experimental and Simulation Benchmarks

As with the batching from empty benchmark, both experimental and simulated data is used to create benchmarks for assessing algorithm performance. Two experimental data sets are provided: a relatively 'stable' data set where the GVF is low and kept nominally constant, so that the parameter variations are expected to be relatively small, and a more 'dynamic' data set where the GVF is varied in order to introduce wider parameter variations.

Although in either data set the true parameter values are unknown, comparing measurement results standard deviation for each algorithm can provide a limited assessment of performance.

Figures 2.9 and 2.10 show sensor data and calculated parameter values collected during a stable two-phase flow experiment (3 kg/s, 5% GVF). The sensor parameters have been calculated using a new signal processing algorithm (which will be introduced in Chapter 4) running in real time on a prototype transmitter, and give a first indication of the measurement tracking that may be achieved with relatively stable two-phase flow conditions.

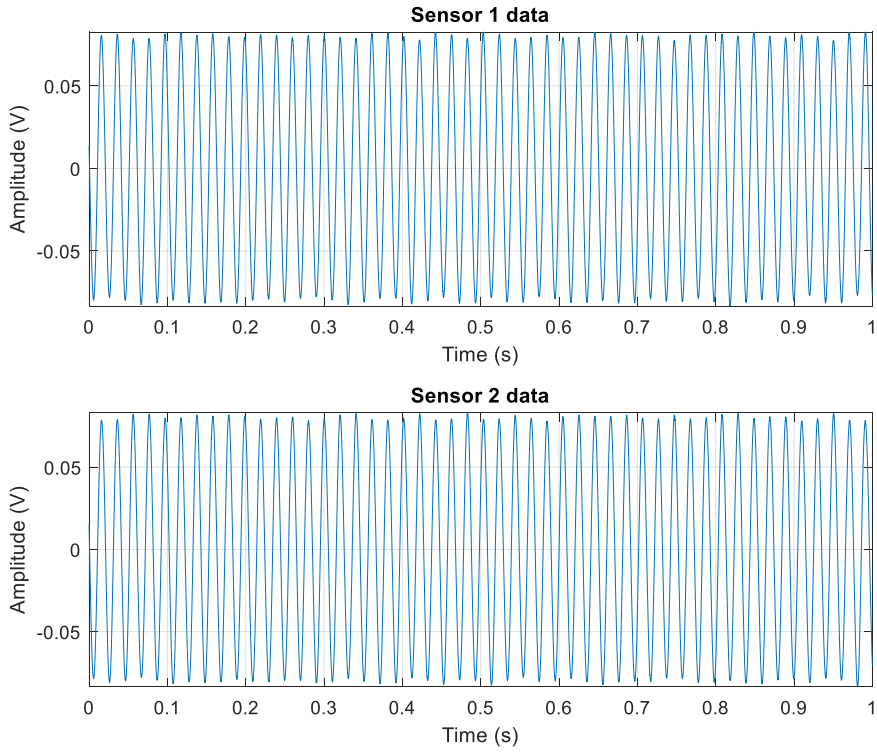


Figure 2.9: Sensor signals during two-phase flow (3 kg/s, 5% GVF)

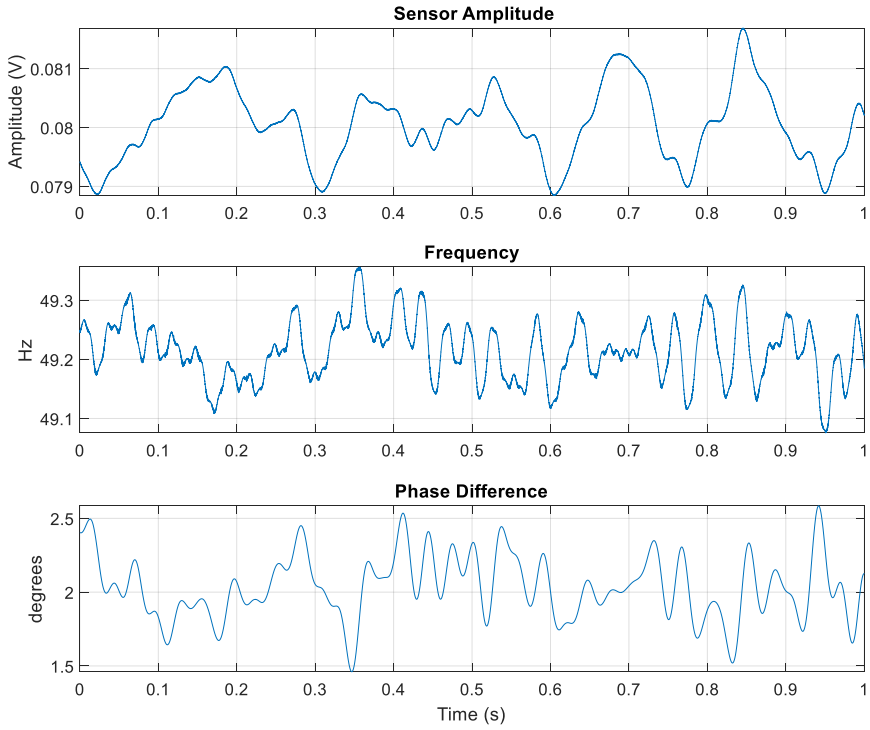


Figure 2.10: Sensor parameters during two-phase flow (3 kg/s, 5% GVF)

In real applications (e.g. upstream oil and gas), it is not unusual for the GVF to vary rapidly in time (see for example the field results reported in [48]). Accordingly, a second experimental data set has been collected with rapidly varying GVF, as shown in Figures 2.11 and 2.12. All of the parameters vary over the 1s period in a complicated way. The calculated phase difference even goes slightly negative; whether this is due to high noise in the sensor signal or real physical effects needs to be further explored.

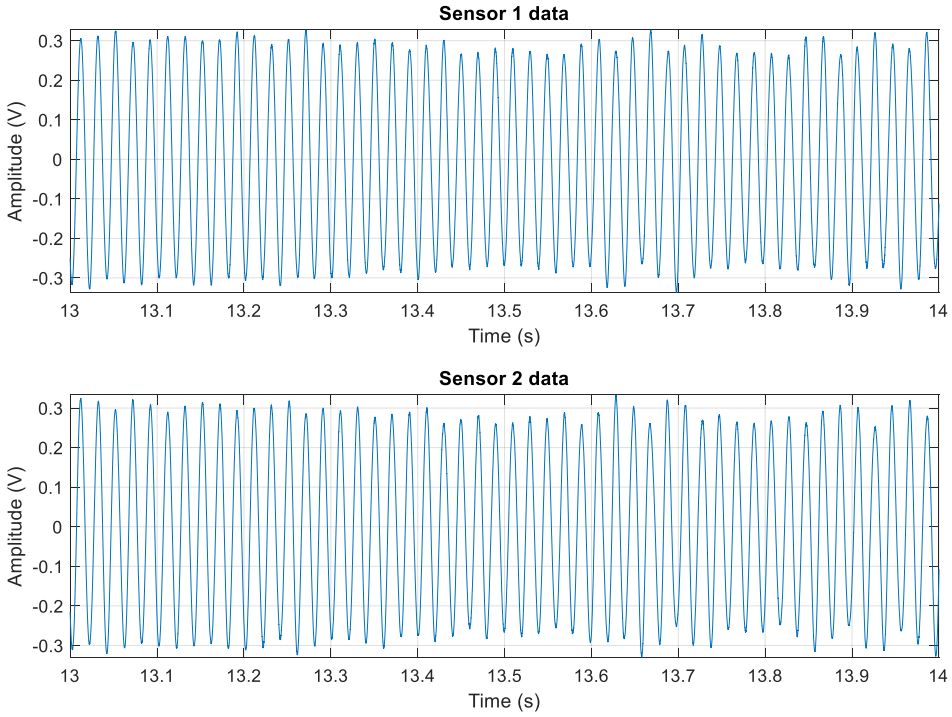


Figure 2.11: Sensor signals during fast varying GVF two-phase flow

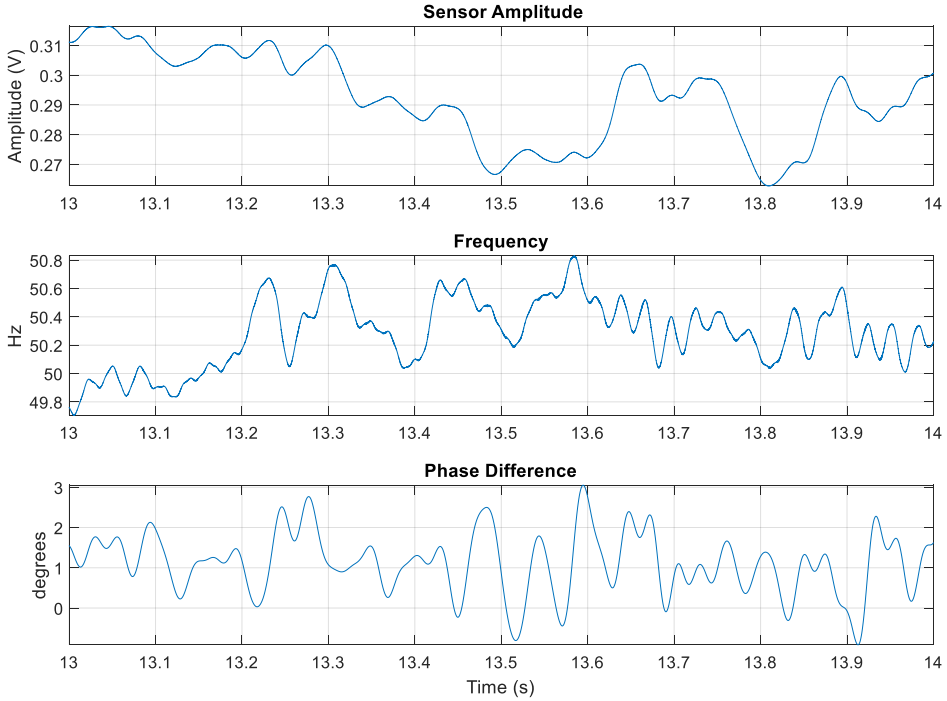


Figure 2.12: Sensor parameters during fast varying GVF two-phase flow (measured by new research transmitter)

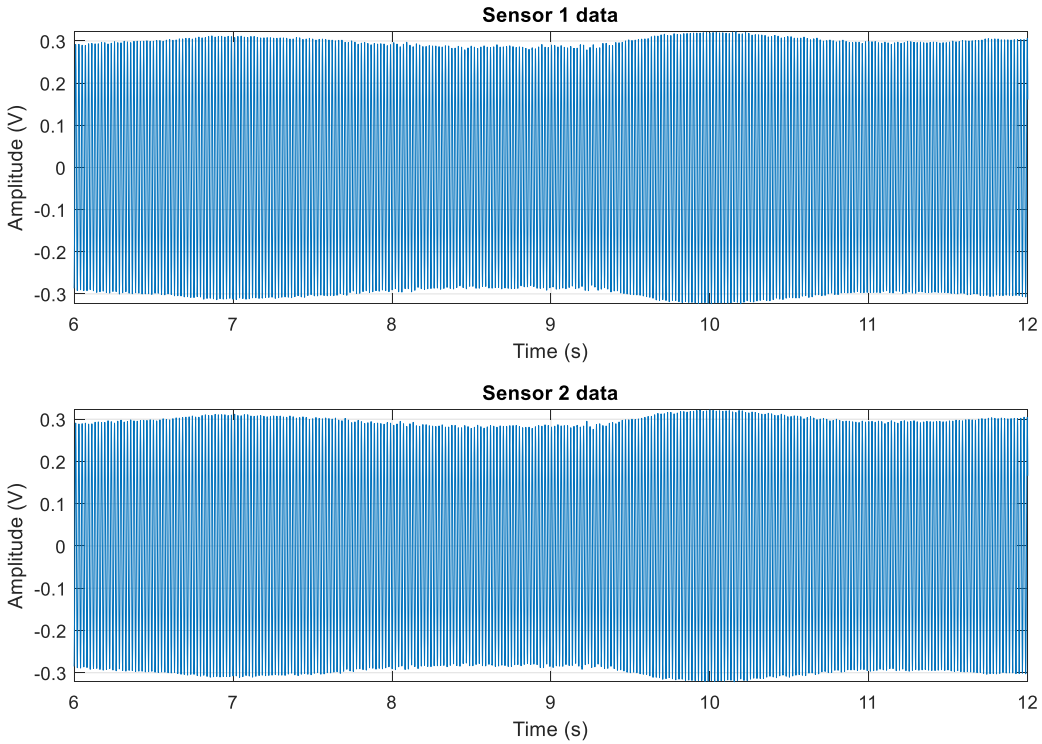


Figure 2.13: Sensor signals during slowly varying GVF two-phase flow

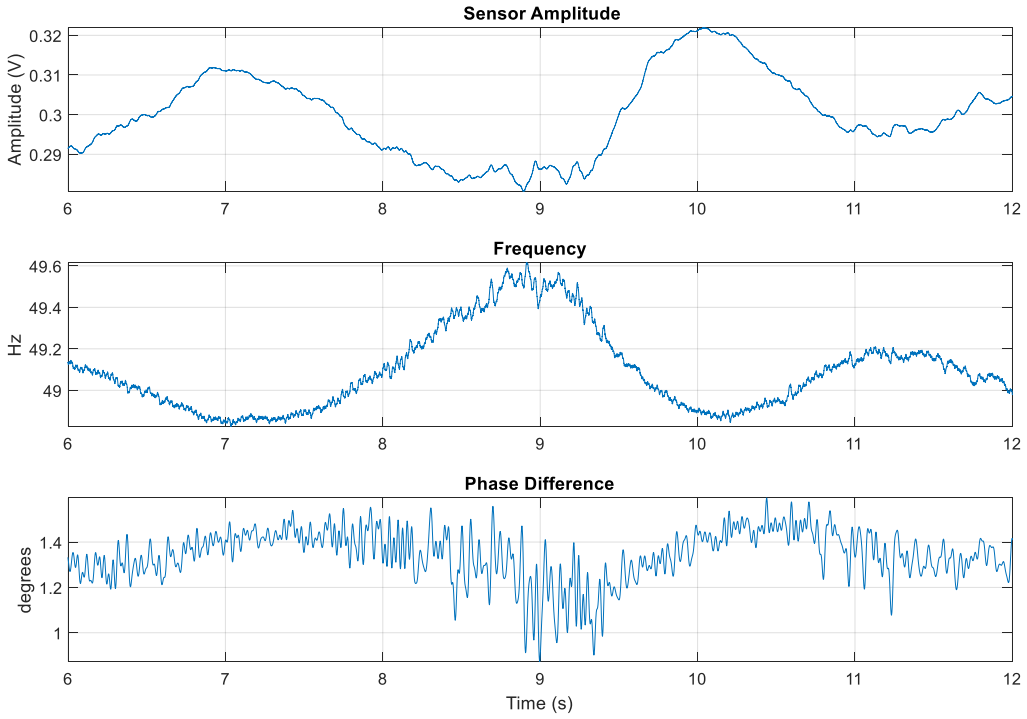


Figure 2.14: Calculated sensor parameters during slowly varying GVF two-phase flow

A final example of experimental data over a 6s period is shown in Figures 2.13 and 2.14 for an experiment where the GVF varies slowly.

It can be seen that there is strong correlation between the calculated frequency, amplitude and phase difference in these results, which may be attributed to a slow variation in GVF. During periods of high GVF (e.g. around t = 9s) the frequency is high (due to low density) while the amplitude is low (due to high damping) and the phase difference is low (due to low liquid flow rate associated with high GVF). During periods of relatively low GVF (e.g. around t = 7 s and t = 10 s), the frequency is low corresponding to higher density, the amplitude is high corresponding to lower damping, and the phase difference is high corresponding to higher mass flow rate of liquid. Given the strong correlation between the parameter values in slowly varying GVF data sets, only the fast varying GVF two-phase flow sensor data over 1s period as shown in Figure 2.11 is used as additional experiment benchmark for testing different algorithms in later chapters, while the slowly varying GVF data is not used.

A simulated benchmark has also been developed to test measurement accuracy, dynamic performance and ability to suppress noise. The main challenge of two-phase flow signal processing is to deal with rapid and simultaneous changes in amplitude, frequency and phase difference, firstly in terms of avoiding large errors, and secondly in minimizing the measurement delay. The importance of a fast dynamic response for single-phase applications has been thoroughly discussed in [36], [73], [76], [78].

In order to simulate the sensor signals arising in two-phase flow conditions with varying GVF, a Random Walk Model (RWM) was proposed by Tu et al. [79]. Time-varying sensor signals are generated by the random walk model, as follows:

$$
\begin{aligned}
x_1(n) &= A(n)\sin[2\pi n f(n)/\ f_s + \phi(n)/2] + \sigma_{e1}\cdot e_1(n) \\
x_2(n) &= A(n)\sin[2\pi n f(n)/\ f_s - \phi(n)/2] + \sigma_{e2}\cdot e_2(n) \\
A(n) &= A(n-1) + \sigma_A \cdot e_A(n) \\
f(n) &= f(n-1) + \sigma_f \cdot e_f(n) \\
\phi(n) &= \phi(n-1) + \sigma_\phi \cdot e_\phi(n)
\end{aligned}
\tag{2.2}
$$

Here $x_1(n)$ and $x_2(n)$ are the simulated sensor signals, with common but time varying amplitude $A(n)$, frequency $f(n)$, and phase difference $\phi(n)$. $e_1(n)$, $e_2(n)$, $e_A(n)$, $e_f(n)$ and $e_\phi(n)$ are un-correlated white noise processes with unit variance, which, like using a common amplitude for the two sensor signals, represents a simplification of actual two-phase flow conditions. In reality, with slowly varying two-phase flow there is likely to be some correlation between the true mass flow and density values – for example, when a slug of liquid passes through the flow tube both parameter values should increase together. σ_{e1}, σ_{e2}, σ_A, σ_f and σ_ϕ are gain factors for the random noise.

A more serious criticism of this model is that there are no limits on the instantaneous change of the parameter values (as discussed in Section 2.1above), since the random sequences are unfiltered. In addition, the RWM does not have a hard boundary for each parameter and so can exceed certain physical limitations during a simulation, as will be shown later. So here we present a more realistic simulation – the Modified Random Walk Model (MRWM) by defining parameters as follows:

$$
\begin{aligned}
x_1(n) &= A(n)\sin[2\pi f(n)n/\ f_s + \phi(n)/2] + \sigma_{e1}\cdot e_1(n) \\
x_2(n) &= A(n)\sin[2\pi f(n)n/\ f_s - \phi(n)/2] + \sigma_{e2}\cdot e_2(n) \\
A(n) &= \frac{(A_l(n) - \min(A_l(n)))\times(A_{\max} - A_{\min})}{\max(A_l(n)) - \min(A_l(n))} + A_{\min} \\
f(n) &= \frac{(f_l(n) - \min(f_l(n)))\times(f_{\max} - f_{\min})}{\max(f_l(n)) - \min(f_l(n))} + f_{\min} \\
\phi(n) &= \frac{(\phi_l(n) - \min(\phi_l(n)))\times(\phi_{\max} - \phi_{\min})}{\max(\phi_l(n)) - \min(\phi_l(n))} + \phi_{\min} \\
A_l(n) &= H_A(n) * e_A(n) \\
f_l(n) &= H_f(n) * e_f(n) \\
\phi_l(n) &= H_\phi(n) * e_\phi(n)
\end{aligned}
\tag{2.3}
$$

where $e_1(n)$ and $e_2(n)$ remain un-correlated white noise sequences, $e_A(n)$, $e_f(n)$ and $e_\phi(n)$ are uniformly distributed random noise in the interval (-1,1), σ_{e1}, σ_{e2} are gain factors for the input noise, $A_{\max}$, $A_{\min}$ are the upper and lower limits for time-varying amplitude, and where $f_{\max}$, $f_{\min}$, $\phi_{\max}$ and $\phi_{\min}$ are the corresponding limits for frequency and phase difference respectively. $H_A(n)$, $H_f(n)$ and $H_\phi(n)$ are low-pass filters to limit the rate of change of parameter values which are the same as those used in the batching from empty-to-full simulation benchmarks and the '*' operator represents a time-domain convolution calculation.

The bound-limited amplitude, frequency and phase difference values are generated via uniform random noise processes and passed through low-pass filters to constrain the rate of change. Then, based on the filtered parameter values, the two sensor signals are generated. Figure 2.15 compares the output of MRWM with that of RWM with $A_{\min}$ = 0.2 V, $A_{\max}$ = 0.3 V, $f_{\min}$ = 70 Hz , $f_{\max}$ = 100 Hz, $\phi_{\min}$ = 0 ºand $\phi_{\max}$ = 4 º. Different flow tube designs can be simulated using different boundary limits.

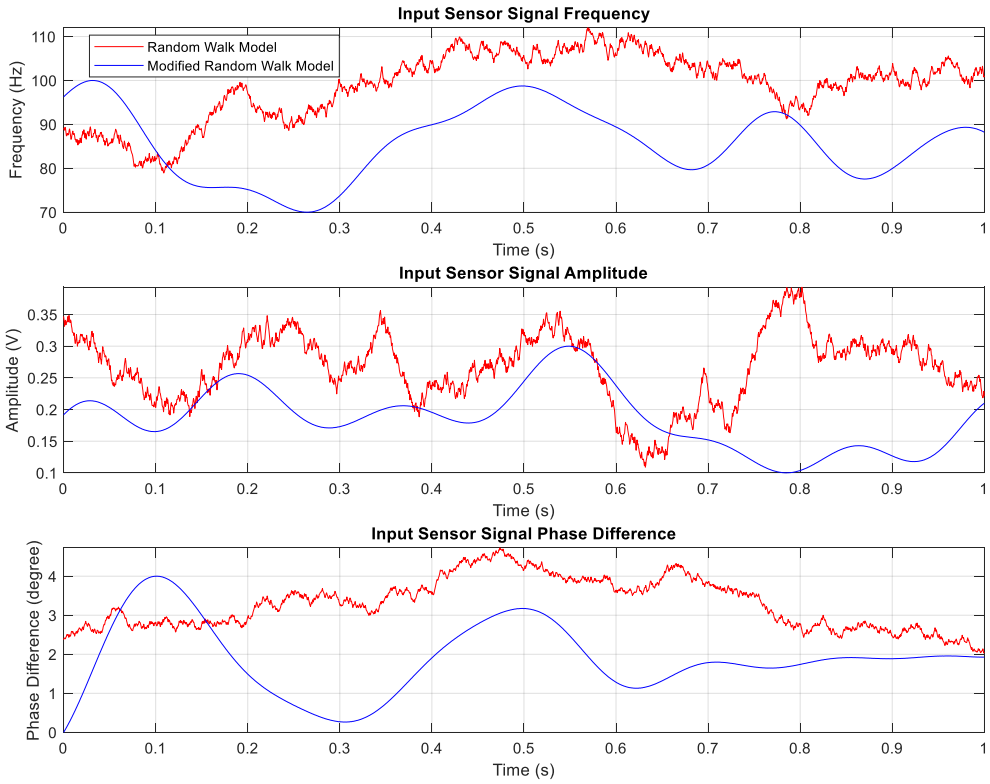


Figure 2.15: Comparison between RWM and MRWM

From Figure 2.15, both the RWM and MRWM range over the desired parameter values in a random fashion. However, MRWM excludes high frequency variations in parameter values which are physically unrealistic, but which will influence the error statistics and hence the performance evaluation of each of the measurement techniques. Also MRWM adds a hard boundary for each parameter so that the parameter is always limited to the defined range.

Figure 2.16 represents a typical simulated input signal using the parameter values given above. The resulting input signal shows a broad similarity with the real two-phase flow sensor signal shown in Figure 1.19. As with the batching from empty-to-full benchmark, different signal processing algorithms are tested with simulated data including variable amounts of white noise. As the instantaneous amplitude is varying, it is unrealistic to

generate fixed SNR signals for simulation. Hence the mid-range simulated amplitude value (0.2 V) is used as the reference for calculating different noise levels, using SNRs at roughly 17 dB, 37 dB, 57 dB and 77 dB. In this way, the benchmarks reasonably simulate sensor signals behaviour at different GVF during two-phase flow. The MRWM benchmarks will be applied to existing and new signal tracking techniques in later chapters.

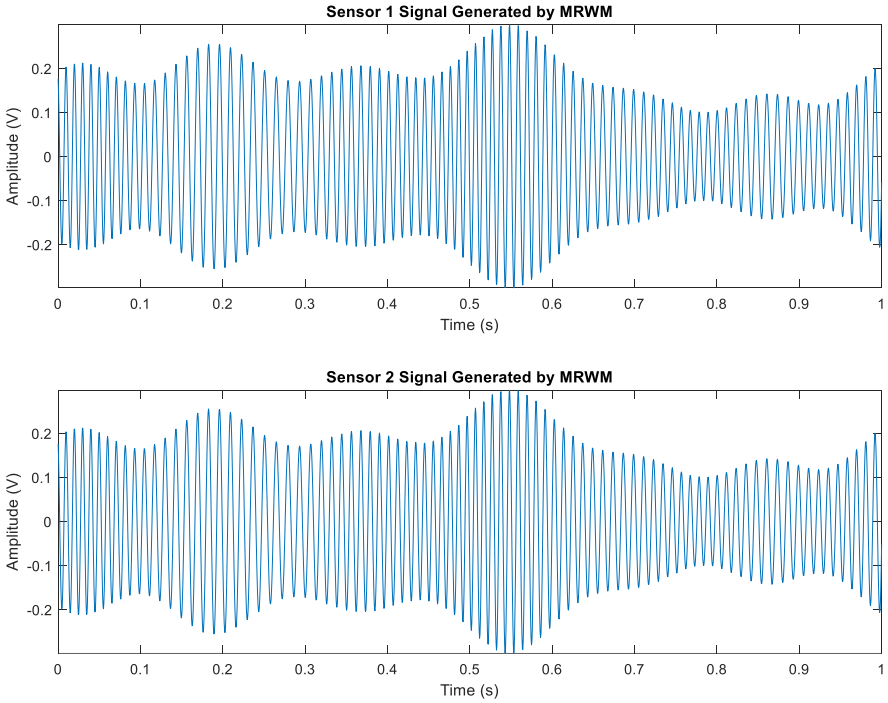


Figure 2.16: Sensor signals generated by MRWM

For quantifying measurement performance during simulations where the true instantaneous parameter values are known, the Root Mean Square Error (RMSE) is used. The RMSE calculation is as follows:

$$RMSE = \sqrt{\frac{1}{n}\sum_{i=1}^{n}(\hat{Y}(i) - Y(i))^2} \tag{2.4}$$

where $Y(i)$ and $\hat{Y}(i)$ are the true and estimated values of the parameter concerned.

3. CURRENT CORIOLIS FLOW METER SIGNAL PROCESSING METHODS

The purpose of this chapter is to evaluate the ability of current signal processing approaches to track rapid changes in the sensor signal properties. With the increasing importance of two-phase flow, this analysis includes the tracking of variable amplitude (often neglected in the prior literature) alongside the calculation of phase difference and frequency.

In this chapter, we consider each algorithm's ability to suppress different levels of white noise and its dynamic performance in simulation. Different levels of noise applied will be 17 dB, 37 dB, 57 dB and 77 dB SNR. Additionally noise free benchmark results will be given for comparing different algorithms' dynamic performance only. For the purposes of pre-filtering, a 5^{th} order low-pass elliptic filter is used with each method since it is a common approach in industry for filtering out noise before applying measurement algorithms to sensor data.

Real sensor data from batching from empty, fast varying GVF two-phase flow experiments will be tested with each algorithm so that the performance in real Coriolis flowmeter applications can be assessed. Note each algorithm's implementations have been carried out by the current author, based on the cited literature.

3.1 Current Methods

3.1.1 Adaptive Notch Filters for Frequency Tracking

There have been many academic and commercial applications of ANFs to Coriolis flowmeter meter frequency tracking, with perhaps the first example described by Derby et al. [20]. Performance improvements are obtained by adopting the Steiglitz-McBride ANF (SMM-ANF) [79], [80]. Typically, a DTFT technique is used to complete the calculation to include phase difference and amplitude. Figure 3.1 shows the structure of SMM-ANF algorithm:

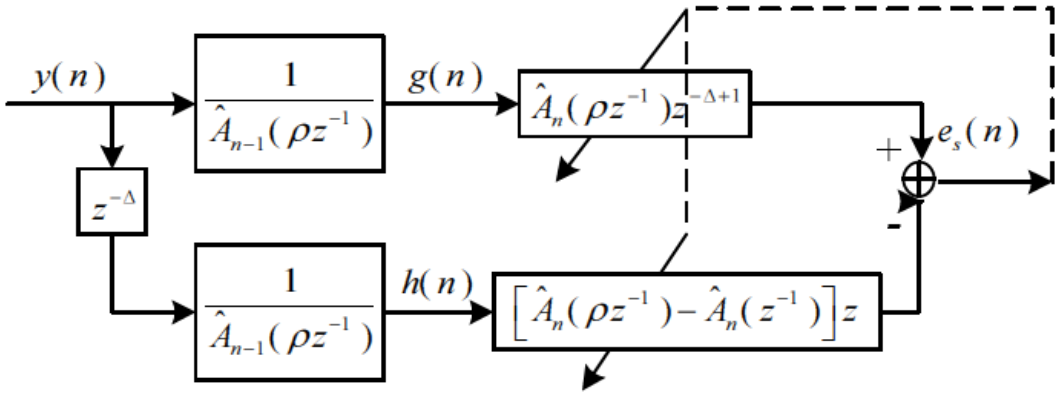


Figure 3.1: A typical structure of SMM-ANF reproduced from[79] (this structure does not reflect equation (3.1))

Here the transform function is:

$$H(z)=\frac{\hat{A}_n(z^{-1})}{\hat{A}_n(\rho z^{-1})}=\prod_{k=1}^{m}\frac{1+\hat{\alpha}_k(n)z^{-1}+z^{-2}}{1+\rho_k(n)\hat{\alpha}_k(n)z^{-1}+\rho_k^2(n)z^{-2}} \tag{3.1}$$

where *m is* the trap number i.e. the number of peak frequencies to be tracked. Since the Coriolis flowmeter signal has a single dominant frequency, m=1. $\rho_k(n)$ is the pole contraction factor which determines the bandwidth of the ANF, given by:

$$BW=2\cos^{-1}\left(\frac{2\rho_k(n)}{1+\rho_k^2(n)}\right) \tag{3.2}$$

The bandwidth is initially broad in order to capture the frequency of the input signal and is then narrowed to achieve convergence and improved accuracy. Hence $\rho_k(n)$ is increased over time [81]:

$$\rho_k(n)=\rho_0\rho_k(n-1)+(1-\rho_0)\rho_\infty \tag{3.3}$$

The weight coefficient $\hat{\alpha}_k(n)=-2\cos\hat{\omega}_k(n)$, with $\hat{\omega}_k(n)$ the notch frequency estimate of the input frequency, is adjusted by a Recursive Mean Square (RMS) algorithm:

$$\hat{\alpha}_k(n+1)=\hat{\alpha}_k(n)-P(n)\psi(n)e_s(n) \tag{3.4}$$

where $\psi(n)$ is the gradient function, $P(n)$ represents the covariance parameters, $\lambda(n)$ is the forgetting factor, and $e_s(n)$ represents the output of ANF shown in Figure 3.1.:

$$\psi(n)=\frac{\partial e_s(n)}{\partial\hat{\alpha}_k(n)}=\frac{y(n-1)-\rho_k(n)e_s(n-1)}{1+\rho_k(n)\hat{\alpha}_k(n)z^{-1}+\rho_k^2(n)z^{-2}} \tag{3.5}$$

$$P(n)=\frac{(1-\lambda(n))P(n-1)}{\lambda(n)+\psi^2(n)P(n-1)} \tag{3.6}$$

$$\lambda(n)=\lambda_0\lambda(n-1)+(1-\lambda_0)\lambda_\infty \tag{3.7}$$

When implementing the SMM-ANF algorithm in the simulation described below, the initial values are:

$$\begin{aligned} &f_s = 2\text{kHz}, \rho(1) = \rho(2) = \rho_0 = 0.9, \rho_\infty = 0.995, \\ &P(1) = P(2) = 100, \lambda(1) = \lambda(2) = \lambda_0 = 0.9, \lambda_\infty = 0.995 \end{aligned} \tag{3.8}$$

There are limitations on how well this technique can track signals with rapidly changing amplitude, as occurs in two-phase flow. Recently, Yin et al.[82] developed the Amplitude Adaptive Notch Filter (AANF) to enable the method to work with an amplitude varying signal. However, AANF was designed for grid signal processing, and the application of AANF in Coriolis flowmeter signal processing remains unexplored.

3.1.2 Discrete Fourier Transform for Amplitude and Phase Difference Tracking

A well-established approach for tracking the frequency of a sinusoid is to calculate the signal's Fourier coefficients and map the results into the frequency domain. The peak in the frequency domain gives the best estimate of the signal's frequency. The phase difference and amplitude can be calculated using the Discrete Time Fourier Transform (DTFT) based on the peak frequency. For efficient real-time implementation and/or to reduce spectral leakage, windowing techniques (e.g. rectangular, Hanning) may be applied. Rectangular windowing can be implemented via a recursive calculation to reduce the computational load, while other windowing techniques can reduce spectral leakage.

Once the current frequency has been determined, the phase difference and amplitude can be calculated using the DTFT, based on the tracked frequency's Fourier coefficients. Tu et al. [83] explored the spectral leakage problem and determined the phase of a periodic signal from an arbitrary number of samples without spectral leakage by considering the negative frequency contribution. Shen et al. [84] further improved

the recursive DTFT algorithm and increased the accuracy of the phase difference tracking. The equation for their most recent recursive DTFT algorithm is as follows:

$$X_{m,N}(\hat{\omega}_m) = \sum_{n=0}^{N-1} x(m+n)\cdot e^{-j\hat{\omega}_m n} = x(m) + x(m+1)\cdot e^{-j\hat{\omega}_m} + x(m+2)\cdot e^{-2j\hat{\omega}_m} + \cdots + x(m+N-1)\cdot e^{-j\hat{\omega}_m (N-1)} \tag{3.9}$$

where m is current sample time, N is window length and $\hat{\omega}_m$ is radian frequency at current sample which is calculated by ANF as before. At the next sample time $m+1$, this becomes:

$$\begin{aligned} X_{m+1,N}(\hat{\omega}_{m+1}) &= \sum_{n=0}^{N-1} x(m+1+n)\cdot e^{-j\hat{\omega}_{m+1} n} \\ &= \left(\sum_{n=0}^{N-1} x(m+n)\cdot e^{-j\hat{\omega}_{m+1} n} - x(m) \right)\cdot e^{-j\hat{\omega}_{m+1}} \\ &\quad + x(m+N)\cdot e^{-j\hat{\omega}_{m+1}(N-1)} \\ &\approx \left(\sum_{n=0}^{N-1} x(m+n)\cdot e^{-j\hat{\omega}_{m} n} - x(m) \right)\cdot e^{-j\hat{\omega}_{m+1}} \\ &\quad + x(m+N)\cdot e^{-j\hat{\omega}_{m+1}(N-1)} \\ &= \left(X_{m,N}(\hat{\omega}_m) - x(m) + x(m+N)\cdot e^{-j\hat{\omega}_{m+1} N} \right)\cdot e^{-j\hat{\omega}_{m+1}} \end{aligned} \tag{3.10}$$

In (3.9) and (3.10), $\hat{\omega}_m$ and $\hat{\omega}_{m+1}$ represent the estimated frequencies for the two adjacent sampling points.

To a limited extent, the DTFT can overcome the interference of harmonics and noise, is operationally efficient, and is easy to implement in real-time hardware. However, the Fast Fourier Transform (FFT) based technologies has inherent performance limitations, such as spectral leakage and the picket fence effect, due to nonsynchronous sampling [85]. Also there is an unavoidable trade-off between time and frequency domain resolution, based on the window length. In two-phase flow situations, the sensor signal varies rapidly, so the measurement needs a fast dynamic response. This requires high

time domain resolution which, for the DTFT method, will result in decreased frequency domain resolution. Hence the DTFT method cannot guarantee high frequency resolution for two-phase flow situations.

For phase difference tracking, the negative frequency-based DTFT algorithm improves the precision but spectral leakage problems still exist with nonsynchronous sampling. Other methods ([86], [87]) have reduced the phase difference error using Rectangular Self-Convolution Windows (RSCWs) but the resulting dynamic response has not been explored.

3.1.3 Zero-crossing Method

Henry et al. [13], [71] have extensively explored the zero-crossing method to track sensor parameters and have applied the techniques to Coriolis flowmeters. The work has been converted into the commercial Foxboro CFT51 transmitter and also applied in batching from empty-to-full and two-phase flow measurement. Hou et al. [88] have explored using a zero-crossing based method to correct fluid measurement errors using neural networks.

The zero-crossing method basically detects the timing of when each sensor signal crosses zero and then extracts the sinusoidal cycle data to calculate amplitude, frequency and phase. The extraction process is shown in the figure below:

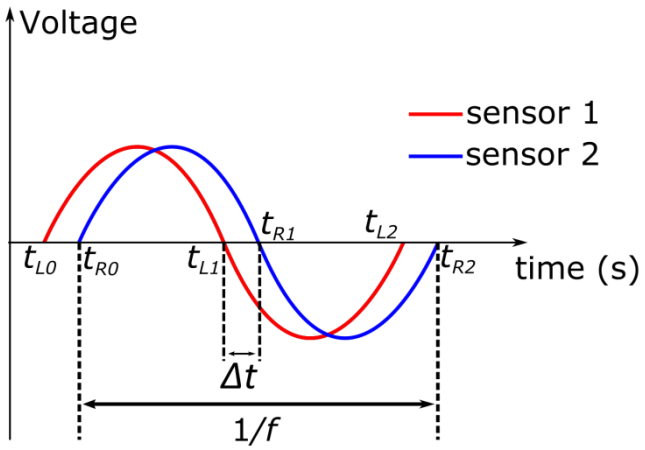


Figure 3.2: Zero-crossing method diagram

Firstly, the frequency is calculated from the time difference between half-cycle end points or full-cycle end points. Assuming the time of the latest zero crossing is t_{R2}, here half-cycle end points are used to achieve a faster dynamic response, using:

$$\hat{f} = \frac{1}{2(t_{R2} - t_{R1})} \tag{3.11}$$

where f is frequency, t_{R1} and t_{R2} are sensor zero-crossing points as shown in the figure above.

Assuming the two sensor signals are :

$$\begin{aligned} x_1 &= A\sin(2\pi ft + \frac{\phi}{2}) \\ x_2 &= A\sin(2\pi ft - \frac{\phi}{2}) \end{aligned} \tag{3.12}$$

where A is the common amplitude of the two sensor signals and ϕ is the phase difference between them, then for the amplitude and phase difference calculation, the estimated frequency is used to generate sine and cosine pairs and then integral values over the period as follows:

$$
\begin{aligned}
I_{L1} &= \int_{t_{L0}}^{t_{L0}+\frac{1}{f}} x_1(t)\sin(2\pi ft)\mathrm{d}t = \frac{1}{2f}A\cos(\frac{\phi}{2}) \\
I_{L2} &= \int_{t_{L0}}^{t_{L0}+\frac{1}{f}} x_1(t)\cos(2\pi ft)\mathrm{d}t = \frac{1}{2f}A\sin(\frac{\phi}{2}) \\
I_{R1} &= \int_{t_{R0}}^{t_{R0}+\frac{1}{f}} x_2(t)\sin(2\pi ft)\mathrm{d}t = \frac{1}{2f}A\cos(-\frac{\phi}{2}) \\
I_{R2} &= \int_{t_{R0}}^{t_{R0}+\frac{1}{f}} x_2(t)\cos(2\pi ft)\mathrm{d}t = \frac{1}{2f}A\sin(-\frac{\phi}{2})
\end{aligned}
\tag{3.13}
$$

Then amplitude and phase difference can be obtained by:

$$
\begin{aligned}
\hat{A} &= 2\hat{f}\sqrt{I_{L1}^2 + I_{L2}^2} \\
\hat{\phi} &= \arctan(\frac{I_{L2}}{I_{L1}}) - \arctan(\frac{I_{R2}}{I_{R1}})
\end{aligned}
\tag{3.14}
$$

For the next calculation, the integrals are updated at t_{L1} and t_{R1} and hence the amplitude and phase difference is updated by every half cycle.

One disadvantage of the zero-crossing method is that it updates the measurement result only every half cycle. Hence it effectively assumes all parameters are stable during the half cycle of the sensor signal, and this limits its dynamic performance.

3.1.4 Digital Phase Locked Loop for Frequency Tracking

Freeman [89] used a Digital Phase Locked Loop (DPLL) to track frequency and phase difference for a Coriolis flowmeter. As shown in Figure 3.3, the signals are multiplied by a modulation function $c(n) = e^{-j2\pi f_h nt}$, where f_h is close to the sensor signal frequency, so that the resulting product is shifted close to zero hertz (DC). Comb filters are used to remove harmonic noise, followed by decimation and down-sampling. Three FIR filters track the down-sampled signals at frequencies $-f_h/16$, 0 and $+f_h/16$ with

linear or quadratic interpolation providing a final estimate of the flow tube resonant frequency.

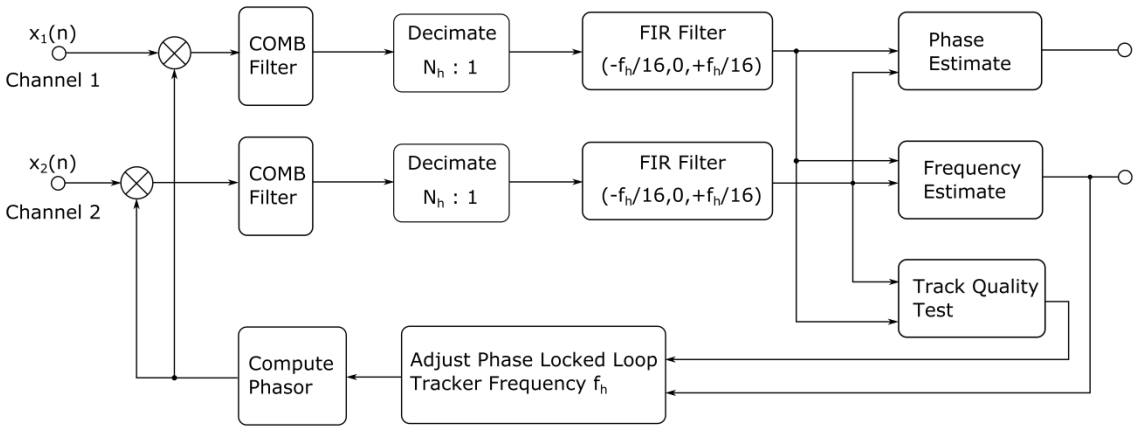


Figure 3.3: Digital Phase Locked Loop diagram [89]

One advantage of this structure is that the DPLL is not affected by an amplitude change of sensor signal which is particularly useful in Coriolis flowmeters measuring two-phase flow where the amplitude is varying. Another advantage is that DPLL can update the measurement result sample by sample which is beneficial for dynamic performance.

3.1.5 Quadrature Demodulation for Amplitude and Phase Difference Tracking

Based on DPLL tracked frequency as above, Quadrature Demodulation (QD) methods can be adopted to track amplitude and phase difference which is widely used in industry [69], [70].

Assuming the sensor signals are the same as before:

$$x_1 = A\sin(\omega t + \frac{\phi}{2})$$
$$x_2 = A\sin(\omega t - \frac{\phi}{2}) \quad (3.15)$$

where A is amplitude, ω is angular frequency and ϕ is phase difference. Multiplying with synthesized signal $\cos(\omega t)$ and $\sin(\omega t)$ by using DPLL tracked frequency ω, we can get:

$$\begin{aligned}
S_{L1}(t) &= x_1 \cos(\omega t) = A\sin(\omega t + \frac{\phi}{2})\cos(\omega t) = \frac{A}{2}\sin\frac{\phi}{2} + \frac{A}{2}\sin(2\omega t + \frac{\phi}{2}) \\
S_{L2}(t) &= x_1 \sin(\omega t) = A\sin(\omega t + \frac{\phi}{2})\sin(\omega t) = \frac{A}{2}\cos\frac{\phi}{2} - \frac{A}{2}\cos(2\omega t + \frac{\phi}{2}) \\
S_{R1}(t) &= x_2 \cos(\omega t) = A\sin(\omega t - \frac{\phi}{2})\cos(\omega t) = \frac{A}{2}\sin(-\frac{\phi}{2}) + \frac{A}{2}\sin(2\omega t - \frac{\phi}{2}) \\
S_{R2}(t) &= x_2 \sin(\omega t) = A\sin(\omega t - \frac{\phi}{2})\sin(\omega t) = \frac{A}{2}\cos(-\frac{\phi}{2}) - \frac{A}{2}\cos(2\omega t - \frac{\phi}{2})
\end{aligned} \tag{3.16}$$

Then applying a low-pass filter to $S_1(t)$ and $S_2(t)$ with cut-off frequency less than 2ω, the high frequency components are filtered out and we can get:

$$\begin{aligned}
S'_{L1}(t) &= \frac{A}{2}\sin\frac{\phi}{2} \\
S'_{L2}(t) &= \frac{A}{2}\cos\frac{\phi}{2} \\
S'_{R1}(t) &= \frac{A}{2}\sin(-\frac{\phi}{2}) \\
S'_{R2}(t) &= \frac{A}{2}\cos(-\frac{\phi}{2})
\end{aligned} \tag{3.17}$$

Hence amplitude and phase difference can be calculated by:

$$\begin{aligned}
\hat{A} &= 2\sqrt{(S'_{L1}(t))^2 + (S'_{L2}(t))^2} \\
\hat{\phi} &= \arctan(\frac{S'_{L1}(t)}{S'_{L2}(t)}) - \arctan(\frac{S'_{R1}(t)}{S'_{R2}(t)})
\end{aligned} \tag{3.18}$$

One advantage of the QD technique is that it incorporates a low-pass filter within the calculation process of amplitude and phase difference. Thus QD does not need pre-filtering compared to other techniques which potentially increases its dynamic performance. However, since the amplitude and phase difference calculation are based on the tracked frequency of DPLL, the dynamic performance is also related to DPLL's

tracking performance where the DPLL technique is sensitive to noise and needs pre-filtering. For QD implementation, a reasonable approach is to design an internal low-pass filter to set the cut-off frequency to be the same as the pre-filtering to ensure consistent performance for each method. Thus pre-filtering is applied only to DPLL and QD and is adopted for amplitude and phase difference calculation without pre-filtering to achieve the best performance for both ability to suppress noise and dynamic response.

3.1.6 Digital Correlation

Wray et al. [90] describe a correlation method for finding the phase difference ϕ between Coriolis flowmeter meter sensor signals, x_1 and x_2. Given:

$$\begin{aligned} x_1 &= A\sin(2\pi ft + \frac{\phi}{2}) \\ x_2 &= A\sin(2\pi ft - \frac{\phi}{2}) \end{aligned} \tag{3.19}$$

Then the cross product $x_1 \otimes x_2$ can be written as:

$$x_1 \otimes x_2 = A^2 \int_0^{2\pi} \sin(2\pi ft + \frac{\phi}{2}) \sin(2\pi ft - \frac{\phi}{2}) dt \tag{3.20}$$

Thus the phase difference can be represented as:

$$\hat{\phi} = 2 \times \frac{x_1 \otimes x_2}{A^2} \tag{3.21}$$

Further techniques are required to track frequency and amplitude. Although this technique was originally developed for analogue signal processing, Ruoff et al. [91] discuss its merits in the context of Coriolis flowmeter digital signal processing.

3.1.7 Hilbert Transform

Duffill et al. [72] applied the Hilbert transform to form an analytic signal for Coriolis flowmeter tracking. Hilbert filtering of the sensor signals creates Hilbert pairs. The original left and right pickoff (i.e. sensor) input signals are defined and take the Euler's formula:

$$\begin{aligned} x_1 &= A_1\cos(\omega t+\phi/2) = (A_1e^{j(\omega t+\phi/2)} + A_1e^{-j(\omega t+\phi/2)})/2 \\ x_2 &= A_2\cos(\omega t-\phi/2) = (A_2e^{j(\omega t-\phi/2)} + A_2e^{-j(\omega t-\phi/2)})/2 \end{aligned} \tag{3.22}$$

where A_1 and A_2 are the amplitudes of the two sensor signals, ω is their common frequency, and ϕ is the phase difference between them. Passing the signals through identical Hilbert filters, negative frequency components are filtered out and complex analytic signals are obtained as follows:

$$\begin{aligned} x_{1a} &= A_1e^{j(\omega t+\phi/2)}/2 \\ x_{2a} &= A_2e^{j(\omega t-\phi/2)}/2 \end{aligned} \tag{3.23}$$

with the equivalent calculation for the right pickoff. Taking the conjugate of the left input Hilbert pairs and multiplying by the right input Hilbert pairs yields the following equation:

$$x_{1a}\times\overline{x_{2a}} = A_1e^{j(\omega t+\phi/2)}\times A_2e^{-j(\omega t-\phi/2)}/4 = A_1A_2e^{j\phi}/4 \tag{3.24}$$

Assuming the left and right sensor signals have equal amplitude simplifies this to:

$$x_{1a}\times\overline{x_{2a}} = A^2e^{j\phi}/4 \tag{3.25}$$

The phase difference can be obtained using:

$$\phi = \arg(x_{1a}\times\overline{x_{2a}}) \tag{3.26}$$

The amplitude is calculated from the Hilbert pairs:

$$A_1 = A_2 = A = 2|x_{1a}| = 2|x_{2a}| \tag{3.27}$$

For frequency calculation, consecutive samples of left sensor signal are taken by:

$$\overline{x_{1a}(n-1)} \times x_{1a}(n) = Ae^{-j(\omega t_{n-1}+\phi/2)} \times Ae^{j(\omega t_n+\phi/2)} / 4 = A^2 e^{j(\omega t_n-\omega t_{n-1})} / 4 \quad (3.28)$$

followed by:

$$\omega t_n - \omega t_{n-1} = \arg(\overline{x_{1a}(n-1)} \times x_{1a}(n)) \quad (3.29)$$

Then frequency is obtained by:

$$\omega = \arg(\overline{x_{1a}(n-1)} \times x_{1a}(n)) \times f_s / 2\pi \quad (3.30)$$

where f_s is the sampling rate of the input signal. Yi et al. [92] claim the Hilbert transform is not suitable for frequency tracking, while Tu et al. [79] use ANF for frequency tracking, and the Hilbert transform for phase difference calculation. However, as shown in the equations above and the results below, the Hilbert technique can be adapted to track frequency, amplitude and phase difference simultaneously.

3.2 Simulation Results

For testing each method, two simulations – empty-to-full batching and continuous two-phase flow - are carried out as discussed in Chapter 2. Simulation is performed using a 2 kHz sampling rate. Results are presented here for the following methods:

- ANF for frequency tracking, combined with DTFT for amplitude and phase difference tracking
- Zero-crossing for amplitude, frequency and phase difference tracking
- DPLL for frequency tracking, combined with QD for amplitude and phase difference tracking
- Hilbert for amplitude, frequency and phase difference tracking

For testing each algorithm's robustness, different levels of white noise are added to the benchmarks to test the performance of each algorithm.

3.2.1 Batching from Empty-to-full Benchmark Simulation

Using the empty-to-full batching benchmarks, this section applies each signal processing method to compare their dynamic performance.

Figures 3.4 – 3.6 below show the tracking performance for amplitude, frequency and phase difference respectively with no white noise added. In each case the tracked values are shown in the upper graph, with the residual errors below.

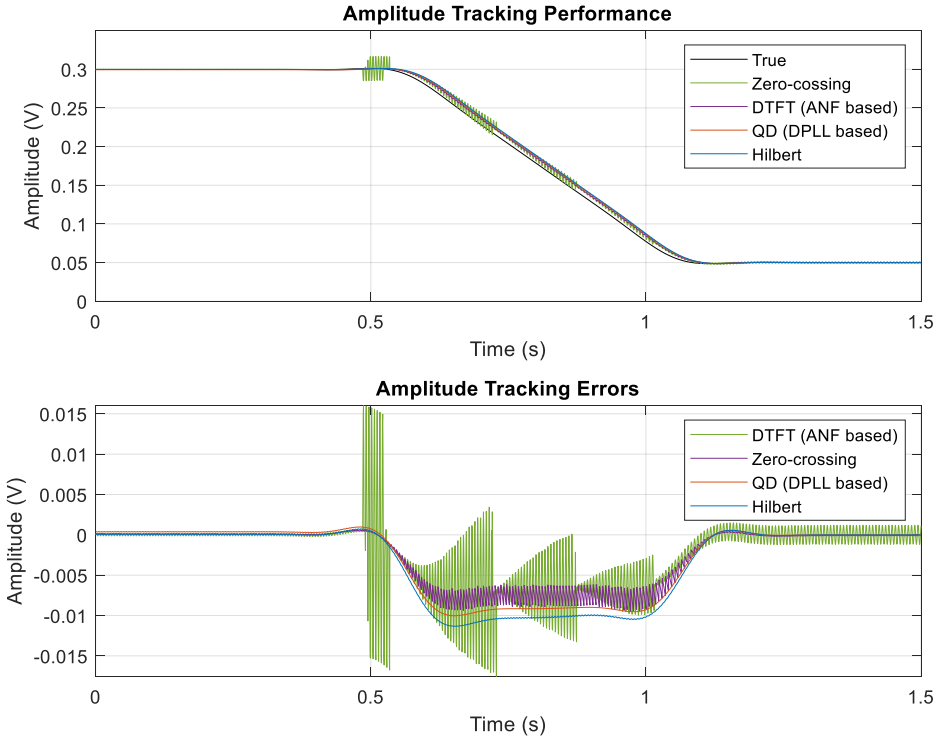


Figure 3.4 : Empty-to-full batching simulation: amplitude tracking performance

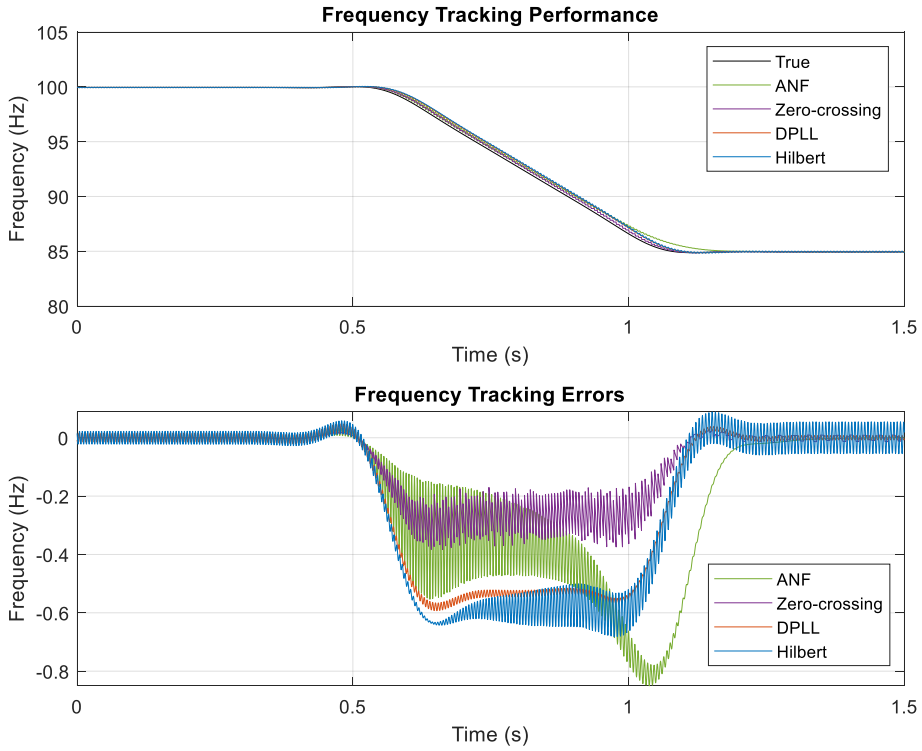


Figure 3.5: Empty-to-full batching simulation: frequency tracking performance

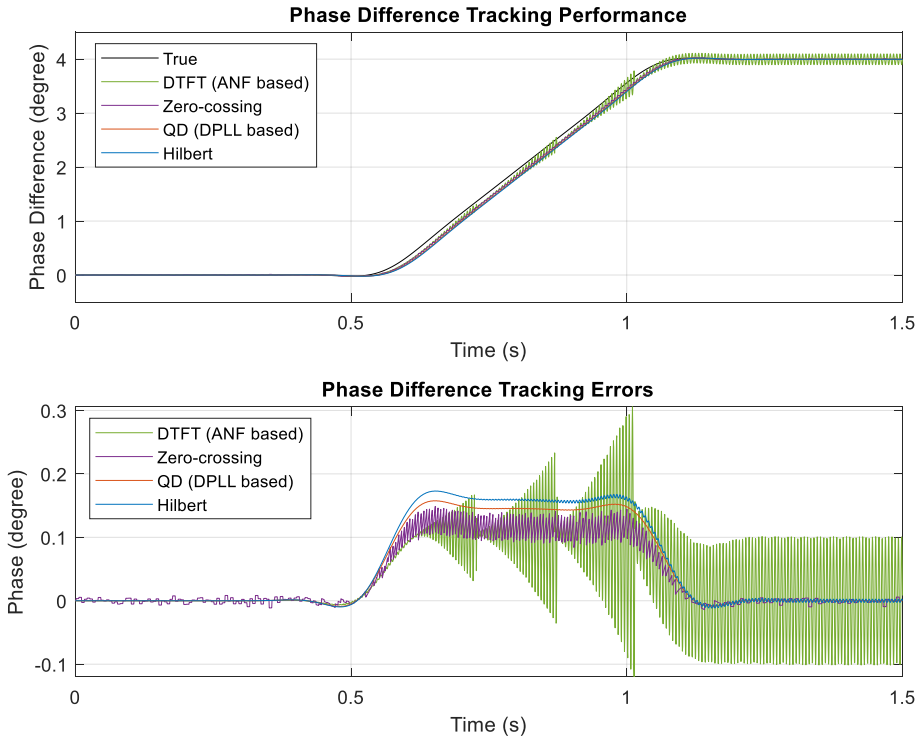


Figure 3.6: Empty-to-full batching simulation: phase difference tracking performance

From the figures, all of Zero-crossing, QD (DPLL based) and Hilbert transform methods track each parameter smoothly and well while the ANF algorithm cannot track fast enough when the amplitude of the signal decreases. The DTFT, which depends upon the frequency tracking result, generates a relatively high level of noise in the amplitude and phase difference results. This suggests that the ANF (DTFT) algorithm's performance is poor. The figures below show the performance for each method in terms of amplitude, frequency, and phase difference RMSEs and amplitude tracking delay comparison.

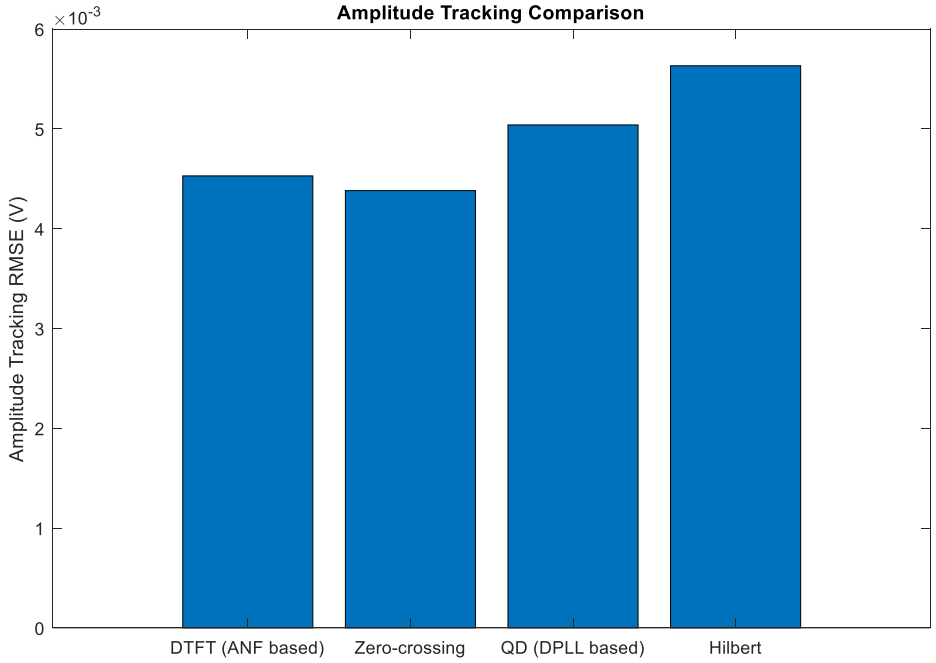


Figure 3.7: Amplitude tracking RMSEs comparison for batch simulation

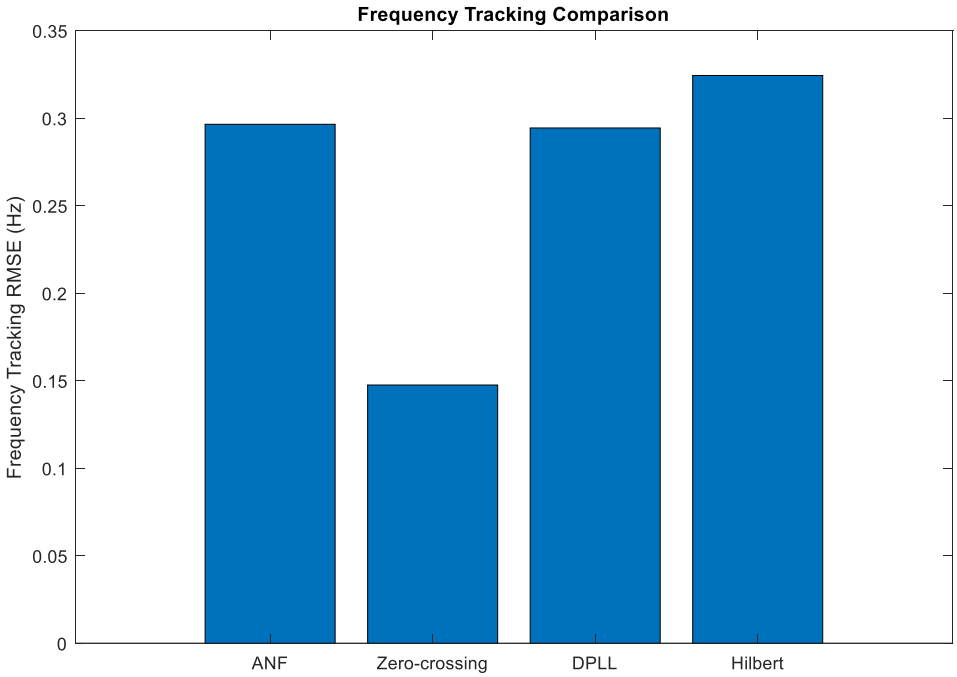


Figure 3.8: Frequency tracking RMSEs comparison for batch simulation

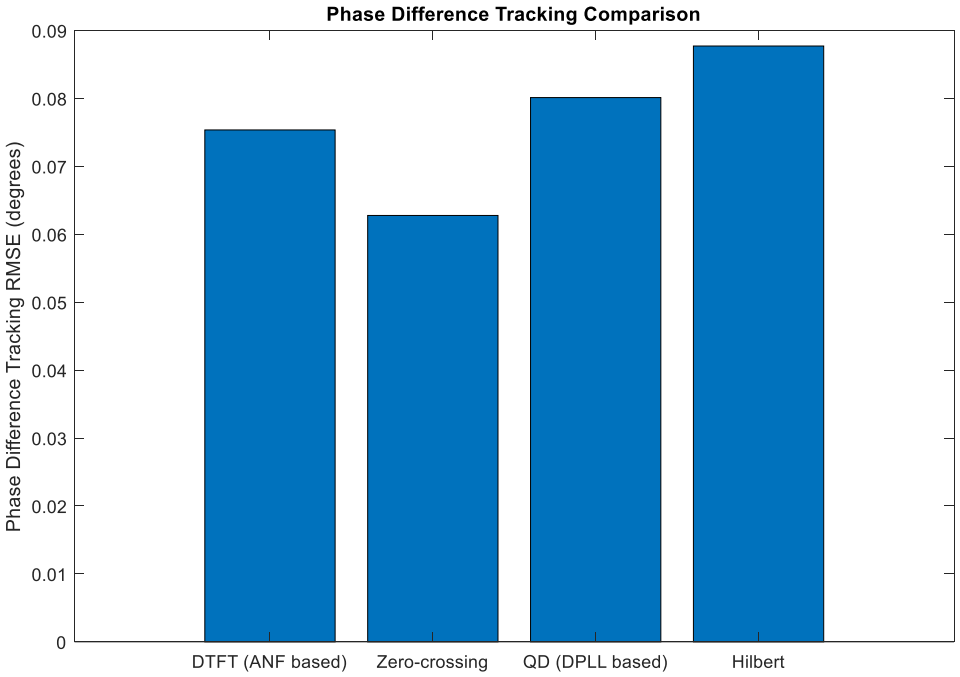


Figure 3.9: Phase difference tracking RMSEs comparison for batch simulation

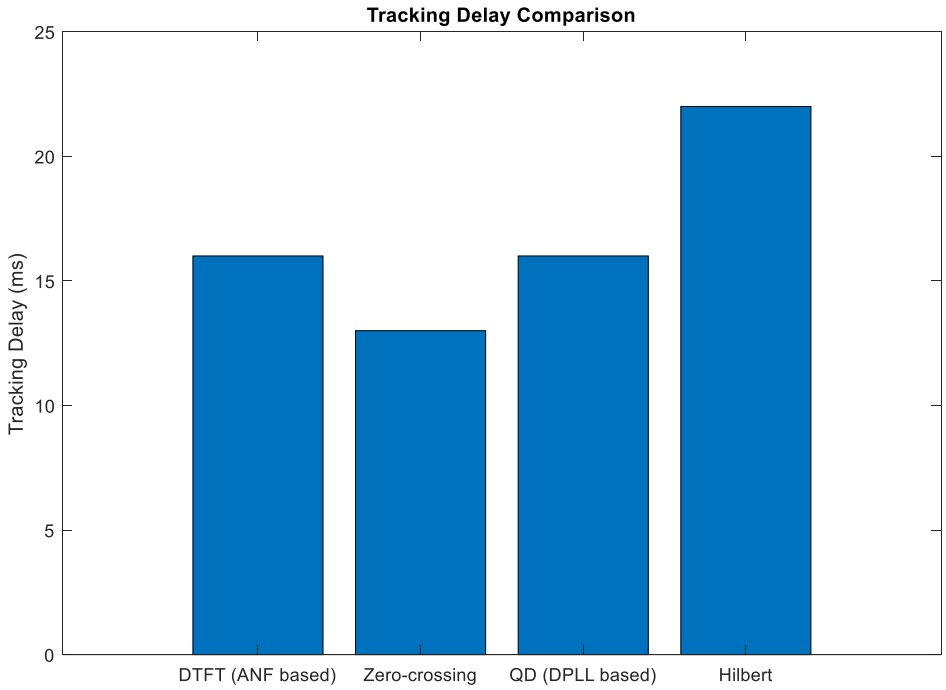


Figure 3.10: Amplitude tracking delay comparison

From the figures, zero-crossing has the best performance overall, including the smallest amplitude tracking delay which represents the fastest dynamic performance.

3.2.2 Batching from Empty-to-full Experimental Data

As discussed in section 2.1, sensor data from batching from empty-to-full experiments has been tested using each algorithm and the tracked results are presented below for the transition period. The figures below show the detailed tracking results for each method.

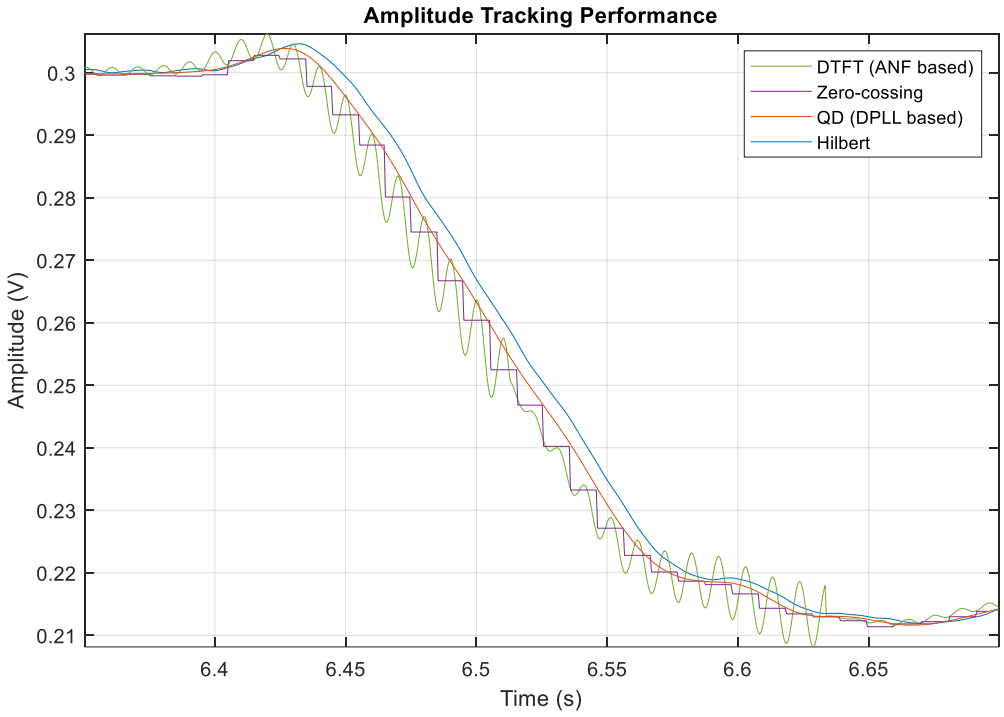


Figure 3.11: Amplitude tracking performance using batching sensor data

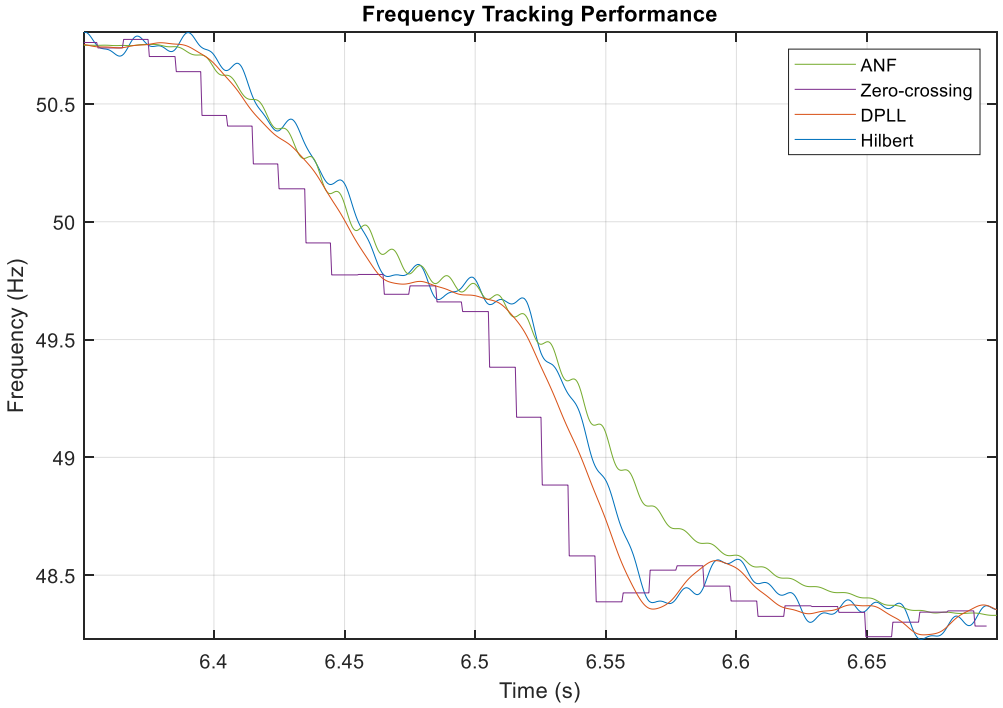


Figure 3.12: Frequency tracking performance using batching sensor data

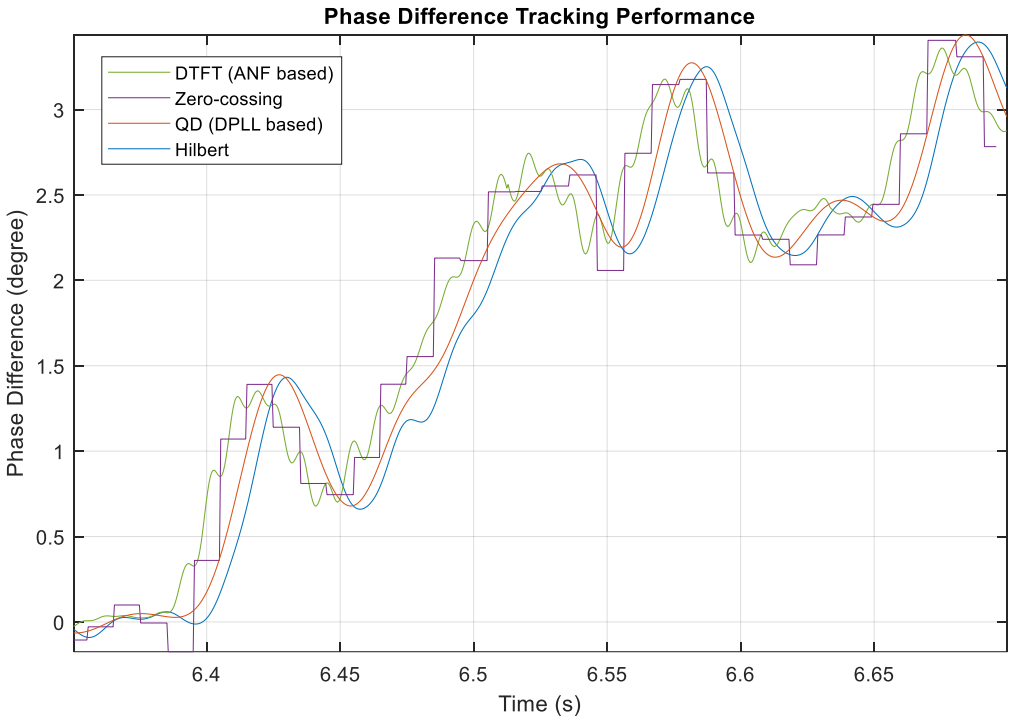


Figure 3.13: Phase difference tracking performance using batching sensor data

From the figures, Zero-crossing, QD (DPLL based) and Hilbert methods all can track the rapidly changing sensor data parameters well while the DTFT (ANF based) method produces amplitude and frequency tracking results which are noisy and delayed. Of the techniques, the zero-crossing method's tracking delay is seen to be the smallest as it leads the parameter changing trend. However, since it only provides an update every half cycle of sensor data, the measurement result is not as smooth as the other methods. The QD (DPLL based) method shows a smooth tracking result with a relatively fast dynamic performance. Hence overall it is concluded that the zero-crossing and QD (DPLL based) methods show the best performance for batching from empty-to-full for both the benchmark simulations and the experimental data tests.

3.2.3 Two-phase Benchmark Simulation

Next, we apply the current methods to the continuous two-phase flow simulation benchmark, as discussed in Section 2.2, using MRWM. The figures below show the performance with no added noise for each method.

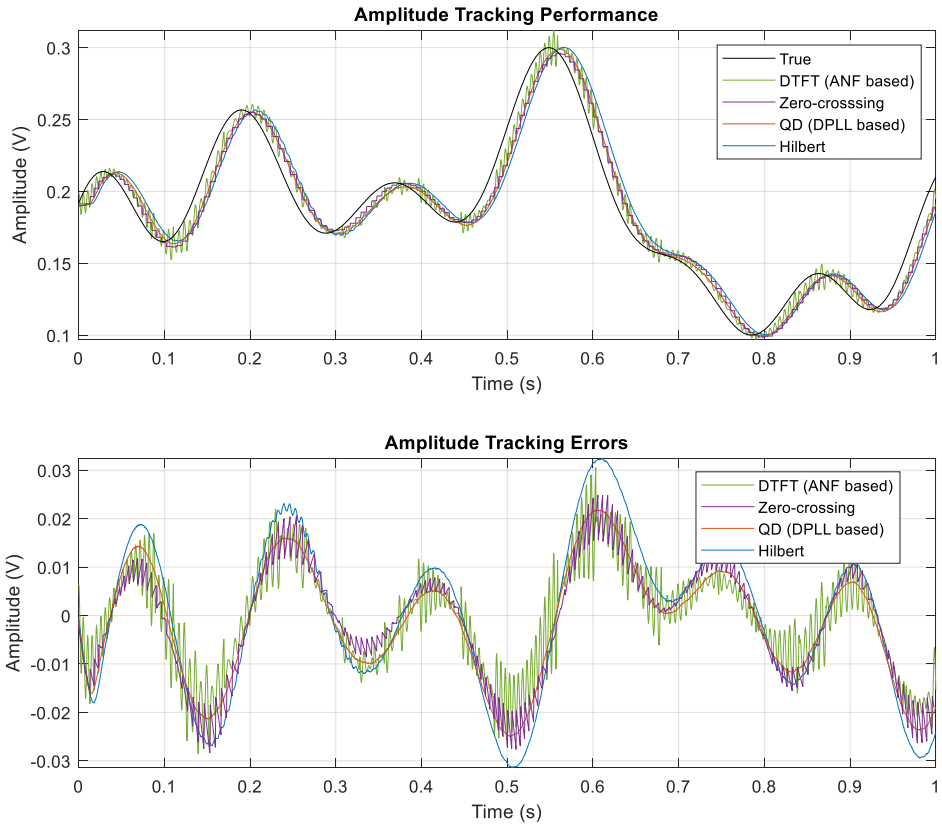


Figure 3.14: Amplitude tracking performance with no added noise

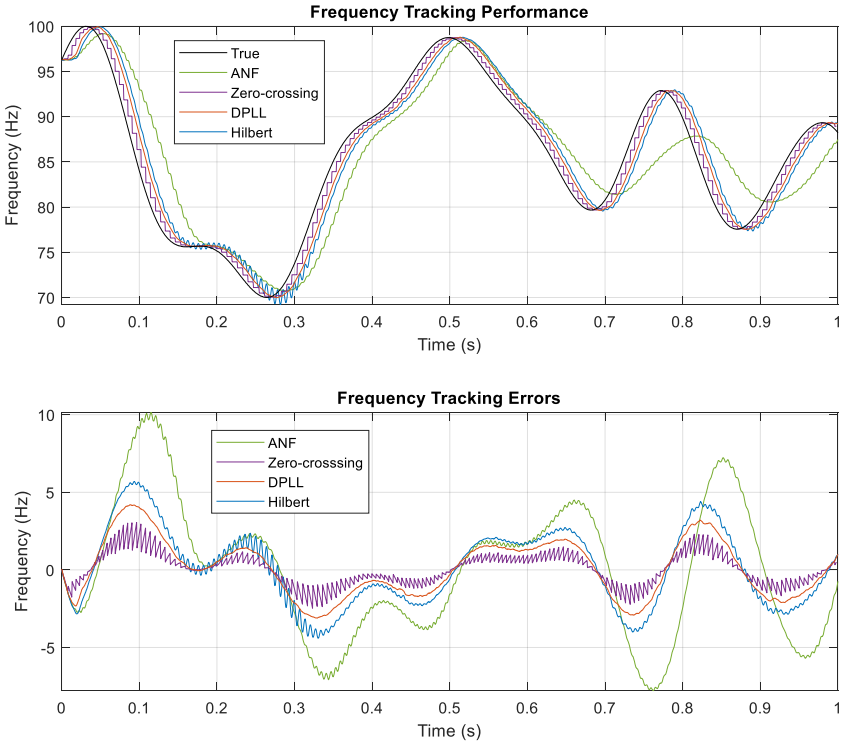


Figure 3.15: Frequency tracking performance with no added noise

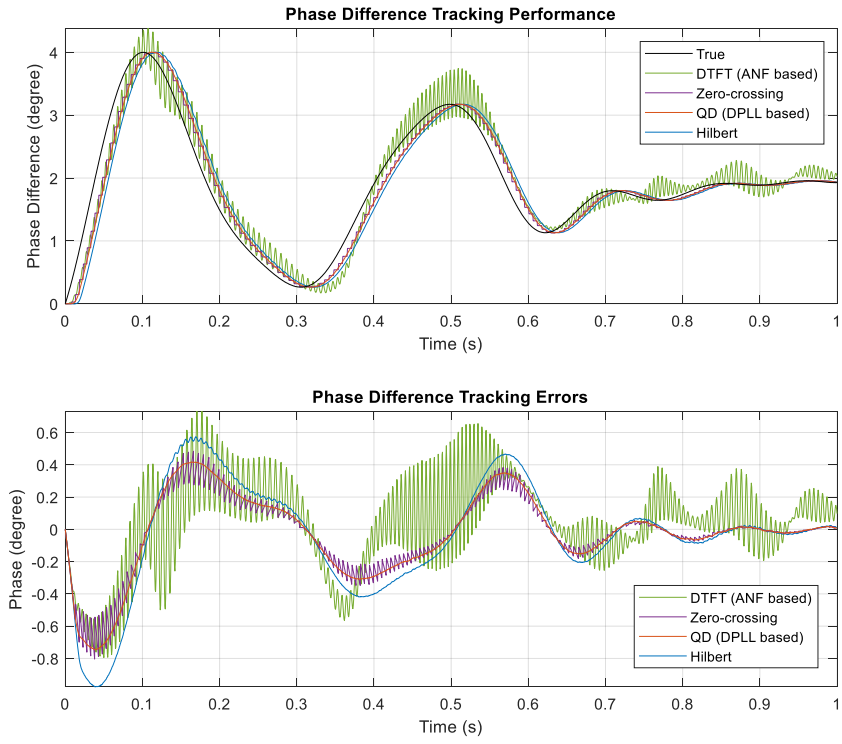


Figure 3.16: Phase difference tracking performance with no added noise

In the noise free case, the zero-crossing, QD (DPLL based) and Hilbert methods all show good tracking with some time delay, while the DTFT results are noisy. As with the batching from empty-to-full simulation, the zero-crossing method has the fastest dynamic performance while the QD (DPLL based) method has the smoothest tracking result with relatively good dynamic performance. The figures below show the RMSEs of each method for different parameter tracking.

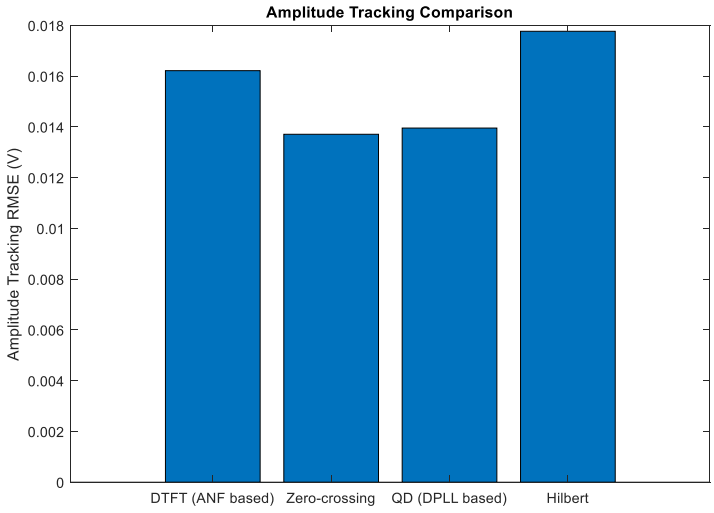


Figure 3.17: Amplitude tracking RMSEs comparison for two-phase simulation

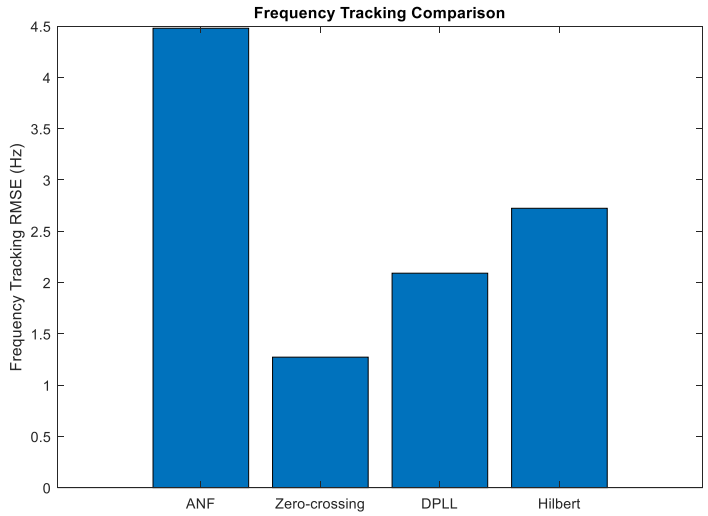


Figure 3.18: Frequency tracking RMSEs comparison for two-phase simulation

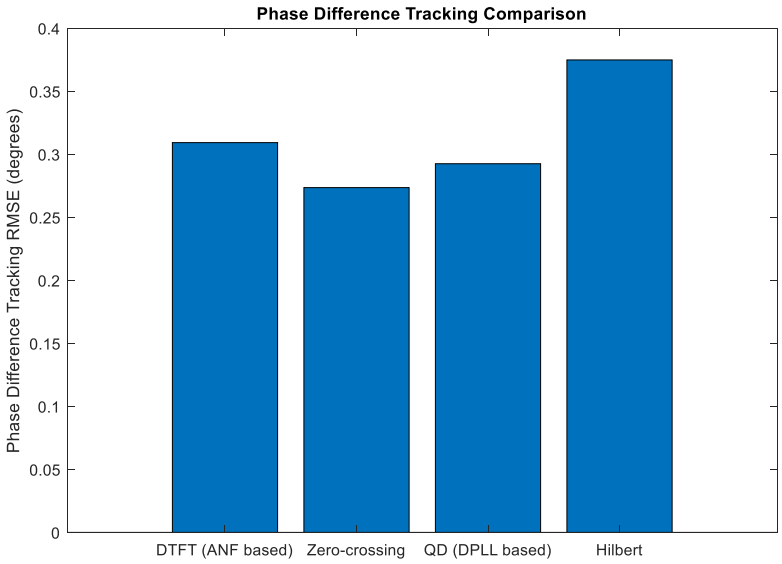


Figure 3.19: Phase difference tracking RMSEs comparison for two-phase simulation

From the figures, the zero-crossing method shows the smallest errors. The QD (DPLL based) method is the most accurate of the sample by sample techniques.

To further test each method's robustness and stability towards spurious sensor input, different levels of random noise are added to the simulated sensor data for testing, and revised RMSEs are calculated. Since the amplitude of the two-phase flow benchmark is varying, it is difficult to add noise to achieve a certain SNR. Hence random noise with fixed standard deviation σ is added to the two-phase flow simulation benchmark experimental sensor data to achieve approximately 17 dB, 37 dB, 57 dB and 77 dB SNR (based on assuming the sensor data mean peak-to-peak amplitude is 0.2V). The figures below show the resulting RMSEs.

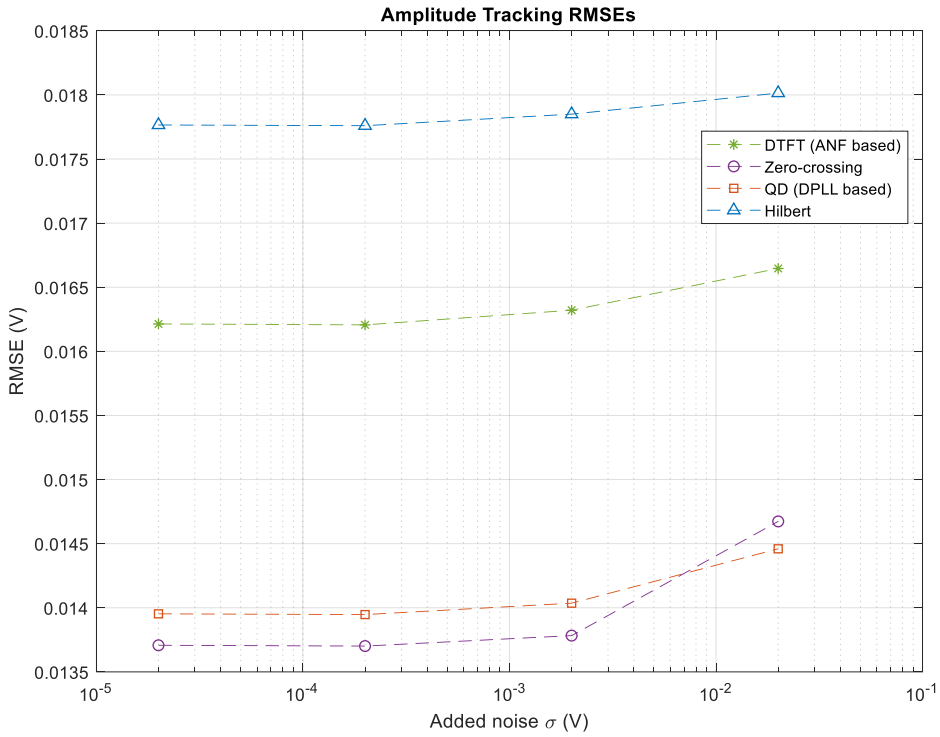


Figure 3.20: Amplitude tracking RMSEs at different level of noise

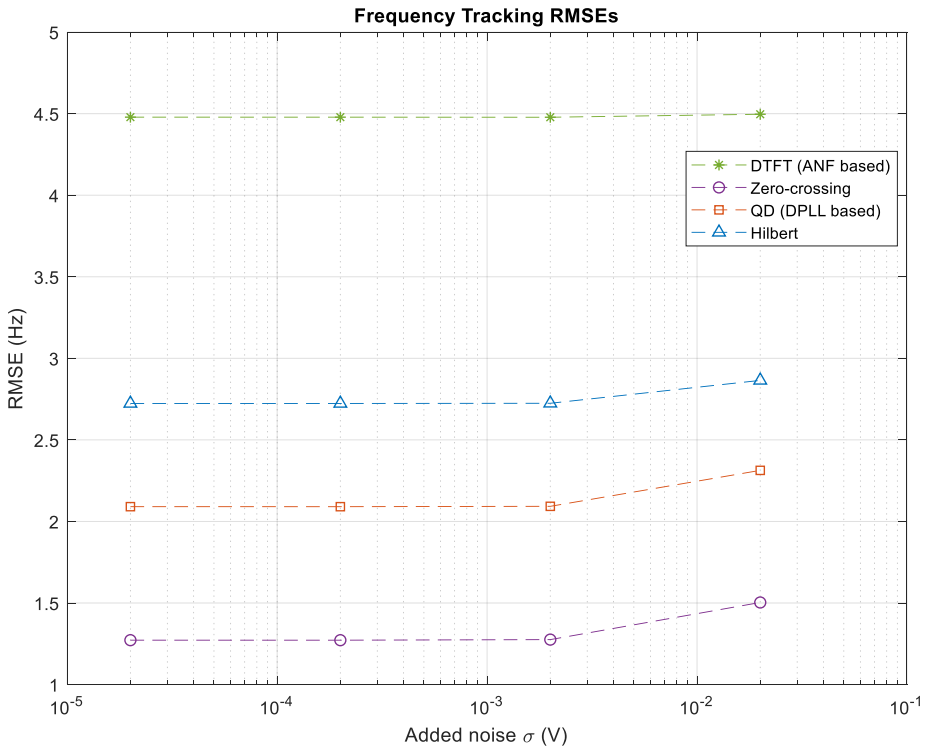


Figure 3.21: Frequency tracking RMSEs at different level of noise

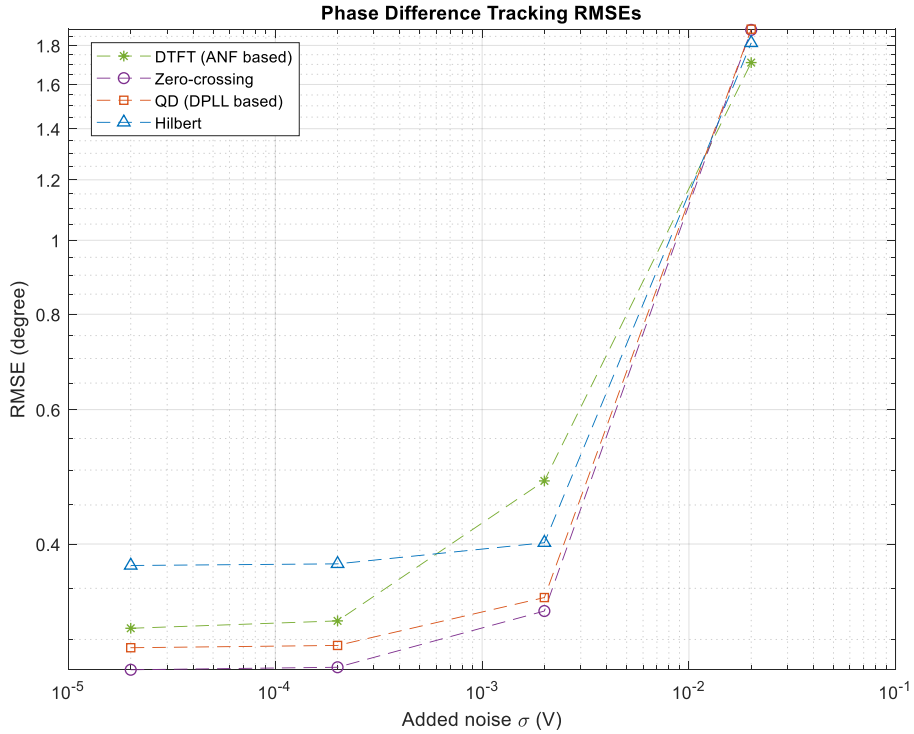


Figure 3.22: Phase difference tracking RMSEs at different level of noise

From the figures, each method's amplitude and frequency tracking RMSEs increase gradually with increasing noise and consistently show good performance. The zero-crossing and QD (DPLL based) methods still perform best with different level of noise. However, the phase difference RMSEs increase sharply when the approximate sensor signal SNR reaches 17 dB for all methods, while the frequency and amplitude RMSEs show only moderate increases. In the case of the zero crossing method, the greater sensitivity to noise of the amplitude and phase difference method can be explained as follows. The amplitude and phase/time difference are calculated based on Fourier integrals which integrate the noise over the whole cycle of signal but which remain vulnerable to noise. A similar analysis may be applied to each of the other techniques. Overall, these results provide an indication of the minimum SNR required to provide reasonable measurement accuracy, of around 37 dB.

3.2.4 Two-phase Flow Experimental data with Varying GVF

Each method has also been tested using the varying GVF sensor data as discussed in Section 2.2. Although quantified results for evaluating each method's parameter tracking results are difficult to calculate since the true parameters' values are unknown, the different methods' ability to deal with this challenging situation and dynamic performance can be virtually observed. The figures below show the tracking performance of each method for each of the sensor signal parameters.

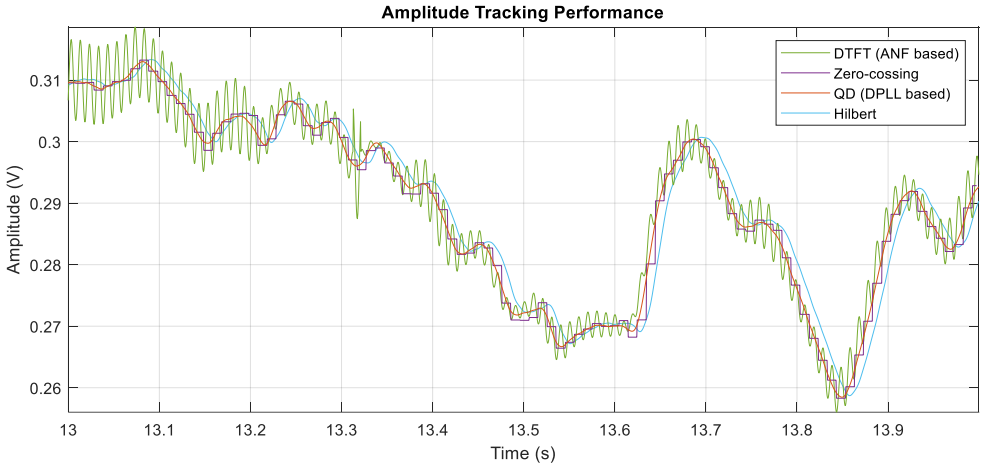


Figure 3.23: Amplitude tracking performance using two-phase sensor data



Figure 3.24: Frequency tracking performance using two-phase sensor data

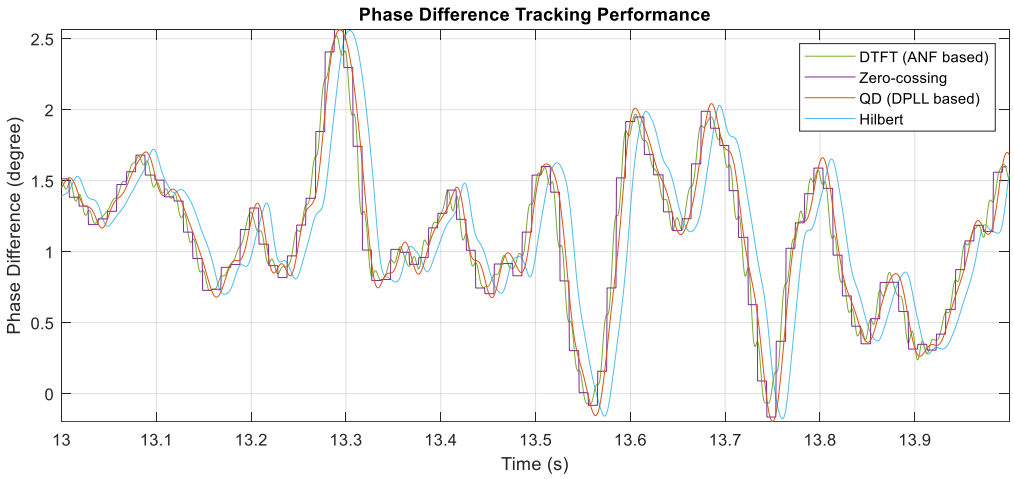


Figure 3.25: Phase difference tracking performance using two-phase sensor data

From the figures, all methods except DTFT (ANF based) method can track sensor parameters well for rapidly varying GVF sensor data. Among them, zero-crossing and QD (DPLL based) methods again show better performance with the fastest dynamic performance. In this situation, QD (DPLL based) method can be identified as the best of the current methods since the measured result is updated sample by sample which delivers a smooth tracking result.

3.3 Summary

With increasing computation power available at low cost and with low power consumption, there are continuing opportunities to improve the signal processing techniques used for Coriolis flowmeters. Two challenging applications for Coriolis flowmeter applications are batching from empty-to-full and two-phase flow, where all of the measurement parameters are subject to large and rapid variations. Previous research into signal processing techniques has not given much consideration to these difficult conditions – specifically, it has commonly been assumed that the amplitude of

the sensor signals is constant. This chapter has discussed the major current signal processing methods for Coriolis flowmeters in academia and industry including DTFT (ANF based), zero-crossing, QD (DPLL based) and Hilbert transform. Their performance has been evaluated in batching from empty-to-full and two-phase flow simulation benchmarks, where frequency, amplitude and phase difference all vary simultaneously. From the results, the zero-crossing and QD (DPLL based) techniques deal with these challenging situations well and demonstrate good dynamic performance. Also they are capable of carrying out good measurement results in noisy conditions when combined with pre-filtering. Furthermore, each method has also been tested with experimental sensor data collected in Chapter 2 to validate their performance. All methods except DTFT (ANF based) show good performance by correctly tracking the sensor parameters. Among them, zero-crossing and QD (DPLL based) techniques again show better performance.

However, it is still possible to improve the performance further by carrying out new signal processing techniques with reduced tracking delay, better noise performance and lower computational cost. In the next chapter new signal processing techniques will be developed suited to improve the performance further for the challenging conditions of batching from empty-to-full and two-phase flow measurement.

4.COMPLEX SIGNAL PROCESSING

In this Chapter, a new family of signal processing techniques is proposed which is better suited to two-phase Coriolis flowmeter signal processing than the current methods. The new methods are based on the concept of the Complex Bandpass Filter (CBF) and Complex Notch Filter (CNF) and their combination.

CBF is used in a wide range of communication systems ([93], [94]) and also in the biomedical area [95]. It has not proved possible to find an earlier application of CBF to conventional signal processing of real signals in an instrumentation application prior to this thesis: it has mainly been used to filter out white noise in a single-sided complex signal to improve SNR. Here we extend CBF to filter out the negative frequency component in a double-sided real Coriolis flowmeter sinusoidal sensor signal in order to track its parameters as well as to improve the SNR.

4.1 Complex Bandpass Filter

The Complex Bandpass Filter (CBF) is derived from a conventional low-pass filter design (for example an elliptic filter) through the application of a complex shift factor $e^{j\theta}$ to the filter coefficients. Define the original filter transform function as:

$$H_r(z) = \frac{\sum_{m=0}^{P} b_m z^{-m}}{\sum_{n=0}^{Q} a_n z^{-n}} \tag{4.1}$$

where P and Q are the numerator and denominator order, and b_m and a_m are the filter coefficients. If Q = 0, the filter is Finite Impulse Response (FIR); otherwise, it is Infinite Impulse Response (IIR).

Applying the complex shift factor $e^{j\theta}$ to $H_r(z)$:

$$H_r(z) \xrightarrow{z^{-1}=e^{j\theta}z^{-1}} H_c(z) = \frac{\sum_{m=0}^{P} b_m e^{j\theta m} z^{-m}}{\sum_{n=0}^{Q} a_n e^{j\theta n} z^{-n}} \tag{4.2}$$

Here the numerator and denominator orders P and Q are unchanged, while the filter coefficients change to $b_m e^{j\theta m}$ and $a_n e^{j\theta n}$.

The complex shift rotates the zeros and poles of the original filter by an angle θ in the z-plane in the anti-clockwise direction. Figure 4.1 shows the resulting zero and pole rotation for an exemplary 5^{th} order elliptic filter.

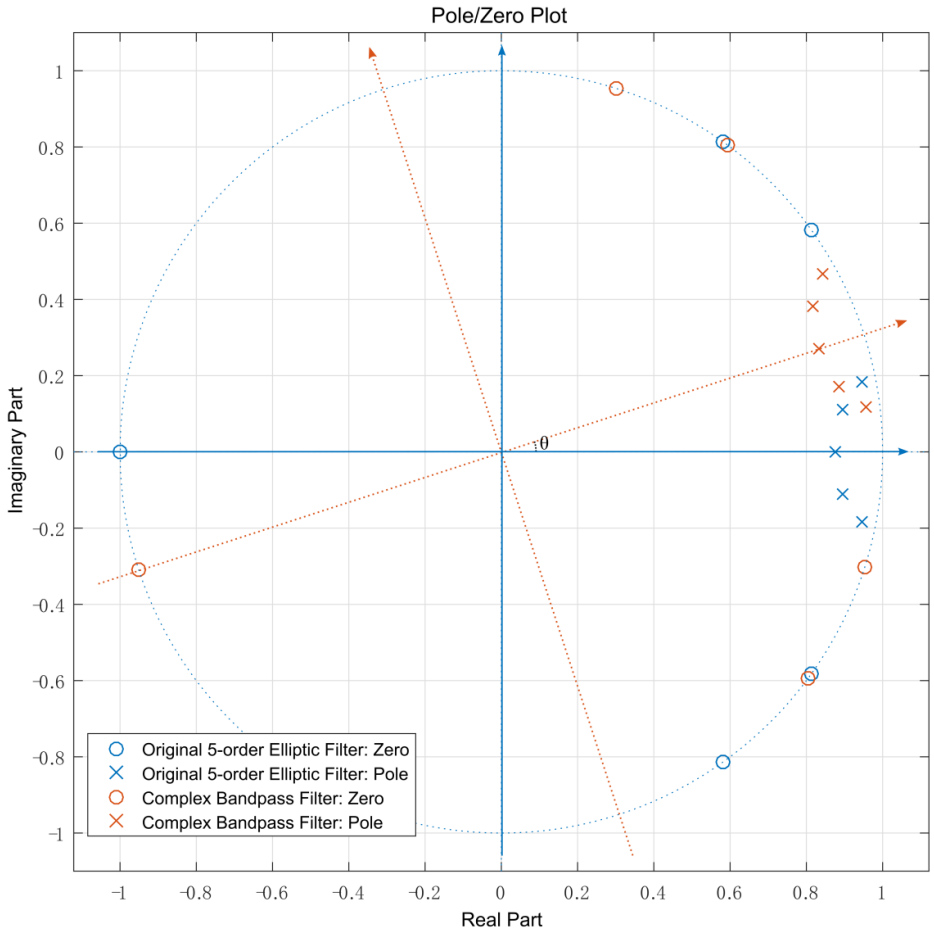


Figure 4.1: Zeros and poles rotation for CBF

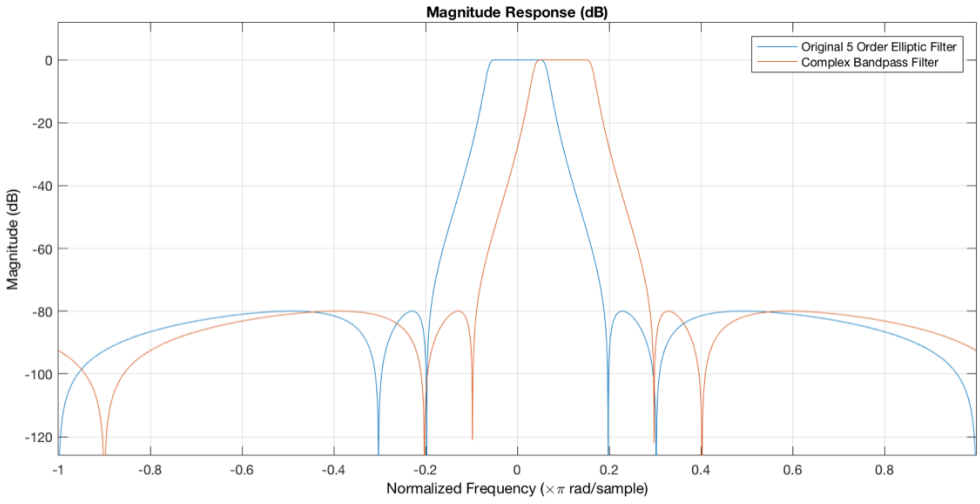


Figure 4.2: Original elliptic filter and shifted CBF magnitude response

The rotation only changes the angle of the poles and zeros in the z-domain, while the radius and relative positions remain the same. Accordingly, the effect on the filter properties is to induce a shift of θ radians/sample in the magnitude response, as shown in Figure 4.2, converting the original low pass filter into a bandpass filter.

When a real signal is passed through the CBF, the negative frequency component is filtered out, resulting in a single-sided analytic form. The filtering process in the frequency domain is shown in Figure 4.3, where the original input is a real double-sided sinusoidal signal with frequency ω_0.

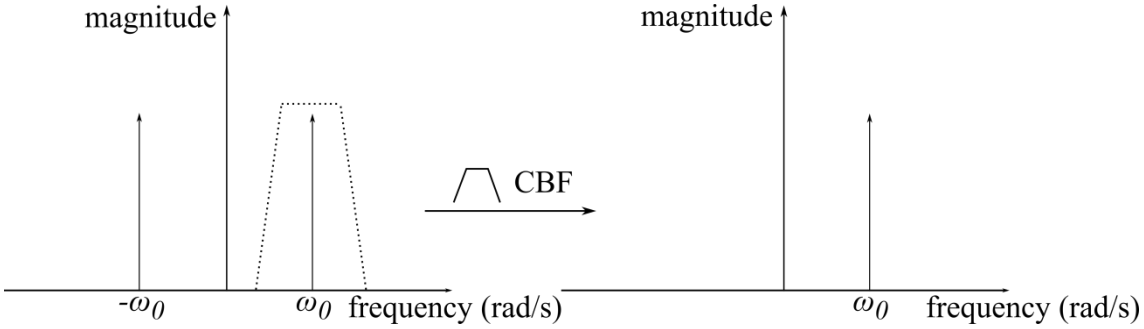


Figure 4.3: Filtering process of CBF

After getting the analytic form of the filtered signal, the calculation of amplitude, frequency, phase are similar to those used in the Hilbert transform method [72]. For Coriolis flowmeter signal processing, where two sensor signals must be tracked, the phase difference is readily calculated from the phases of the individual signals. Assume the Coriolis flowmeter sensor signals take the Euler's form:

$$\begin{aligned} x_1 &= A_1\cos(\omega t+\phi/2) = (A_1 e^{j(\omega t+\phi/2)} + A_1 e^{-j(\omega t+\phi/2)})/2 \\ x_2 &= A_2\cos(\omega t-\phi/2) = (A_2 e^{j(\omega t-\phi/2)} + A_2 e^{-j(\omega t-\phi/2)})/2 \end{aligned} \tag{4.3}$$

where A_1 and A_2 are the amplitudes of the two sensor signals, ω is their common frequency, and ϕ is the phase difference between them. Passing the signals through identical CBF filters, complex analytic signals are obtained as follows:

$$\begin{aligned} x_{1a} &= A_1 e^{j(\omega t+\phi/2)} / 2 \\ x_{2a} &= A_2 e^{j(\omega t-\phi/2)} / 2 \end{aligned} \tag{4.4}$$

The signal amplitude can be obtained by taking conjugate terms as follows:

$$x_{1a} \times \overline{x_{2a}} = A_1 e^{j(\omega t+\phi/2)} \times A_2 e^{-j(\omega t-\phi/2)} / 4 = A_1 \times A_2 e^{j\phi} / 4 \tag{4.5}$$

For brevity we assume here that the two input signals have the same amplitude ($A_1 = A_2 = A$); this is a reasonable first approximation for the Coriolis flowmeter, and further computational steps can be taken to account for any sensor imbalance.

The phase difference may now be calculated using:

$$\hat{\phi} = \arg(x_{1a} \times \overline{x_{2a}}) \tag{4.6}$$

while the amplitude can be obtained using:

$$A_1 = A_2 = 2|x_{1a}| = 2|x_{2a}| \tag{4.7}$$

The frequency may be derived from the change of phase over a number of samples. For example, consider adjacent samples from the first sensor signal:

$$\begin{aligned} \overline{x_{1a}(n-1)} \times x_{1a}(n) &= A e^{-j(\omega t_{n-1}+\phi/2)} \times A e^{j(\omega t_n+\phi/2)} / 4 \\ &= A^2 e^{j(\omega t_n-\omega t_{n-1})} / 4 \end{aligned} \tag{4.8}$$

followed by:

$$\omega t_n - \omega t_{n-1} = \arg(\overline{x_{1a}(n-1)} \times x_{1a}(n)) \tag{4.9}$$

Converting into Hz:

$$\hat{f} = \frac{(\omega t_n - \omega t_{n-1}) \times f_s}{2\pi} \tag{4.10}$$

where f_s is the sampling frequency. Using adjacent samples to calculate frequency provides a short response time but is susceptible to noise; comparing the phase shift over a larger number of samples is equally possible, leading to a trade-off between measurement noise and response time.

By selecting the 'shift' frequency and passband of the CBF, the range of frequencies that may be tracked can be matched to the resonant frequency range of the corresponding flow tube. Another advantage of CBF is that it does not require pre-filtering due to its natural bandpass feature which will contribute to reducing tracking delay and improving dynamic performance.

4.2 Complex Notch Filter

Another way to generate the analytic form of a real sinusoidal signal is to apply a Complex Notch Filter (CNF) to filter out the negative frequency component. CNF is advantageous in that the tracking delay may be close to zero at the retained positive frequency. The CNF is designed such that the notch frequency is located at the negative frequency of the real sensor signal. For a Coriolis flowmeter, where a range of frequencies may be output from a flow tube, a bandstop filter can be created by shifting a high-pass filter to the negative side of the frequency domain. In this case, shifting factor $e^{-j\theta}$ is multiplied to the coefficients of a high-pass filter which means the zeros and poles rotate clock-wise in the z-plane by θ. The transfer function becomes:

$$H_r(z) \xrightarrow{z^{-1}=e^{-j\theta}z^{-1}} H_c(z) = \frac{\sum_{m=0}^{P} b_m e^{-j\theta m} z^{-m}}{\sum_{n=0}^{Q} a_n e^{-j\theta n} z^{-n}} \tag{4.11}$$

The figure below shows the filtering process diagram of CNF:

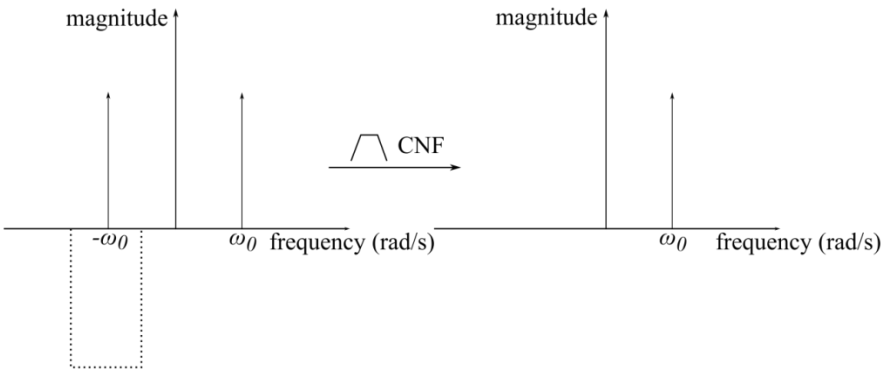


Figure 4.4: Filtering process of CNF

Figure 4.5 shows a rotated CNF's zeros and poles from a 5th-order elliptic high-pass filter with central notch frequency ω_c = -0.1π rad/sample.

From Figure 4.6, the CNF's group delay at the corresponding positive frequencies (around 0.1 rad/s) is close to 2 samples. Generally, it would be expected that the CNF tracking delay should be significantly reduced compared to that of the CBF. A comparison via simulation will be given later.

CNF may be extended to form a comb filter to remove harmonic noise, e.g. a mains frequency (50 or 60 Hz) along with its harmonics. By adding notches at a series of harmonics, the CNF can be turned into a comb structure while still retaining a small delay at the positive tracking frequency.

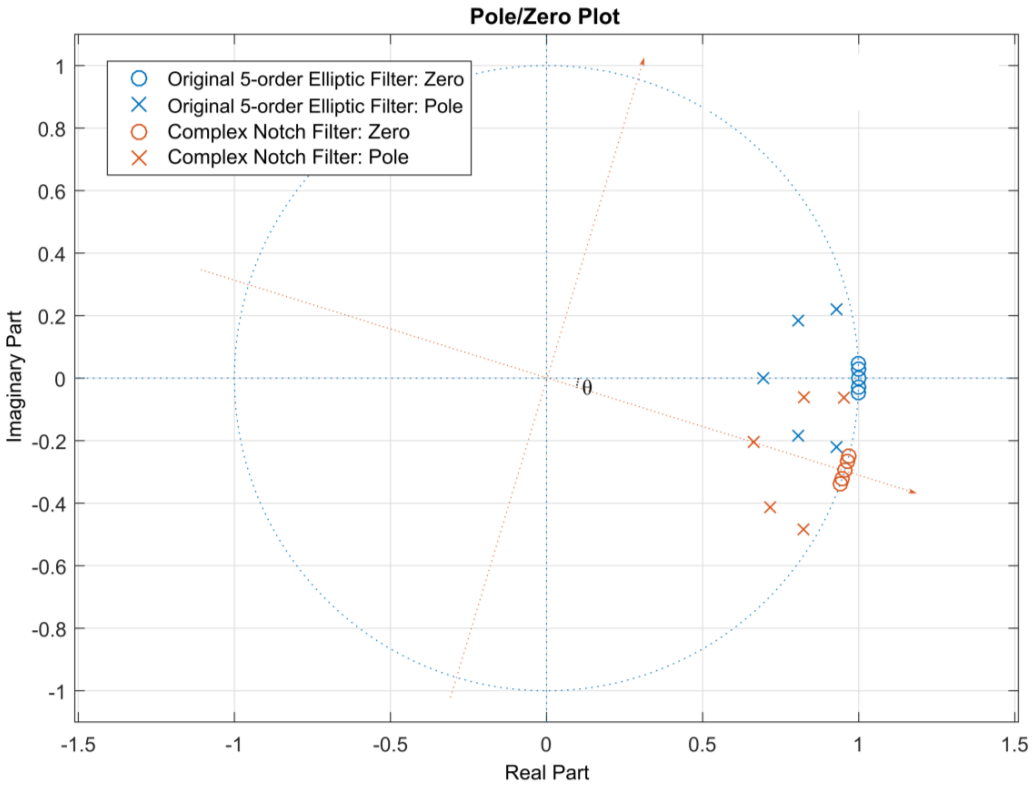


Figure 4.5: Zeros and poles rotation for CNF

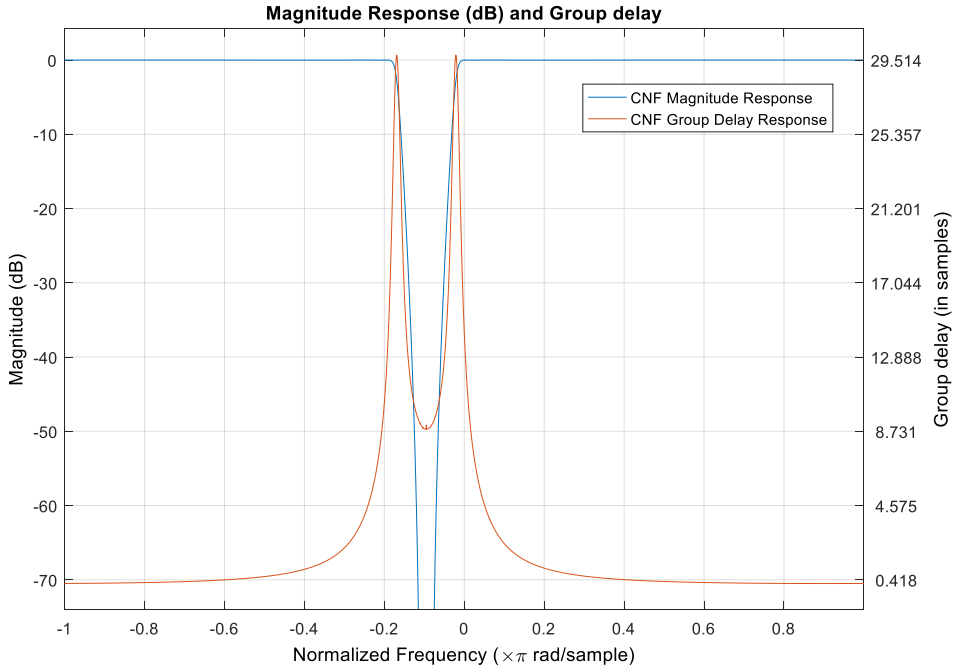


Figure 4.6: Group delay of 5th order CNF

One disadvantage of CNF is that it provides limited noise reduction compared with the bandpass characteristic of the CBF. This results from the fact that only the notched negative frequency is attenuated, while all other noise components are passed through into the sinusoid parameter tracking calculations.

4.3 Complex bandpass filter with complex notch filter

While CBF has good noise suppression but a relatively large tracking delay, CNF is sensitive to noise but has a short tracking delay. So there is a trade-off between noise performance and tracking delay for complex signal processing.

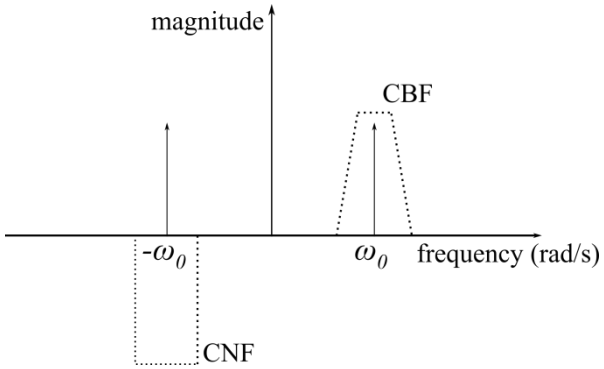


Figure 4.7: Filtering process of CBF-CNF

To achieve greater flexibility in this trade-off, particularly for industrial applications, CBF and CNF can be cascaded together (CBF-CNF) for sensor signal tracking. In this way, CBF need not be designed with a narrow passband, sharp roll-off, and high stop band attenuation. This approach has the potential to reduce tracking time delay and thereby increase accuracy during dynamic change.

The CBF-CNF can be designed to provide a desired trade-off between noise performance and tracking delay performance which also does not need pre-filtering.

4.4 Simulation Results

In this section, the CBF and CBF-CNF techniques are applied to the two benchmarks described in Chapter 2. As discussed above, CNF used in isolation is sensitive to noise, and so it is not included in the simulation study. The results are compared alongside with zero-crossing and QD (DPLL) based methods examined earlier as they present best performance among the existing methods as shown in the last Chapter.

4.4.1 Batching from Empty-to-full Benchmark Simulation

Firstly, the new techniques are applied to the empty-to-full batching simulation in order to test their dynamic response. CBF, CNF and CBF-CNF can be used to filter real input signals in order to generate complex analytic forms from which amplitude, frequency and phase difference can be calculated. The tracking performance is shown in Figures 4.8 – 4.10 below:

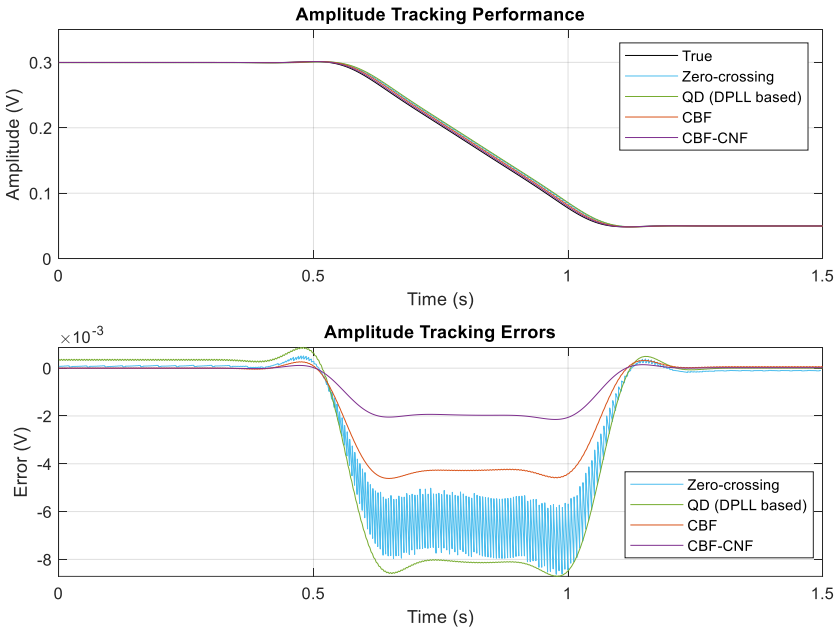


Figure 4.8: Amplitude tracking of CBF during empty-to-full batch process

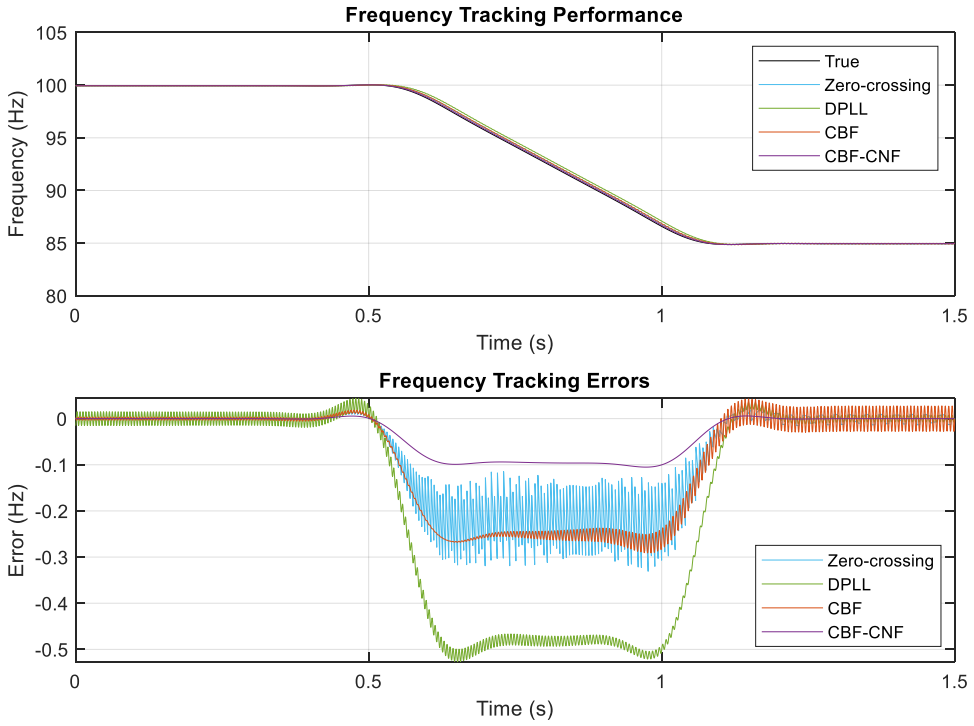


Figure 4.9: Frequency tracking of CBF during empty-to-full batch process

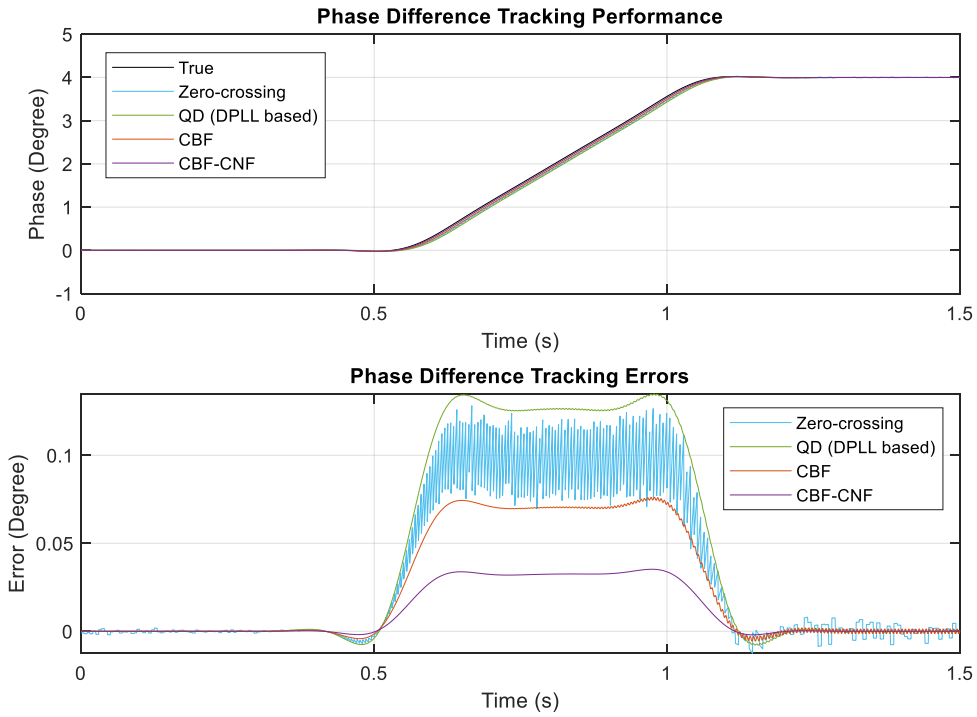


Figure 4.10: Phase difference tracking of CBF during empty-to-full batch process

From these figures, we can observe that CBF and CBF-CNF perform well with reduced tracking delay and smooth result compared to the zero-crossing and QD (DPLL based) methods. The bar charts below show the quantified RMSEs and amplitude dynamic performance of each method for comparison.

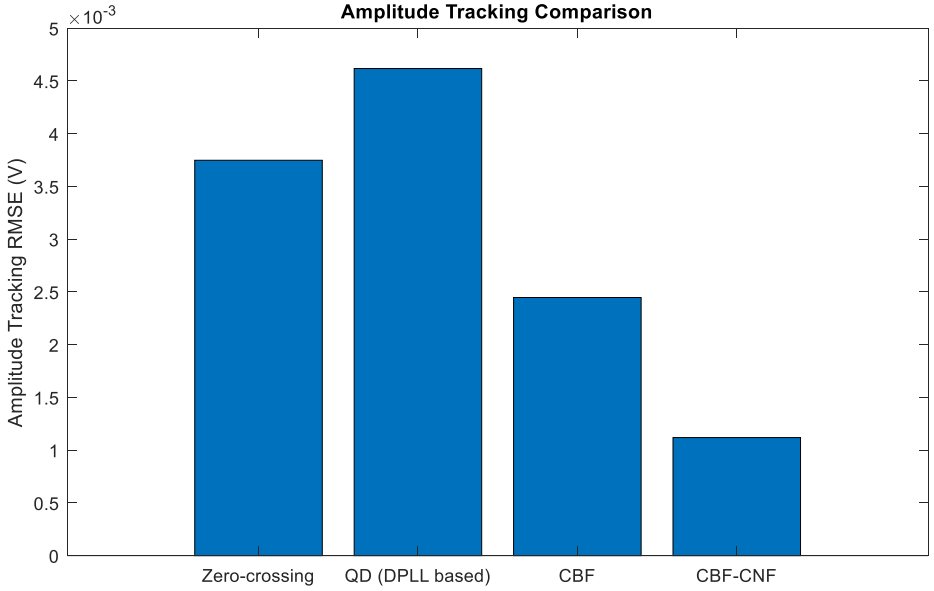


Figure 4.11: Amplitude tracking RMSEs comparison for batch simulation

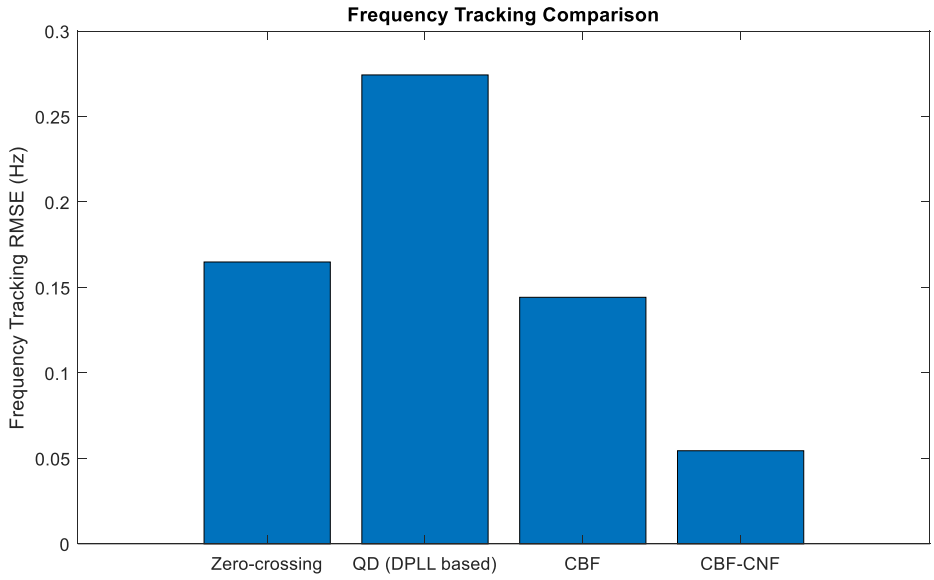


Figure 4.12: Frequency tracking RMSEs comparison for batch simulation

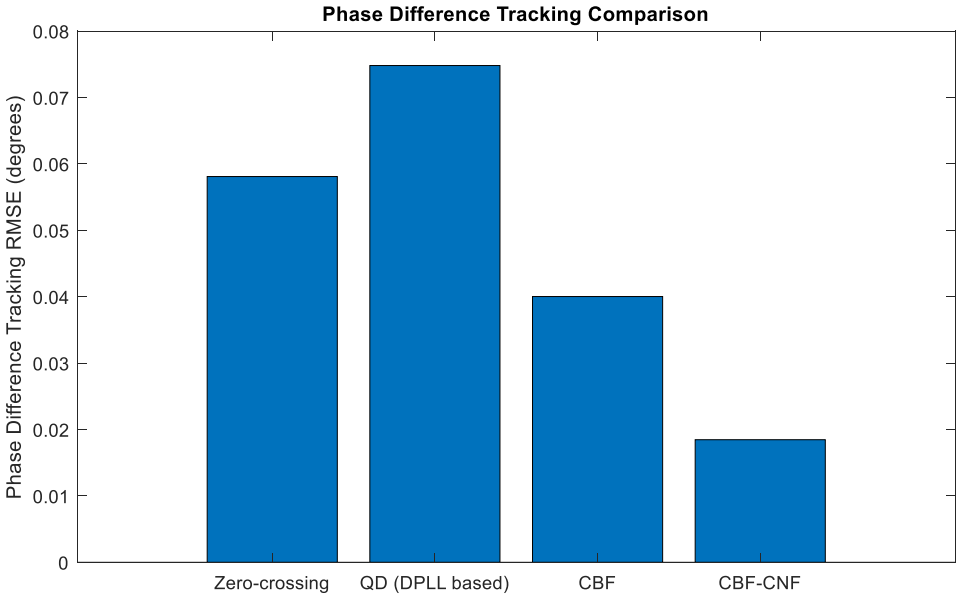


Figure 4.13: Phase difference tracking RMSEs comparison for batch simulation

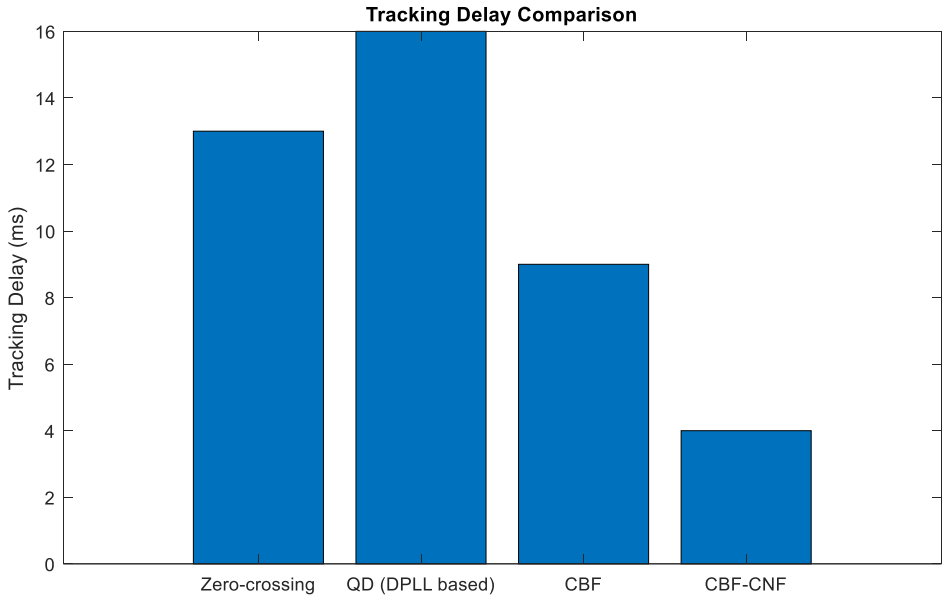


Figure 4.14: Amplitude tracking delay comparison

From the result, CBF-CNF has smallest error with shortest amplitude tracking delay while CBF also perform better than zero-crossing and QD (DPLL based). CBF reduces amplitude tracking delay roughly two times compared to zero-crossing and QD (DPLL

based) methods while CBF-CNF reduces delay further as much as 3 times. Hence both CBF and CBF-CNF show good potential to be applied to challenging situations.

4.4.2 Batching from Empty-to-full Sensor Data Test

As described in Chapter 2, CBF and CBF-CNF have also been tested with batching from empty-to-full experimental sensor data and compared with the corresponding zero-crossing and QD (DPLL based) methods, as shown below:

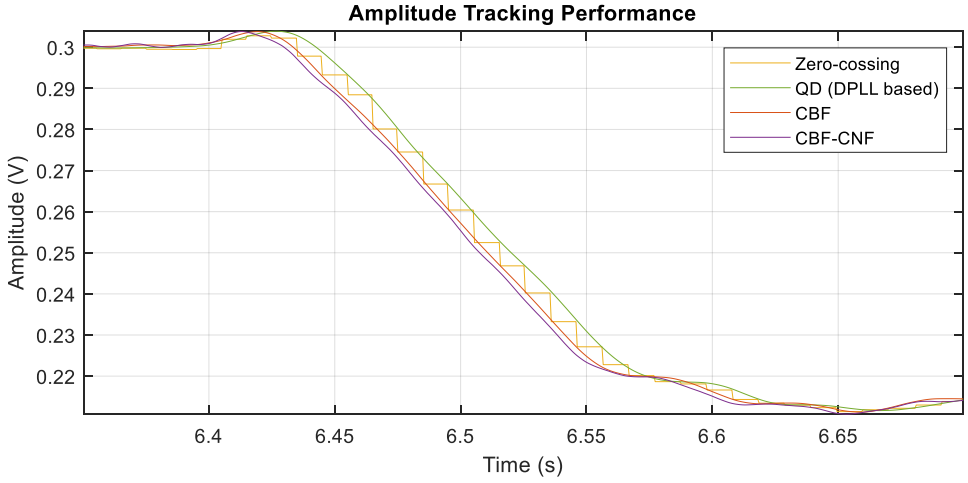


Figure 4.15: Amplitude tracking performance using batching sensor data

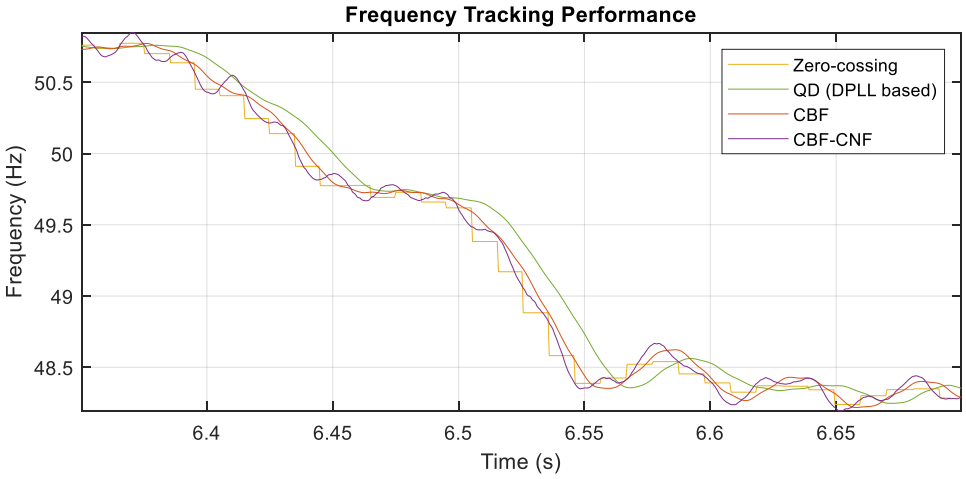


Figure 4.16: Frequency tracking performance using batching sensor data

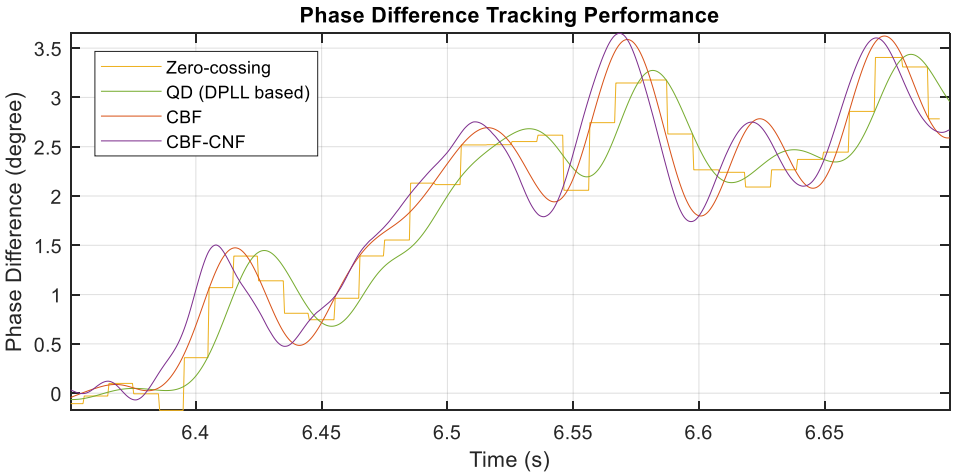


Figure 4.17: Phase difference tracking performance using batching sensor data

From the results, CBF and CBF-CNF show better dynamic performance by being the first to respond to changes in each parameter. CBF-CNF method's frequency measurement is slightly more noisy due to a more shallow stopband attenuation compared with CBF. These results also illustrate that sensor noise during batching from empty-to-full is relatively high and filtering is necessary.

4.4.3 Two-phase Benchmark Simulation

In order to further evaluate their tracking performances, the CBF and CBF-CNF techniques are compared with the zero-crossing and QD (DPLL based) methods for the two-phase flow simulation benchmark as described in Chapter 2. As discussed above, CNF used in isolation is sensitive to noise, and so it is not included in the simulation study.

The figures below show the tracking result and RMSEs with the noise-free two-phase flow benchmark for each method which is a good indication of dynamic performance.

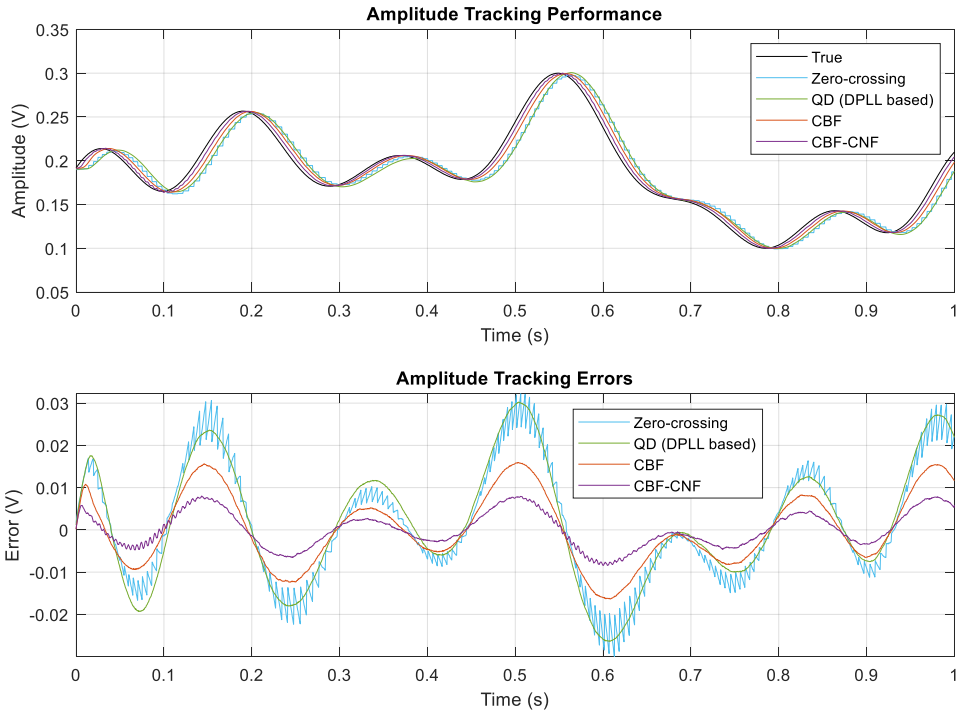


Figure 4.18: Amplitude tracking performance with no noise

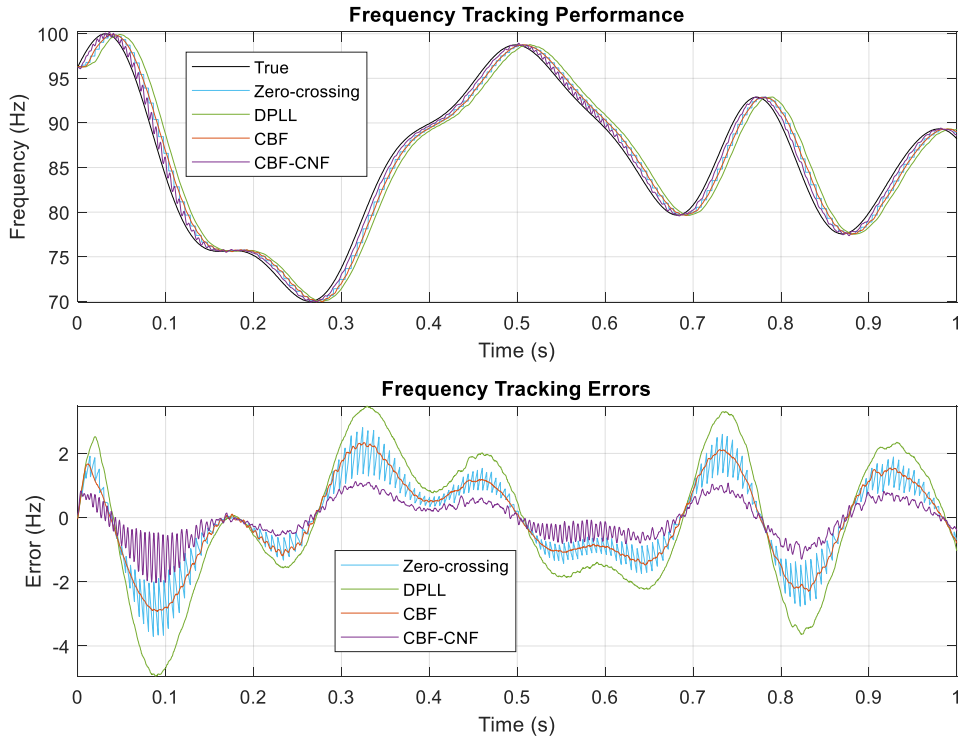


Figure 4.19: Frequency tracking performance with no noise

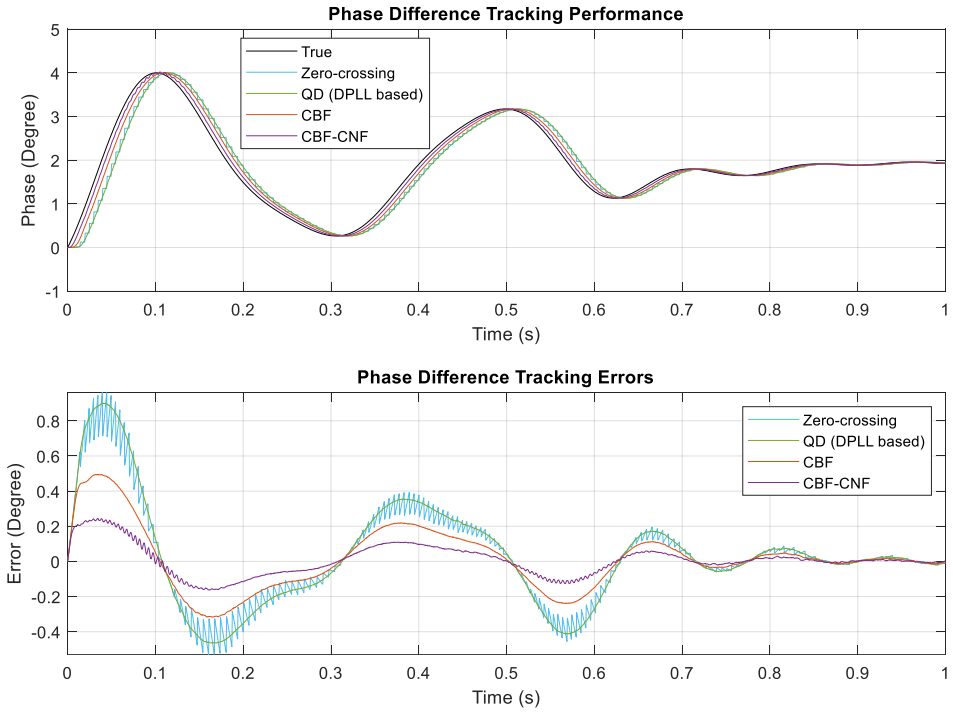


Figure 4.20: Phase difference tracking performance with no noise

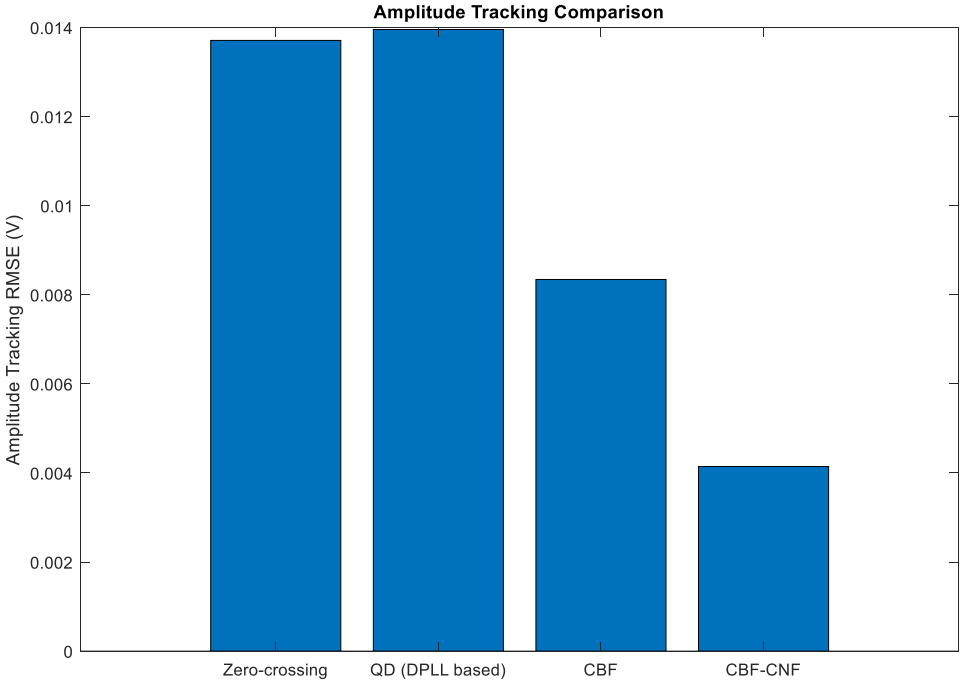


Figure 4.21: Amplitude tracking RMSEs comparison for two-phase simulation

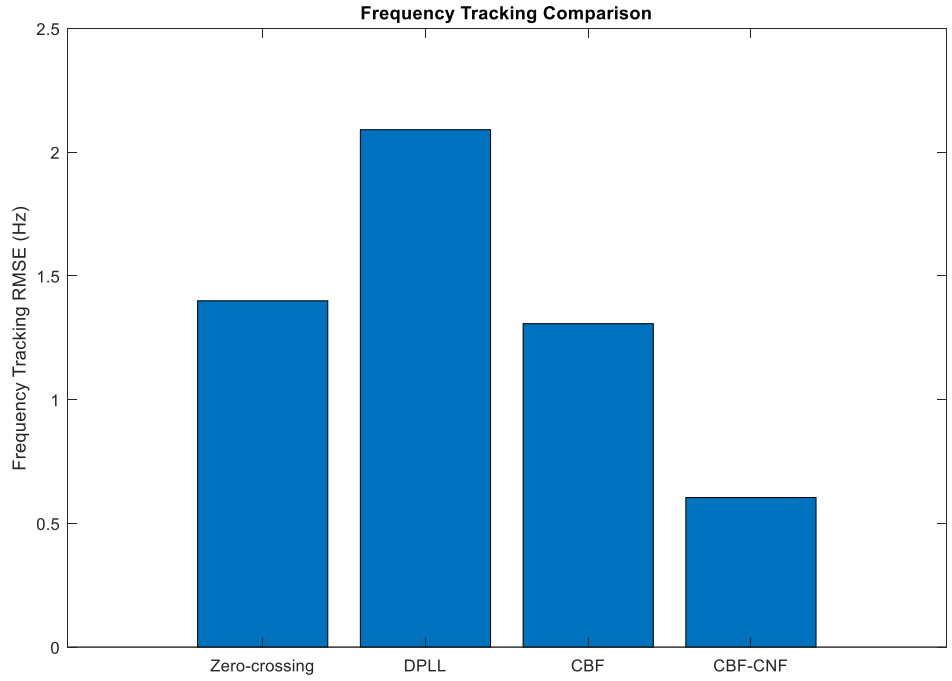


Figure 4.22: Frequency tracking RMSEs comparison for two-phase simulation

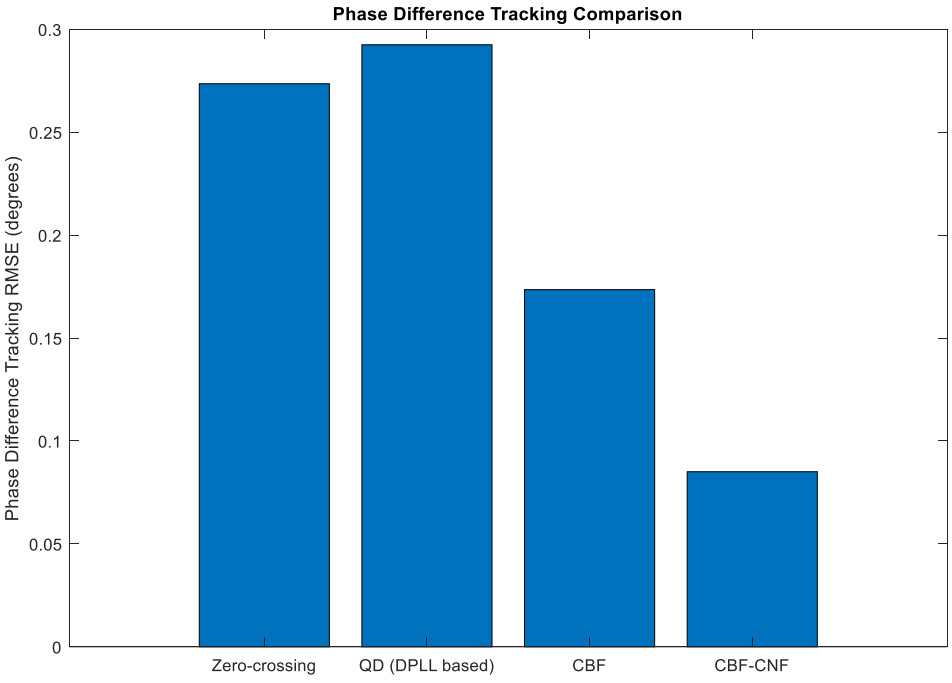


Figure 4.23: Phase difference tracking RMSEs comparison for two-phase simulation

From the results, CBF and CBF-CNF show improved performance compared to the zero-crossing and QD (DPLL based) methods with smooth measurement results and reduced tracking delay.

CBF and CBF-CNF have also been tested with the two-phase flow benchmark alongside zero-crossing and QD (DPLL based) methods with different noise levels to validate robustness for spurious inputs. The results are shown below:

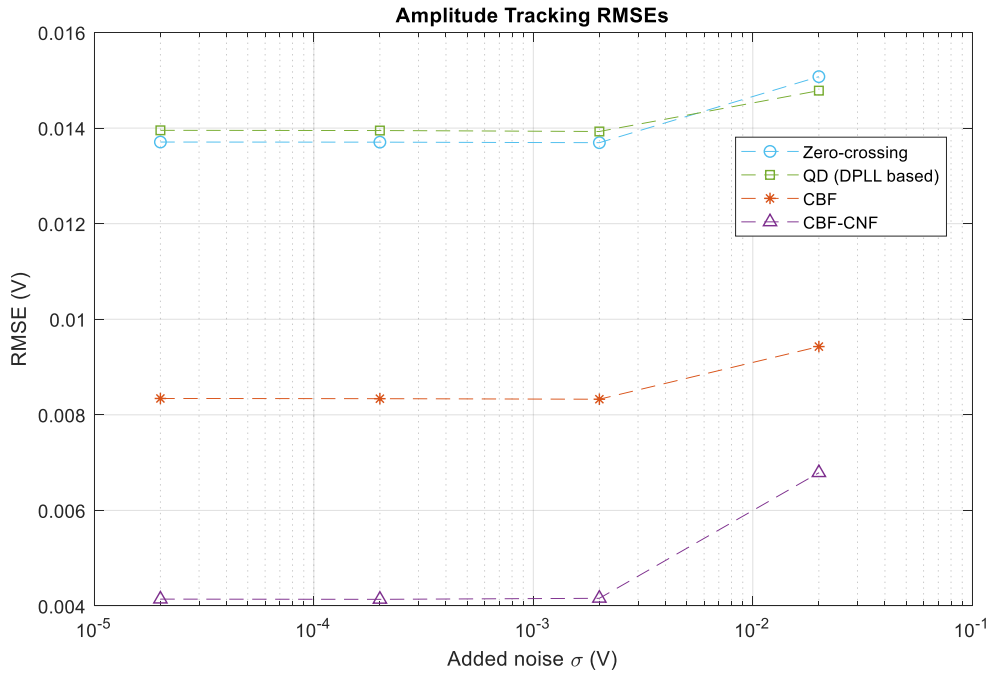


Figure 4.24: Amplitude tracking RMSEs at different level of noise

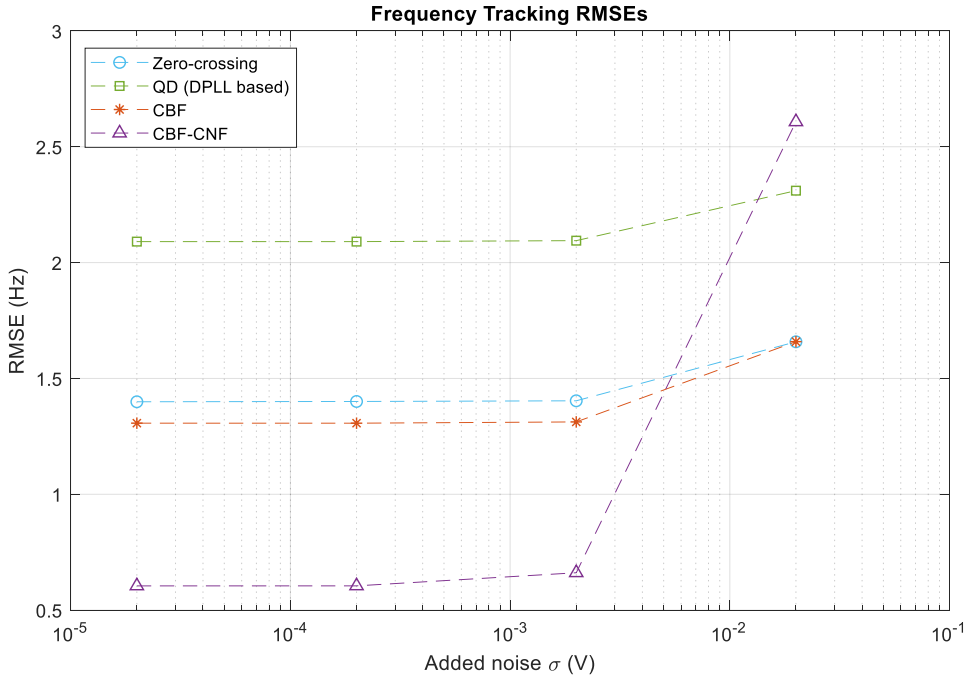


Figure 4.25: Frequency tracking RMSEs at different level of noise

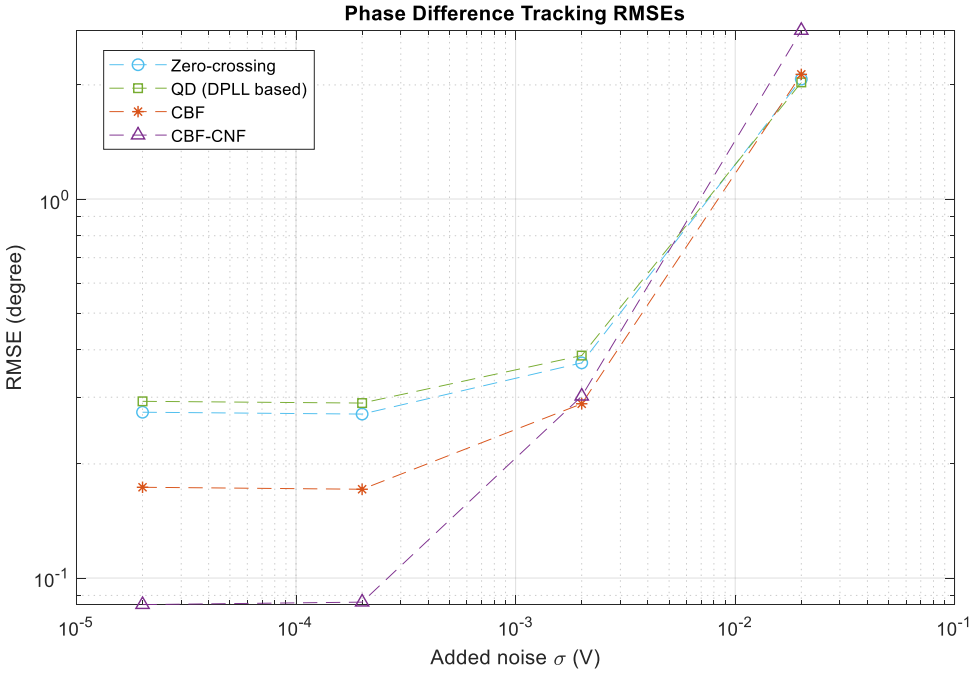


Figure 4.26: Phase difference tracking RMSEs at different level of noise

From the results, CBF and CBF-CNF perform better than the zero-crossing and QD (DPLL based) methods when sensor SNR is larger than approximately 37 dB. CBF and CBF-CNF phase difference measurement result increases sharply when SNR reaches 17 dB, which matches the behaviour shown by all the current techniques presented in Section 3.2.3. CBF-CNF performs worse for frequency and phase difference with high noise due to its shallower stopband attenuation. This demonstrates the trade-off between noise performance and dynamic response for the CBF-CNF method.

4.4.4 Two-phase Flow Experimental Data Test

The CBF and CBF-CNF techniques have also been tested using the experimental sensor data set with fast varying GVF, and compared with the zero-crossing and QD (DPLL based) methods to observe their performance. The figures below show their tracking results.

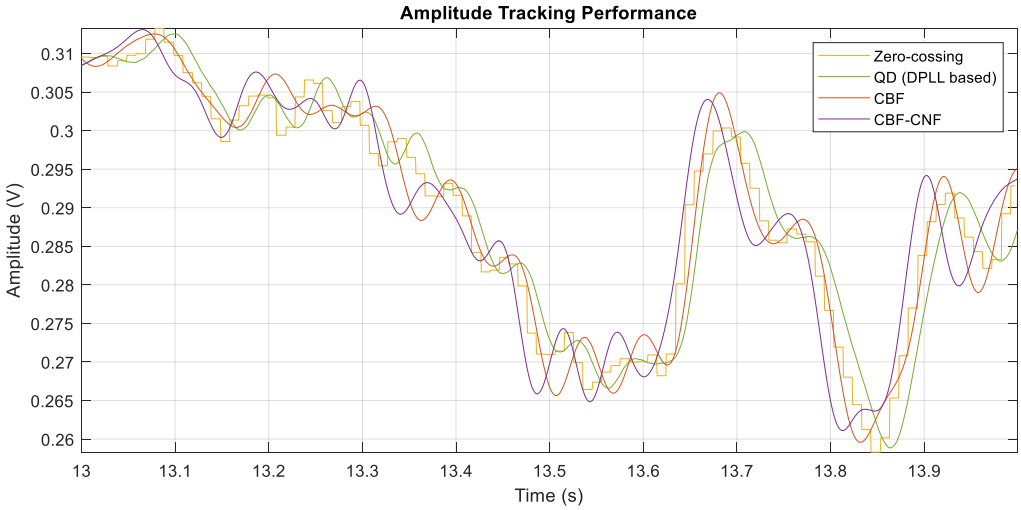


Figure 4.27: Amplitude tracking performance using two-phase sensor data

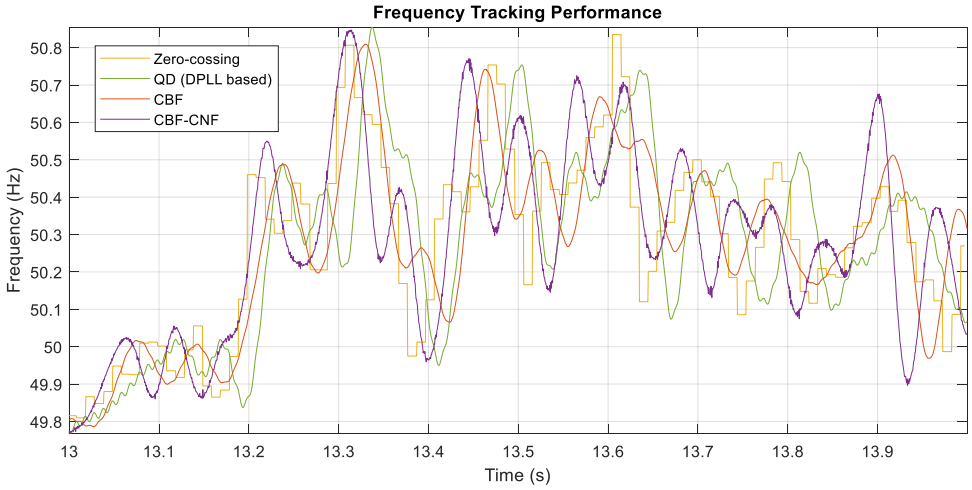


Figure 4.28: Frequency tracking performance using two-phase sensor data

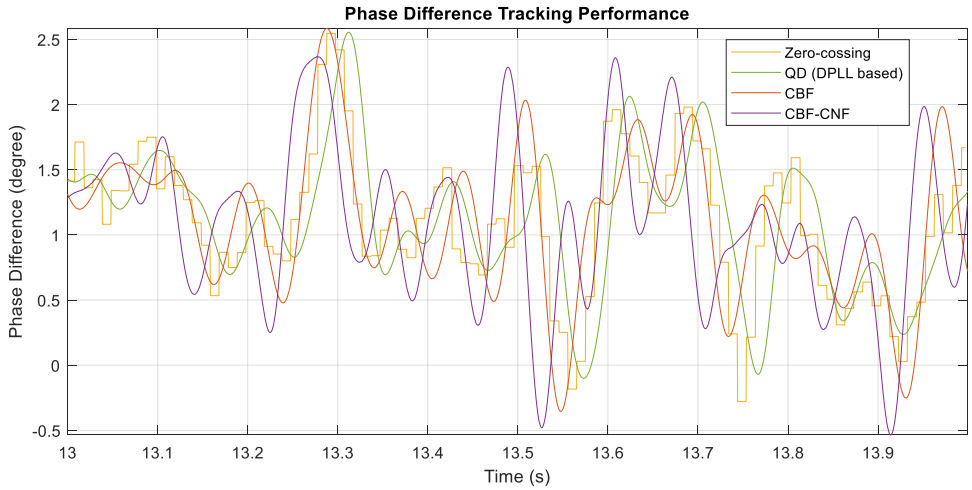


Figure 4.29: Phase difference tracking performance using two-phase sensor data

From the results, CBF and CBF-CNF are the fastest to respond to parameter change and provide smooth measurement results when applied to real two-phase flow sensor data. Hence the new methods not only show improved dynamic performance but also a good ability to suppress noise which make them ideal techniques for the next generation Coriolis flowmeter.

4.4.5 Algorithm Complexity

Further key aspects of algorithm assessment include the computational complexity and data storage requirements, as Coriolis flowmeters' measurement algorithms need to be implemented in embedded systems and to run in real-time. Table 4.1 compares the conventional and new techniques in terms of the static memory size required for buffering data and storing variables, and the number of additions (or subtractions) and multiplications (or divisions) required to process each new sample. The assessment of complexity includes the full calculation from pre-filtering through to the estimation of frequency, amplitude and phase difference. The zero-crossing method is excluded from the comparison since it updates the measurement result every half cycle, not every sample. The table also excludes the arctangent calculation used once per sample which is common to all the methods listed.

Method	DTFT (ANF)	QD (DPLL)	Hilbert	CBF	CNF	CBF-CNF
Additions	21	40	99	21	21	25
Multiplications	53	52	108	26	26	30
Static Storage (bytes)	432	512	800	320	320	448

Table 4.1: Complexity of each algorithm

From Table 4.1, it can be seen that the CBF, CNF and CBF-CNF techniques have relatively low computational requirements. This will support the use of the newly developed techniques in real-time and low cost implementations.

4.5 Summary

This chapter has described a family of complex signal processing methods and has applied them to Coriolis flowmeter signal processing. The CBF can be derived from a simple low-pass filter with a selectable central frequency and bandwidth. The calculation is simple and the computational cost is low. Due to the nature of the bandpass filter, the CBF can not only track amplitude, frequency and phase difference at the same time, but it also applies strong noise suppression, which is increasingly important in Coriolis flowmeter applications. Additionally, CBF combined with CNF has been explored to reduce tracking delay and improve accuracy. Simulation studies suggest its tracking performance is generally superior to that of the existing best performing zero-crossing and QD (DPLL based) techniques.

The next chapter will describe experimental results in which the real-time measurement and control performance of the CBF and CBF-CNF algorithms are compared with that of the zero crossing algorithm over a range of batching from empty-to-full and two-phase flow conditions. These results will further demonstrate that CBF and CBF-CNF offer a good signal processing solution to meet future Coriolis flowmeter signal processing requirements.

5. EXPERIMENTS

The newly developed CBF and CBF-CNF algorithms have been implemented on a prototype transmitter for experimenting with two-phase flow. This chapter describes the hardware platform, signal generator testing, the experiment facilities, and single-phase experiment, batching from empty-to-full experiment and two-phase experiment results including a comparison to the performance of Oxbox which uses the zero-crossing technique.

Here the Oxbox is driving the Foxboro flow tube to vibrate at its lowest mode. This is different from the conventional operation of the commercial CFT-50/51 product which vibrates the flow tube at its second mode, an arrangement inherited from the historical development of the product. Here, vibrating in lowest mode, simplifies the comparison between old and new techniques, as the signal processing algorithms do not need to deal with other modes of vibration (e.g. Coriolis mode vibration, harmonics) and specifically a lower mode of vibration, since a simple low-pass pre-filter will filter out all other interferences.

5.1 Hardware Platform

The CBF and CBF-CNF algorithms have been implemented to run on a dual ARM core Xilinx Zynq 7000 series FPGA programmed using C++. The hardware platform consists of two parts – the digital board and analog board. The digital board is an off-the-shelf Zynq prototyping card called the Zedboard [96], which supports the FPGA/processor, peripherals including two 24-bit audio quality Analog-to-Digital Converters (ADC) and two 24-bit Digital-to-Analog Converters (DAC) with 48 kHz sampling rate, and so on. The analogue board was developed by other members of the research group to provide a suitable interface to Coriolis flow tubes, and contains operational amplifiers, analogue peripherals and so on. The hardware platform is shown in Figure 5.1.

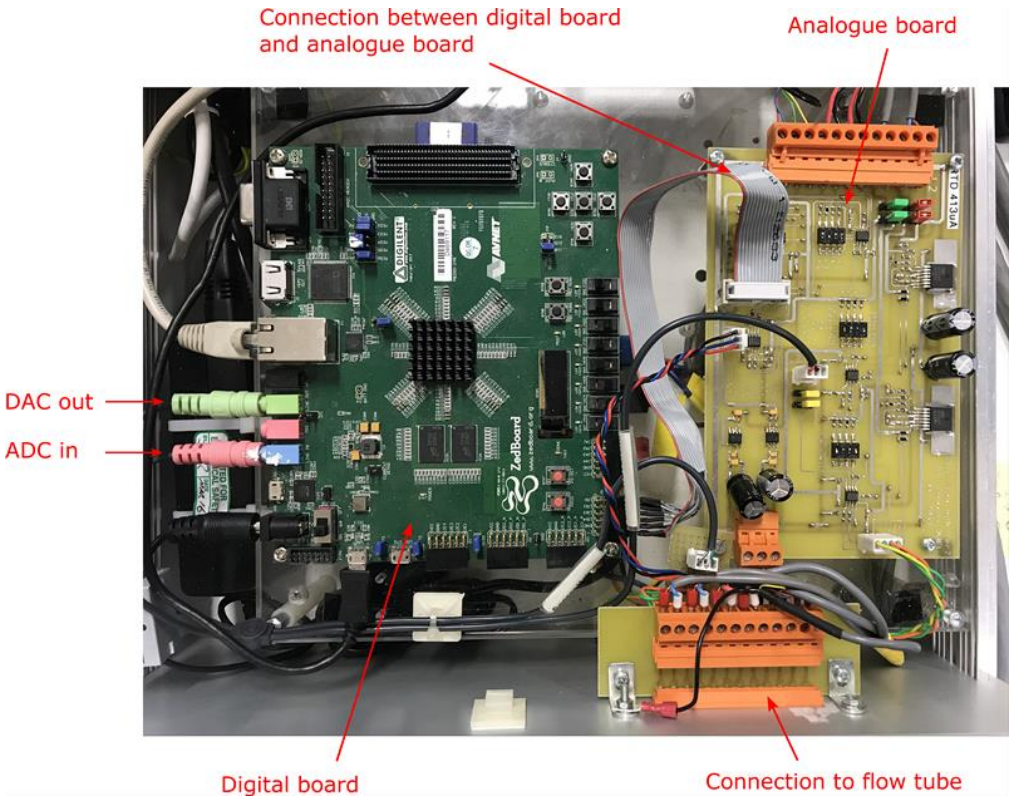


Figure 5.1: Hardware platform for transmitter

The analogue board is primarily responsible for signal amplification and for converting the voltage drive signal to a current drive signal in order to vibrate the flow tube. The digital board is responsible for sensor data sampling, algorithm running, driver signal generation and so on. In summary, the hardware platform has been built by senior research members in the group and my prime responsibility has been to implement the measurement algorithms to run on the platform and to carry out the experimental work.

5.2 Signal Generator Test

A first step towards testing a Coriolis flowmeter implementation is to use a signal generator as a signal source. This has a number of advantages. Firstly, the true properties of the input signals are known, so that measurement performance can be assessed accurately. Secondly, the successful operation of a Coriolis flowmeter flow tube requires, in addition to good measurement, a suitable drive control system, including a special procedure for flow tube startup where no measurement may be available. The use of a signal generator bypasses the need to have the drive control and startup systems in place, so that measurement algorithm development may take place independently.

For testing with a signal generator, both steady sinusoidal signals and the MRWM signal (section 2.2) have been programmed into the signal generator to simulate the sensor input signals. These sensor input signals are fed into the ADC of the transmitter for signal processing, in order to estimate amplitude, frequency and phase difference. Statistics on the performance of each algorithm are collected. Then, in order to provide an indication of the real-time performance of the whole transmitter using these

measurement algorithms, the following real-time output is generated. Based on the estimated parameters, the input sensor signal is re-constructed and generated through a DAC output. Both the ADC input and DAC output are monitored on an oscilloscope for comparison. In this way, we can validate all stages of transmitter operation, including the measurement algorithms by matching the ADC input to the DAC output. The overall transmitter time delay including ADC sampling delay, signal processing delay, DAC output delay, and analogue circuit delay is compensated to reflect the real drive signal generation as shown in Figure 1.20. Other than the signal processing delay, all other sources of delay can be lumped together into a single 'hardware delay' (e.g. ADC and DAC sampling delays). When generating transmitter output signals, this 'hardware delay' is converted into a corresponding phase delay (multiplying by $2\pi f$). This is added to the output sinusoidal signal's phase to compensate for the delay and synchronise the input and output which can be viewed as extrapolating the input signal over the time delay period based on the current best estimates of the sinusoid parameters.

Overall, these tests provide the most direct and quantifiable evidence of the suitability of the new algorithms for successfully tracking flow tube parameters in real time. Indirectly, of course, the successful use of these algorithms when actually driving a flow tube, whether in single or two-phase flow is the most important test: results for this are given in later sections of this Chapter. At first, we start with steady sinusoidal inputs which represent single-phase flow conditions. The tracked frequency, amplitude and phase difference are recorded on the prototype transmitter and compared with the signal generator's input parameters to verify the algorithm is correctly tracking. Examples of sample-by-sample results are shown in the next figures:

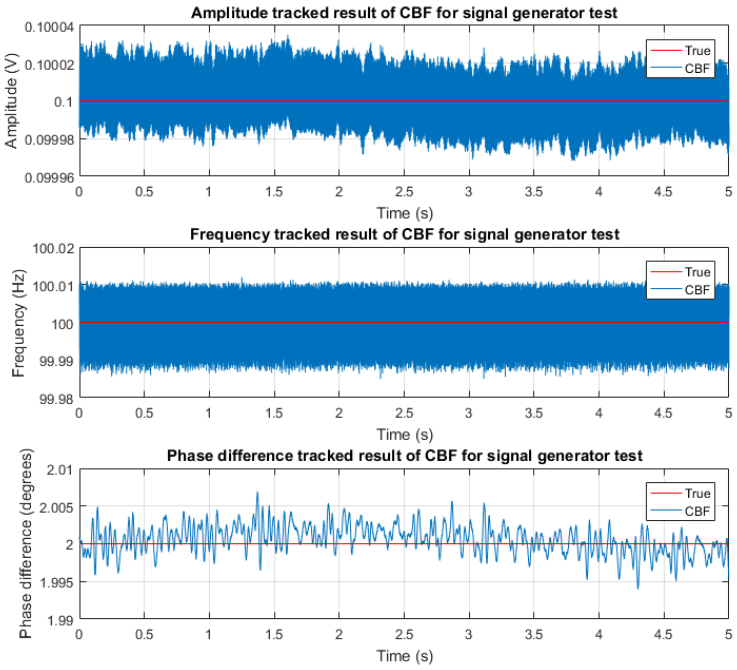


Figure 5.2: Signal generator input parameters and CBF tracked results (0.1V input measurement)

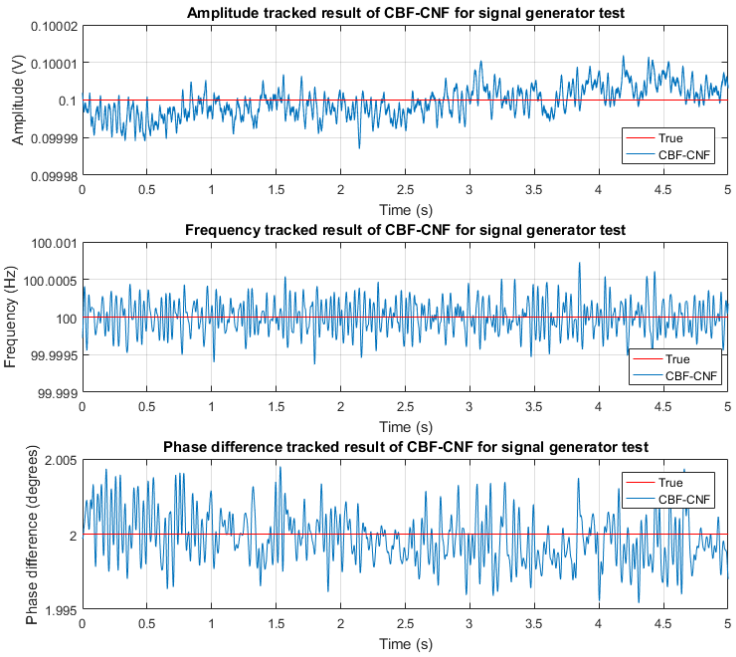


Figure 5.3: Signal generator input parameters and CBF-CNF tracked results (0.1V input measurement)

From performing a series of such experiments, the RMSE statistics of the CBF and CBF-CNF algorithms can be calculated while changing independently each of the amplitude, frequency and phase difference parameters, covering the Foxboro flow tube operating range. The full quantified result is shown in Appendix 1 at the end of the thesis, and demonstrates that both complex processing techniques are able to track steady state sinusoids well over the desired operating range.

Based on the tracked parameters, we can reconstruct the signal generator input signal as a real-time output for demonstrating the real-time performance. Examples of the input signal and reconstructed output signal, recorded simultaneously on the oscilloscope, are shown below:

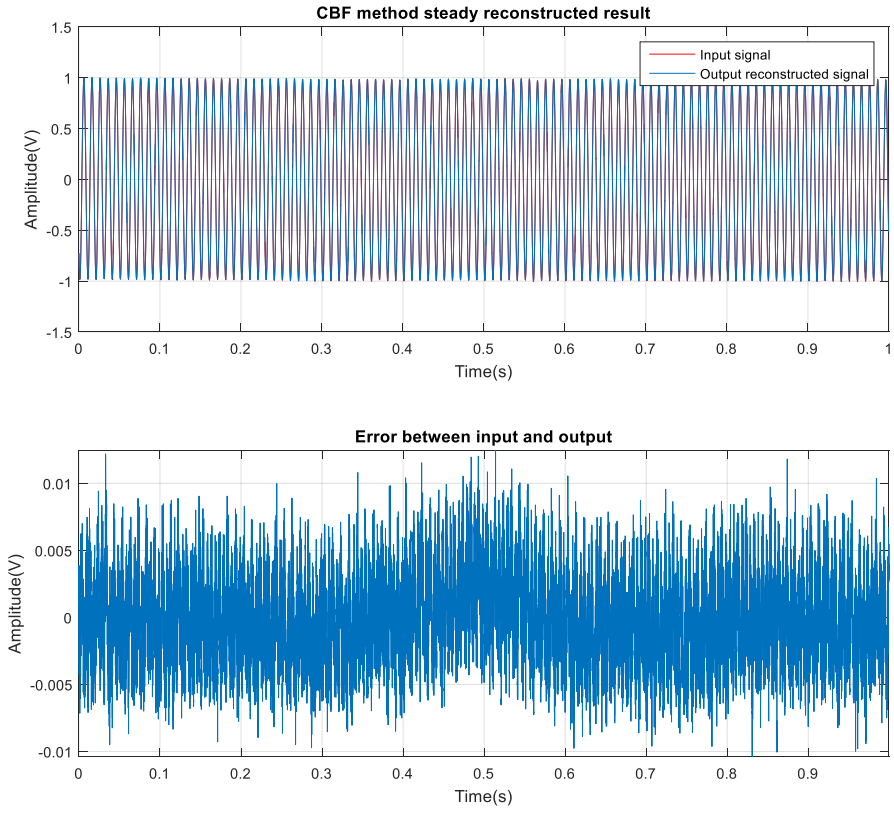


Figure 5.4: CBF transmitter steady state test result of signal generator (input and output normalized to 1V)

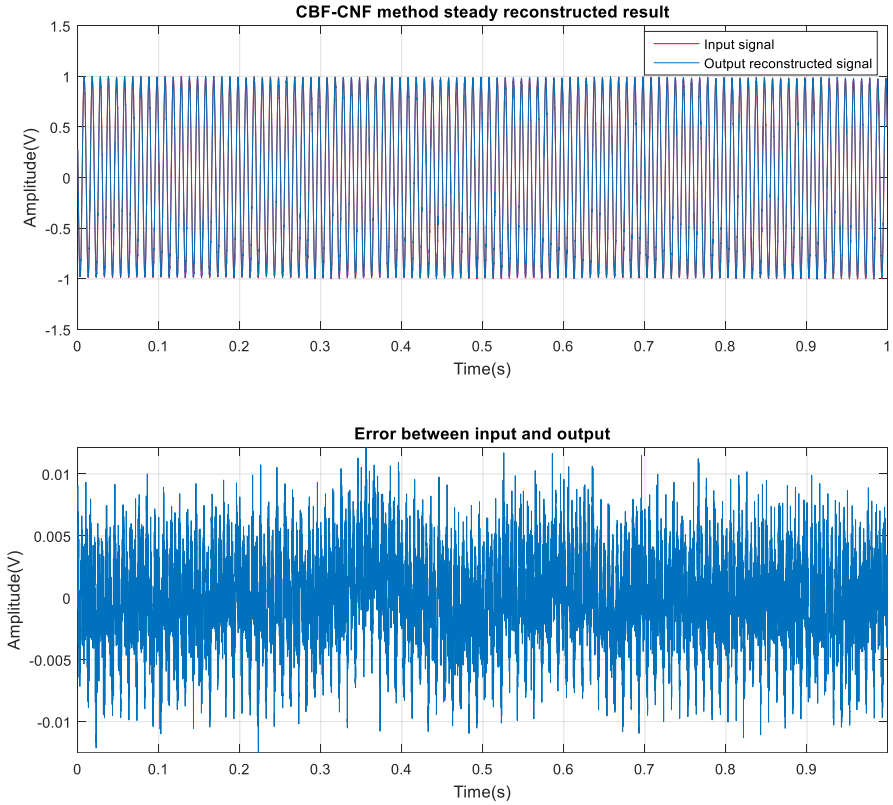


Figure 5.5: CBF-CNF transmitter steady state test result of signal generator (input and output normalized to 1V)

Since there are analogue circuit gains in the transmitter, the input and output are normalized to 1 V for direct comparison. From these results, we can verify that the new CBF and CBF-CNF based transmitters track properly the signal generator input signals and reconstruct the output drive signal in-phase with input sensor signals with small errors. In this way, we can prove that the new algorithms running on the prototype transmitter are ready for single-phase flow test with the Foxboro flow tube.

Next, we test the new algorithms with MRWM signal generated by signal generator. The programmed signal generator is shown as below:

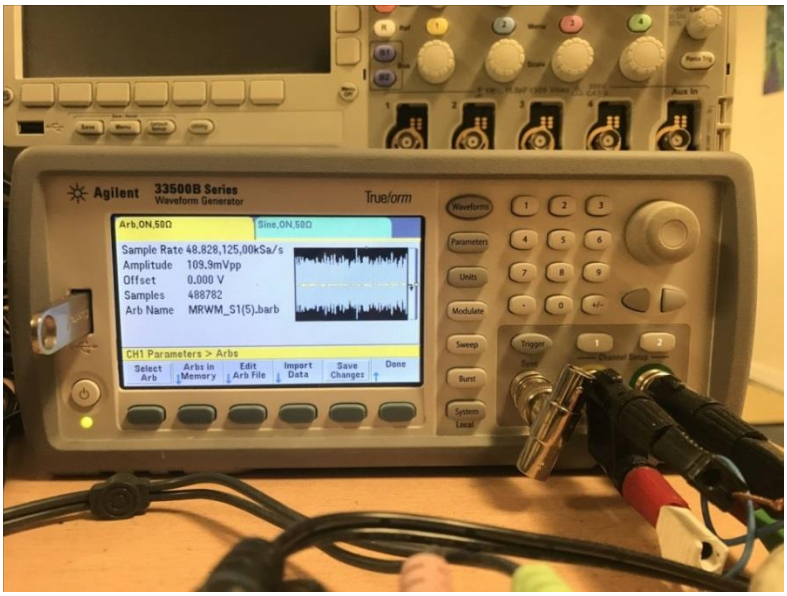


Figure 5.6: MRWM signal programmed into signal generator

The MRWM input signal from the signal generator and transmitters' reconstructed output signal are plotted together in the Figures below:

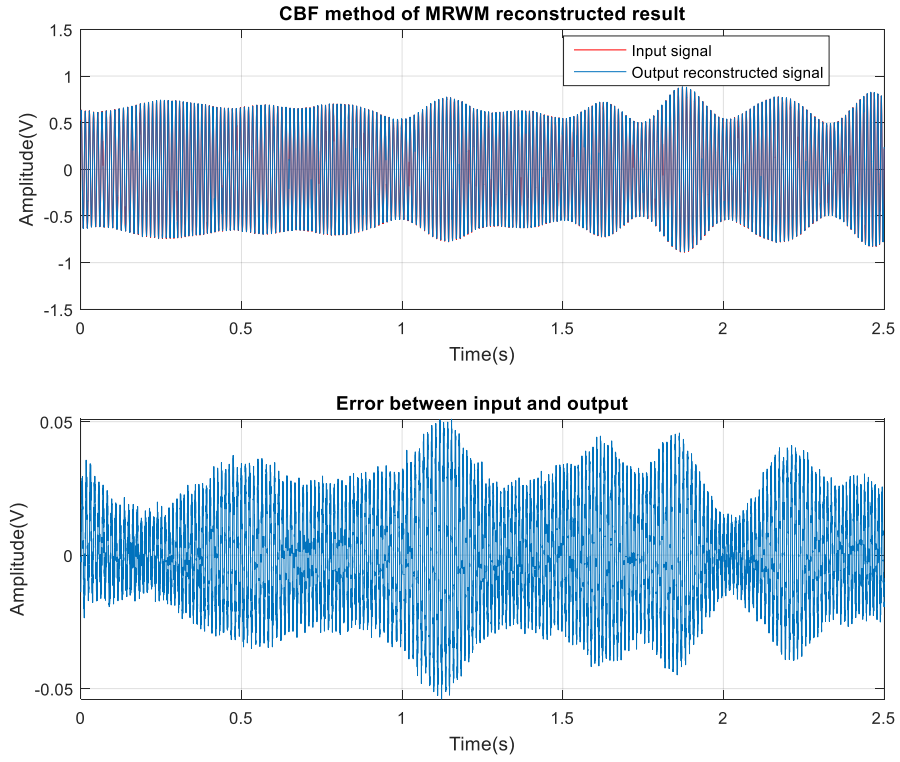


Figure 5.7: CBF transmitter MRWM test result of signal generator

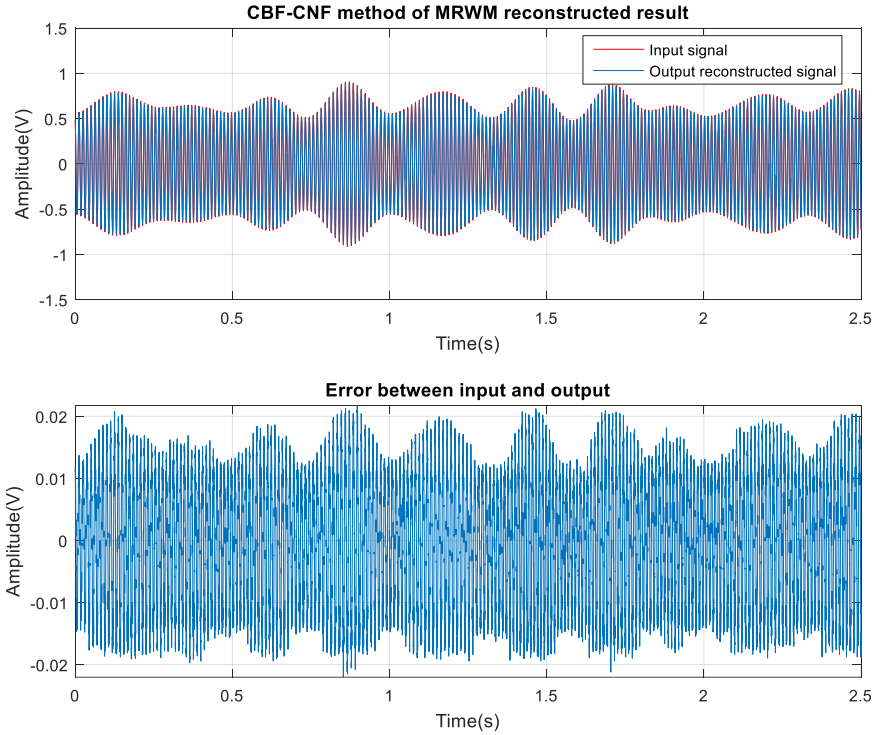


Figure 5.8: CBF-CNF transmitter MRWM test result of signal generator

From the figures, we can observe that both transmitter algorithms reconstruct the MRWM input signal well with small errors. CBF-CNF generally has smaller errors due to smaller tracking delay than CBF. In this way, we prove that both transmitters are ready for the later two-phase flow tests.

5.3 Single-phase Experiments

With the signal generator validation complete, the CBF and CBF-CNF algorithms running on the hardware platform are connected to the flow tube for testing. Initially, single-phase tests are performed against a reference meter to verify the linearity between the phase difference or time delay observed and the true mass flow rate as

proven theoretically in section 1.3.5. The single-phase experimental facility diagram is shown in Figure 5.9.

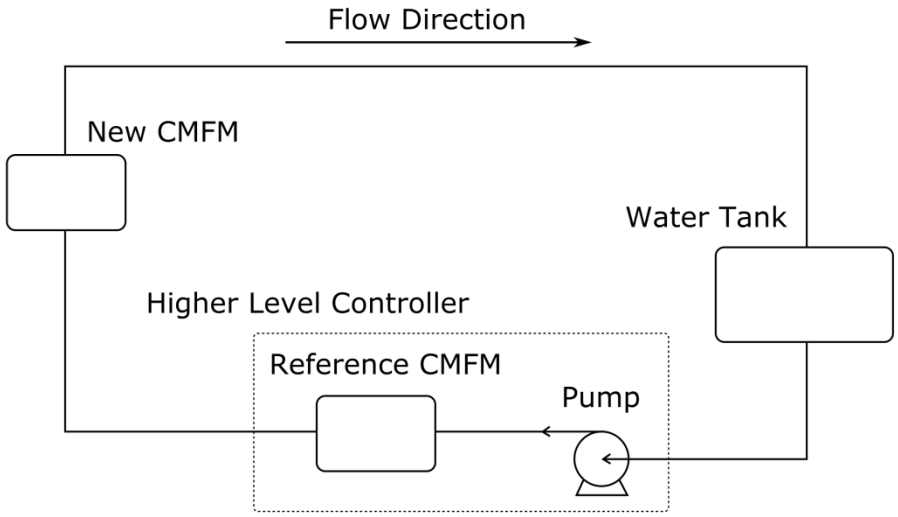


Figure 5.9: Single-phase experiment facility

In the figure, a 2 inch Foxboro CFT-51 Coriolis flowmeter is used as a reference meter to compare with the newly developed Coriolis flowmeter transmitter results. This meter was calibrated at the UK National Flow Laboratory NEL with an uncertainty of approximately 0.1% over the flow ranges used in these experiments. The pump together with the reference Coriolis flowmeter is connected to a fluid measurement controller for maintaining the flow rate at a steady level – e.g. 1kg/s water flow. The experimental facility is shown in Figure 5.10 and the prototype transmitter is connected to a 1 inch Foxboro flow tube. The fluid measurement controller interface is shown in Figure 5.11:

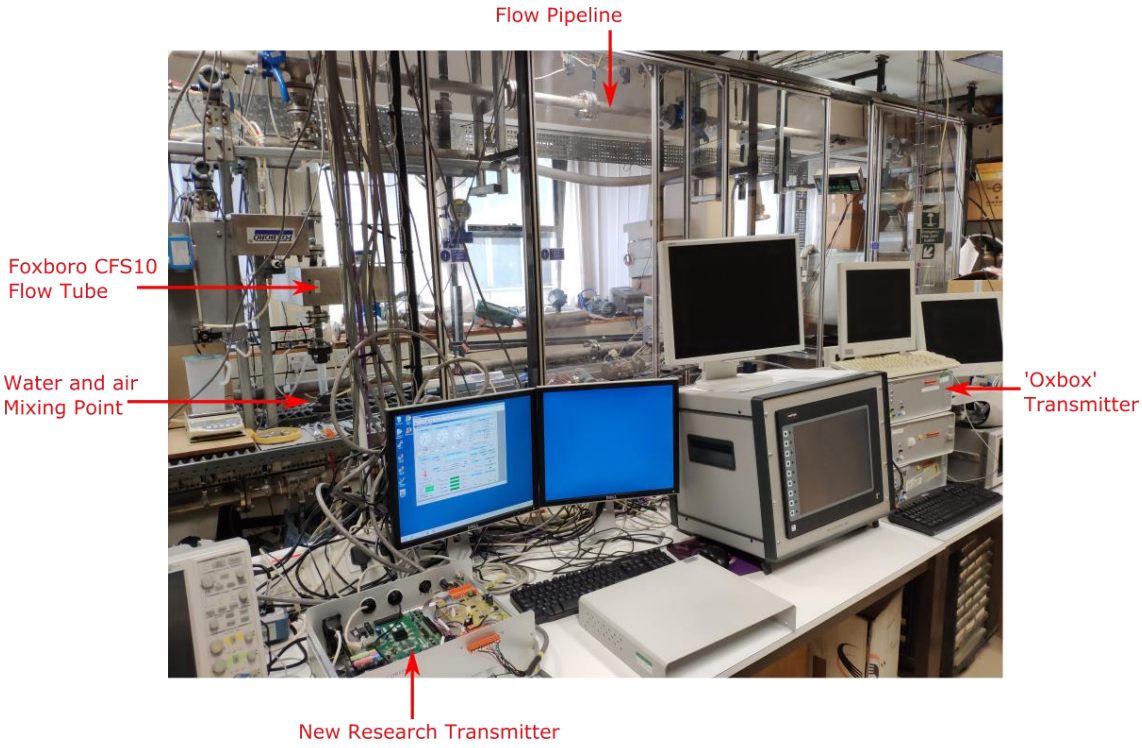


Figure 5.10: Experiment facility



Figure 5.11: Fluid measurement controller user interface

From the interface, many experiment parameters can be changed, including flow rates, pump control, GVF control for two-phase testing and so on. The fluid measurement controller and its interface were developed by senior members of the research group.

After setting up the experiment facilities, we carried out single-phase flow tests at 5 different flow rate points: 0kg/s, 1kg/s, 2kg/s, 3kg/s and 4kg/s. The time difference of two sensors calculated by the CBF and CBF-CNF algorithms is recorded in each experiment. A zero-intercept linear fit is used to verify the linearity between the reference flow rate and the measured time difference of two sensors following equation (1.33). Note that other factors – such as pressure and temperature – which may affect the phase-difference/flow rate relationship are assumed constant in these tests. The results are shown in Figure 5.12:

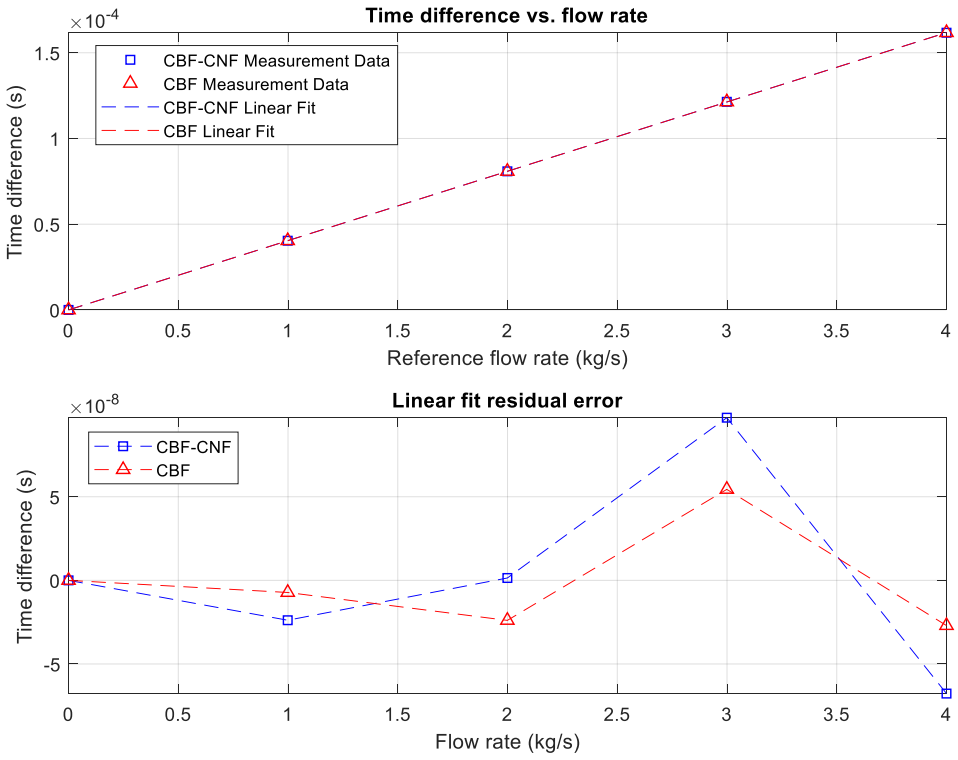


Figure 5.12: Zero-intercept linear fitting for phase difference and mass flow rate

From the figure, the time difference generated by both the CBF and CBF-CNF algorithms track the reference flow rate well; assuming a linear relationship the errors remain within approximately a maximum of ±1e-7 s. If temperature and pressure are taken into account, this error is expected to be reduced further. These results demonstrate that the prototype transmitters, following the basic physical principle of the Coriolis flowmeter, generate acceptable measurement results for single-phase flow. Hence we conclude that the newly developed CBF and CBF-CNF-based transmitters, working together with a commercial flow tube, work properly as a Coriolis flowmeter and are ready for two-phase flow experiments.

5.4 Batching From Empty-to-full Experiments

As mentioned in Section 1.4, batching from empty-to-full is important for some industrial applications and experiments have taken place using the newly developed research transmitter running CBF and CBF-CNF algorithms combined with the Foxboro CFS10 1/4 inch flow tube. A diagram of the batching from empty-to-full experiment is shown below:

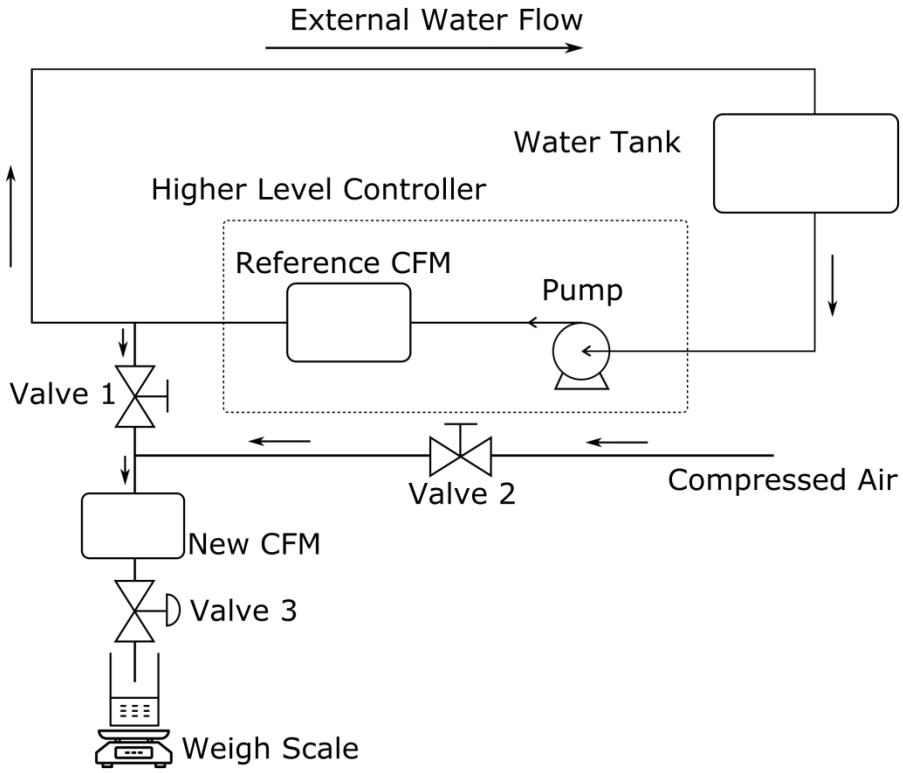


Figure 5.13: Batching from empty-to-full experiment facility diagram

Before each batching from empty-to-full test begins, Valve 2 and 3 are opened to push air through in order to purge all remaining water from the flow tube and ensure the starting GVF is 100%. The drive gain dropping to its conventional value for the dry flow tube is used as an indication that the purging is complete. Valve 3 is a Motor Operated Valve (MOV) used during the experiments to control the batching period. After the flow tube is purged, Valve 3 is opened and then Valve 1 is opened manually. Water passes through the Coriolis flowmeter until stopped by Valve 3 when it is closed at the end of the batch. The total batch process lasts approximately 10s. The weigh scale measures how much water has passed through the meter which is used as a reference to compare with the totalized measured result from the Coriolis flowmeter in order to calculate measurement accuracy. One thing to note is that there will be a nominally

constant offset between the weigh scale measured mass and the totalized Coriolis flowmeter measured mass (totalized CFM measured mass > weigh scale measured mass) since the water mass lying between the new Coriolis flowmeter and Valve 3 will not be measured by weigh scale but will be measured by the new Coriolis flowmeter (as originally the line between new Coriolis flowmeter and Valve 3 is empty). Since the mass shift is constant, it can simply be added up to the weigh scale measured result to compare with the new Coriolis flowmeter measured result. In practice, it is a common approach to add the constant offset to the Coriolis flowmeter measured result in order to calculate the total mass during batching from empty-to-full process [97]. For future industrial applications, where this process is often applied to filling lines or fuel bunkering, Valve 3 and the new Coriolis flowmeter may be combined together to provide a feedback loop control system to control the exact amount of liquid mass passing through the process.

Another experimental issue is that the batch process time is not strictly identical for every experiment. The reason is that Valve 1 is manually opened after Valve 3 is open and opening time gap between two valves is not identical for every experiment. Hence the final batch process time will be between the opening of Valve 1 and closing of Valve 3. Even if the Valve 1 is replaced by a MOV, there will still be a slight difference for every batch process experiment time since the opening and closing behaviour of MOV for every experiment is not identical. However, in this experiment, it does not affect the result since we are primarily comparing the weigh scale measurement to the totalized Coriolis flowmeter result, and allowing for a fixed offset.

To evaluate repeatability, 5 independent batching from empty-to-full trials are carried out, each of approximately 10s duration. The figures below show the tracking results of amplitude, frequency, phase difference, mass flow rate and totalized mass for typical batching from empty experiments for CBF, CBF-CNF and Oxbox.

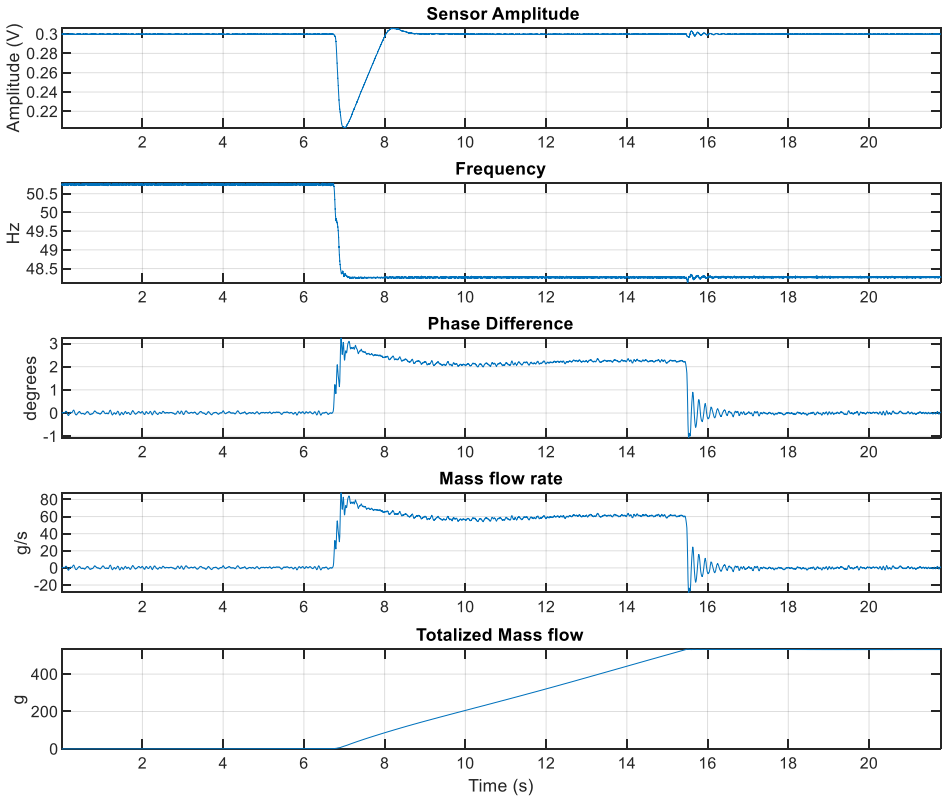


Figure 5.14: CBF based transmitter performance of batching process

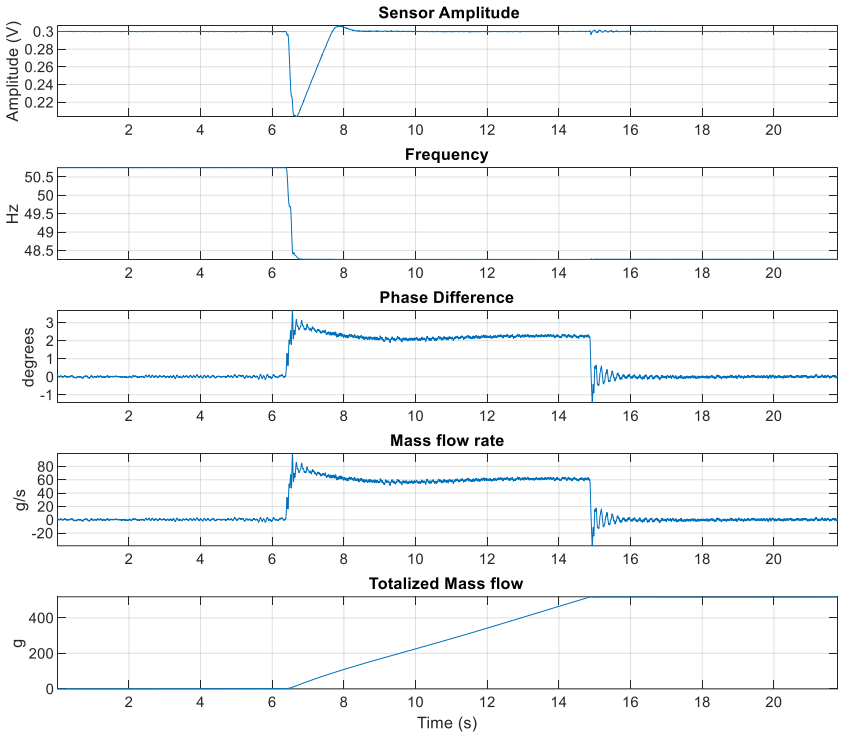


Figure 5.15: CBF-CNF based transmitter performance of batching process

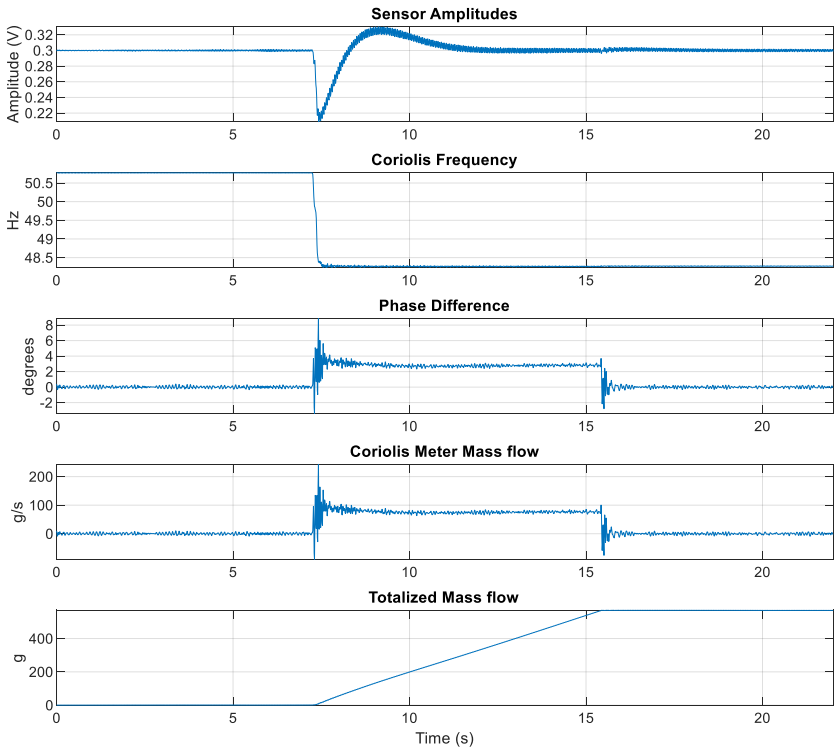


Figure 5.16: Oxbox performance of batching process

As we are primarily interested in the transition period at the start of each batch, the tracked amplitude, frequency and phase difference are shown in the following figures for each method during the flow tube filling process.

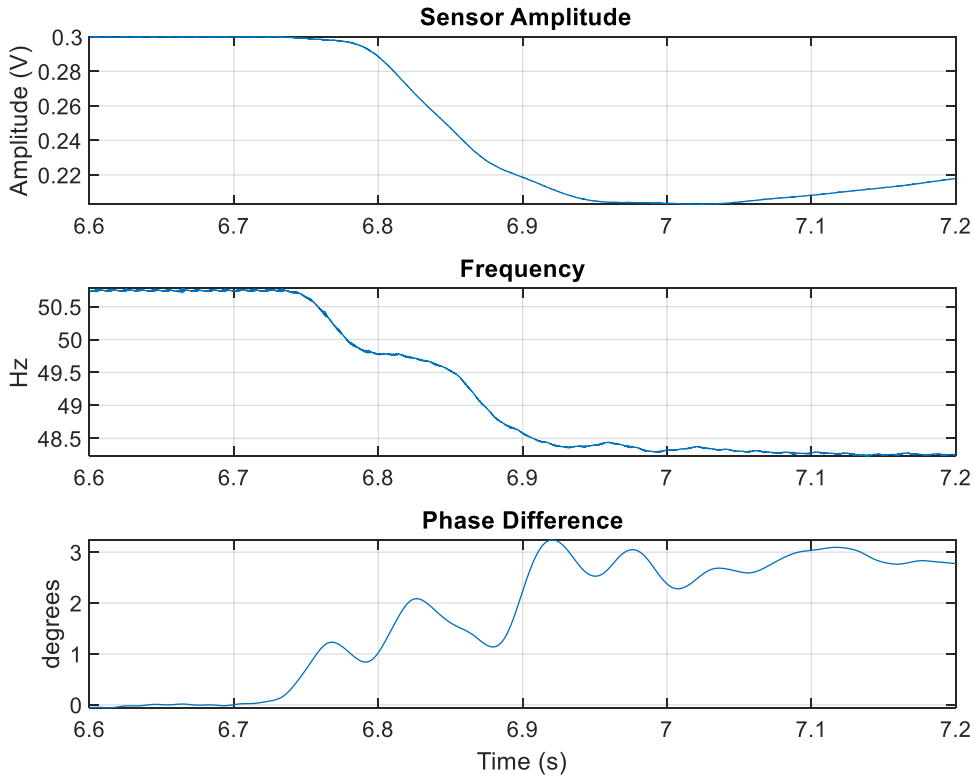


Figure 5.17: CBF tracked parameters during the transition

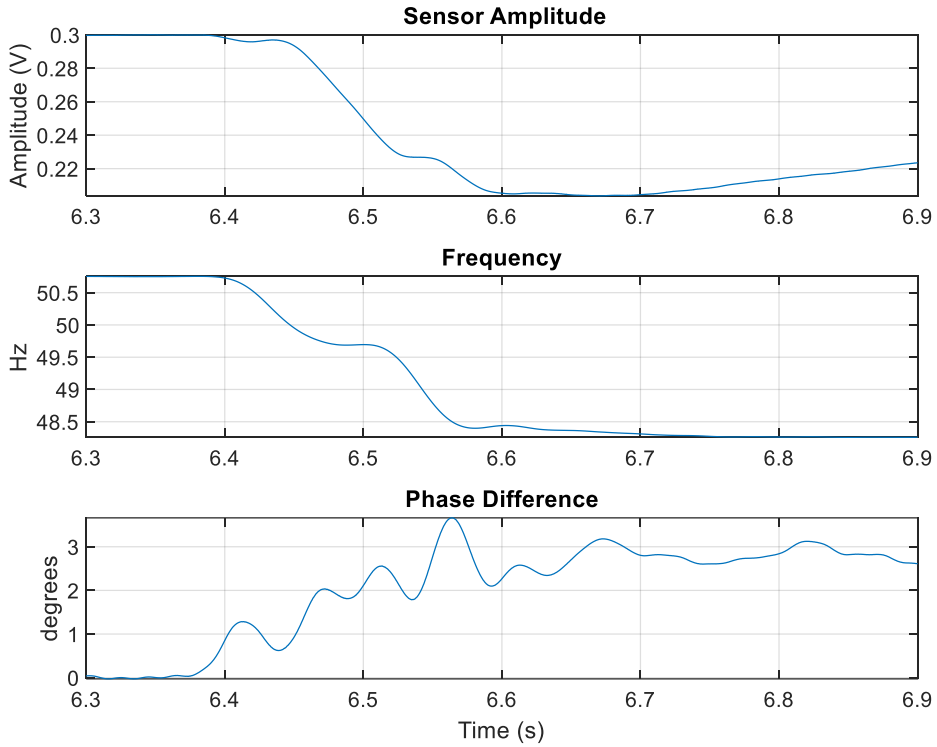


Figure 5.18: CBF-CNF tracked parameters during the transition

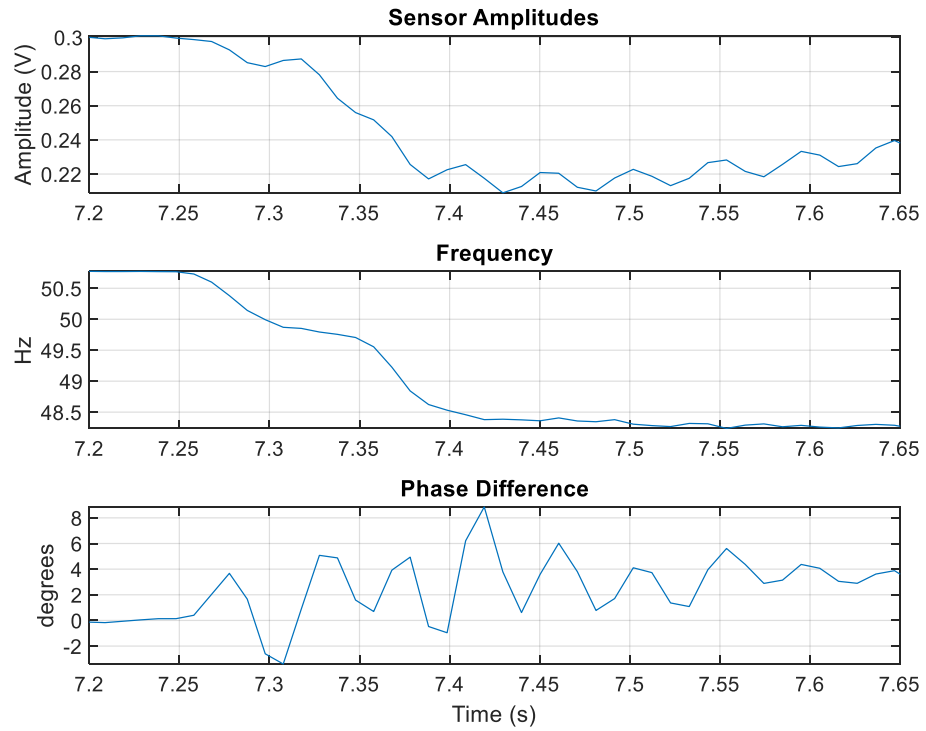


Figure 5.19: Oxbox tracked parameters during the transition

From the figures, the transition period can be as short as 0.3s. The transition period of the batch process is decided by many factors including flow tube geometry, size, pressure drop and so on. In [98], Wang and Hussain also carried out a series of experiments batching from empty-to-full and back to empty using Krohne's straight flow tube. However, the details of the exact transition period of the batch process are not presented due to the relatively slow measurement update rate of 0.1s. The paper carries out detailed comparison between Coriolis flowmeter measured totalized mass and weigh scale measured mass and claiming good repeatability. In the current experiment, the result update rate is 48 kHz thus providing detailed tracking of the transition period and enabling more detailed analysis. If the update rate in the current experiments were 10 Hz (0.1s sample period), it would mean that only 3 measurement points would be provided over the transition period which would make analysis limited. Hence for research purposes and aiming to develop a faster dynamic response Coriolis flowmeter, higher sampling rate of the result is beneficial.

The table below shows the Coriolis flowmeters' (CMF) measured totalized mass compared to weigh scale (WS) measured mass and their differences (Shift) using CBF, CBF-CNF based and 'Oxbox' transmitters.

	CBF		
	CMF (g)	WS (g)	Shift (g)
Trial 1	532.34	484.30	48.04
Trial 2	521.31	471.71	49.6
Trial 3	551.69	501.70	49.99

Trial 4	514.53	464.81	49.72
Trial 5	540.04	491.26	48.78

Table 5.1: Totalized mass measurement result of CBF based transmitter

	CBF-CNF		
	CMF (g)	WS (g)	Shift (g)
Trial 1	517.18	468.61	48.57
Trial 2	491.51	441.79	49.72
Trial 3	504.61	454.73	49.88
Trial 4	582.80	533.14	49.66
Trial 5	608.02	559.46	48.56

Table 5.2: Totalized mass measurement result of CBF-CNF based transmitter

	Oxbox		
	CMF (g)	WS (g)	Shift (g)
Trial 1	571.55	523.20	48.35
Trial 2	589.13	540.30	48.83
Trial 3	565.20	516.32	48.88
Trial 4	581.77	534.63	47.14
Trial 5	557.77	507.24	50.53

Table 5.3: Totalized mass measurement result of Oxbox transmitter

Based on the measurement results, the mean and the spread (minimum and maximum values) of mass shift between Coriolis flowmeters and weigh scale measured mass. Figures below show the result.

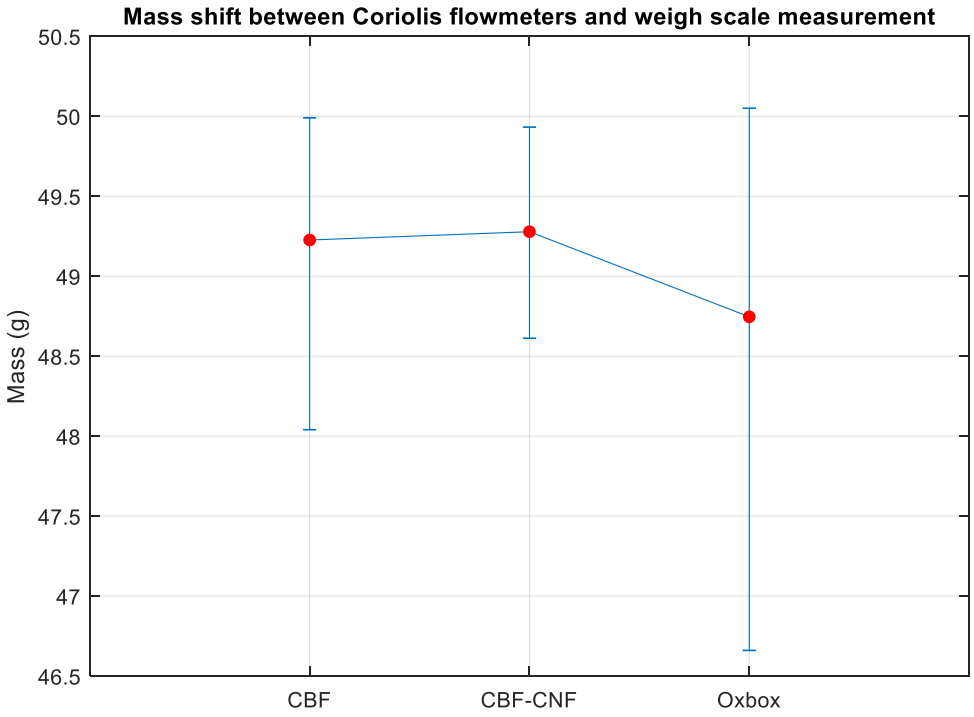


Figure 5.20: Mean and spread of shift mass

In actual industrial applications, the batching from empty-to-full process is often used in filling lines and repeatability is the primary concern which can be reflected as standard deviation of mass shift. The figure below shows the spread of modified CMF measurement mass result with added shift mean mass for each transmitter.

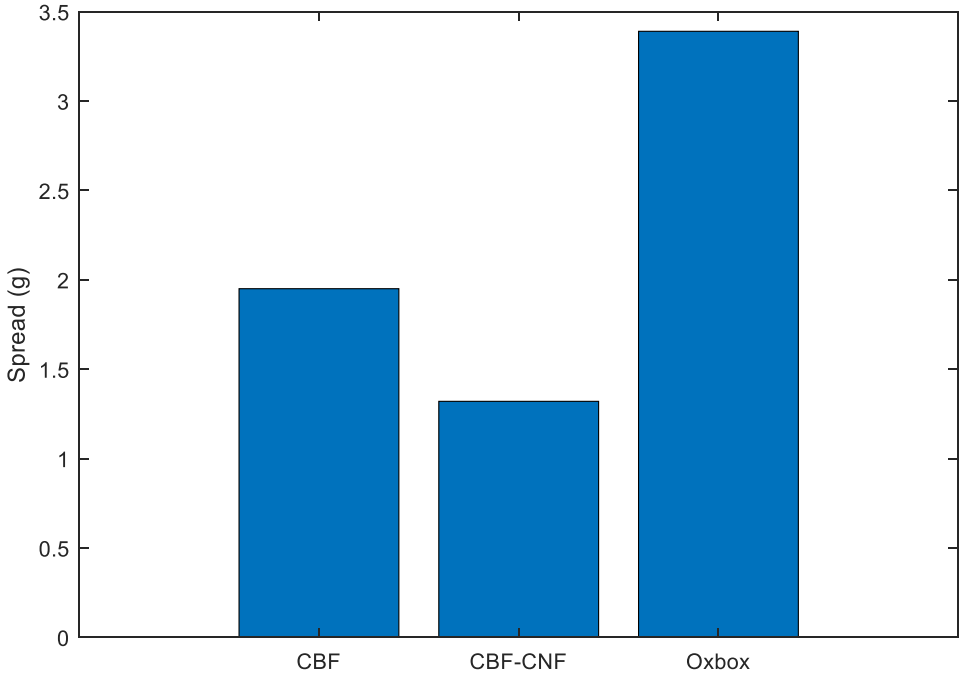


Figure 5.21: Spread of modified CMF totalized mass result comparison

From the result, all of three methods show good repeatability for batching from empty-to-full process with roughly 1 gram deviation for total 500 gram batching process. Furthermore, CBF and CBF-CNF based transmitters show a smaller standard deviation compared to the Oxbox thus providing better repeatability due to more accurate and smoother tracking during batching from empty-to-full transition period.

5.5 Two-phase Experiments

After validating the newly developed Coriolis flowmeter prototype for single-phase flow, two-phase flow (water mixed with air) tests have been carried out using different liquid flow rates and different Gas Void Fractions (GVF). The two-phase flow experiment setup is shown in Figure 5.22:

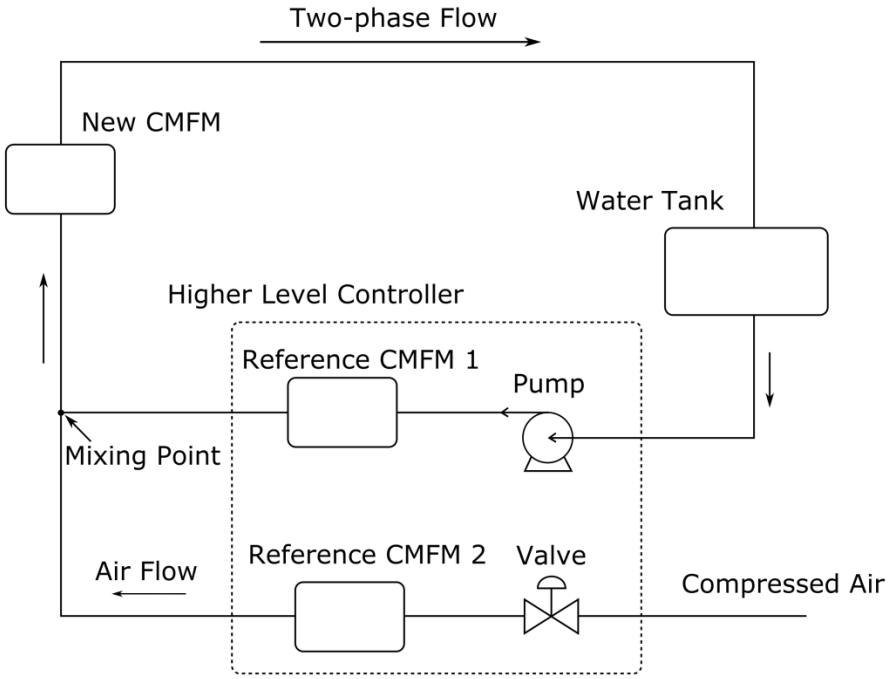


Figure 5.22: Two-phase Flow Experiment Diagram

The compressed air is fed into the flow loop to create a two-phase flow. Reference Coriolis flowmeters together with a pump (water) and valve (air) are connected to the fluid measurement controller to regulate the water flow rate and GVF as required; the controller interface is shown in Figure 5.11.

Before carrying out two-phase flow experiments, the maximum pressure drop for Coriolis flowmeters needs to be considered, i.e. the pressure difference between inlet and outlet of the flow tube. For testing two-phase performance, we have tested water flow rate from 0.5 kg/s up to 4 kg/s with 0.5 kg/s step and varied the GVF between 1% up to 75%. At each flow rate, testing continued from the lowest to the highest GVF not exceeding a pressure drop limit of 1.5 bar. The testing points of two-phase flow experiments and the nominal pressure drop limit line are shown in the figure below:

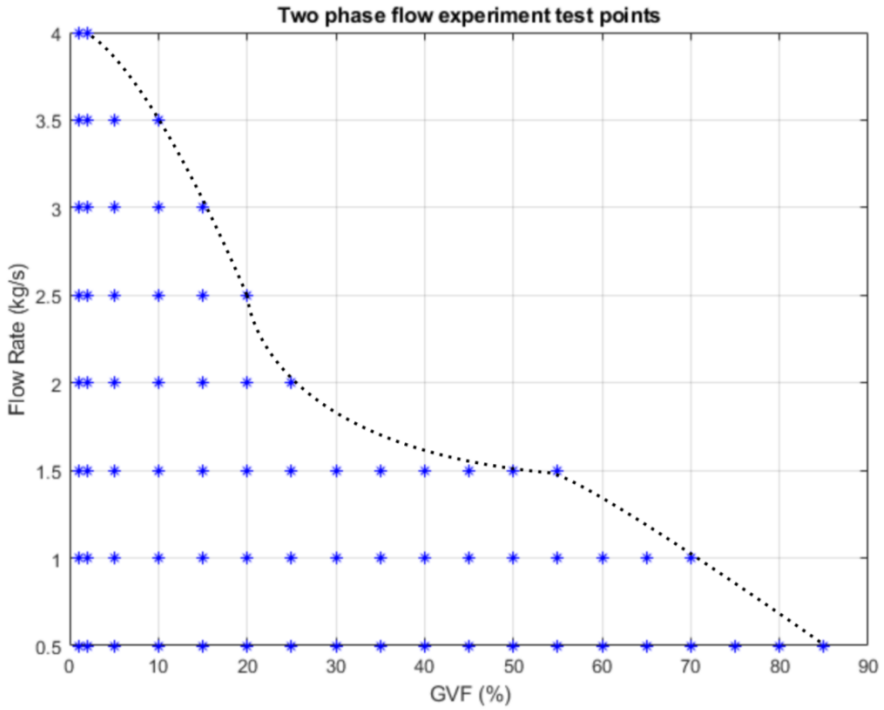


Figure 5.23: Two-phase flow experiment testing points

The pressure drop limit line varies by different flow tube design, size and so on. It can give a view of the maximum range of GVF that can be reached for different water mass flow rate.

When assessing the performance of frequency, amplitude and phase difference tracking in two-phase flow experiments, a number of basic difficulties arise. The first is the absence of any ‘true’ reference measurements: given the random nature of two-phase flow, the instantaneous values of the sensor signal parameters are not known. The second is that, even though reference measurements are available for the time-averaged mass flow and density, ‘true’ instantaneous values are not available either. The third difficulty is that irrespective of any short-term variation, it is well established that there are fluid measurement errors in the average mass flow and density measurements with two-phase flow, requiring modelling and correction [99]. Finally, the frequency,

amplitude and phase measurements are complicated by the closed loop control of the flow tube oscillation – their variations are a function of the control loop responsiveness as well as the time delay and errors associated with the measurement algorithms. Accordingly, it has been important to demonstrate first the capabilities of the new algorithms with a signal generator (where the true values are known) and for single-phase flow working with a flow tube, as well as through simulation studies where the true value of each parameter is known at each time step.

Given these difficulties, the approach taken to assess the performance of the CBF and CBF-CNF algorithms is as follows: for a given set of experimental conditions (flow rate and GVF), the standard deviation of frequency, phase difference and amplitude are compared with those generated by a current commercial transmitter, working with the same flow tube in the same experimental conditions. The commercial transmitter used is a laboratory version of the CFT-50/1 (the 'Oxbox'), which was developed by the Oxford team in collaboration with Invensys Foxboro. The experimental philosophy is to assume that, given the same flow tube and experimental conditions, and a broadly similar flow tube control strategy (programmed by the same team in each case), any improvement in measurement quality (as indicated by reduced standard deviation) will be attributable to an improvement in the measurement algorithms, in terms of accuracy and/or reduced delay, rather than any other factor. Note that the measurement algorithm used in the Oxbox transmitter consists of the following stage: low pass filtering, zero crossing to obtain the resonant frequency, and then DTFT to determine amplitude, phase and phase difference, as described in Chapter 3. The demonstration of a performance advantage over a commercialised technology which has been certified for

upstream oil and gas multi-phase operation is seen as a useful indication that a 'next generation' capability has been achieved.

To assess the performance across the whole flow range between 0.5kg/s to 4kg/s with different GVFs, we calculate the ratio between the CBF and CBF-CNF standard deviations to those of the Oxbox transmitter for amplitude, frequency and phase difference, and finally for density and the mass flow rate. Thus a number below 1.0 indicates that the standard deviation of the corresponding complex signal processing technique is lower than that generated by the Oxbox. The measurement results for all testing points with the water flow rate ranging from 0.5 kg/s to 4 kg/s, and the GVF ranging from 1% to 85% are summarized in the Figures below:

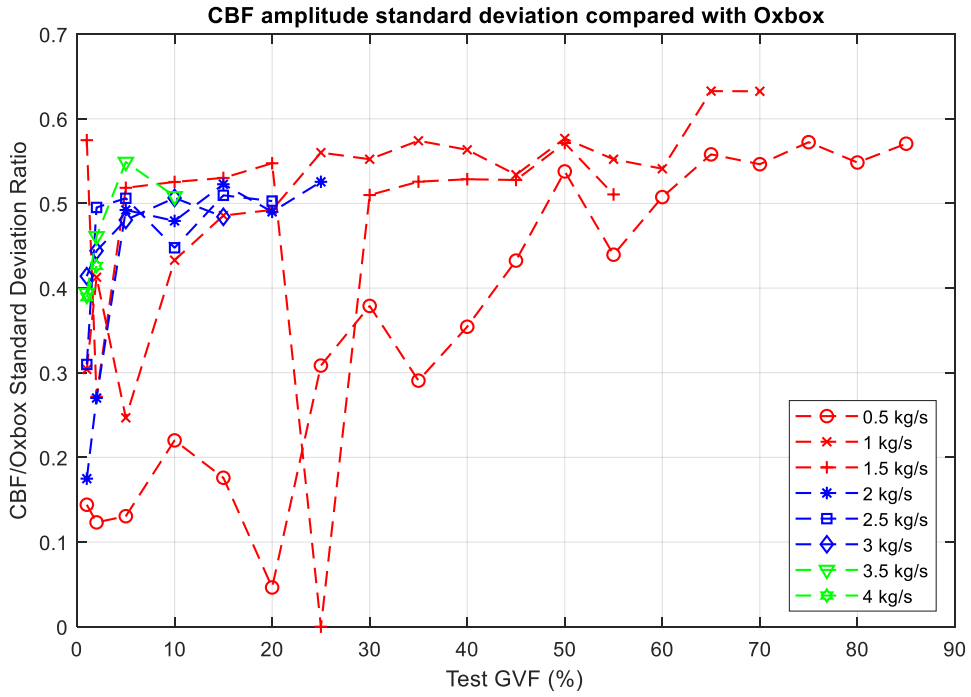


Figure 5.24: Amplitude standard deviation comparison between CBF and Oxbox

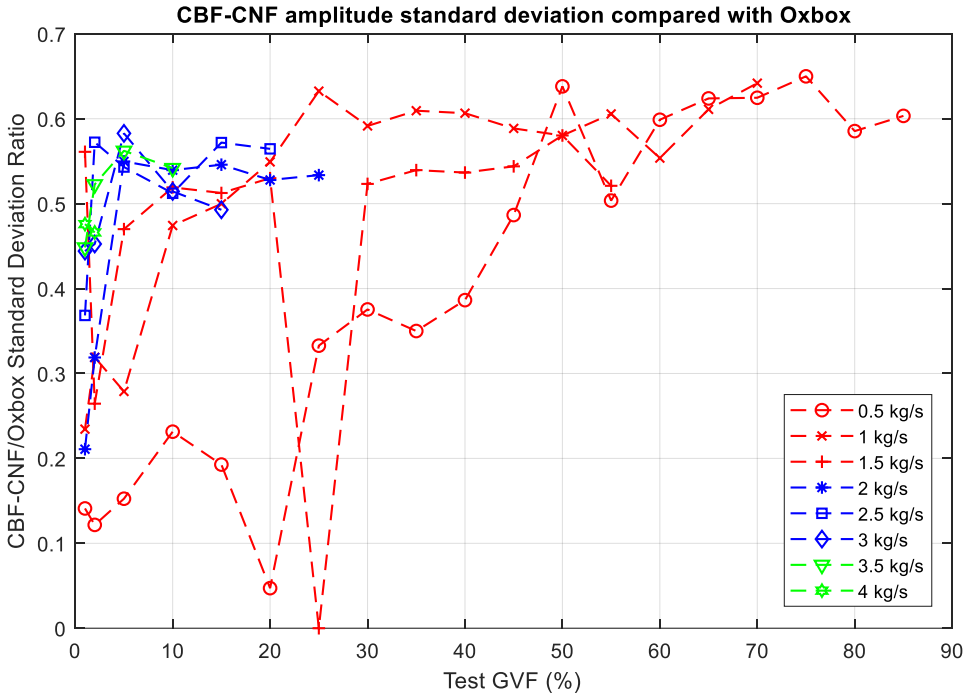


Figure 5.25: Amplitude standard deviation comparison between CBF-CNF and Oxbox

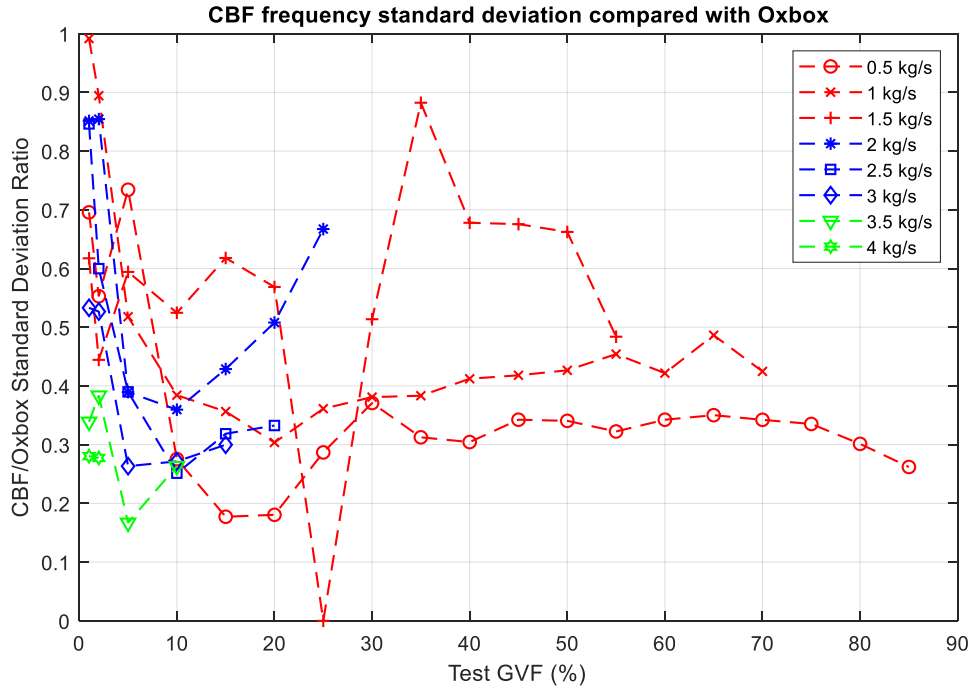


Figure 5.26: Frequency standard deviation comparison between CBF and Oxbox

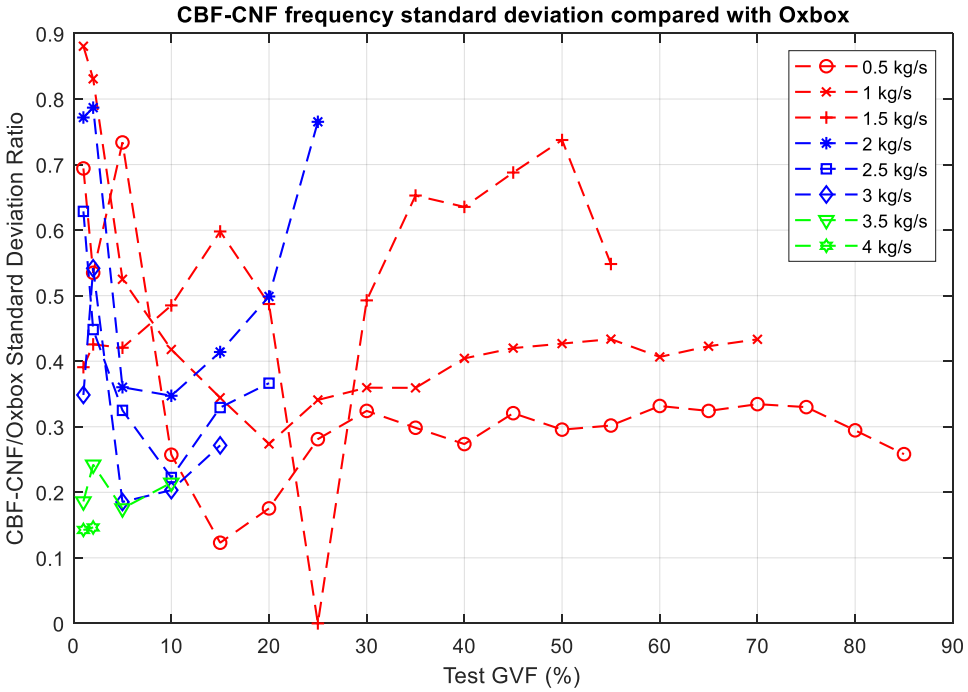


Figure 5.27: Frequency standard deviation comparison between CBF-CNF and Oxbox

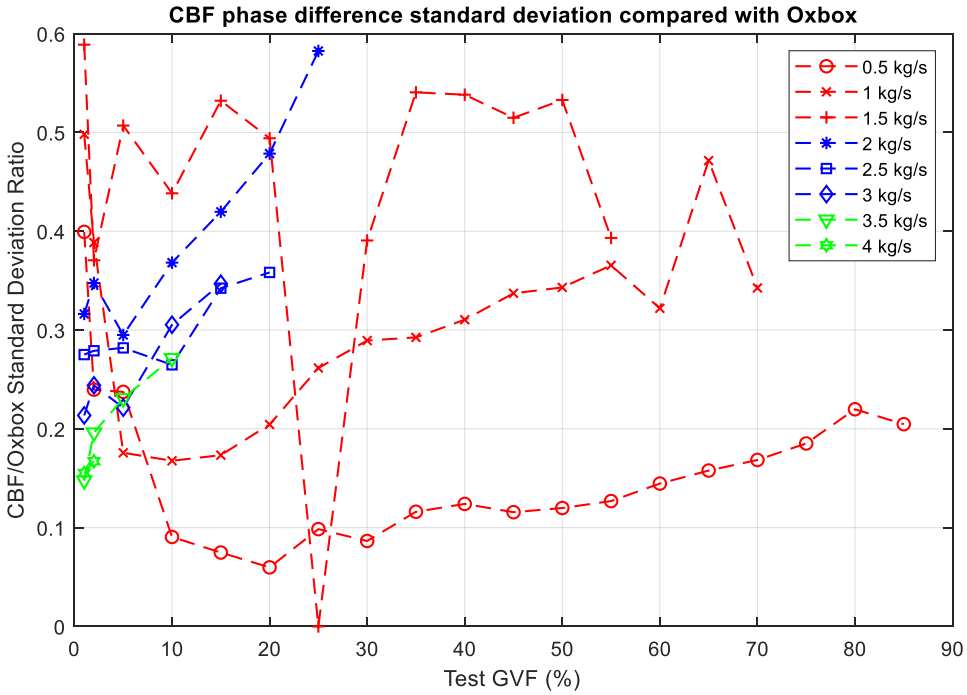


Figure 5.28: Phase difference standard deviation comparison between CBF and Oxbox

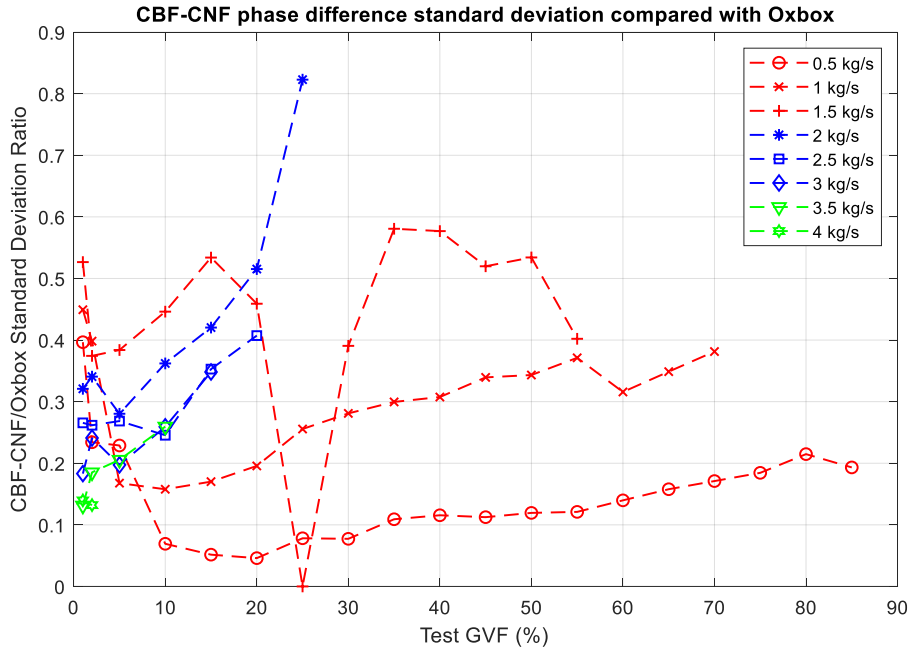


Figure 5.29: Phase difference standard deviation comparison between CBF-CNF and Oxbox

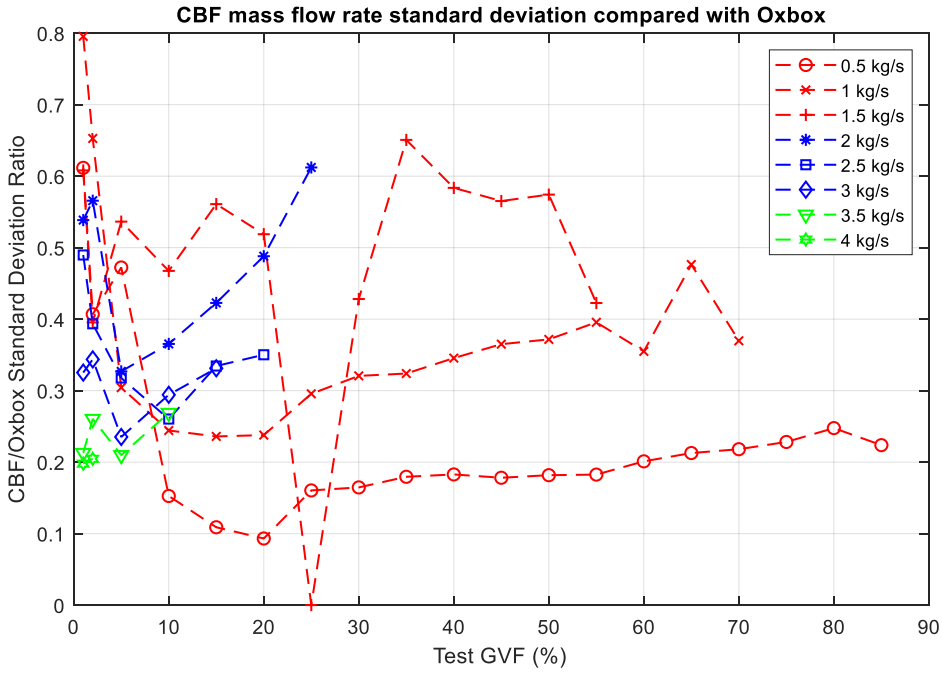


Figure 5.30: Mass flow rate standard deviation comparison between CBF and Oxbox

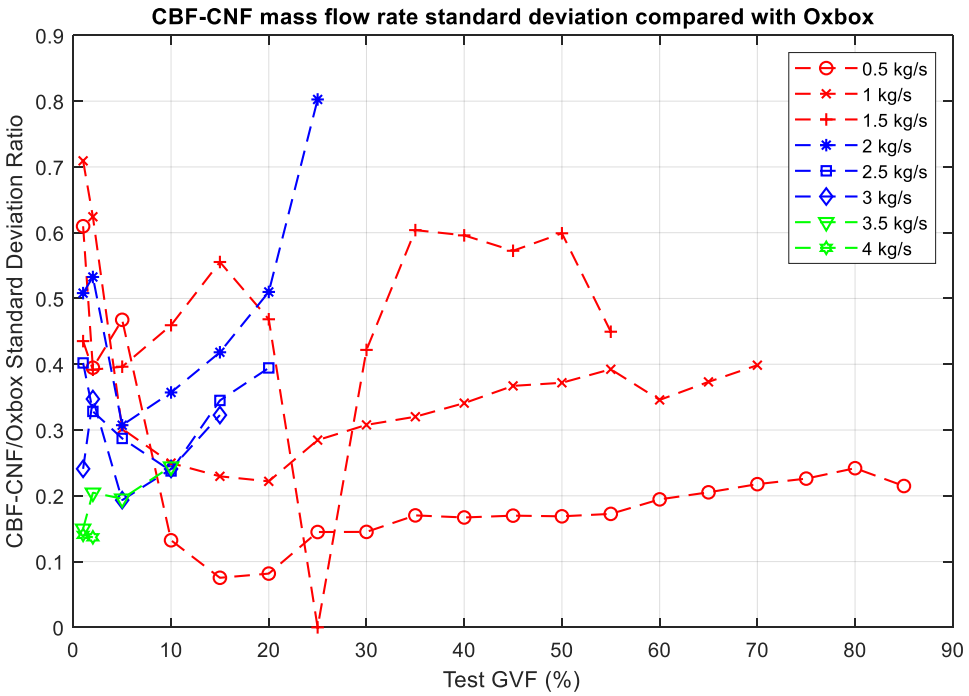


Figure 5.31: Mass flow rate standard deviation comparison between CBF-CNF and Oxbox

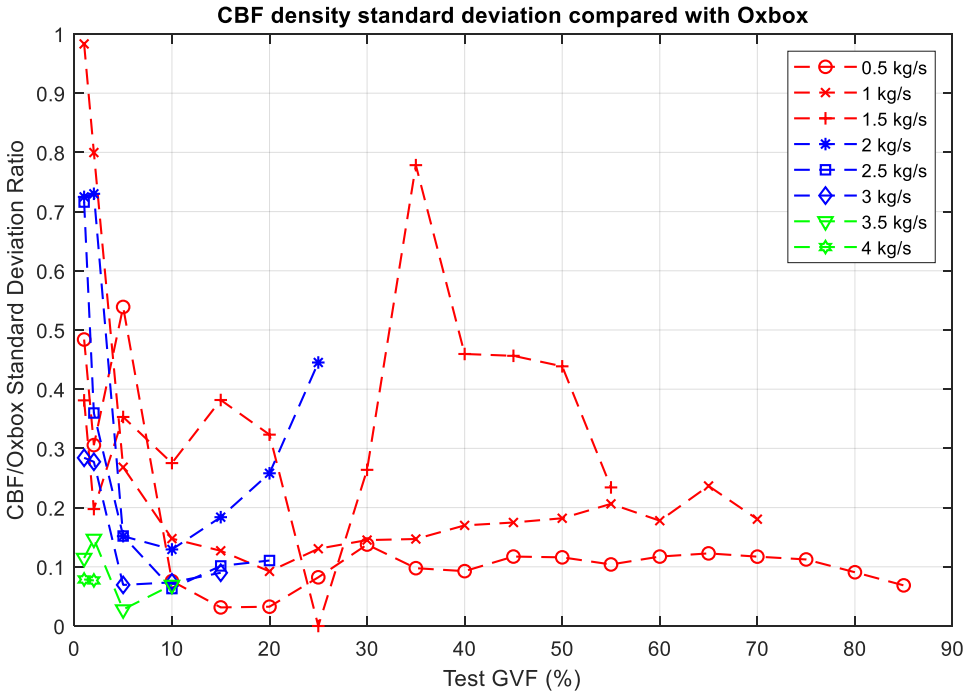


Figure 5.32: Density standard deviation comparison between CBF and Oxbox

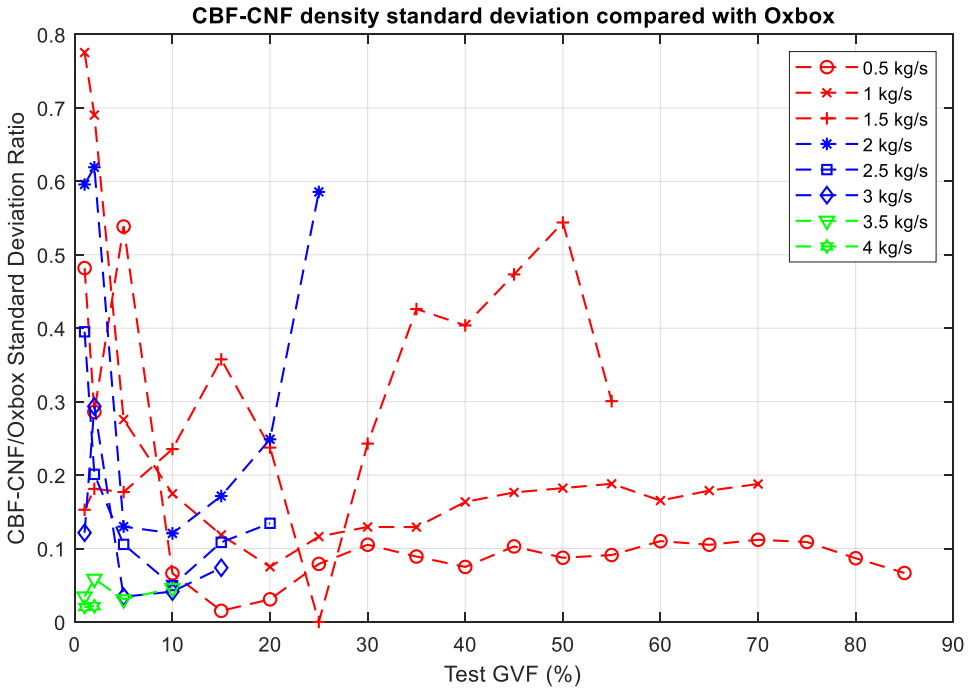


Figure 5.33: Density standard deviation comparison between CBF-CNF and Oxbox

From Figure 5.24 and 5.25, the amplitude standard deviation is consistently reduced for CBF and CBF-CNF against the Oxbox (i.e. the ratio < 1.0). This demonstrates a combination of better measurement resulting in better flow tube control using the new signal processing techniques.

At 1.5 kg/s water flow rate and 25% GVF, the Oxbox transmitter stalls and cannot maintain flow tube vibration. The exact reason for this stall for the Oxbox is unclear. However, the standard deviation ratios between the CBF and Oxbox methods for this point are represented as 0 to assume infinite standard deviation of the Oxbox.

Comparing CBF and CBF-CNF amplitude standard deviation improvements, CBF generally shows a better performance. This can be seen more clearly in the cumulative probability plots in figures 5.34-5.38. CBF show a better ability to suppress noise than CBF-CNF due to its deeper stopband attenuation. Hence for achieving better control

during two-phase, both the dynamic performance and noise supersession ability of measurement algorithms are important.

The frequency measurement results are similar to those for amplitude, with CBF and CBF-CNF based transmitters show good improvement against Oxbox where the improvement can be as high as 10 times better. CBF and CBF-CNF together show similar performance for frequency tracking.

The phase difference measurement of CBF and CBF-CNF improvement reaches up to 10 times better than the Oxbox as well. Mass flow rate measurement improvement is similar to phase difference improvement which suggests that the mass flow rate error is primarily affected by the phase difference error (as opposed to the frequency error). The most impressive improvement is for the density measurement, where CBF and CBF-CNF show more than 5 times improvements for a large proportion of the testing data points.

Over the eight flow lines a wide variety of standard deviation ratios are generated, arising from a number of factors including the particular pattern of two phase flow created in the flow tube, the possibility of interfering resonances being stimulated and so on. In order to summarise performance across different liquid mass flow rates and GVFs, the cumulative probability distribution for each parameters' standard deviation ratio has been calculated, as shown in the following figures.

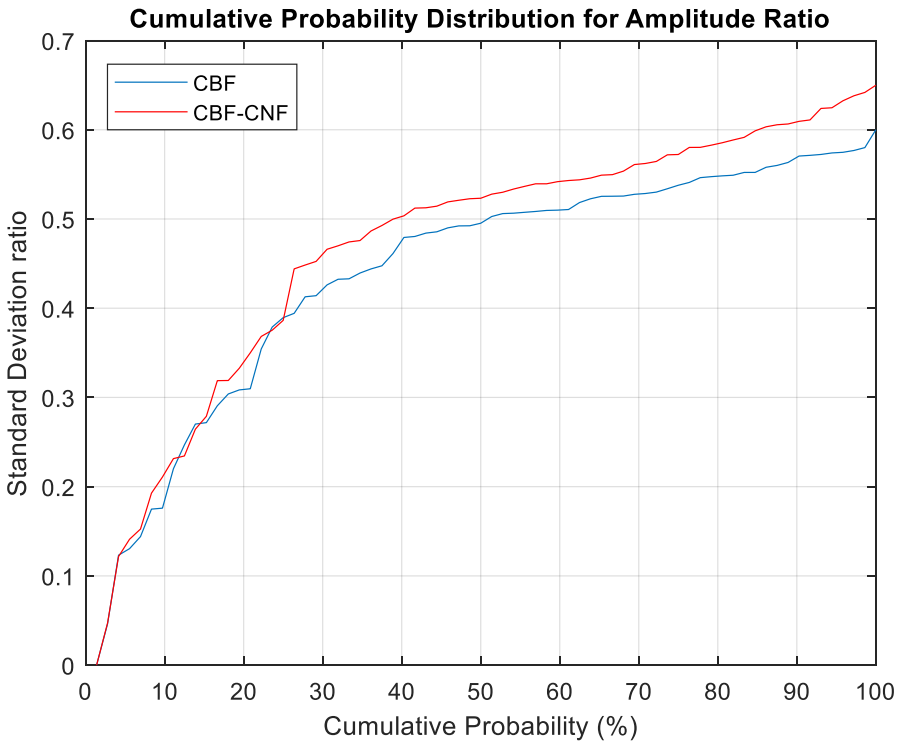


Figure 5.34: Result of amplitude standard deviation ratio

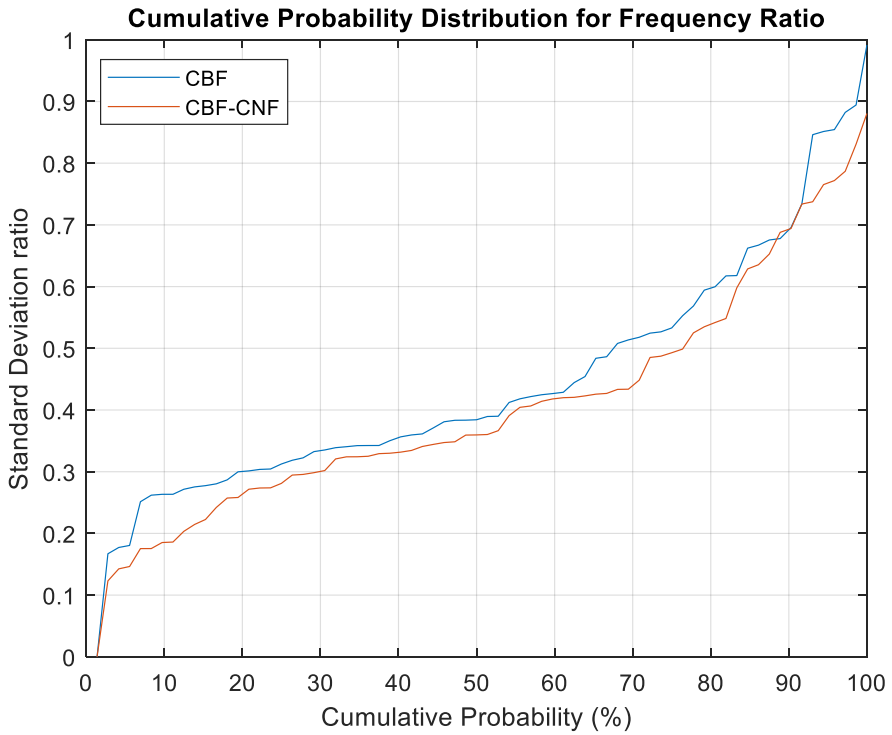


Figure 5.35: Result of frequency standard deviation ratio

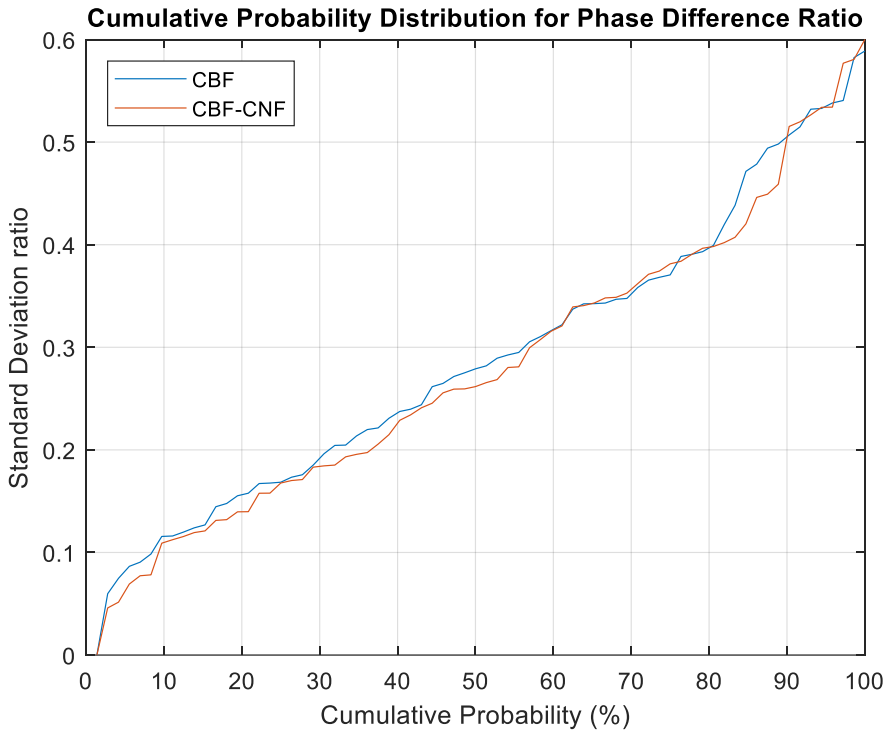


Figure 5.36: Result of phase difference standard deviation ratio

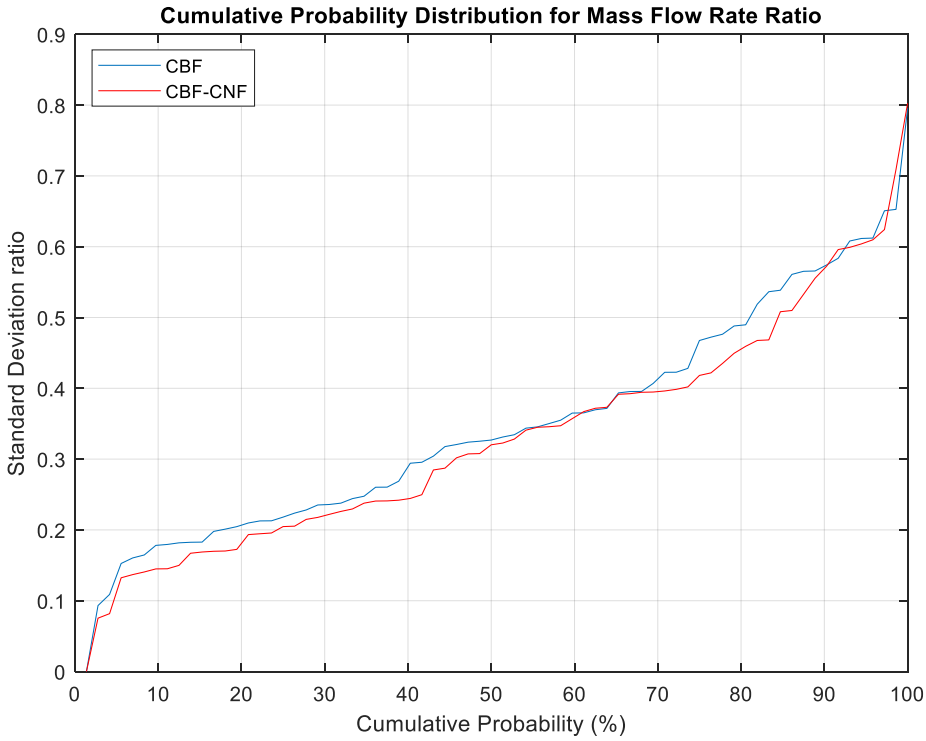


Figure 5.37: Result of mass flow rate standard deviation ratio

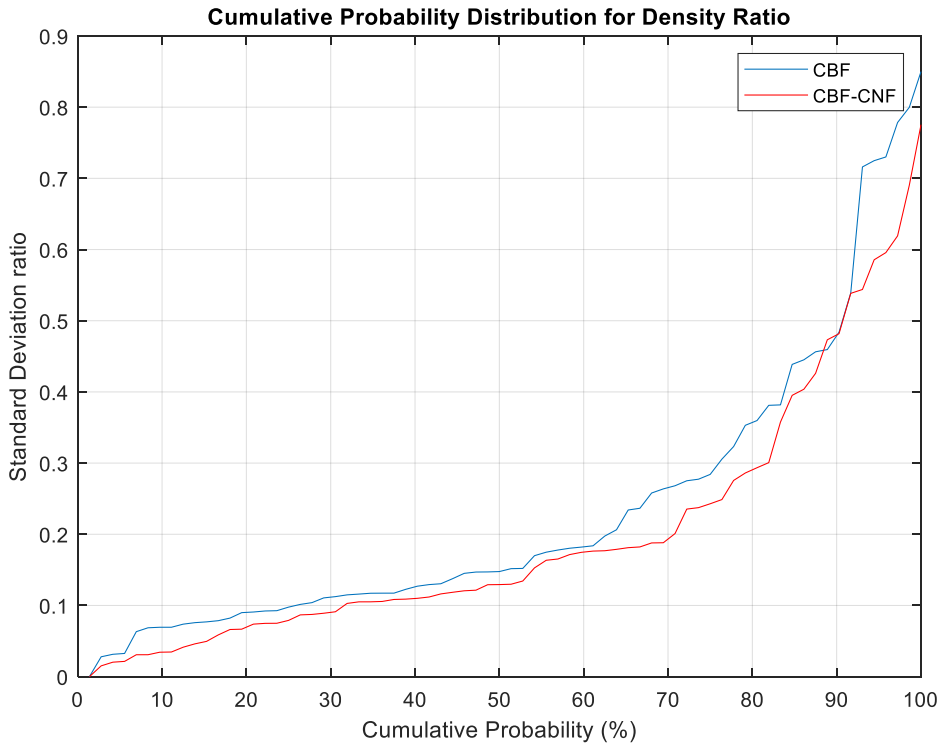


Figure 5.38: Result of density standard deviation ratio

From the figures, the amplitude standard deviation for the CBF and CBF-CNF methods are at least two times better than the Oxbox in 50% of the experiments. For frequency, the CBF and CBF-CNF methods are roughly 2.5 times better than the Oxbox for 50% of the experiments. For phase difference, the improvement is more significant than for amplitude and frequency, with 50% of values with more than 3 times improvement compared to the Oxbox.

Finally, the results for the signal tracking are propagated through into the flow and density measurements to see the resulting reductions in standard deviation. For the mass flow rate result, the improvement is similar to that of phase difference where 80% values are two times better than the Oxbox, and all results show at least a 1.2 times improvement. Furthermore, 50% of results are at least 3 times better than Oxbox. For

density, the improvement is very promising, where 50% values are at least 6 times better than the Oxbox and at least two times improvement is given in 90% of the results.

Overall, these results demonstrate that CBF and CBF-CNF methods can operate successfully in real time over a range of liquid mass flow rates and GVFs without flowtube stalling. Furthermore, significant improvements are achieved for CBF and CBF-CNF methods over the Oxbox zero-crossing technique, which show a promising future for two-phase applications.

For correcting density and mass flow rate calculation fluid measurement error, further correction techniques are needed such as bubble model and neural networks since the surface of phase difference versus flow rate (it can be imagined as a three-dimensional surface area by plotting GVF, mass flow rate and phase difference together in a single plot) is highly nonlinear, as discussed in [99].

5.6 Summary

In this chapter, we have introduced the hardware platform which is used to implement the newly developed CBF and CBF-CNF techniques. Then we have introduced the experimental facilities and described various kinds of experiments including signal generator tests, single-phase flow tests and two-phase flow tests. From the single-phase flow tests, we have proved that newly developed CBF and CBF-CNF algorithms on a prototype transmitter connected to a flow tube perform properly as a Coriolis flowmeter. Then we carried out two-phase flow tests for various GVFs and the results show that the new algorithms perform better than existing state-of-art commercial products in most two-phase conditions, especially for the amplitude and phase-difference measurements.

Additional calculations, such as temperature compensation and two-phase flow correction, are also needed in order to make the newly developed transmitter a potential commercial product.

6.NON-LINEAR STATE SPACE MODEL

Using a Kalman filter based on a state space model has become a popular method for tracking a non-stationary sinusoidal signal, since it can track rapidly changing signals in conditions where the Signal-to-Noise Ratio (SNR) is low. It has been applied to many areas, such as speech recognition, smart grid, power systems, satellite/mobile communications and radar signal processing [100]–[103]. This chapter explores the possibility of using a non-linear state space model with an Extended Kalman Filter (EKF) to track the non-stationary sensor data for two-phase Coriolis flowmeter signal processing. We present a new basic non-linear model for generating the non-stationary sinusoidal signal, which allows full dynamic changes in frequency, amplitude and phase. The non-linear state space model is derived from a second order Ordinary Differential Equation (ODE) that describes a closed-form solution for the non-stationary sinusoidal signal. The model is firstly represented as a continuous time state-space model and then incorporated into the Continuous-Discrete (hybrid) Extended Kalman Filter (CD-EKF) to estimate the frequency, amplitude and phase of the signal in real

time. By solving the second order ODE, it is discretized into a discrete time state-space model and incorporated into a discrete EKF for real time tracking. The performance of the new models are compared to existing state space models as well as previously developed CBF based techniques, and its potential application to Coriolis flowmeter signal processing is discussed.

6.1 Existing State Space Models

Adopting a non-linear state space model with EKF to track a non-stationary sinusoidal signal has been explored by various researchers [100]–[106]. EKF is sometimes called the "optimal filter" and it shows a good tracking ability with small tracking delay. We firstly review existing state space models for the non-stationary sinusoidal tracking problem.

6.1.1 Modified Cartesian Model

Among the existing state space models for tracking, the Cartesian model is long-established for tracking a frequency varying sinusoidal signal. It is a discretized model and widely used in many fields [100]–[105]. The original Cartesian model is described as:

$$\begin{bmatrix} x_1(\mathrm{k}+1) \\ x_2(\mathrm{k}+1) \\ x_3(\mathrm{k}+1) \end{bmatrix} = \begin{bmatrix} x_1(\mathrm{k})\cos(x_3(\mathrm{k})T_s) - x_2(\mathrm{k})\sin(x_3(\mathrm{k})T_s) \\ x_1(\mathrm{k})\sin(x_3(\mathrm{k})T_s) + x_2(\mathrm{k})\cos(x_3(\mathrm{k})T_s) \\ x_3(\mathrm{k}) \end{bmatrix} + \begin{bmatrix} 0 \\ 0 \\ w(\mathrm{k}) \end{bmatrix} \tag{6.1}$$

where $w(\mathrm{k})$ is the process noise which is usually assumed to follow a Gaussian distribution, $x_1(\mathrm{k})$ is the measurement input signal, $x_2(\mathrm{k})$ is the inner state which is ontological to $x_1(\mathrm{k})$, $x_3(\mathrm{k})$ corresponds to frequency and T_s is the sample period.

However, it was found that the traditional Cartesian model could be extended to track an amplitude varying signal, which is important in many applications [101], [102], [107]–[111]. Habib et al. [112] developed the Modified Cartesian Model (MCM) for tracking an amplitude and frequency varying signal. The MCM is a discrete state space model which is represented as:

$$\begin{bmatrix} x_1(\mathrm{k}+1) \\ x_2(\mathrm{k}+1) \\ x_3(\mathrm{k}+1) \\ x_4(\mathrm{k}+1) \end{bmatrix} = \begin{bmatrix} x_4(\mathrm{k})\left[x_1(\mathrm{k})\cos(x_3(\mathrm{k})T_s) - x_2(\mathrm{k})\sin(x_3(\mathrm{k})T_s)\right] \\ x_4(\mathrm{k})\left[x_1(\mathrm{k})\sin(x_3(\mathrm{k})T_s) + x_2(\mathrm{k})\cos(x_3(\mathrm{k})T_s)\right] \\ x_3(\mathrm{k}) \\ x_4(\mathrm{k}) \end{bmatrix} + \begin{bmatrix} 0 \\ 0 \\ w_1(\mathrm{k}) \\ w_2(\mathrm{k}) \end{bmatrix} \tag{6.2}$$

where $x_4(\mathrm{k})$ corresponds to the amplitude. The associated observation model is:

$$y(\mathrm{k}) = x_1(\mathrm{k}) + v(\mathrm{k}) \tag{6.3}$$

This state space model can be incorporated into EKF to track a non-stationary sinusoidal signal. The signal parameters (ω for frequency, A for amplitude and φ for phase) can be recovered using:

$$\begin{aligned} \omega(\mathrm{k}) &= x_3(\mathrm{k}) \\ A(\mathrm{k}) &= \sqrt{x_1(\mathrm{k})^2 + x_2(\mathrm{k})^2} \\ \varphi(\mathrm{k}) &= \arctan\left(\frac{x_2(\mathrm{k})}{x_1(\mathrm{k})}\right) \end{aligned} \tag{6.4}$$

6.1.2 Nearly Constant Frequency Model

William et al. [113] introduced the Nearly Constant Frequency (NCF) model as part of a non-linear Kalman filter which is able to track an amplitude and frequency varying non-stationary sinusoidal signal. The NCF model can be described as:

$$\begin{bmatrix} x_1(\mathrm{k}+1) \\ x_2(\mathrm{k}+1) \\ x_3(\mathrm{k}+1) \end{bmatrix} = \begin{bmatrix} 1 & T_s & 0 \\ 0 & 1 & 0 \\ 0 & 0 & 1 \end{bmatrix} + \begin{bmatrix} T_s^2/2 & 0 \\ T_s & 0 \\ 0 & T_s \end{bmatrix} \begin{bmatrix} w_1 \\ w_2 \end{bmatrix} \tag{6.5}$$

where w_1 and w_2 are process noise following Gaussian distributions and T_s is the sample period. x_2(k) corresponds to the angular frequency and the associated observation model is:

$$y(\mathrm{k}) = \cos(x_1(\mathrm{k})) + v(\mathrm{k}) \tag{6.6}$$

where v is Gaussian white noise.

This state space model can be incorporated into an EKF to track a non-stationary sinusoidal signal. The sinusoidal parameters (ω for frequency, A for amplitude and φ for phase) can be recovered directly from the model using:

$$\begin{aligned} \omega(\mathrm{k}) &= x_2(\mathrm{k}) \\ A(\mathrm{k}) &= x_3(\mathrm{k}) \\ \varphi(\mathrm{k}) &= x_1(\mathrm{k}) \end{aligned} \tag{6.7}$$

The MCM and NCF model will now be compared with our new models in both empty-to-full batch and continuous two-phase simulations.

6.2 New Continuous Time Model

Previous state space models are approximate representations of non-stationary sinusoidal signals and these approximations introduce modelling errors into the EKF. In this section, we present a new continuous time model for explicitly representing a non-stationary sinusoidal signal in order to eliminate modelling errors. The non-stationary sinusoidal sensor signal in continuous time is described as:

$$y(t) = A(t)\cos(\varphi(t)) \tag{6.8}$$

where $A(t)$ is time varying amplitude and $\varphi(t)$ is a time varying phasor. Here noise is excluded for model derivation purposes but is introduced later for the Kalman filter implementation.

The phasor function $\varphi(\mathrm{t})$ can be further represented by time varying frequency $\omega(\mathrm{t})$ and initial phase $\phi(0)$ as:

$$\varphi(\mathrm{t}) = \int_0^t \omega(\tau)\tau + \phi(0) \tag{6.9}$$

In later equations, for simplicity, we represent $y(\mathrm{t})$ as y, $A(\mathrm{t})$ as A, $\varphi(\mathrm{t})$ as φ and $\omega(\mathrm{t})$ as ω. Differentiating (6.8), gives:

$$y' = A'\cos\varphi - A\omega\sin\varphi \tag{6.10}$$

and then differentiating again, gives:

$$y'' = (A'' - A\omega^2)\cos\varphi - (2\omega A' + A\omega')\sin\varphi \tag{6.11}$$

From (6.8), we also obtain:

$$\cos\varphi = \frac{y}{A} \tag{6.12}$$

Substituting this result into (6.10) and solving for $\sin\varphi$:

$$\sin\varphi = \frac{\cos\varphi}{A\omega}A' - \frac{1}{A\omega}y' = \frac{y}{A^2\omega}A' - \frac{1}{A\omega}y' \tag{6.13}$$

By substituting (6.12) and (6.13) into (6.11), we obtain:

$$y'' - (\frac{2}{A}A' + \frac{\omega'}{\omega})y' - (\frac{A''}{A} - 2(\frac{A'}{A})^2 - \frac{A'}{A}\frac{\omega'}{\omega} - \omega^2)y = 0 \tag{6.14}$$

Equation (6.14) can be used to generate a non-stationary sinusoidal signal directly given initial values of y and y' and the varying values of A'' and ω'. Since frequency and amplitude are both physically non-negative, it is convenient to transform the derivative terms in (6.14) using logarithms:

$$\begin{aligned}(\ln\omega)' &= \frac{\omega'}{\omega}\\ (\ln A)' &= \frac{A'}{A}\\ (\ln A)'' &= \frac{A''}{A} - (\frac{A'}{A})^2\end{aligned} \tag{6.15}$$

and substituting (6.15) into (6.14), we obtain:

$$y'' - (2(\ln A)' + (\ln \omega)')y' - ((\ln A)'' - ((\ln A)')^2 - (\ln A)'(\ln \omega)' - \omega^2)y = 0 \quad (6.16)$$

This becomes a second-order ODE, which fully represents the non-stationary sinusoidal signal. In the following sections, we will express this ODE as a state space model and then incorporate this model into an EKF for tracking.

6.3 Continuous-Discrete Extended Kalman Filter

Based on (6.16), and assuming $(\ln A)''$ and $(\ln \omega)''$ are process noise inputs for the Kalman filter, we can incorporate the model into a Continuous-Discrete EKF (CD-EKF) to track the parameters of a non-stationary sinusoidal signal [114]. The model can be re-written as a continuous state-space model which is referred to as a Full Continuous-Time Model (FCTM). For FCTM, we define the state variables in (6.16) as:

$$x = (y, y', (\ln A)', (\ln A)'', \ln \omega, (\ln \omega)') \quad (6.17)$$

Then by re-writing (6.16), The FCTM is:

$$\frac{d}{dt}\begin{bmatrix} y \\ y' \\ (\ln A)' \\ (\ln A)'' \\ \ln \omega \\ (\ln \omega)' \end{bmatrix} = \begin{bmatrix} y' \\ f_1(x) \\ (\ln A)'' \\ 0 \\ (\ln \omega)' \\ 0 \end{bmatrix} + \begin{bmatrix} 0 \\ 0 \\ 0 \\ w_1 \\ 0 \\ w_2 \end{bmatrix} \quad (6.18)$$

where

$$f_1(x) = (2(\ln A)' + (\ln \omega)')y' + ((\ln A)'' - ((\ln A)')^2 - (\ln A)'(\ln \omega)' - \omega^2)y \quad (6.19)$$

and where w_1 and w_2 are noise terms. The system equation can be written as:

$$\begin{aligned} x' &= f(x,t) + w(t) \\ y_k &= Cx_k + v_k \\ w(t) &= N(0,Q) \\ v_k &= N(0,R_k) \end{aligned} \tag{6.20}$$

where

$$C = \begin{bmatrix} 1 & 0 & 0 & 0 & 0 & 0 \end{bmatrix},\ w(\mathrm{t}) = B\begin{bmatrix} w_1(\mathrm{t}) \\ w_2(\mathrm{t}) \end{bmatrix},\ B = \begin{bmatrix} 0 & 0 \\ 0 & 0 \\ 0 & 0 \\ 1 & 0 \\ 0 & 0 \\ 0 & 1 \end{bmatrix} \tag{6.21}$$

and $f(x,t)$ is the state-space evolving model as shown in (6.18), w(t) is continuous-time white noise representing $w_1(\mathrm{t})$ and $w_2(\mathrm{t})$ with covariance Q and the measurement noise v_k is discrete-time white noise with covariance R_k. Here x is integrated every measurement time step representing continuous evolution of the state space model and y_k is the discrete measurement input which is y in (6.18). The typical CD-EKF process is as follows:

1) Initialize the filter :

$$\begin{aligned} \hat{x}_0^+ &= E[x_0] \\ P_0^+ &= E[(x_0 - \hat{x}_0^+)(x_0 - x_0^+)^T] \end{aligned} \tag{6.22}$$

2) For discrete samples $k = 1, 2, \ldots$, perform the following steps. Integrate the state estimate and its covariance from time $(k-1)^+$ to time k^- as follows:

$$\begin{aligned} \dot{\hat{x}} &= f(x,t) \\ P' &= AP + PA^T + BQB^T \end{aligned} \tag{6.23}$$

where

$$A = \left.\frac{\partial f}{\partial x}\right|_{\hat{x}} \tag{6.24}$$

We begin the integration process with $x = x_{k-1}^{+}$ and $P = \hat{x}_{k-1}^{+}$. At the end of this integration we have $x = x_k^-$ and $P = P_k^-$.

3) At time k, use the measurement y_k to update the state estimate and estimation covariance as follows:

$$\begin{aligned} K_k &= P_k^- C^T (C P_k^- C^T + R_k)^{-1} \\ x_k &= x_k^- + K_k[y_k - C x_k^-] \\ P_k^+ &= (I - K_k C) P_k^- (I - K_k C)^T + K_k R_k K_k^T \end{aligned} \tag{6.25}$$

The derived FCTM (CD-EKF) can track a non-stationary sinusoidal signal with discrete measurements y_k and estimated frequency, amplitude and phase estimation. The parameters calculated at the k^{th} sampling point are given by:

$$\begin{aligned} \omega_k &= e^{\hat{x}_k^+(5)} \\ A_k &= \sqrt{\hat{x}_k^+(1)^2 + \left(\frac{\hat{x}_k^+(2)}{\omega_k}\right)^2} \\ \varphi_k &= \arctan\left(\frac{\hat{x}_k^+(2)}{\omega_k \hat{x}_k^+(1)}\right) \end{aligned} \tag{6.26}$$

where ω_k, A_k and φ_k are frequency, amplitude and phase respectively.

6.4 Discrete Time Model

Although FCTM can track a non-stationary sinusoidal signal using discrete measurements, the computational requirement is high since the integration process for CD-EKF is performed at every sampling point. In this section, we discretize the FCTM into a Full Discrete-Time Model (FDTM) by solving the ODE (6.16). Since (6.16) is a second-order ODE, we can solve it and obtain closed-form solutions. There will be

three different solutions depending on whether $4\omega^2 - 4(\ln A)'' - ((\ln \omega)')^2$ is larger than 0, equal to 0 or smaller than 0. Here we assume the changes of amplitude $(\ln A)''$ and frequency $(\ln \omega)'$ do not have extreme values which correspond to $4\omega^2 - 4(\ln A)'' - ((\ln \omega)')^2 > 0$. In this situation, (6.16) has the following exact solution:

$$y = e^{\sigma t}(C_1 \cos \rho t + C_2 \sin \rho t) \tag{6.27}$$

where C_1 and C_2 are arbitrary constants, $\sigma = \frac{2(\ln A)' + (\ln \omega)'}{2}$ and $\rho = \frac{\sqrt{4\omega^2 - 4(\ln A)'' - ((\ln \omega)')^2}}{2}$.

Further differentiating (6.27), we obtain:

$$y' = \sigma e^{\sigma t}(C_1 \cos \rho t + C_2 \sin \rho t) + e^{\sigma t}(-C_1 \sin \rho t + C_2 \cos \rho t) \tag{6.28}$$

We assume a sampling period T, so that at the k^{th} sampling point, $t = kT$ gives y:

$$\begin{aligned} y(kT) &= e^{\sigma kT}(C_1 \cos(\rho kT) + C_2 \sin(\rho kT)) \\ y'(kT) &= \sigma e^{\sigma kT}(C_1 \cos(\rho kT) + C_2 \sin(\rho kT)) \\ &\quad + e^{\sigma kT}(-C_1 \sin(\rho kT) + C_2 \cos(\rho kT)) \end{aligned} \tag{6.29}$$

For simplicity, we define $y(kT)$ as y_k, $y'(kT)$ as y'_k. At the next sampling point k+1,

$$\begin{aligned} y_{k+1} &= e^{\sigma T} e^{\sigma kT}(C_1 \cos(\rho kT + \rho T) + C_2 \sin(\rho kT + \rho T)) \\ y'_{k+1} &= \sigma e^{\sigma T} e^{\sigma kT}(C_1 \cos(\rho kT + \rho T) + C_2 \sin(\rho kT + \rho T)) \\ &\quad + e^{\sigma T} e^{\sigma kT}(-C_1 \sin(\rho kT + \rho T) + C_2 \cos(\rho kT + \rho T)) \end{aligned} \tag{6.30}$$

Then we can use the k^{th} sample variables to represent the $(k+1)^{th}$ sample variables by eliminating the constants C_1 and C_2:

$$\begin{bmatrix} y_{k+1} \\ y'_{k+1} \\ (\ln A_{k+1})' \\ (\ln A_{k+1})'' \\ \ln \omega_{k+1} \\ (\ln \omega_{k+1})' \end{bmatrix} = \begin{bmatrix} e^{\sigma T} y_k \cos \rho T + \dfrac{e^{\rho T} \sin \rho T}{\rho}(y'_k - \sigma y_k) \\ e^{\sigma T}(y'(kT)(\dfrac{\sigma}{\rho}\sin \rho T + \cos \rho T) - \dfrac{y(kT)}{\rho}(\rho^2 + \sigma^2)\sin \rho T \\ (\ln A_k)' + T*(\ln A_k)'' \\ (\ln A_k)'' \\ \ln \omega_k + T*(\ln \omega_k)' \\ (\ln \omega_k)' \end{bmatrix} + \begin{bmatrix} 0 \\ 0 \\ 0 \\ w_1(\mathrm{k}) \\ 0 \\ w_2(\mathrm{k}) \end{bmatrix} \tag{6.31}$$

where $w_1(\mathrm{k})$ and $w_2(\mathrm{k})$ are white Gaussian noise. By incorporating the state space model into EKF, we can track the non-stationary sinusoidal signal and estimate its parameters.

6.5 Extended Kalman Filter

After obtaining FDTM, an EKF [114] is used to track the non-stationary sinusoidal signal. The system and measurement equations are assumed to be:

$$\begin{aligned} x_k &= g_f(x_{k-1}, k) + Bw_k \\ y_k &= Cx_k + v_k \\ w_k &= N(0, Q) \\ v_k &= N(0, R) \end{aligned} \tag{6.32}$$

where $g_f(x, w)$ is the FDTM state-space evolution model and y_k is the measurement at sampling point *k*. The process noise w_k represents w_1 and w_2 with covariance *Q* and the measurement noise is v_k with covariance R.

For the prediction step, we have:

$$\begin{cases} \hat{x}_{k|k} = g_f(x_{k-1|k-1}) + K_k(y_k - C\hat{x}_{k-1|k-1}) \\ K_k = P_k C^T (\mathrm{C}\, P_{k|k-1} C^T + BR_k B^T)^{-1} \\ P_{k|k} = (I - CK_k)(F_k P_{k-1|k-1} F_k^T + Q) \end{cases} \tag{6.33}$$

where

$$F_k = \left.\frac{\partial g_f(x)}{\partial x}\right|_{\hat{x}_{k-1}}, \; Q = diag(0,0,0,w_1,0,w_2) \tag{6.34}$$

and K_k and $P_{k|k}$ are the Kalman filter gain and error covariance matrices at k^{th} sampling point. The measurement update equations are the same as in (6.25).

6.6 Simulation

In this section, the FDTM (EKF) is applied to the batching and two-phase flow benchmarks (as discussed in Chapter 1), together with the other state space models in order to compare the tracking performance. FCTM is not included since it is a continuous time model and FDTM is a full discrete form of FCTM. In addition they are compared to the Complex Bandpass methods developed earlier in order to explore the performance and the possibility of applications.

6.6.1 Batching from Empty-to-full Benchmark Simulation

Here we compare the new EKF models with CBF-CNF (the best complex signal processing technique for the empty-to-full batch benchmark) along with the current EKF methods on the empty-to-full batch benchmark. The figures below show the resulting tracking performance, RMSEs and amplitude tracking delay for each method along with the tracking errors.

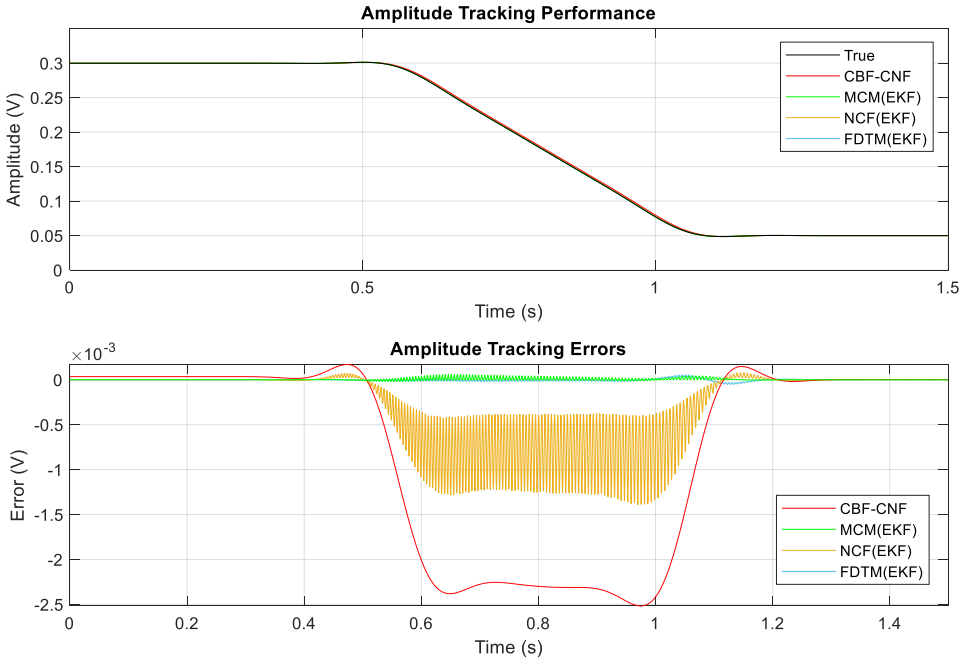


Figure 6.1: Amplitude tracking performance for empty-to-full batch process

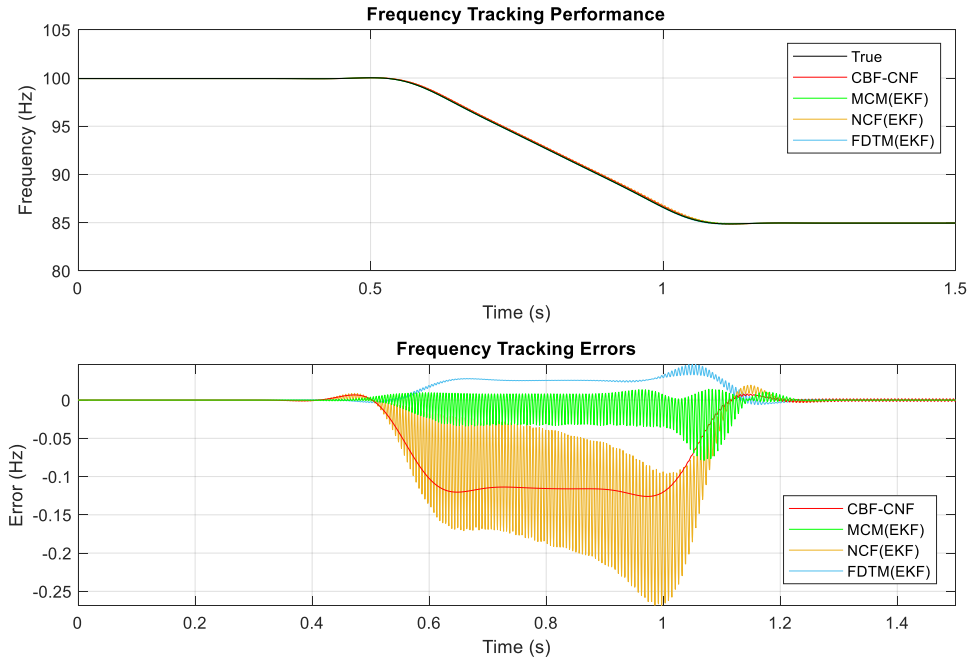


Figure 6.2: Frequency tracking performance for empty-to-full batch process

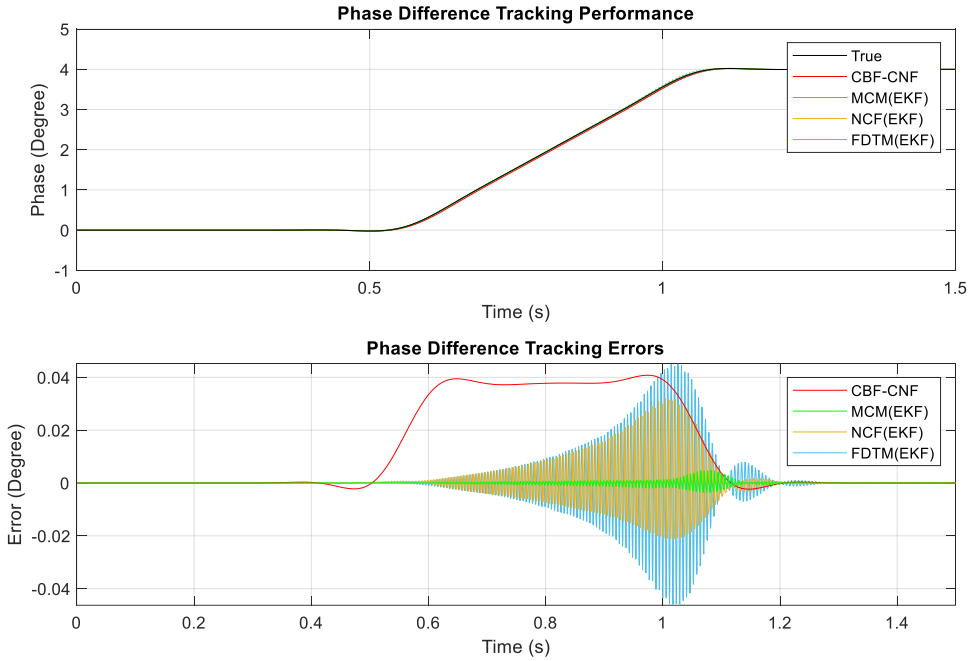


Figure 6.3: Phase difference tracking performance for empty-to-full batch process

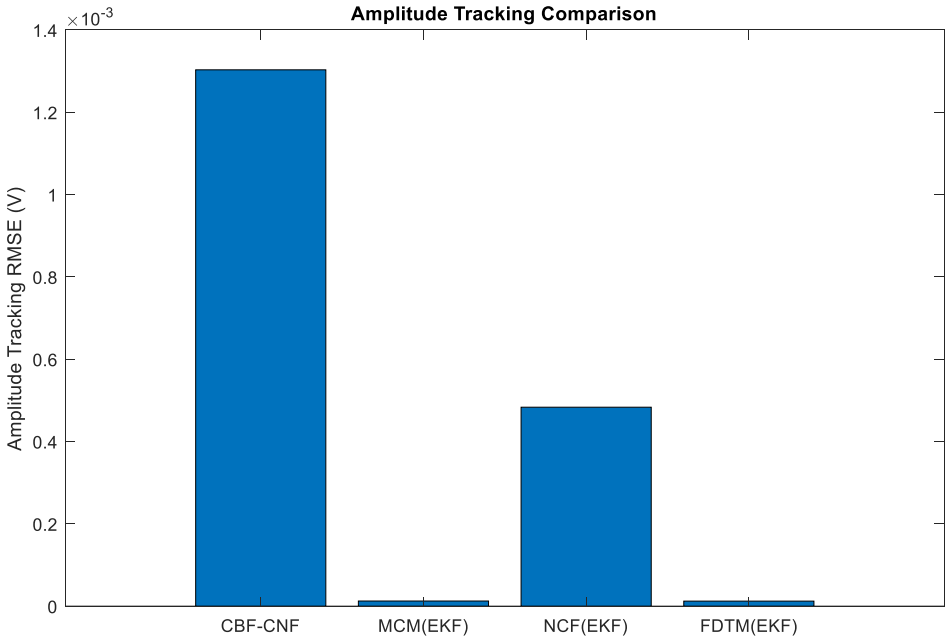


Figure 6.4: Amplitude tracking RMSEs comparison for batch simulation

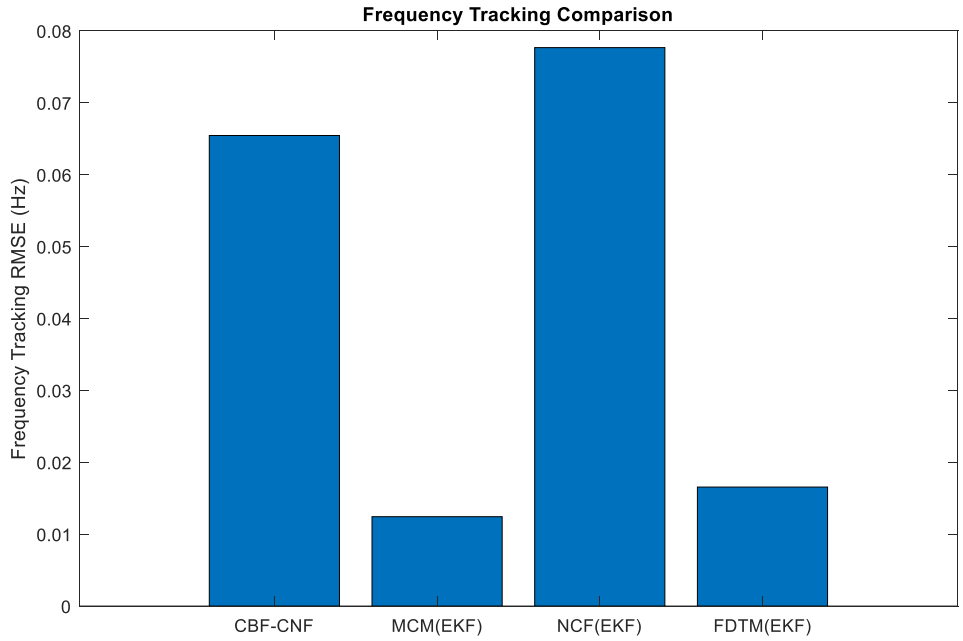


Figure 6.5: Frequency tracking RMSEs comparison for batch simulation

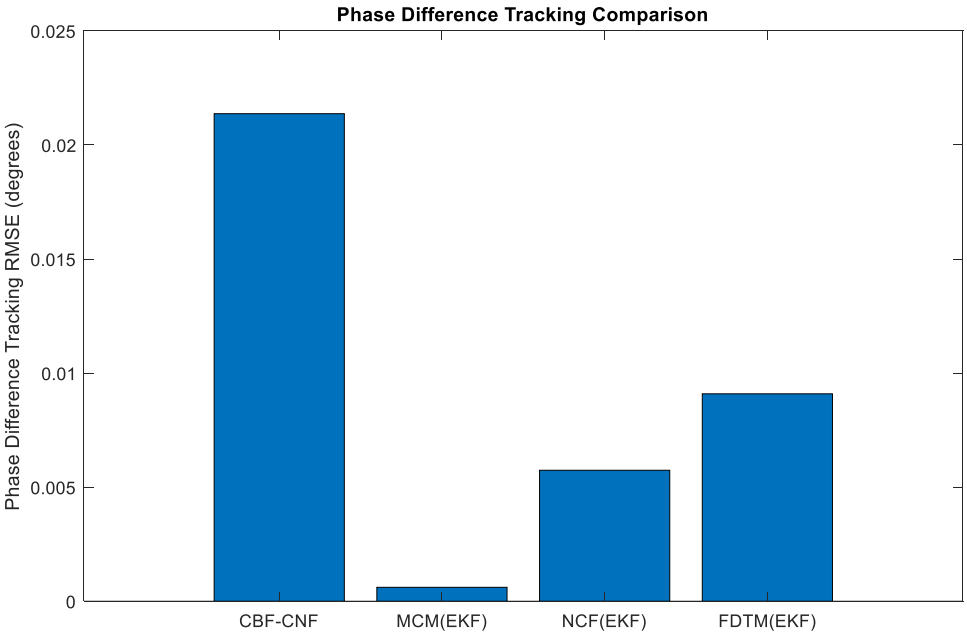


Figure 6.6: Phase difference tracking RMSEs comparison for batch simulation

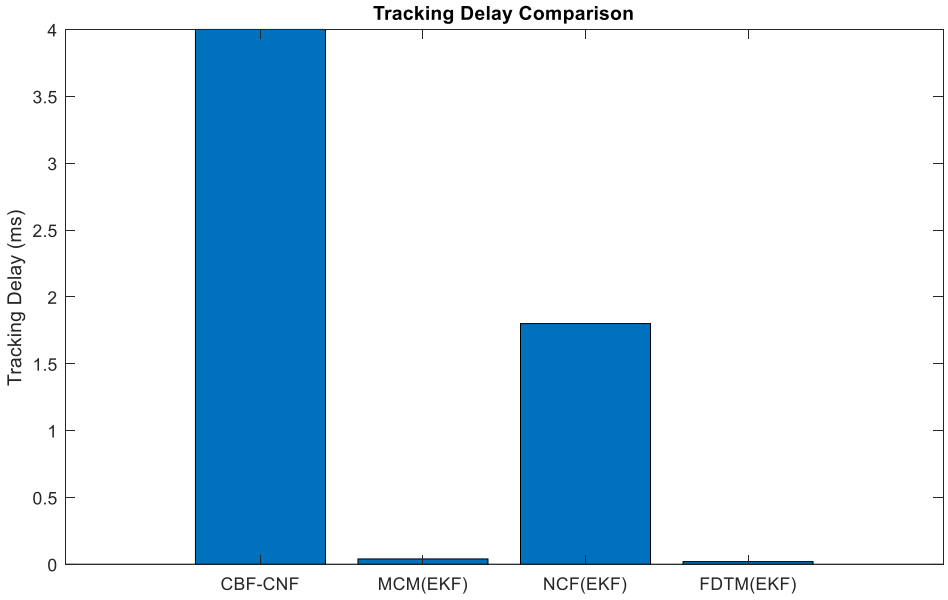


Figure 6.7: Amplitude tracking delay comparison

From these results, we observe that FDTM and MCM have the best performance with the shortest amplitude tracking delay, which is reduced by as much as 10 times compared to CBF-CNF for MCM and FDTM. This suggests that the FDTM and MCM with EKF could be promising techniques for empty-to-full batch process with fast dynamic performance.

6.6.2 Batching from Empty-to-full Experimental Sensor Data Test

The newly developed EKF based methods have also been tested with experimental batching from empty-to-full process sensor data alongside with CBF-CNF to validate their performance. Figures below show their relevant performance:

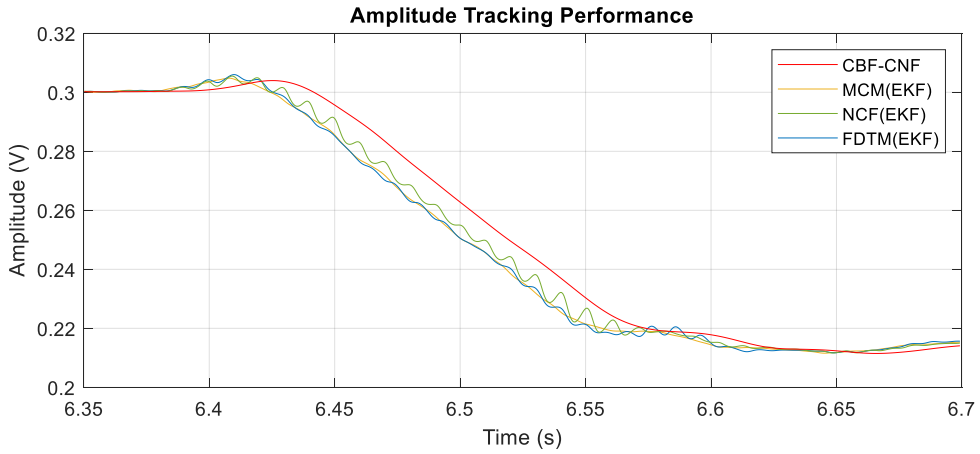


Figure 6.8: Amplitude tracking performance using batching sensor data

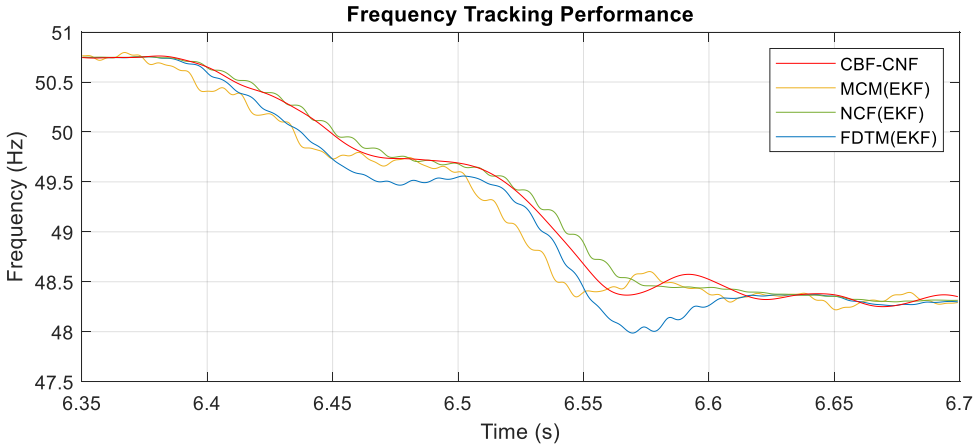


Figure 6.9: Frequency tracking performance using batching sensor data

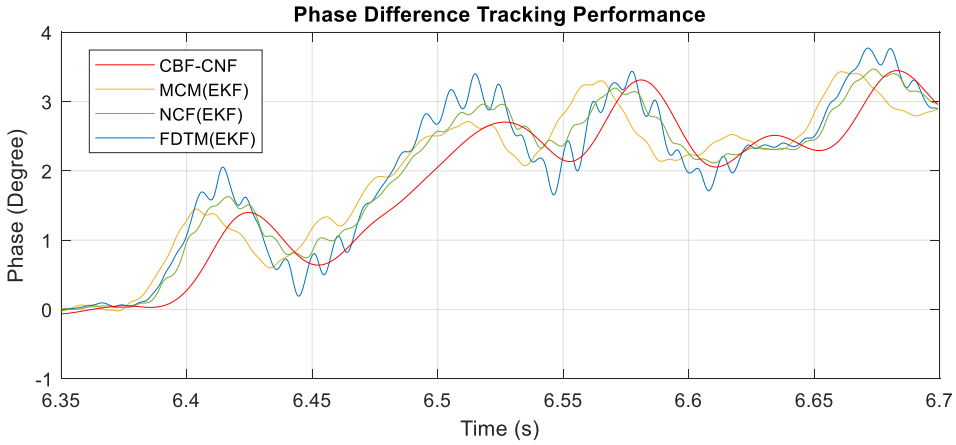


Figure 6.10: Phase difference tracking performance using batching sensor data

The results show that the EKF based FDTM and MCM methods lead the varying trend especially for amplitude tracking. For phase difference tracking results, EKF based methods show greater variation than CBF-CNF. This again verifies the argument offered in Chapter 3 that when true parameters are unknown, an exact comparison is difficult. However using faster algorithms like EKF based methods, it is possible to observe more varying details especially for phase difference during the transition period.

6.6.3 Two-phase Flow Benchmark

We also test FDTM with MCM and NCF for the two-phase benchmark using EKF. The CBF-CNF method is also included since it performed best among old and new methods tested in Section 4.4.3. The figures below show the tracking performance and RMSEs with no noise:

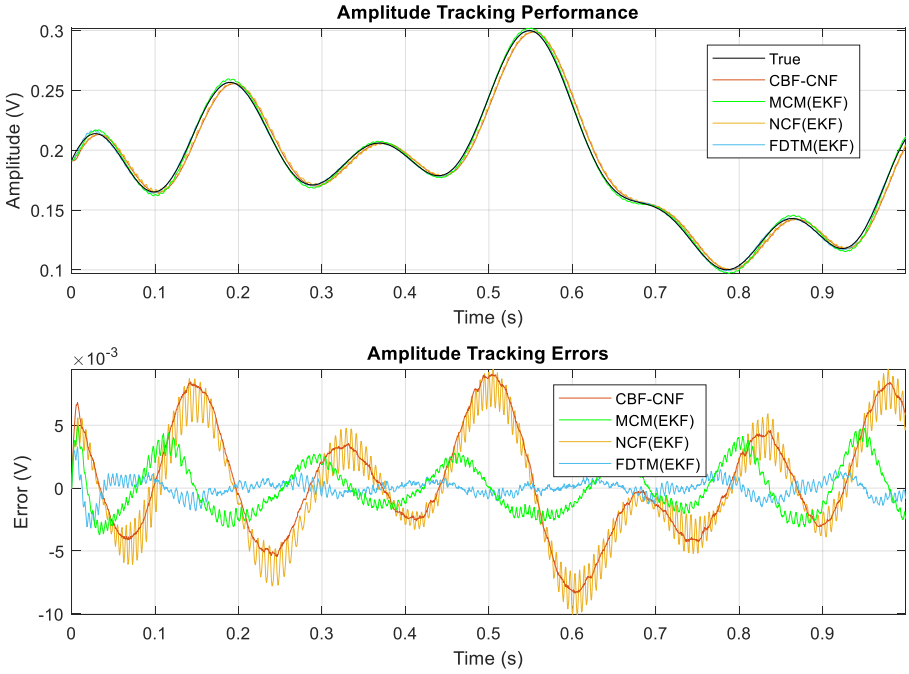


Figure 6.11: Amplitude tracking performance with no noise

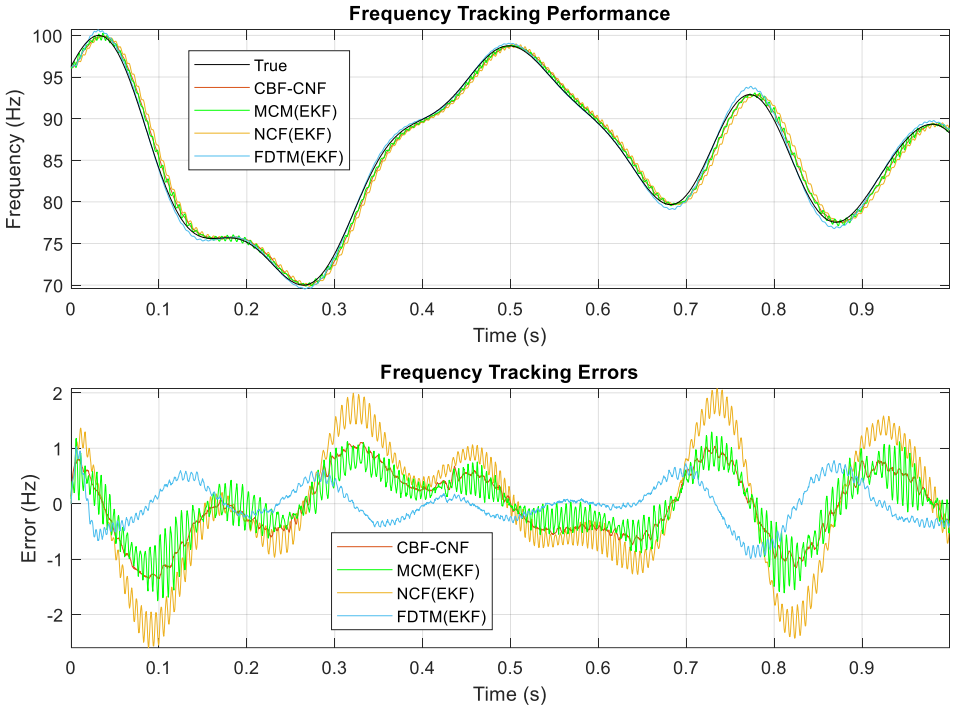


Figure 6.12: Frequency tracking performance with no noise

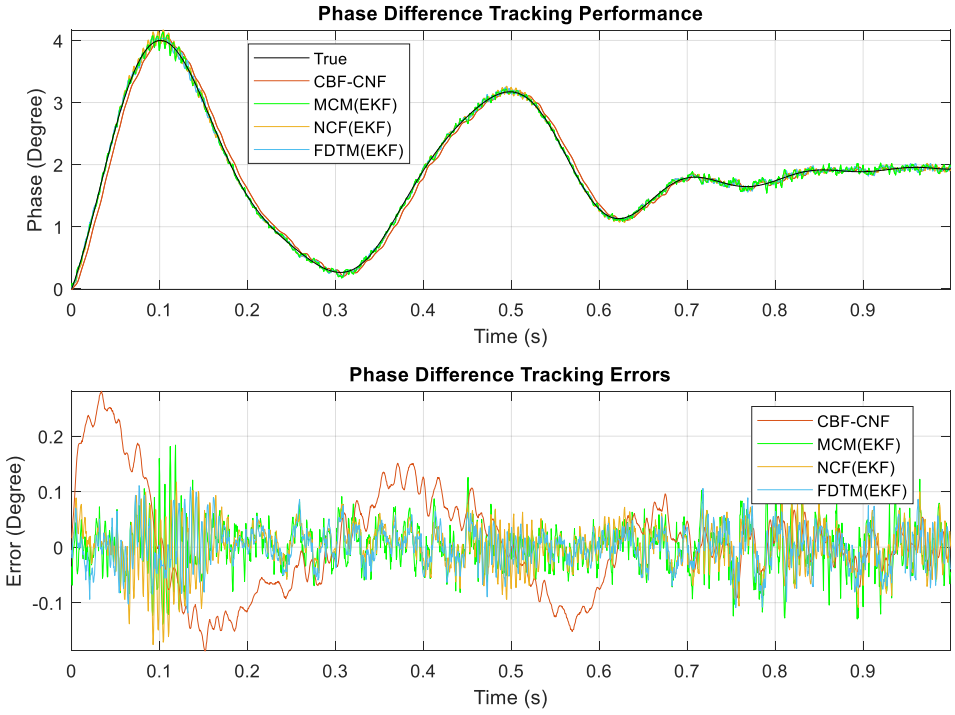


Figure 6.13: Phase difference tracking performance with no noise

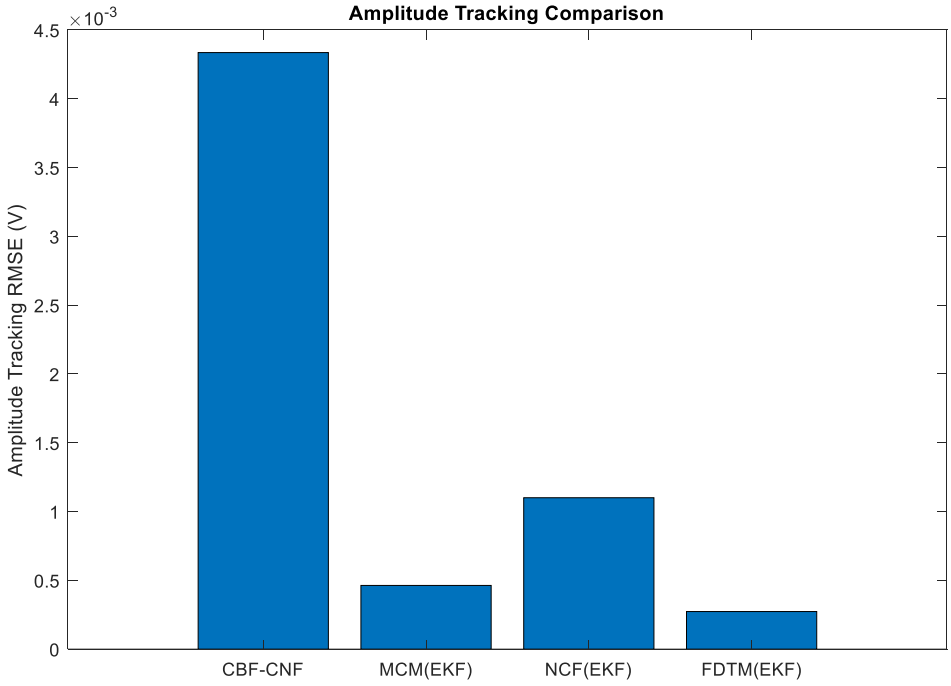


Figure 6.14: Amplitude tracking RMSEs comparison for two-phase simulation

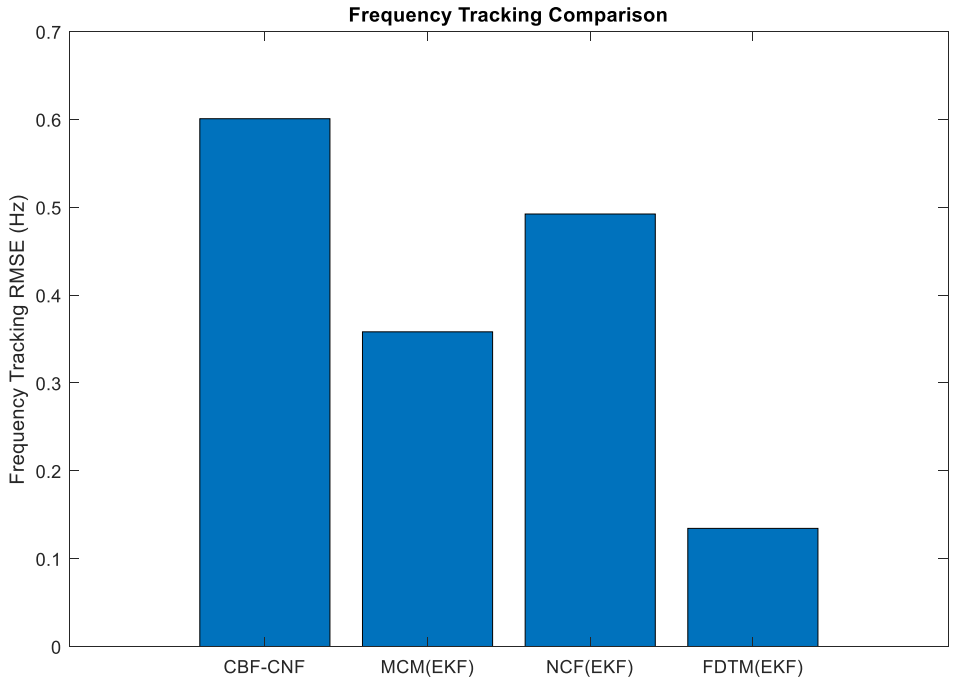


Figure 6.15: Frequency tracking RMSEs comparison for two-phase simulation

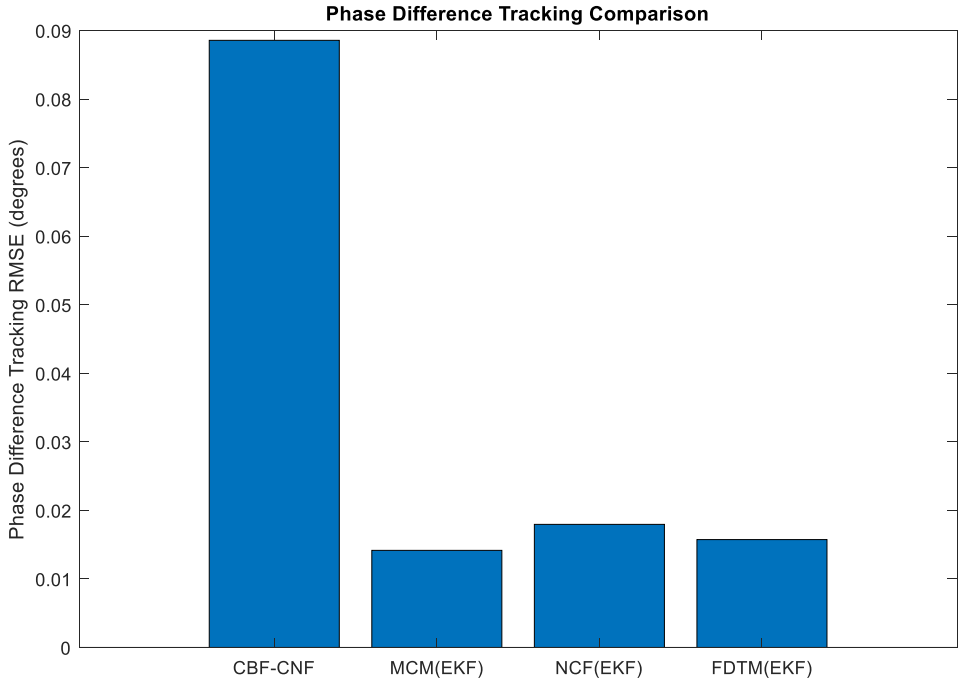


Figure 6.16: Phase difference tracking RMSEs comparison for two-phase simulation

From the figures, we can observe that the MCM and FDTM perform best with a small delay for no noise situation, which is the same result found in the empty-to-full batch benchmark. Also the EKF based methods perform better than the CBF-CNF, especially for amplitude and phase difference tracking, which shows good potential for better control and better measurement for Coriolis flowmeters during a two-phase flow.

Different noise levels are now added to the two-phase flow simulation benchmark to test each method's robustness against spurious inputs. However, the EKF based methods need to tune the measurement noise covariance R parameter as mentioned in Section 6.4. Without proper tuning, the EKF based methods can diverge and become unstable; this needs extra care when implementing them in industrial applications. The figures below show the tracking results' RMSEs for each method:

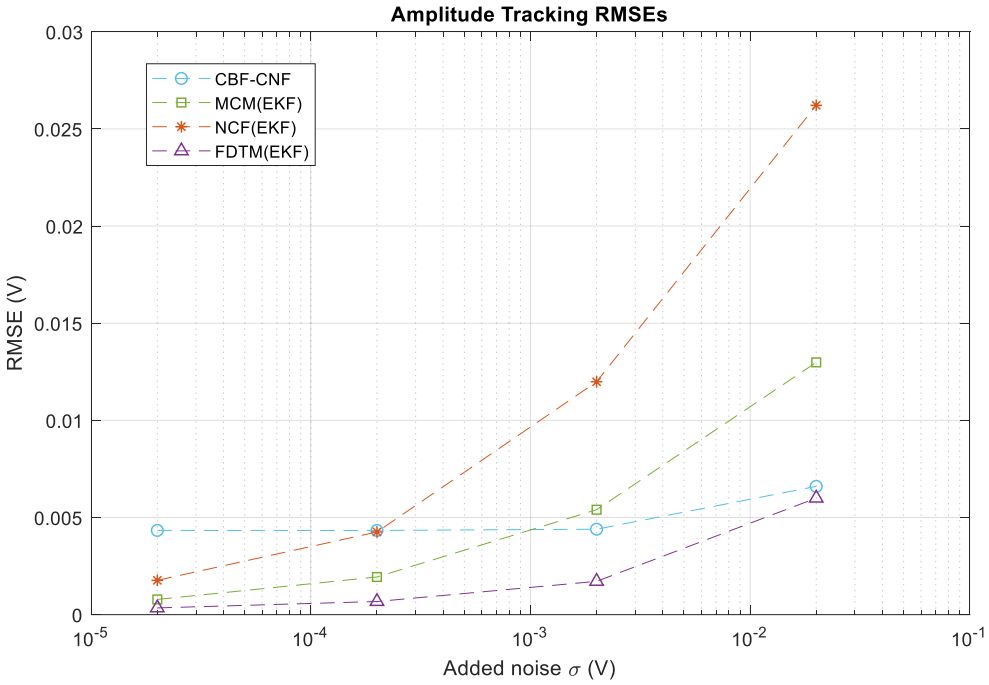


Figure 6.17: Amplitude tracking RMSEs at different level of noise

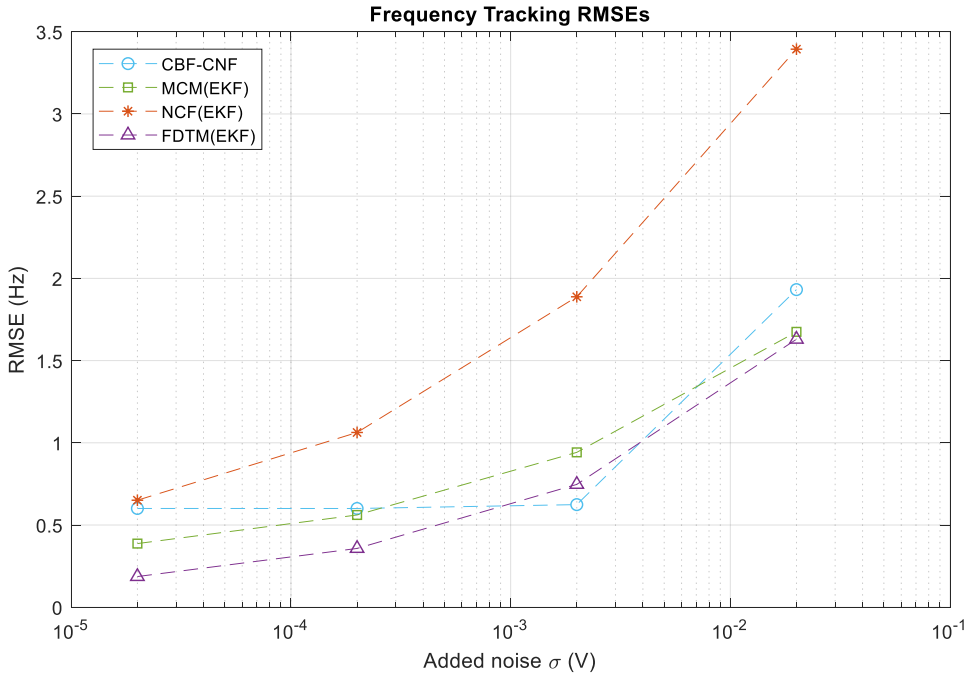


Figure 6.18: Frequency tracking RMSEs at different level of noise

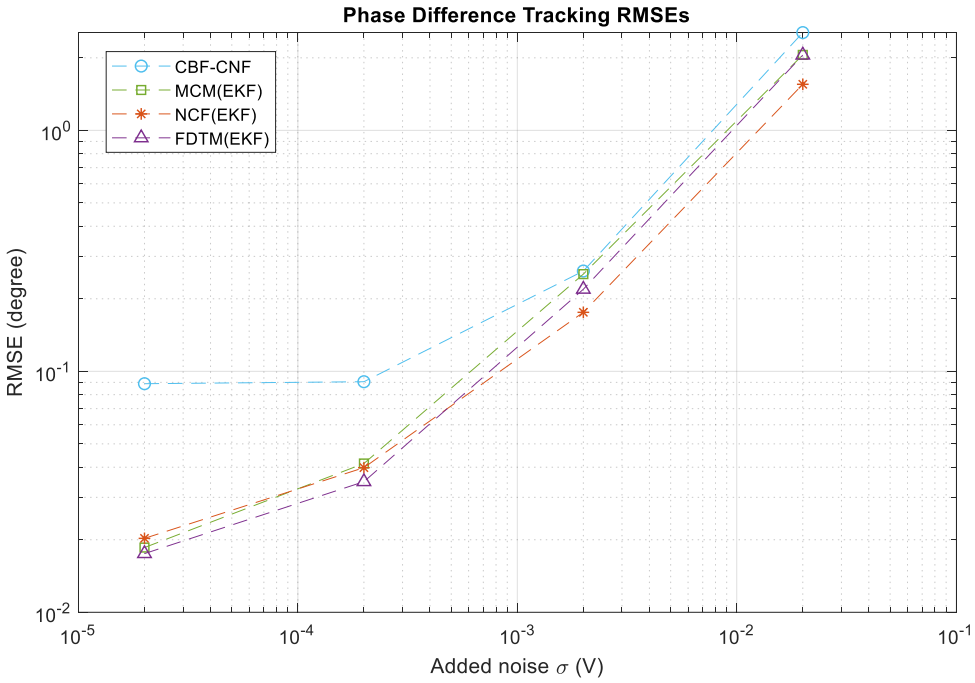


Figure 6.19: Phase difference tracking RMSEs at different level of noise

From the results, when the SNR decreases with the addition of noise, overall the FDTM maintains a better performance than the other methods, showing a good ability to suppress noise. Also it shows that phase difference measurement results become noisy at low SNR levels and hence Coriolis flowmeters should be set to operate above minimum amplitude in order to generate good measurement results. Overall the FDTM with EKF is a promising new signal processing technique for empty-to-full batch processing and two-phase flow applications.

6.6.4 Two-phase Flow Varying GVF Sensor Data Test

Fast varying GVF sensor data are applied to the EKF based methods alongside with the best performing previous method (CBF-CNF) to observe and validate their performance. The figures below show the tracking results:

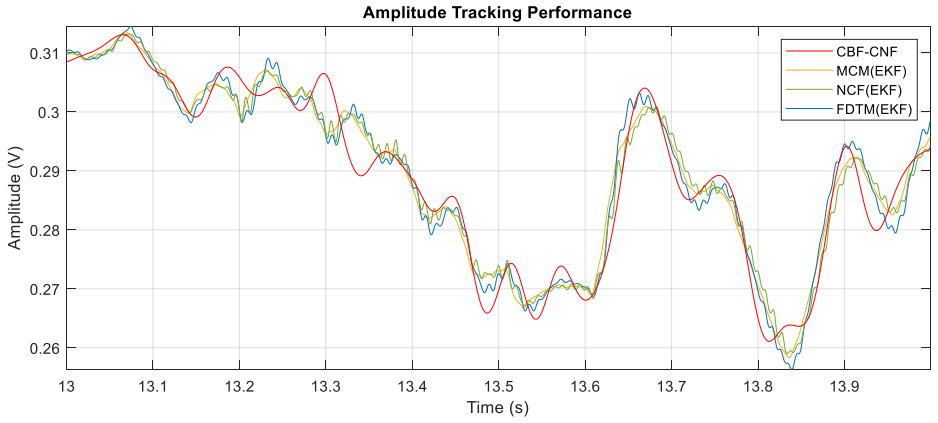


Figure 6.20: Amplitude tracking performance using two-phase sensor data

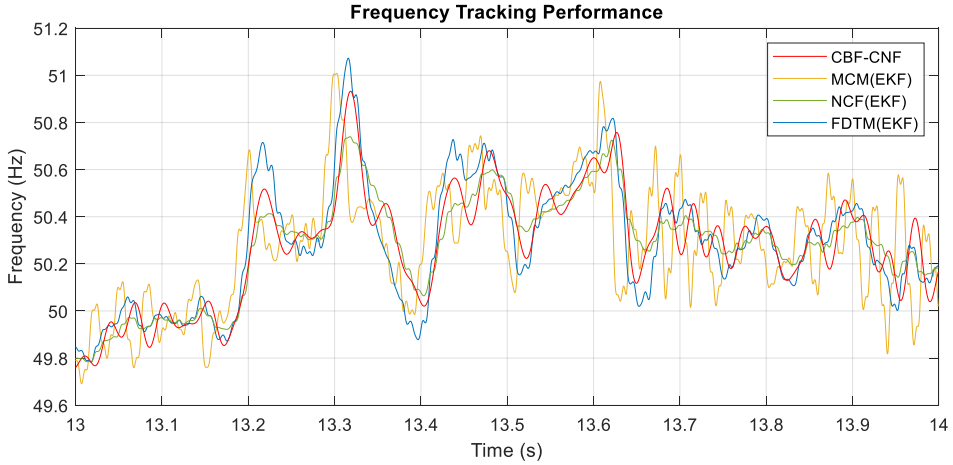


Figure 6.21: Frequency tracking performance using two-phase sensor data

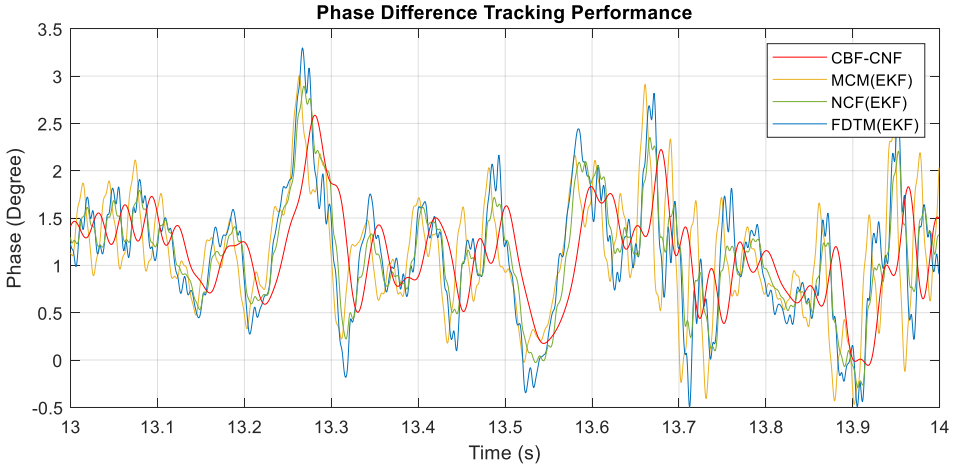


Figure 6.22: Phase difference tracking performance using two-phase sensor data

From the results, the EKF perform better compared to CBF-CNF. However, as with the batching from empty-to-full sensor data test, the EKF based tracking method results are not as smooth as those of CBF-CNF, especially for phase difference. Again this verifies the previous argument that the true parameters variations are unknown, which makes an exact comparison of different methods using sensor data difficult.

6.7 Summary

In this chapter, we have presented a new state space model for the non-stationary sinusoidal signal tracking problem which could form a possible solution for Coriolis flowmeter signal processing. Existing state space models (MCM and NCF) have been compared with FDTM using the two benchmark simulations. The FDTM has a small tracking delay with a good ability to suppress noise and therefore it may be a promising technique for Coriolis flowmeter two-phase flow applications.

Before applying FDTM to Coriolis flowmeter signal processing, several challenges still need to be addressed:

i. The phase response and group delay of the FDTM (EKF) should be explicitly calculated for the Coriolis flowmeter operating frequency range in order to generate the in-phase driver signal.

ii. The measurement and process noise parameters of the EKF should be tuned adaptively to match the varying SNR of the sensor signal. Inappropriate tuning will cause instability to the EKF.

iii. Matrix calculations in embedded systems generally take a lot of computational cost and need efficient and careful design.

7. CONCLUSION

This thesis has developed new Coriolis flowmeter signal processing techniques for challenging two-phase flow situations. Notably, a set of benchmark tests have been developed derived from empty-to-full batching and multi-phase conditions, and have been used for comparing a range of signal processing methods. Comparisons have been developed via simulation (to test 'pure' algorithm performance), and also (via a signal generator) as real-time voltage signals to test complete hardware/software implementations. Then current signal processing techniques, including DTFT combined with ANF, Zero-crossing, QD combined with DPLL and Hilbert Transform, have been tested with different benchmarks. Two new signal processing approaches have been developed, one based on complex signal processing techniques and the other based on FDTM combined with EKF. Both new techniques in simulation show better dynamic performance and noise suppression than the current methods. CBF improves the dynamic response by roughly two times compared to the zero-crossing and QD (DPLL based) methods while CBF-CNF improves by as much as 3 times. Both new methods

maintain good measurement results at different levels of noise. EKF based FDTM further improves dynamic performance by as much as 10 times compared to CBF-CNF (though with a higher sensitivity to noise). Overall, these new approaches offer promising signal processing techniques for Coriolis flowmeters, especially for two-phase flow conditions.

The CBF and CBF-CNF techniques have been implemented in a real-time embedded system using C++. Signal generator tests have been carried out to validate the algorithms. With the new algorithms, single-phase flow tests were carried out to verify that the prototype transmitter together with the flow tube operates properly as a Coriolis flowmeter. Then two-phase flow tests were carried out, while comparing results with the research equivalent of a commercial product – the Oxbox transmitter - using the same commercial flow tube.

From two-phase flow experiments, the amplitude standard deviation for the CBF and CBF-CNF methods are at least two times better than the Oxbox in 50% of the experiments. For frequency, the CBF and CBF-CNF methods are roughly 2.5 times better than the Oxbox for 50% of the experiments. For phase difference, the improvement is more significant than for amplitude and frequency, with 50% of values with more than 3 times improvement compared to Oxbox. The improvements in frequency and phase lead to corresponding improvements in the mass flow and density performance. The mass flow rate measurement results show that the new transmitters perform at least 3 times better than Oxbox for 50% of measured values and at least two times better for 90% of the measured values. For density result, the improvement is very promising where 50% values are almost 10 times better than Oxbox and show at least

two times improvement up to 80% GVF points. The final 20% of GVF points still show improvement compared to the Oxbox. In general, CBF shows better noise resistance, including lower standard deviations in the presence of two-phase flow, while CBF-CNF shows a faster dynamic response, for example when batching from empty-to-full.

To illustrate how the improved results are reflected in reduced signal tracking errors, the figures below show the improved measurement results for mass flow rate and density at 0.5 kg/s water mass flow rate with GVF ranging from 1% to 85% using the CBF algorithm.

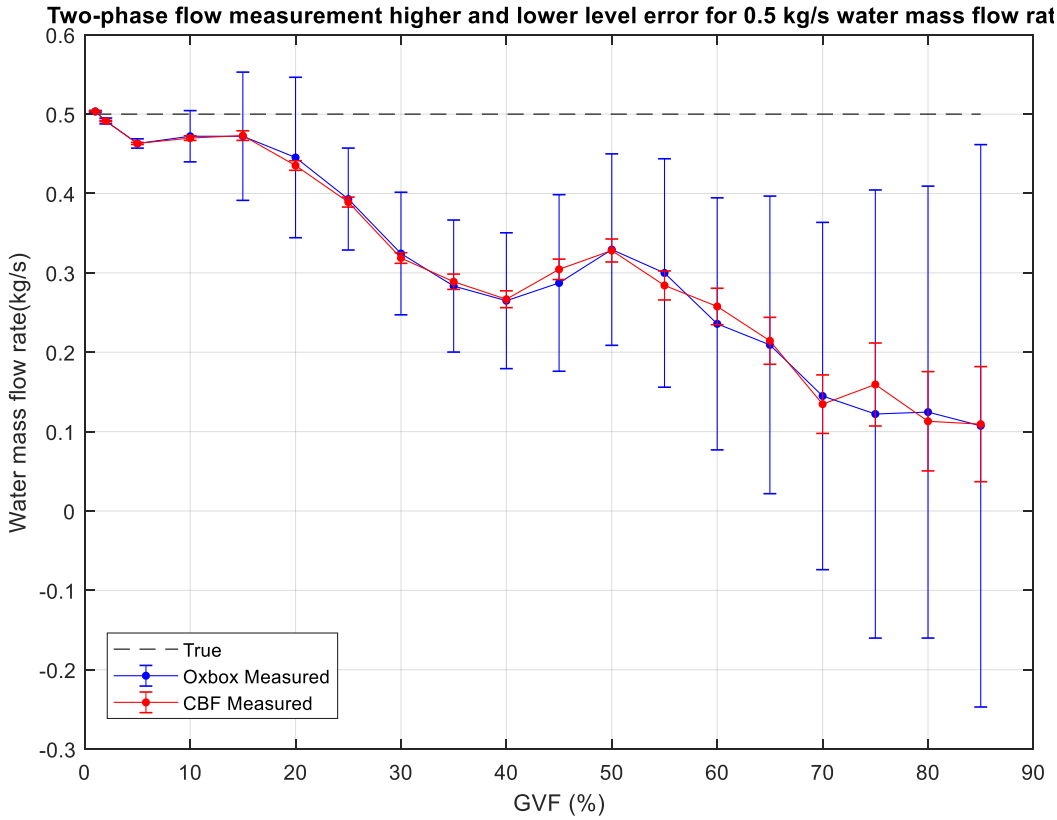


Figure 7.1: Comparison of standard deviations for Oxbox and CBF techniques for mass flow rate at 0.5 kg/s

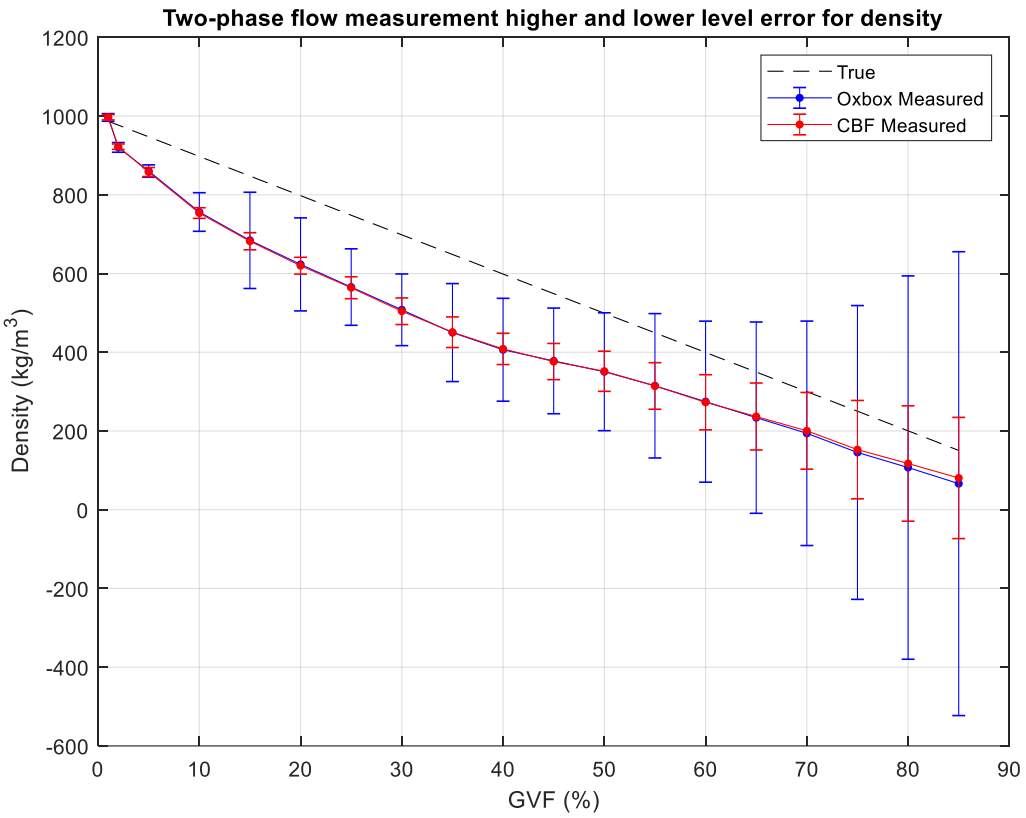


Figure 7.2: Comparison of standard deviations for Oxbox and CBF techniques for density at 0.5 kg/s

From the result, compared to the Oxbox result, CBF and CBF-CNF method show clear improvement across the whole GVF by reducing signal tracking errors and makes the measurement result usable for fluid measurement error correction. Again the effects of the signal tracking errors feeding into the fluid measurement errors can be clearly observed from the above plots. Reduced signal tracking errors not only decrease measurement standard deviation but also help to improve fluid measurement correction.

Finally, a new EKF based method is presented which demonstrates further performance improvements using the simulation benchmarks, but the implementation into hardware and flow experiments have not yet been carried out.

7.1 Further Improvements

There are still many problems and challenges that need to be addressed. In addition, new techniques are emerging in the Coriolis flowmeter arena which provide potential solutions for better measurement of batching from empty-to-full, two-phase flow and other challenging situations.

7.1.1 Experimental Facility

Firstly, the Oxford experimental facility for batching from empty-to-full needs to be further improved to carry out batching from empty-to-full and back to empty test as described in [98]. This will allow for detailed analysis of the full-to-empty transition to complete the current work on empty-to-full. Of course, many industrial applications both start and end with an empty flowtube, so this experimental setup would be more representative of industrial operation. In addition, the mass offset between the weigh scale and Coriolis flowmeter total (as discussed in Section 5.4) will be eliminated and will make the experiments more comprehensive. The proposed improvement will involve using compressed air to clear the water remaining in the flow tube at the end of the batch – as practiced for example in the bunkering industry.

Based on my experience of using the two-phase flow experiment facilities, further useful improvements can be identified. During the two-phase flow test, when the GVF and water flow rate are set to a high level, the water pump output shows some variation due to the back pressure applied by the pump. Thus it causes true flow rate variation that affects the reference liquid and gas phase. To improve this, a controlled regulation valve could be added to the two-phase flow line as mentioned in Figure 5.22. This

arrangement is mentioned in [47] where it is claimed that the maximum deviation of water reference flow rate at different GVF is reduced to 1.85%. However, the relationship between the water pump controller, regulation valve controller and air reference valve controller needs to be carefully designed to avoid interaction between the components.

7.1.2 Faster Batching Applications

Faster batching applications can also be carried out to further test the dynamic performance of newly developed signal processing algorithms. For example Coriolis metering is being used to monitor fast fuel injection for car engines [115], where the 'batch' time can be as short as 1 ms. This and other applications could benefit from the improved dynamic response of the new signal processing methods developed in this thesis.

7.1.3 Fluid Measurement Error Correction

Since this thesis has focused on reducing signal tracking errors during two-phase flow, techniques for correcting fluid measurement errors can also be further explored and developed. Current techniques for correcting the fluid measurement error are based on results obtained with large signal tracking errors. By adopting better signal processing algorithms, such as the complex bandpass techniques developed here, signal tracking errors can be reduced (as shown in Figure 7.1 and 7.2), which will in turn, reduces the noise fed into the measurement error models, resulting in improved performance. Currently, the common approach to correct fluid measurement errors are using neural networks [99] or soft computing [59] techniques by training models using data from

different flow rates, GVF, pressure, etc. With the recent booming development in neural networks and machine learning, different kinds of neural networks such as Deep Neural Network (DNN) [116][117], Convolutional Neural Network (CNN) [118], Recurrent Neural Network (RNN) [119], reinforcement learning [120] and so on are now available and these can be explored for better correction of the fluid measurement error, especially when combined with the improved signal processing algorithms. With increased training input data, many neural networks have been approved to improve the performance by a large scale. For example, in the famous ImageNet image recognition challenge [121], Krizhevsky et al. [118] achieved 15.3% recognition error rate with DNNs outperforming the previous best recognition error rate which is 26.2%. This suggests another future work programme which is automated two-phase flow testing and collecting of experiment data to generate more input to train the neural networks. Hence the two-phase flow experiment rig could be improved by increasing the level of automation.

7.1.4 Two/Multi-mode Vibration

Another technological trend in two-phase flow measurement for Coriolis flowmeters is to drive the flow tube in two or more modes of vibration simultaneously, with the intention of generating independent measures of amplitude, frequency and phase difference for each mode. Thus combining the two measurement results, compensating for two-phase mass flow rate and density is possible, where additional information may be provided because the mass flow and density errors (and therefore the observed measurements) may be different for the two modes of vibration. It will also benefit further multi-phase processing (e.g. water, oil and gas mixed together) by observing

dual mode results tracked individually. Krohne [69], Endress+Hauser [122], [123] and Micro Motion [124] have filed several patents for dual mode vibration and have carried out initial compensation for density using the two mode measurement information together. Hence this approach can potentially provide simpler, more robust and/or more accurate corrections for the fluid measurement errors. However, dual mode vibration can suffer from decreased SNR for individual mode sensor signals, which will increase measurement noise since the overall drive current is limited for intrinsic safety requirements. Dual mode vibration needs to share drive energy between each mode and the vibration amplitude of each mode will therefore be reduced compared to single mode vibration. Hence the signal tracking errors are increased for each mode measurement and using better signal processing algorithms to suppress noise is even more important. Thus combining the correction of the fluid measurement errors using dual mode vibration with better signal processing algorithms to decrease signal tracking error could be a promising solution for two-phase flow measurement using Coriolis flowmeters.

However, dual mode also raises another challenge for the current CBF approach. Coriolis sensor signals have numerous peaks other than the desired vibration mode - arising from other modes of flowtube vibration, harmonics, and so on. Improved results could be obtained by applying higher filter attenuation in these regions. This would be particularly important with dual mode operation where the amplitude of each mode is high and therefore cross-contamination is likely when tracking each mode. One possibility is to extend the complex notch filtering approach currently used to remove negative frequencies to target known, undesired positive frequencies.

7.1.5 Better Control Algorithm Design

Another area that is worth exploring is designing a better control algorithm by modelling signal tracking time delay. Most of current control algorithms used in Coriolis flowmeters are simple PI control algorithms [22] since they are relatively robust and reliable. Although control algorithm design is out of the scope of this thesis, there are many researchers focusing on modelling and predicting measurement time delay in control using techniques such as Model Predictive Control (MPC), forward prediction control, PI controller design for time delay systems, fuzzy predictive PI control, which are not yet applied to Coriolis flowmeters and could be explored. Another interesting research area in control is to adopt an active control strategy to make the Coriolis flowmeters less sensitive to external vibration noise [125], [126]. By adopting a better control algorithm, it is expected that the dynamic performance of flow tube could be further improved, which helps to reduce signal tracking errors during two-phase flow measurement.

7.1.6 Kalman Filter Improvement

Kalman filtering based techniques are good candidates for further improving the measurement and control for Coriolis flowmeters. But they need to tune the process and measurement noise parameters for inputs with different levels of noise. One possible way of overcoming this issue is to adaptively tune the parameters based on the inputs, which is also known as adaptive Kalman filtering [127]–[129], which can be further combined with robust Kalman filtering [130]–[133] to ensure the accuracy and

robustness of the method. However, the application of these techniques to Coriolis flowmeters is unexplored yet and needs careful implementation.

Overall, with the new signal processing algorithms discussed in this thesis, Coriolis flowmeters are a promising approach to accurately measuring challenging batching and two-phase flow situations.

8.REFERENCES

[1] M. Henry, “Self-validating digital Coriolis mass flow meter,” *Comput. Control Eng. J.*, vol. 11, no. 5, pp. 219–227, Oct. 2000.

[2] T. Wang and R. Baker, “Coriolis flowmeters: a review of developments over the past 20 years, and an assessment of the state of the art and likely future directions,” *Flow Meas. Instrum.*, vol. 40, pp. 99–123, Dec. 2014.

[3] R. C. Baker, “Coriolis flowmeters: industrial practice and published information,” *Flow Meas. Instrum.*, vol. 5, no. 4, pp. 229–246, Oct. 1994.

[4] Y. Li and S. Lee, “A Fast-Response True-Mass-Rate Flowmeter,” *Trans. ASME*, vol. 75, pp. 835–841, 1953.

[5] J. Smith, C. Sasenz, and D. Stainton, “Apparatus and method for measuring fluid mass flow,” G.B. Patent 1535817, December 13, 1978.

[6] P. Tullis and J. Smith, “Coriolis flowmeter,” *NEL Fluid Mech. Silver Jubil. Conf.*, 1979, p. Paper 6.3.

[7] F. Durst and H. Raszillier, “Flow in a Rotating Straight Pipe, With a View on Coriolis Mass Flow Meters,” *J. Fluids Eng.*, vol. 112, no. 2, p. 149, Jun. 1990.

[8] H. Raszillier and F. Durst, “Coriolis-effect in mass flow metering,” *Arch. Appl. Mech.*, vol. 61, no. 3, pp. 192–214, Feb. 1990.

[9] G. Sultan and J. Hemp, “Modelling of the Coriolis mass flowmeter,” *J. Sound Vib.*, vol. 132, no. 3, pp. 473–489, Aug. 1989.

[10] B. M. Cox and F. A. Gonzalez, “Coriolis mass flow rate metering means,” U.S. Patent 4127028, June 07, 1977.

[11] K. T. Liu and D. E. Revus, “Net-oil computer improves water-cut determination,” *Oil Gas J.; (United States)*, vol. 86:51, Dec. 1988.

[12] M. P. Henry and D. W. Clarke, “The self-validating sensor: rationale, definitions and examples,” *Control Eng. Pract.*, vol. 1, no. 4, pp. 585–610, Aug. 1993.

[13] M. P. Henry, D. W. Clarke, N. Archer, J. Bowles, M. J. Leahy, R. P. Liu, J. Vignos, and F. B. Zhou, “A self-validating digital Coriolis mass-flow meter: an overview,” *Control Eng. Pract.*, vol. 8, no. 5, pp. 487–506, May 2000.

[14] M. Tombs, M. Henry, H. Yeung, and R. Lansangan, “Coriolis mass flow meter developments: increasing the range of applications in oil & gas production and processing,” *22nd North Sea flow metering Work.*, 2004.

[15] M. Henry, M. Duta, M. Tombs, H. Yeung, and W. Mattar, “How a Coriolis mass flow meter can operate in two-phase (gas/liquid) flow,” *Tech. Pap. ISA*, 2004, vol. 454, pp. 17–30.

[16] M. Henry, H. Yeung, and M. Mattar, “Coriolis Flow: The two phases of Coriolis

flow," *InTech Mag.*, 2005.

[17] Y. H. Morita A., "Method of measuring phase difference in Coriolis mass flowmeter," *Proc. Int. Conf. Adv. Instrum. Control*, 1996.

[18] M. Henry, C. Clark, and B. Cheesewright, "Pushing coriolis mass flowmeters to the limit," *IEE Comput. Control Eng.*, vol. 14, no. 3, pp. 24–28, 2003.

[19] D. Harrold, "coriolis flowmeters. new and improved: what's that mean?," *Control Eng*, p. 48, 2001.

[20] H. V. Derby, T. Bose, and S. Rajan, "Method and apparatus for adaptive line enhancement in Coriolis mass flow meter measurement," U.S. Patent 5555190, September 10, 1996.

[21] M. P. Henry, D. W. Clarke, and J. H. Vignos, "Digital Flowmeter," U.S. Patent 6311136, November 26, 1997.

[22] D. W. Clarke, "Non-linear Control of the Oscillation Amplitude of a Coriolis Mass-Flow Meter," *Eur. J. Control*, vol. 4, no. 3, pp. 196–207, Jan. 1998.

[23] M. P. Henry, "Coriolis meter digital transmiter technology," *IEE Comput. Control Eng.*, vol. 14, no. 4, pp. 34–35, 2003.

[24] C. Clark, M. Zamora, M. Henry, R. Cheesewright, and M. Henry, "The dynamic performance of a new ultra-fast response Coriolis flow meter," *Flow Meas. Instrum.*, vol. 17, no. 6, pp. 391–398, Dec. 2006.

[25] J. Kutin, A. Smrečnik, and I. Bajsić, "Phase-locking control of the Coriolis meter's resonance frequency based on virtual instrumentation," *Sensors Actuators A Phys.*, vol. 104, no. 1, pp. 86–93, Mar. 2003.

[26] K. H. Röck, “Advanced Phasor Control Of Coriolis Mass Flow Meter,” *XIX IMEKO world Congr.*, 2009.

[27] H. C. Corben, *Classical Mechanics*. Dover Publications Inc, 1960.

[28] M. Atia, “Improved Coriolis mass-flow Meter,” University of Oxford, 1999.

[29] E. Kreyszig, *Advanced engineering mathematics*. Wiley, 2011.

[30] “ISO 10790:2015 - Measurement of fluid flow in closed conduits -- Guidance to the selection, installation and use of Coriolis flowmeters (mass flow, density and volume flow measurements),” 2015. [Online]. Available: https://www.iso.org/standard/57407.html. [Accessed: 20-Aug-2018].

[31] J. E. Smith, “Method and structure for flow measurement,” U.S. Patent 4187721, July 20, 1978.

[32] M. Henry, M. Tombs, M. Duta, F. Zhou, R. Mercado, F. Kenyery, J. Shen, M. Morles, C. Garcia, and R. Langansan, “Two-phase flow metering of heavy oil using a Coriolis mass flow meter: A case study,” *Flow Meas. Instrum.*, vol. 17, no. 6, pp. 399–413, Dec. 2006.

[33] D. Gregory, M. West, R. Paton, R. Casimiro, S. Boo, Y. K. Low, M. Henry, M. Tombs, M. Duta, F. Zhou, M. Zamora, R. Mercado, M. Machacek, and D. Clarke, “Two-Phase Flow Metering Using A Large Coriolis Mass Flow Meter Applied To Ship Fuel Bunkering,” *Meas. Control*, vol. 41, pp. 208–212, 2008.

[34] M. Henry, “Precision Polyethylene Batch Processing,” *Control Mag.*, Jul. 2004.

[35] J. Reizner, “Batch accuracy: Good, bad, and ugly of Coriolis,” *InTech*, vol. 52, no. 3, pp. 1–4, Mar. 2005.

[36] C. Clark, R. Cheesewright, and S. Wang, “Prediction of the Dynamic Performance of Fast Response Coriolis Meter Systems,” *IEEE Trans. Instrum. Meas.*, vol. 57, no. 1, pp. 95–99, Jan. 2008.

[37] M. Henry, M. Zamora, C. Clarke, R. Cheesewright, and W. Mattar, “The dynamic response of Coriolis mass flow meters: Theory and applications,” *4th Annu. Emerg. Technol. Conf. ISA EXPO 2004*, 2004.

[38] M. Zamora and M. P. Henry, “An FPGA Implementation of a Digital Coriolis Mass Flow Metering Drive System,” *IEEE Trans. Ind. Electron.*, vol. 55, no. 7, pp. 2820–2831, Jul. 2008.

[39] R. J. Reizner, “Coriolis - The almost perfect flow meter,” *Comput. Control Eng. J.*, vol. 14, no. 4, pp. 28–33, Sep. 2003.

[40] W. H. Ahmed and B. I. Ismail, “Innovative Techniques For Two-Phase Flow Measurements,” *Recent Patents Electr. Electron. Eng. (Formerly Recent Patents Electr. Eng.*, vol. 1, no. 1, p. 1–13(13), 2008.

[41] NFOGM, “Handbook of Multiphase Flow Metering,” 2005.

[42] K. Adefila, Y. Yan, L. Sun, and T. Wang, “Flow measurement of wet CO2 using an averaging pitot tube and coriolis mass flowmeters,” *Int. J. Greenh. Gas Control*, vol. 63, pp. 289–295, Aug. 2017.

[43] L. Wang, Y. Yan, X. Wang, T. Wang, Q. Duan, and W. Zhang, “Mass flow measurement of gas-liquid two-phase CO2 in CCS transportation pipelines using Coriolis flowmeters,” *Int. J. Greenh. Gas Control*, vol. 68, pp. 269–275, Jan. 2018.

[44] J. A. Weinstein, "The motion of bubbles and particles in oscillating liquids with applications to multiphase flow in Coriolis meters". Thesis (Ph.D.)--University of Colorado at Boulder, 2008.

[45] N. T. Basse, “A review of the theory of Coriolis flowmeter measurement errors due to entrained particles,” *Flow Meas. Instrum.*, vol. 37, pp. 107–118, Jun. 2014.

[46] N. T. Basse, “Coriolis flowmeter damping for two-phase flow due to decoupling,” *Flow Meas. Instrum.*, vol. 52, pp. 40–52, Dec. 2016.

[47] J. Liu, T. Wang, Y. Yan, X. Wang, and L. Wang, “Investigations into the behaviours of Coriolis flowmeters under air-water two-phase flow conditions on an optimized experimental platform,” *2018 IEEE Int. Instrum. Meas. Technol. Conf.*, 2018, pp. 1–6.

[48] J. Hemp and J. Kutin, “Theory of errors in Coriolis flowmeter readings due to compressibility of the fluid being metered,” *Flow Meas. Instrum.*, vol. 17, no. 6, pp. 359–369, Dec. 2006.

[49] D. L. Gysling, “An aeroelastic model of Coriolis mass and density meters operating on aerated mixtures,” *Flow Meas. Instrum.*, vol. 18, no. 2, pp. 69–77, Apr. 2007.

[50] J. Hemp and G. Sultan, “On the theory and performance of Coriolis mass flowmeters,” *Int. Conf. mass flow Meas.*, 1989, pp. 21–22.

[51] J. A. Weinstein, D. R. Kassoy, and M. J. Bell, “Experimental study of oscillatory motion of particles and bubbles with applications to Coriolis flow meters,” *Phys.*

Fluids, vol. 20, no. 10, p. 103306, Oct. 2008.

[52] L. Xing, Y. Geng, C. Hua, H. Zhu, A. Rieder, W. Drahm, and M. Bezdek, "A combination method for metering gas–liquid two-phase flows of low liquid loading applying ultrasonic and Coriolis flowmeters," *Flow Meas. Instrum.*, vol. 37, pp. 135–143, Jun. 2014.

[53] M. Henry, M. Tombs, and F. Zhou, "Field experience of well testing using multiphase Coriolis metering," *Flow Meas. Instrum.*, vol. 52, pp. 121–136, Dec. 2016.

[54] H. Yeung and J. Hemp, "Coriolis meters in two phase conditions," *Comput. Control Eng.*, vol. 14, no. 4, pp. 36–36, Aug. 2003.

[55] M. Anklin, W. Drahm, and A. Rieder, "Coriolis mass flowmeters: Overview of the current state of the art and latest research," *Flow Meas. Instrum.*, vol. 17, no. 6, pp. 317–323, Dec. 2006.

[56] M. Henry, M. Tombs, M. Duta, F. Zhou, R. Mercado, F. Kenyery, J. Shen, M. Morles, C. Garcia, and R. Langansan, "Two-phase flow metering of heavy oil using a Coriolis mass flow meter: A case study," *Flow Meas. Instrum.*, vol. 17, no. 6, pp. 399–413, Dec. 2006.

[57] T. Wang, "Coriolis mass flowmeter," U.S. Patent 10024703, April 17, 2015.

[58] Krohne, "OPTIMASS series Complete portfolio of Coriolis mass flowmeters." [Online]. Available: https://cdn.krohne.com/dlc/CA_OPTIMASS_Highlights_en_180612.pdf.

[59] Y. Yan, L. Wang, T. Wang, X. Wang, Y. Hu, and Q. Duan, "Application of soft

computing techniques to multiphase flow measurement: A review," *Flow Meas. Instrum.*, vol. 60, pp. 30–43, Apr. 2018.

[60] M. Li and M. P. Henry, "Signal Processing Methods for Coriolis Mass Flow Metering in Two-Phase Flow Conditions," *2016 IEEE Int. Conf. Ind. Technol.*, 2016, pp. 690–695.

[61] G. Falcone, G. F. Hewitt, C. Alimonti, and B. Harrison, "Multiphase Flow Metering: Current Trends and Future Developments," *J. Pet. Technol.*, vol. 54, no. 04, pp. 77–84, Apr. 2002.

[62] C. Xie, I. Atkinson, and C. Lenn, "Multiphase flow measurement in oil and gas production," *5th World Congr. Ind. Process Tomogr.*, pp. 723–736, 2007.

[63] R. Thorn, G. A. Johansen, and B. T. Hjertaker, "Three-phase flow measurement in the petroleum industry," *Meas. Sci. Technol.*, vol. 24, no. 1, p. 012003, Jan. 2013.

[64] H. Van Santen, Z. I. Kolar, and A. M. Scheers, "Photon energy selection for dual energy γ- and/or X-ray absorption composition measurements in oil-water-gas mixtures," *Nucl. Geophys.*, vol. 9, no. 3, pp. 193–202, 1995.

[65] M. Sharifi and B. Young, "Electrical resistance tomography (ert) applications to chemical engineering," *Chem. Eng. Res. Des.*, vol. 91, no. 9, pp. 1625–1645, 2013.

[66] J. Jia, Y. Faraj, Q. Wang, C. Xie, G. Oddie, K. Primrose, and C. Qiu, "A new visualisation and measurement technology for water continuous multiphase flows," *Flow Meas. Instrum.*, vol. 46, pp. 204–212, Dec. 2015.

[67] M. Henry, M. Tombs, M. Zamora, and F. Zhou, “Coriolis mass flow metering for three-phase flow: A case study,” *Flow Meas. Instrum.*, vol. 30, pp. 112–122, Apr. 2013.

[68] M. Tombs, F. Zhou, and M. Henry, “Two-phase coriolis mass flow metering with high viscosity oil,” *Flow Meas. Instrum.*, vol. 59, pp. 23–27, Mar. 2018.

[69] K. Kolahi and R. Storm, “Process for operation of a Coriolis mass flow rate measurement device,” U.S. Patent 7647841, July 03, 2007.

[70] D. Kuttler and C. Matt, “Coriolis flowmeter and method for flow measurement,” World Patent 2006128774, May 08, 2006.

[71] M. P. Henry, D. W. Clarke, and J. H. Vignos, “Digital Flowmeter,” U.S. Patent 6311136, October 30, 2001.

[72] G. R. Duffill, S. M. Jones, and A. T. Patten, “Meter electronics and methods for determining a liquid flow fraction in a gas flow material,” U.S. Patent 7974792, July 05, 2011.

[73] C. Clark, R. Cheesewright, S. Wang, M. Henry, M. Zamora, and M. Tombs, “A radically new dynamic response capability for Coriolis flow meters,” *Sensors Actuators A Phys.*, vol. 123–124, pp. 54–62, Sep. 2005.

[74] C. Clark, R. Cheesewright, and S. Wang, “Prediction of the Dynamic Performance of Fast Response Coriolis Meter Systems,” *IEEE Trans. Instrum. Meas.*, vol. 57, no. 1, pp. 95–99, Jan. 2008.

[75] M. P. Henry, C. Clark, M. Duta, R. Cheesewright, and M. Tombs, “Response of a Coriolis mass flow meter to step changes in flow rate,” *Flow Meas. Instrum.*, vol.

14, no. 3, pp. 109–118, Jun. 2003.

[76] C. Clark and R. Cheesewright, “Experimental determination of the dynamic response of Coriolis mass flow meters,” *Flow Meas. Instrum.*, vol. 17, no. 1, pp. 39–47, Mar. 2006.

[77] M. Henry, “‘Breakthrough’ Coriolis meter allows filling machine to operate with exceptional precision,” *Control Eng. Eur.*, pp. 8–9, 2004.

[78] M. P. Henry, C. Clark, M. Duta, R. Cheesewright, and M. Tombs, “Response of a Coriolis mass flow meter to step changes in flow rate,” *Flow Meas. Instrum.*, vol. 14, no. 3, pp. 109–118, Jun. 2003.

[79] Y. Tu, H. Yang, H. Zhang, and X. Liu, “CMF Signal Processing Method Based on Feedback Corrected ANF and Hilbert Transformation,” *Meas. Sci. Rev.*, vol. 14, no. 1, pp. 41–47, 2014.

[80] H. Y. Yang, Y. Q. Tu, and H. T. Zhang, “A Frequency Tracking Method Based on Improved Adaptive Notch Filter for Coriolis Mass Flowmeter,” *Appl. Mech. Mater.*, vol. 128–129, pp. 450–456, Oct. 2011.

[81] W. Ni and K. Xu, “An improved signal processing method for Coriolis mass flowmeter based on time-varying signal model,” *Fifth World Congr. Intell. Control Autom. (IEEE Cat. No.04EX788)*, 2004, vol. 4, pp. 3787–3790.

[82] G. Yin, L. Guo, and X. Li, “An Amplitude Adaptive Notch Filter for Grid Signal Processing,” *IEEE Trans. Power Electron.*, vol. 28, no. 6, pp. 2638–2641, Jun. 2013.

[83] Y. Tu and H. Zhang, “Method for CMF Signal Processing Based on the

Recursive DTFT Algorithm With Negative Frequency Contribution," *IEEE Trans. Instrum. Meas.*, vol. 57, no. 11, pp. 2647–2654, Nov. 2008.

[84] T. Shen, Y. Tu, and H. Zhang, "A novel time varying signal processing method for Coriolis mass flowmeter.," *Rev. Sci. Instrum.*, vol. 85, no. 6, p. 065116, Jun. 2014.

[85] H. Wen, J. Zhang, Z. Meng, S. Guo, F. Li, and Y. Yang, "Harmonic Estimation Using Symmetrical Interpolation FFT Based on Triangular Self-Convolution Window," *IEEE Trans. Ind. Informatics*, vol. 11, no. 1, pp. 16–26, Feb. 2015.

[86] T. Shen, Y. Tu, M. Li, and H. Zhang, "A new phase difference measurement algorithm for extreme frequency signals based on discrete time Fourier transform with negative frequency contribution.," *Rev. Sci. Instrum.*, vol. 86, no. 1, p. 015104, Jan. 2015.

[87] Y. Tu, T. Shen, H. Zhang, and M. Li, "Two New Sliding DTFT Algorithms for Phase Difference Measurement Based on a New Kind of Windows," *Meas. Sci. Rev.*, vol. 14, no. 6, pp. 350–356, Jan. 2014.

[88] Q.-L. Hou, K.-J. Xu, M. Fang, Y. Shi, B.-B. Tao, and R.-W. Jiang, "Gas–Liquid Two-Phase Flow Correction Method for Digital CMF," *IEEE Trans. Instrum. Meas.*, vol. 63, no. 10, pp. 2396–2404, Oct. 2014.

[89] B. S. Freeman, "Digital phase locked loop signal processing for coriolis mass flow meter," U.S. Patent 5804741, September 08, 1998.

[90] T. Wray, "Coriolis flow meter with adjustable excitation phase," U.S. Patent 6332366, December 25, 2001.

[91] J. Ruoff, W. Gauchel, and H. Kück, “Advances in Signal Acquisition and Signal Processing of Coriolis Flow Meters,” *Procedia Eng.*, vol. 87, pp. 1585–1588, 2014.

[92] P. Yi, Y. Tu, M. Xie, and T. Shen, “Analysis of phase difference tracking methods for signal of coriolis mass flowmeter,” *Proc. 10th World Congr. Intell. Control Autom.*, 2012, pp. 4368–4373.

[93] K. W. Martin, “Complex Signal Processing is Not Complex,” *IEEE Trans. Circuits Syst. I Regul. Pap.*, vol. 51, no. 9, pp. 1823–1836, Sep. 2004.

[94] K. Wang, “The implementation of MSK based on DSP and complex analytic bandpass filter,” *2011 IEEE Int. Conf. Comput. Sci. Autom. Eng.*, 2011, vol. 1, pp. 229–232.

[95] A. Link, M. Burghoff, A. Salajegheh, D. Poeppel, L. Trahms, and C. Elster, “Comparing a template approach and complex bandpass filtering for single-trial analysis of auditory evoked M100.,” *Biomed. Tech. (Berl).*, vol. 52, no. 1, pp. 106–10, Feb. 2007.

[96] “Zedboard.” [Online]. Available: http://www.zedboard.org/. [Accessed: 03-Apr-2018].

[97] M. Henry and F. Zhou, “Flowmeter batching techniques,” U.S. Patent 20050274200, May 25, 2005.

[98] T. Wang and Y. Hussain, “Investigation of the batch measurement errors for single-straight tube Coriolis mass flowmeters,” *Flow Meas. Instrum.*, vol. 17, no. 6, pp. 383–390, Dec. 2006.

[99] R. P. Liu, M. J. Fuent, M. P. Henry, and M. D. Duta, “A neural network to correct mass flow errors caused by two-phase flow in a digital coriolis mass flowmeter,” *Flow Meas. Instrum.*, vol. 12, no. 1, pp. 53–63, Mar. 2001.

[100] R. Luke and J. Wouters, “Kalman Filter Based Estimation of Auditory Steady State Response Parameters,” *IEEE Trans. Neural Syst. Rehabil. Eng.*, vol. 25, no. 3, pp. 196–204, Mar. 2017.

[101] S. Reza, M. Ciobotaru, and V. G. Agelidis, “Accurate Estimation of Single-Phase Grid Voltage Fundamental Amplitude and Frequency by Using a Frequency Adaptive Linear Kalman Filter,” *IEEE J. Emerg. Sel. Top. Power Electron.*, vol. 4, no. 4, pp. 1226–1235, Dec. 2016.

[102] X. Wang and E. E. Yaz, “Smart Power Grid Synchronization With Fault Tolerant Nonlinear Estimation,” *IEEE Trans. Power Syst.*, vol. 31, no. 6, pp. 4806–4816, Nov. 2016.

[103] I. Sadinezhad and V. G. Agelidis, “Frequency Adaptive Least-Squares-Kalman Technique for Real-Time Voltage Envelope and Flicker Estimation,” *IEEE Trans. Ind. Electron.*, vol. 59, no. 8, pp. 3330–3341, Aug. 2012.

[104] J.-L. Dion, C. Stephan, G. Chevallier, and H. Festjens, “Tracking and removing modulated sinusoidal components: A solution based on the kurtosis and the Extended Kalman Filter,” *Mech. Syst. Signal Process.*, vol. 38, no. 2, pp. 428–439, Jul. 2013.

[105] S. Bittanti and S. M. Savaresi, “On the parametrization and design of an extended Kalman filter frequency tracker,” *IEEE Trans. Automat. Contr.*, vol. 45, no. 9,

pp. 1718–1724, 2000.

[106] P. Regulski and V. Terzija, “Estimation of Frequency and Fundamental Power Components Using an Unscented Kalman Filter,” *IEEE Trans. Instrum. Meas.*, vol. 61, no. 4, pp. 952–962, Apr. 2012.

[107] N.-K. C. Nair and J. J. Liu, “Estimation of power quality using an unscented Kalman filter,” *TENCON 2007 - 2007 IEEE Reg. 10 Conf.*, 2007, pp. 1–4.

[108] F. Cupertino, E. Lavopa, P. Zanchetta, M. Sumner, and L. Salvatore, “Running DFT-Based PLL Algorithm for Frequency, Phase, and Amplitude Tracking in Aircraft Electrical Systems,” *IEEE Trans. Ind. Electron.*, vol. 58, no. 3, pp. 1027–1035, Mar. 2011.

[109] M. Chakraborty, “A New Adaptive Filter for Estimating and Tracking the Delay and the Amplitude of a Sinusoid,” *IEEE Trans. Instrum. Meas.*, vol. 59, no. 11, pp. 3049–3057, Nov. 2010.

[110] G. Yin, L. Guo, and X. Li, “An Amplitude Adaptive Notch Filter for Grid Signal Processing,” *IEEE Trans. Power Electron.*, vol. 28, no. 6, pp. 2638–2641, Jun. 2013.

[111] G. Saeed, H. Habib, S.-Z. Hamid, and A. Rassoul, “Instantaneous fundamental frequency estimation of non-stationary periodic signals using non-linear recursive filters,” *IET Signal Process.*, vol. 9, no. 2, pp. 143–153, Apr. 2015.

[112] H. Habib, T. Reza, and S.-Z. Hamid, “Extended Kalman Filter frequency tracker for nonstationary harmonic signals,” *Measurement*, vol. 45, no. 1, pp. 126–132, Jan. 2012.

[113] W. Ng, C. Ji, W. K. Ma, and H. C. So, “A study on particle filters for single-tone frequency tracking,” *IEEE Trans. Aerosp. Electron. Syst.*, vol. 45, no. 3, pp. 1111–1125, Jul. 2009.

[114] D. Simon, *Optimal state estimation : Kalman, H [infinity] and nonlinear approaches*. Wiley-Interscience, 2006.

[115] F. Leach, M. Davy, M. Henry, M. Tombs, and F. Zhou, “A New Method for Measuring Fuel Flow in an Individual Injection in Real Time,” *WCX SAE World Congr. Exp.*, 2018.

[116] G. Hinton, L. Deng, D. Yu, G. Dahl, A. Mohamed, N. Jaitly, A. Senior, V. Vanhoucke, P. Nguyen, T. Sainath, and B. Kingsbury, “Deep Neural Networks for Acoustic Modeling in Speech Recognition: The Shared Views of Four Research Groups,” *IEEE Signal Process. Mag.*, vol. 29, no. 6, pp. 82–97, Nov. 2012.

[117] Y. LeCun, Y. Bengio, and G. Hinton, “Deep learning,” *Nature*, vol. 521, p. 436, May 2015.

[118] A. Krizhevsky, I. Sutskever, and G. E. Hinton, “ImageNet Classification with Deep Convolutional Neural Networks,” in *Advances in Neural Information Processing Systems 25*, F. Pereira, C. J. C. Burges, L. Bottou, and K. Q. Weinberger, Eds. Curran Associates, Inc., 2012, pp. 1097–1105.

[119] A. Graves, A. Mohamed, and G. Hinton, “Speech recognition with deep recurrent neural networks,” *2013 IEEE Int. Conf. Acoust. Speech Signal Process.*, 2013, pp. 6645–6649.

[120] R. S. Sutton, A. G. Barto, and F. Bach, *Reinforcement learning : an introduction*, 2nd ed. MIT Press, 2018.

[121] "ImageNet Object Localization Challenge." [Online]. Available: https://www.kaggle.com/c/imagenet-object-localization-challenge. [Accessed: 21-Nov-2018].

[122] W. Drahm, A. Rieder, and H. Zhu, "Coriolis mass flow/density measuring devices and method for compensating measurement errors in such devices," World Patent 2006122881, May 18, 2005.

[123] D. Kuttler and C. Matt, "Coriolis flow meter and method for flow measurement," U.S. Patent 7289917, May 31, 2006.

[124] A. T. Patten, G. R. Duffill, and D. M. Henrot, "Coriolis flow meter and method for determining flow characteristics," U.S. Patent 7716995, March 29, 2005.

[125] L. van de Ridder, M. A. Beijen, W. B. J. Hakvoort, J. van Dijk, J. C. Lötters, and A. de Boer, "Active vibration isolation feedback control for Coriolis Mass-Flow Meters," *Control Eng. Pract.*, vol. 33, pp. 76–83, Dec. 2014.

[126] L. van de Ridder, W. B. J. Hakvoort, D. M. Brouwer, J. van Dijk, J. C. Lötters, and A. de Boer, "Coriolis mass-flow meter with integrated multi-DOF active vibration isolation," *Mechatronics*, vol. 36, pp. 167–179, Jun. 2016.

[127] L. Liu, H. Zhang, and K. Xiong, "Adaptive robust extended Kalman filter for nonlinear stochastic systems," *IET Control Theory Appl.*, vol. 2, no. 3, pp. 239–250, Mar. 2008.

[128] C. A. Lightcap and S. A. Banks, "An Extended Kalman Filter for Real-Time

Estimation and Control of a Rigid-Link Flexible-Joint Manipulator," *IEEE Trans. Control Syst. Technol.*, vol. 18, no. 1, pp. 91–103, Jan. 2010.

[129] M.-J. Yu, "INS/GPS Integration System using Adaptive Filter for Estimating Measurement Noise Variance," *IEEE Trans. Aerosp. Electron. Syst.*, vol. 48, no. 2, pp. 1786–1792, 2012.

[130] J. Zhao, M. Netto, and L. Mili, "A Robust Iterated Extended Kalman Filter for Power System Dynamic State Estimation," *IEEE Trans. Power Syst.*, vol. 32, no. 4, pp. 3205–3216, Jul. 2017.

[131] X. Kai, C. Wei, and L. Liu, "Robust Extended Kalman Filtering for Nonlinear Systems With Stochastic Uncertainties," *IEEE Trans. Syst. Man, Cybern. - Part A Syst. Humans*, vol. 40, no. 2, pp. 399–405, Mar. 2010.

[132] A. G. Kallapur, I. R. Petersen, and S. G. Anavatti, "A Discrete-Time Robust Extended Kalman Filter for Uncertain Systems With Sum Quadratic Constraints," *IEEE Trans. Automat. Contr.*, vol. 54, no. 4, pp. 850–854, Apr. 2009.

[133] A. Chatterjee and F. Matsuno, "A Neuro-Fuzzy Assisted Extended Kalman Filter-Based Approach for Simultaneous Localization and Mapping (SLAM) Problems," *IEEE Trans. Fuzzy Syst.*, vol. 15, no. 5, pp. 984–997, Oct. 2007.

9. APPENDICES

APPENDIX 1 210

APPENDIX 1

Amplitude independently changes (frequency stays at 100 Hz, phase difference stays at 2 ⁰)						
	Measured A Mean (mV)		**Measured F Mean (Hz)**		**Measured P Mean (⁰)**	
A (mV)	CBF	CBF-CNF	CBF	CBF-CNF	CBF	CBF-CNF
300.0	300.1572	300.1512	100.0025	100.0016	1.9997	1.9998
200.0	200.2403	200.226	99.9975	100.0016	2.0001	1.9998
100.0	100.1714	100.1626	99.9988	100.0016	2.0000	2.0002
50.0	50.2587	50.2690	100.0053	100.0016	2.0003	2.0004
Frequency independently changes (amplitude stays at 0.3 V, phase difference stays at 2 ⁰)						
	Measured A Mean (mV)		**Measured F Mean (Hz)**		**Measured P Mean (⁰)**	
F (Hz)	CBF	CBF-CNF	CBF	CBF-CNF	CBF	CBF-CNF
80.0	300.2355	300.3119	80.0130	80.0013	1.9994	1.9994
90.0	300.2121	300.3166	90.0145	90.0014	1.9995	1.9997
100.0	300.2131	300.3112	100.0090	100.0015	1.9997	2.0005
110.0	300.2856	300.2961	110.0017	110.0017	1.9997	2.0002
Phase difference independently changes (amplitude stays at 0.3 V, frequency stays at 100 Hz)						
	Measured A Mean (mV)		**Measured F Mean (Hz)**		**Measured P Mean (⁰)**	
P (⁰)	CBF	CBF-CNF	CBF	CBF-CNF	CBF	CBF-CNF
0.0	300.2943	300.2562	100.0076	100.0015	-0.0002	0.0001
1.0	300.2502	300.2400	99.9997	99.9967	0.9991	1.0002
2.0	300.1921	300.2999	99.9983	100.0015	1.9996	2.0004
3.0	300.2241	300.2552	100.0052	100.0016	2.9990	3.0005
4.0	300.2030	300.2465	100.0092	100.0015	3.9995	3.9999

Note: A represents amplitude, F represents frequency and P represents phase difference.

Table 9.1: Signal generator test mean result of new methods

Amplitude independently changes (frequency stays at 100 Hz, phase difference stays at 2 ⁰)						
	Measured A STD (%) (%)		**Measured F STD (%) (%)**		**Measured P STD (%) (%)**	
A (mV)	CBF	CBF-CNF	CBF	CBF-CNF	CBF	CBF-CNF
300.0	3.72e-3	3.34e-3	6.98e-4	1.00e-4	5.64e-4	6.92e-4
200.0	2.87e-3	3.65e-3	8.39e-4	1.14e-4	7.40e-4	7.16e-4
100.0	4.17e-3	5.03e-3	1.73e-3	1.97e-4	1.46e-3	1.83e-3
50.0	5.06e-3	5.50e-3	2.25e-3	3.69e-4	2.63e-3	2.26e-3
Frequency independently changes (amplitude stays at 0.3 V, phase difference stays at 2 ⁰)						
	Measured A STD (%) (%)		**Measured F STD (%) (%)**		**Measured P STD (%) (%)**	
F (Hz)	CBF	CBF-CNF	CBF	CBF-CNF	CBF	CBF-CNF
80.0	4.21e-3	3.61e-3	6.24e-4	4.55e-4	1.24e-3	1.19e-3
90.0	3.78e-3	3.30e-3	5.65e-4	7.66e-4	8.38e-4	9.07e-4
100.0	3.61e-3	3.85e-3	5.92e-4	9.93e-5	7.90e-4	8.11e-4
110.0	1.68e-2	3.35e-3	7.97e-4	7.12e-5	6.42e-4	6.48e-4
Phase difference independently changes (amplitude stays at 0.3 V, frequency stays at 100 Hz)						
	Measured A STD (%) (%)		**Measured F STD (%) (%)**		**Measured P STD (%) (%)**	
P (⁰)	CBF	CBF-CNF	CBF	CBF-CNF	CBF	CBF-CNF
0.0	6.41e-3	3.17e-3	8.87e-4	1.01e-4	5.69e-4	6.72e-4
1.0	2.95e-3	3.45e-3	5.44e-4	1.04e-4	5.45e-4	7.20e-4
2.0	4.49e-3	3.63e-3	8.67e-4	1.03e-4	5.29e-4	7.17e-4
3.0	3.05e-3	3.79e-3	6.06e-4	1.03e-4	5.61e-4	7.43e-4
4.0	2.90e-3	3.30e-3	8.46e-4	1.04e-4	5.14e-4	7.28e-4

Note: Std represents standard deviation.

Table 9.2: Signal generator test standard deviation result of new transmitters